UNIVERSITÉ DE GENÈVE FACULTÉ DES SCIENCES

Département de physique nucléaire et corpusculaire Professeure T. Montaruli

Maximum Likelihood Estimation: a Method for Calibration, Reconstruction and Data Analysis of Cherenkov Telescopes

THÈSE

Présentée à la Faculté des sciences de l'Université de Genève
Pour obtenir le grade de Docteur ès sciences, mention physique

Par

Cyril Martin ALISPACH

de

Hemmiken (BL)

Thèse N°5527

GENÈVE

2020

UNIVERSITÉ DE GENÈVE

FACULTÉ DES SCIENCES

DOCTORAT ÈS SCIENCES, MENTION PHYSIQUE

Thèse de Monsieur Cyril Martin ALISPACH

intitulée :

«Maximum Likelihood Estimation: a Method for Calibration, Reconstruction and Data Analysis of Cherenkov Telescopes»

La Faculté des sciences, sur le préavis de Madame T. MONTARULI, professeure ordinaire et directrice de thèse (Département de physique nucléaire et corpusculaire), Monsieur T. GOLLING, professeur associé (Département de physique nucléaire et corpusculaire), Monsieur R. WALTER, docteur (Département d'astronomie) et Monsieur R. MODERSKI, professeur (Polish Acadaemy of Sciences, Warsaw, Poland), autorise l'impression de la présente thèse, sans exprimer d'opinion sur les propositions qui y sont énoncées.

Genève, le 17 décembre 2020

Thèse - 5527 -

Le Doyen

N.B. - La thèse doit porter la déclaration précédente et remplir les conditions énumérées dans les "Informations relatives aux thèses de doctorat à l'Université de Genève".

Résumé

Depuis la découverte en 1912 des rayons cosmiques, un nouveau domaine de recherche a été ouvert. L'étude des rayons cosmiques a permis aux physiciens de découvrir des nouvelles particules élémentaires. Cela a également permis d'ajuster le modèle standard de la physique des particules. Parmi les découvertes qui ont suivi, certaines ont été récompensées d'un prix Nobel de Physique. À ce jour, plusieurs des questions fondamentales adressées après la première observation du rayonnement cosmique n'ont pas trouvé de réponses. Par exemple, bien que théorisées, l'accélération, l'interaction et la propagation des rayons cosmiques à travers l'univers sont toujours sujet à débat. L'amélioration des techniques de détection des instruments spatiaux et terrestres ont permis de compléter le puzzle du rayonnement cosmique. La construction de la prochaine génération d'expériences d'astrophysique de haute énergie, qui repousse les limites de détection de source de rayonnement cosmique, pourrait répondre aux questions en suspens dans ce domaine de recherche. Plus particulièrement, ce domaine est en train d'entrer dans une nouvelle ère avec les débuts de l'astronomie à longueurs d'ondes multiples et à messagers multiples.

Cette thèse se concentre sur deux expériences d'astrophysique des hautes énergies: le Cherenkov Telescope Array (CTA: réseau de télescopes à effet Cherenkov) et IceCube (cube de glace). Ce travail analyse les données et simulations à plusieurs niveaux de reconstruction : des données brutes aux données calibrées; des données calibrées à une liste d'évènements et d'une liste d'évènements à une contrainte sur le flux des rayons cosmiques. Les méthodes de reconstructions sont toutes basées sur l'estimation du maximum de vraisemblance. Ainsi, dans ce travail, j'ai exploré deux types de télescopes Cherenkov (télescope Cherenkov à imagerie atmosphérique et télescope à neutrino) de la calibration, en passant par la reconstruction, à l'analyse de données en se basant sur des méthodes maximisant la vraisemblance à l'aide d'algorithmes que j'ai développé.

Le Cherenkov Telescope Array est un observatoire terrestre de rayons gammas en développement. Le réseau de télescopes est composé de plusieurs types de télescopes. Parmi ceux-ci, le télescope SST-1M qui était proposé pour l'observatoire de l'hémisphère sud. La caméra du télescope SST-1M a été développée à l'Université de Genève. Dans ce travail, la calibration de ce prototype est relatée. Plus particulièrement, les calibrations au laboratoire et sur le site d'observation sont présentées. Les paramètres de calibration de tous les pixels de la caméra ont été obtenus par maximisation de la vraisemblance du spectre à photo-électron. Le modèle inclut les effets de diaphonie optique qui sont sources de bruit dans les photo-multiplicateurs à silicium. La calibration de la caméra a confirmé ses excellentes capacités en terme de résolution de la charge et du temps.

Dans la continuation de ces résultats, une nouvelle méthode de paramétrisation des images utilisant une méthode maximisant la vraisemblance a été développée. La fonction de

vraisemblance découle du spectre à photo-électron des photo-multiplicateurs à silicium. La méthode a été utilisée dans le but de décrire de manière exacte les sources de bruits corrélés et non-corrélés lors du comptage des photo-électrons. Elle utilise des contraintes spatiales et temporelles qui découlent du développement de la lumière Cherenkov dans les gerbes atmosphériques. La paramétrisation des images est utilisée pour déterminer pour chaque évènement : l'énergie, la direction et le type de la particule. Cette reconstruction est faite à l'aide de modèles d'apprentissage machine entraînés sur des simulations Monte Carlo. Avec cette méthode de reconstruction unique, les performances du télescope SST-1M à son site de mise en service (à Cracovie) ont été obtenues. Elles montrent que les conditions de bruit de fond du ciel au site de Cracovie ne sont pas favorables à l'astronomie gamma. Cependant, les observations de Cracovie ont été reconstruites et la méthode a été validée sur les données. La méthode a été comparée aux techniques standards de reconstruction du télescope de grande taille de l'observatoire CTA. Des améliorations encourageantes en matière de flux de sensibilité ont été observées. Plus particulièrement, le flux de sensibilité du télescope de grande taille de CTA atteint une sensibilité similaire à celui du système stéréoscopique à deux télescopes: MAGIC pour lequel une sensibilité de 1% du flux de la nébuleuse du Crabe à 0.5 TeV est attendue. De plus, le potentiel de cette analyse n'a pas été complètement exploré. Des ajustements des contraintes spatiales et temporelles ainsi que son utilisation en observation stéréoscopique pourraient montrer des améliorations supplémentaires.

Finalement, des évènements de neutrinos à hautes énergies de l'observatoire IceCube ont été utilisés dans le cadre d'une étude de corrélation avec les rayons cosmiques à très hautes énergies. L'analyses cherche des sources de rayons cosmiques avec des énergies au-delà de 50 EeV regroupés dans la direction d'incidence de neutrinos astrophysiques. Les déviations de trajectoire dues au champ magnétique galactique sont prises en compte avec une dépendance en énergie. L'analyse compte le nombre de rayons cosmiques à très hautes énergies étant corrélés avec les neutrinos en estimant le maximum de vraisemblance. Cette analyse est la continuation d'un travail précédent conduit à l'Université de Genève. Elle avait montré une signifiance de corrélation proche de 3σ entre ces deux messagers de l'univers. La ré-analyse avec des données nouvelles ainsi qu'avec un modèle de champ magnétique galactique amélioré n'a montré aucune corrélation signifiante entre la direction d'arrivée des neutrinos astrophysiques et des rayons cosmiques à très hautes énergies. Cette observation se confirme par les résultats obtenus dans deux autres analyses similaires.

Abstract

Since the cosmic-ray discovery in 1912, a whole new field of research has been opened. The study of the cosmic-rays has allowed physicists to discover many new fundamental particles as well as refine the standard model of particle physics. Among these discoveries, some were awarded the Nobel Prize in physics. Nowadays, some of the fundamental questions raised after the cosmic-ray first observation are still unanswered. For instance, although theorized, the acceleration, interaction, and propagation of cosmic-rays in the Universe are still a matter of debate. The improved detection techniques of space-based and ground-based instruments have allowed over the years to complete the cosmic-ray puzzle. The construction of next-generation high-energy astrophysics experiments, pushing our sensitivity to the highest-energy sources in the Universe, might answer the unsettled questions of this research field. In particular, the field is entering a new era since the start of multi-wavelength and multi-messenger astronomy.

This thesis focuses on two high-energy astrophysics observatories: the Cherenkov Telescope Array and IceCube. The work analyses data and simulations at different stages of the entire reconstruction pipeline: from the raw data to calibrated data; from calibrated data to event lists and from event lists to the result on the measurement of an upper limit on the cosmic-ray flux in case of lack of signal. The reconstructions are based on maximum likelihood estimations. Hence, in this work, I explored data from two different kinds of Cherenkov telescopes (Atmospheric Cherenkov and in - ice Cherenkov) from calibration to reconstruction and finally data analysis with likelihood methods with algorithms mostly developed by myself.

The Cherenkov Telescope Array is a developing ground-based gamma-ray observatory. The array is composed of several kinds of telescopes, among which the SST-1M telescope was proposed for the southern array. The SST-1M camera has been developed at UNIGE. Here the calibration of the prototype is shown. In particular, on-site and off-site characterization are presented. The calibration parameters of all the camera pixels were obtained by the use of the likelihood maximization of the photo-electron spectra. The model includes optical cross-talk effects which is a source of excess noise in silicon photo-multipliers. The calibration of the camera confirmed its excellent performance in terms of charge and time resolution.

Following the results obtained on the camera calibration, a novel method for reconstruction of the image parameters using a maximum likelihood method has been developed. The likelihood derives from the photo-electron spectra of the camera silicon photo-multipliers. This method was developed to accurately propagate the sources of correlated and uncorrelated noise in the photo-electron reconstruction and to fully exploit the time development of the photon signal (called the waveform). The method uses time and spatial constraints defined by the extensive air-shower Cherenkov light development.

The image parameters are used to reconstruct the event energy, direction, and identity the particle type. This reconstruction is done with Monte Carlo trained random forest decision trees. Through this unique reconstruction, the performances of the SST-1M telescope at its commissioning site in Kraków have been obtained. As expected, the result is affected by the night-sky background conditions (order of a GHz per pixel) at the Kraków site, which is not favorable for gamma-ray astronomy. Nonetheless, events were successfully reconstructed and the method I developed could be fully demonstrated on data. The method has been compared to standard reconstruction methods of the CTA large size telescope first prototype. Improvements in terms of flux sensitivity have been observed. In particular, the flux sensitivity of the large size telescope of CTA has been found to reach the one of the MAGIC stereoscopic system, a system of two telescopes sensitive to sources with fluxes of about 1% of the Crab Nebula flux at 0.5 TeV. Moreover, the full potential of this analysis has not yet been completely explored. Fine-tuning of the spatial and time image models as well as the use of this method in stereoscopic observational mode might show even greater improvements.

Finally, high-energy neutrino events from the IceCube observatory have been used in the context of a correlation study with ultra-high energy cosmic-rays. The analysis looks for sources of EeV cosmic-rays clustered in the arrival direction of astrophysical neutrinos. The galactic magnetic deflection has been taken into account in an energy-dependent manner. This analysis counts the number of correlated ultra-high energy cosmic-rays with neutrinos by using a maximum likelihood estimation. It is the continuation of a previous work conducted at UNIGE that revealed a hint of a correlation between the two messengers of the Universe at a level close to 3σ significance. The re-analysis with increased statistics and improved magnetic deflection models showed no significant correlation between astrophysical neutrinos and ultra-high energy cosmic-rays. This observation is also confirmed by two similar correlation studies that have been conducted by others.

Remerciements

L'aboutissement de ce travail n'aurait pu être possible sans le soutien, l'aide, la collaboration et l'encouragement des personnes qui m'entourent. Je tiens à exprimer, par les lignes qui suivent, ma profonde gratitude envers toutes celles et ceux que je nommerai. La liste étant longue, je m'excuse d'ores et déjà envers les personnes que j'ai omis.

En premier lieu, je veux remercier mes collègues et proches collaborateurs. Ce sont eux et elles qui font que j'ai pu travailler dans les meilleures conditions. Tout d'abord je remercie ma directrice de thèse: la Professeure Teresa Montaruli. Grâce à son exigence, j'ai pu approfondir mes connaissances et développer de nouvelles compétences qui vont bien au-delà de mon domaine de recherche. Dès mon arrivé, elle m'a impliqué dans des taches importantes. Certains de mes travaux étaient exploratoires et j'ai pu librement m'y attarder. Pour m'avoir attribué cette confiance, je la remercie. Je remercie ensuite l'ensemble des membres du groupe de la Professeure Teresa Montaruli qui ont collaboré avec moi: Le Docteur Matthieu Heller, est sans doute la personne qui a suivi au plus proche mon travail. J'ai apprécié son regard critique et l'estime qu'il a porté à mes travaux. Plus qu'un supérieur il restera pour moi un exemple dans sa façon d'aborder les problèmes dans le fond. Le Docteur Victor Coco, avec qui j'ai travaillé pendant ma première année. Ses connaissances en terme d'analyse et de programmation ont pu poser des bases solides pour la suite de mon doctorat. Le Docteur Andrii Nagai, dont la rigueur de travail a été source d'exemplarité. De lui, j'ai pu développer des connaissances expérimentales. Le Docteur Yves Renier, pour avoir initié des recherches sur lesquels j'ai pu prendre exemple. La Docteure Anastasia Maria Barbano, avec qui j'ai partagé une partie de ce travail. D'elle j'ai pu développer mes compétences en statistique. Le Docteur Domenico della Volpe, dont l'expérience a apporté un jugement nouveau à mon entreprise. Viennent ensuite mes camarades doctorants: Stéphanie Bron, je suis reconnaissant du soutien moral apporté. Les moments que nous avons passé ensemble dans les différentes écoles et séminaires resteront mémorables. Docteure Tessa Carver, j'ai apprécié nos discussions qu'elles soient professionnelles ou amicales. Docteur Theodore Rodrigue Stephane Njoh Ekoume, sa détermination m'a inspiré. Francesco Lucarelli, j'admire son sens analytique. Luis David Medina Miranda, sa force d'esprit et sa capacité de résilience m'ont inspiré. Je remercie également le Docteur Jakub Juryšek qui a participé à la production de données simulées que j'ai utilisé dans le cadre de mes travaux. D'autre part, je remercie mes collègues qui sont arrivés vers la fin de ma thèse: Docteur Luca Foffano, Docteure Lucia Anna Damone, Docteur Mykhailo Dalchenko, Docteur Alessandro Carosi et Docteur Gabriel Emery pour leurs précieux conseils.

J'exprime ma profonde gratitude aux membres du jury; le Professeur Tobias Golling, le Professeur Rafał Moderski ainsi que le Docteur Roland Walter, pour avoir apporté un regard critique à ce travail ainsi que pour le temps consacré à son évaluation.

Je dois adresser mes remerciements envers mes amis proches. Sans eux les week-ends, les vacances et les moments de détente n'existeraient pas. Ils ont su également me soutenir lors de moments difficiles. Je remercie Naïke Bravo, qui m'a encouragé jusqu'à la ligne d'arrivée. Tiago Alexandre Lima Caiado, pour les bons moments. André Gruaz, dont la créativité a permis d'organiser des week-ends exceptionnelles.

J'exprime également mes remerciements à ma petite famille. Ma mère, Marie-Louise Alispach qui a tout donné pour mon éducation. Mon frère Alexandre Alispach, j'admire la force dont il fait preuve au quotidien. Ma soeur Virginie Alispach, son courage est ma plus belle leçon de vie.

List of Abbreviations

ADC Analog to Digital Converter

AGN Active Galactic Nucleus

AUC Area Under Curve

C.U. Crab Units

CAD Computer-Aided Design

CC Charged Current

CCD Charge-Couple Device

CL Confidence Level

CMB Cosmic Microwave Background

CTA Cherenkov Telescope Array

CTAO Cherenkov Telescope Observatory

CTS Camera Test Setup

DCR Dark Count Rate

DGE Diffuse Galactic gamma-ray Emission

DOM Digital Optical Module

DPNC Département de Physique Nucléaire et Corpusculaire

EAS Extensive Atmospheric Shower

EBL Extra-galactic Background Light

EHE Extremely High-Energy

ERIC European Research Infrastructure Consortium

ETHZ Eidgenössische Technische Hochschule Zürich

FACT First G-APD Cherenkov Telescope

FADC Flash Analog to Digital Converter

FoV Field of View

FPGA Field-Programmable Gate Array

GCT Gamma-Ray Telescope

GRB Gamma-Ray Burst

GZK Greisen-Kuzmin-Zatsepin

H.E.S.S. High Energy Stereoscopic System

HESE High-Energy Starting Event

IC Inverse-Compton

IFJ PAN Institute of Nuclear Physics Polish Academy of Sciences

IGRB Isotropic Gamma-Ray Background

ISM Inter-Stellar Medium

LED Light Emitting Diode

LSB Least Significant Bit

LST Large-Sized Telescope

MAGIC Major Atmospheric Gamma Imaging Cherenkov

MC Monte Carlo

MST Medium-Sized Telescope

NC Neutral Current

NSB Night-Sky Background

NTC Negative Temperature Coefficient

p.e. photo-electron

PAO Pierre Auger Observatory

PDE Photo-Detection Efficiency

PDF Probability Density Function

PDP Photo-Detection Plane

PMT Photo-Multiplier Tubes

PSF Point Spread Function

RF Random Forest

ROC Receiver Operating Characteristic

SCB Slow-Control Board

SCT Schwarzschild-Couder Telescope

SED Spectral Energy Distribution

SiPM Silicon Photo-Multiplier

SPAD Single Photon Avalanche Diode

SST Small-Sized Telescope

SST-1M single Mirror Small Sized Telescope

TA Telescope Array

TS Test Statistic

UHECR Ultra-High Energy Cosmic Rays

UNIGE Université de Genève

UV Ultra Violet

VERITAS Very Energetic Radiation Imaging Telescope Array System

VHE Very-High Energy

Contents

Chapter I

The discovery of cosmic rays and the multi-messenger era

I.1 Early twentieth century ionization experiments

At the end of the 19th century, physicist discovered radioactivity. It led to the discovery of new elements and isotopes. At that time it was suggested that a natural form of radiation originates from Earth's ground and its activity should decrease with altitude (as the air absorbs the radiation).

In the beginning of the 20th century experiments measuring the radiation level with an electrometer[1] were conducted. Electrometers were measuring the level of ionization induced by the natural radiation. The electrometers were shielded with different substances and exposed to radioactive sources. This allowed to measure the absorption power of different materials. By placing them at various distances of the source, the adsorption coefficient λ[2] of the air was determined. This allowed to estimate at which altitude the radiation level would decrease significantly. For instance, 99% of the gamma-rays emitted by radium would be absorbed at an altitude of about 1000 m. An other interesting observation from the electrometer experiments was that, even for well shielded apparata, there seems to be a form of constant ionization coming from highly-penetrating radiation.

Later on, a number of experiments were conducted to measure the level of radioactivity at different altitudes and depths. In 1909, T. Wulf observed a drop of ionisation rate at the top of the Eiffel tower not compatible with the hypothesis of a radiation originating from the Earth's surface [1]. Shortly after, in 1911, D. Pacini confronted the Earth's crust model of cosmic-rays by measuring ionization on a boat far from the coast. The electrometer was supposedly shielded from the Earth's radiation by the 4-m deep water. Pacini estimated that 2/3 of the radiation is not coming from the Earth's surface [1]. In 1912, V. Hess equipped with high precision electrometers, confirmed the results reported by its predecessors. V. Hess carried the electrometers to high altitudes (up to 5200 m) [2]. V. Hess collected ionization measurements over 7 flights. The first flight was performed

[1] Instrument able to measure the electric charge consisting of two thin gold (or other metal) foils mounted on a metallic rod. When the rod is charged the charge distributes over the golden leafs and they repel each-other because of the identical charge. The displacement of foils is a measurement of the electric charge quantity.

[2] The intensity I at a distance d is given by $I = I_0 e^{-\lambda d}$, where I_0 is the intensity at the source.

during a solar eclipse. He observed no significant difference in the level of ionization during the solar eclipse of April 17th. This observation ruled out the hypothesis of the solar origin of such radiation. The observations reported by Hess' balloon flights are illustrated in fig. I.1, together with the supporting data from W. Kolhörster in 1914 [3]. As can be seen the rate of ionization per unit volume increases with altitude. The rate presented in fig. I.1 represents the ionization excess compared to the sea level. Hess concluded that a source of natural radiation comes from the top of the atmosphere.

The observations of Hess were rapidly confirmed by others. For instance the Swiss physicist Auguste Piccard[3] studied cosmic-rays at very high altitude (up to 16.2 km) in 1932. At that time it was the highest altitude ever reached. Later, E. Regener showed that there is a maximum of ionization rate at a certain altitude. This maximum, named the Regener-Pfotzer maximum, is between 16-25 km [4]. Regener's observations of the ionization rate flattening at these altitudes allowed him to conclude that the radiation coming from the cosmos finds its origin in other forms than the known radioactive substances. As a matter of fact, the gamma-radiation was supposedly less penetrating than the cosmic radiation.

In the pursuance to solve the cosmic radiation puzzle, J. Clay et al. reported a magnetic latitude dependence of the ionization rate. In fact the ionization rate is less at the magnetic equator than at the magnetic poles. It was latter observed, during boat trips in 1933 between the two hemispheres of the globe, that there exists also a longitude dependence [5]. Clay's observations showed that cosmic radiation is composed of charged particles, as it is affected by Earth's magnetic field.

By the 1930's it became clear that there exists a natural form of radiation that comes from space. The composition of the radiation was not yet clearly identified. But the experimental results suggested that it was composed of charged particles and highly penetrating radiation. Their origin has still to be understood today.

In 1934, W. Baade and F. Zwicky proposed a possible solution to the puzzle on the origin for cosmic radiation [6] at energies below $\sim$ 1000 GeV. The fact that the cosmic radiation was almost constant with time indicated to them that the sources of these highly penetrating rays were nor the Sun nor the Milky Way. They thought the sources to be of extra-galactic origin producing a diffuse flux. They speculated that supernovae[4] would have enough energy to explain the ionization rate observed by Regener and others. From the estimated amount of cosmic ray energy produced by a supernova and the rate of the supernovae [5] in the Universe, they concluded that the intensity of this radiation reaching the Earth should be $\sigma = 0.8 - 8 \times 10^{-3}\ \mathrm{ergs \cdot cm^{-2} \cdot s^{-1}}$. Although it is now believed that the supernova remnants are responsible for the galactic cosmic-rays, this estimate was in accordance with the measurements of Regener ($\sigma_{Regener} = 3.53 \times 10^{-3}\ \mathrm{ergs \cdot cm^{-2} \cdot s^{-1}}$) and Millikan ($\sigma_{Millikan} = 3.2 \times 10^{-3}\ \mathrm{ergs \cdot cm^{-2} \cdot s^{-1}}$) from their balloon flights [1]. Millikan estimated the total cosmic-ray energy flux by integrating the total ionization rate along altitude and by assuming that the ionization energy is 32 eV [7].

Hess's findings were awarded the Nobel Prize in Physics in 1936 "for his discovery of cosmic radiation", shared with C. Anderson "for his discovery of the positron" [6]. The positron (anti-electron) was observed in tracks of cloud chambers [7] produced by secon-

[3]The character of Prof. Calculus in Tintin from Hergé was inspired by A. Piccard.

[4]Powerful explosion of stars.

[5]A cloud of dust in the interstellar medium.

[6]The Nobel Prize in Physics 1936. NobelPrize.org. Nobel Media AB 2020. Thu. 19 Mar 2020.

[7]A sealed chamber filled with a supersaturated gas. On the passage of a charged particle the gas

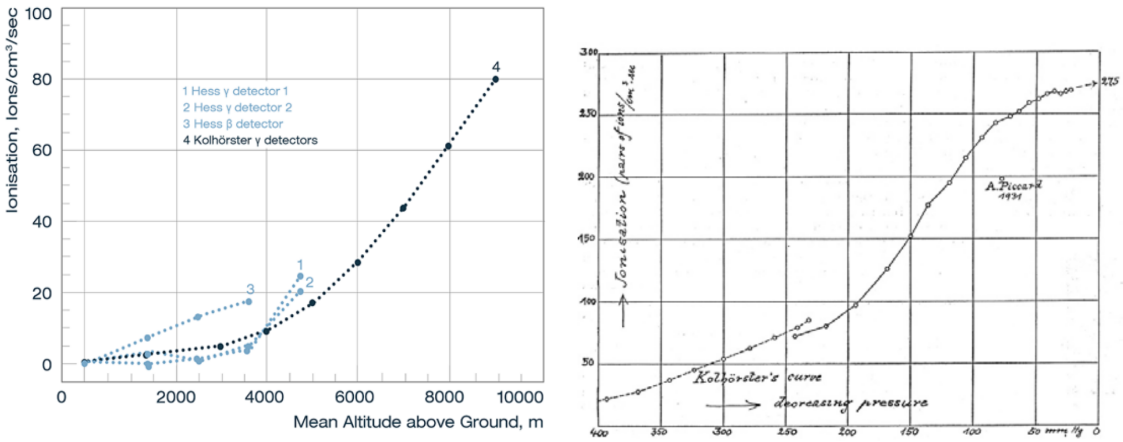

Figure I.1. Left: The ionization rate per cubic centimeter as function of the altitude measured by Hess in 1912 [2] and Kolhörster in 1914 [3] up to 9300 m. Taken from [1]. Right: Measurement of the ionization rate by Kolhörster and Piccard in 1931 (at 15.78 km) and Regener in 1932. Taken from [10]

daries of cosmic rays in 1932 by Anderson [8]. The observed particle carried the mass of the electron, while having an opposite charge. This was the first anti-particle observed, hence named positron. Anderson's new discovery was followed latter by the discovery of the muon in 1937. Anderson, together with Neddermeyer, measured the energy loss of charged particle passing through a 1 cm platinum plat. They found evidence of a highly penetrating particle which had a much lower mass than the proton and higher of the electron [9]. The cosmic rays discovery opened many doors for particle physics and astrophysics. Many new particles were discovered in cosmic-ray interactions in the atmosphere.

I.2 The cosmic-ray spectrum and composition

Since the discovery of cosmic radiation in the beginning of the 20th century, a great number of experiments have tried to study the composition of cosmic-rays and to measure the energy of this radiation. As already indicated in the previous section, the quest for cosmic-rays [8] revealed new particles and allowed to elaborate the standard model of particle physics. In particular, hadronic and electromagnetic particles are found in the cosmic radiation. In fig. I.2 the measured energy spectrum for all particles is shown and for some of the constituents (protons, electrons, positrons, gamma-rays, neutrinos, anti-neutrinos and anti-protons). It can be seen that cosmic rays are composed by stable elementary particles, principally by protons. The spectrum extends over 12 order of magnitude from few GeV up to hundreds of EeV. Moreover, the spectrum of the charged cosmic-rays decreases for energies below few GeV. This does not indicate that cosmic-rays energies start at couples of billions of electron-volts but rather that they are not detectable by us at lower energies. In fact, the solar magnetic activity modifies the flux of cosmic-

condensates along the particle path allowing to visualize it. Cloud chambers are usually embedded in magnetic fields to measure particles' curvatures, which are related to their momentum and charge.

[8] In this section the terminology "cosmic-rays" refers to particles coming from the cosmos and hitting the atmosphere, but sometimes in this thesis "cosmic-rays" refer to preferentially to protons, which are the dominant constituents.

rays at rigidity[9] below 10 GV. Moreover the geomagnetic field deviates the low energy cosmic-rays as well [11].

From fig. I.3, it can be seen that heavy nuclei below 1 PeV (= 10^{15} eV) are about 10% of the total flux, while the dominant form of cosmic particle are protons. This is not surprising as the majority of matter in the Universe is composed of hydrogen.

The cosmic-ray community distinguishes the cosmic-rays into 2 categories : primary cosmic-rays, and secondary cosmic-rays. The primary cosmic-rays are the ones accelerated in astrophysical sources while the secondaries result from the interaction of the first ones with surrounding matter or radiation. All synthesized particles in stellar nuclear interaction are considered as primaries. Among the primaries, one can cite: electrons, protons; helium; oxygen; iron and carbon [11]. Elements such as lithium ($Z = 3$), beryllium ($Z = 4$), and boron ($Z = 5$) are considered as secondaries. They are less abundant in stellar nucleosynthesis. This can be seen in fig. I.4, where the abundance of galactic cosmic-rays and particles accelerated in the Sun are compared [11]. The similarity of the abundance of solar particles and cosmic rays reveals their origin from stars or their death. The zig-zag observed in fig. I.4 is due to the fact that elements with odd Z or odd atomic mass number A have weaker bounds and thus are less frequent in stellar nucleosynthesis. The excess abundance of e.g. beryllium in the galactic cosmic-rays reveals that it is produced from the spallation of heavier nuclei when wandering in the galaxy. Additionally, most electrons and positrons are of secondary origin, aside a possible contribution from dark matter of those directly accelerated in supernovae or pulsars.

All cosmic ray energy spectra can be described by power-law spectra (above 10 GeV for protons), as seen clearly in fig. I.3, of the form:

$$\frac{dN(E)}{dE} = \Phi_0 E^{-\gamma}, \;\; \gamma > 0 \tag{I.1}$$

with γ the spectral index, Φ_0 the normalization and E the energy of the cosmic-ray particle. Spectra are given for all particles, or nucleons composing them and as a function of total or kinetic energy of particle or nucleon, and also in rigidity. Decreasing power laws mean that the highest energetic particles are rarer that lower ones. The power-law nature of the cosmic-ray spectrum is distinct from thermal radiation which shows a black-body spectrum such as for the Sun. This shows that other non-thermal radiation processes take place in the Universe. For this reason, high-energy astrophysics is sometimes referred as the study of the non-thermal Universe.

The energy flux of protons (see fig. I.2) can be divided into three energy regions. These regions correspond to changes of spectral index γ. They are delimited by the so-called: knee at few PeV and the ankle above 10^{18} eV. They are named after the resemblance of the spectrum features to those of a leg.

The spectral indices of these region are:

$$\gamma = \begin{cases} 2.7, & 10^6 < \frac{E}{eV} \leq 2 \times 10^{15} \\ 3.1, & 2 \times 10^{15} < \frac{E}{eV} \leq 3.5 \times 10^{18} \\ 2.5, & E > 3.5 \times 10^{18}\ eV \end{cases} . \tag{I.2}$$

Changes of slope can be attributed to different reasons, e.g. acceleration or propagation effects. For instance, the steepening of the spectrum may indicate an absorption mecha-

[9]The rigidity is the ratio of the particle momentum p and its charge Ze: $R = \frac{pc}{Ze}$, with c the speed of light in vacuum and Z the atomic number.

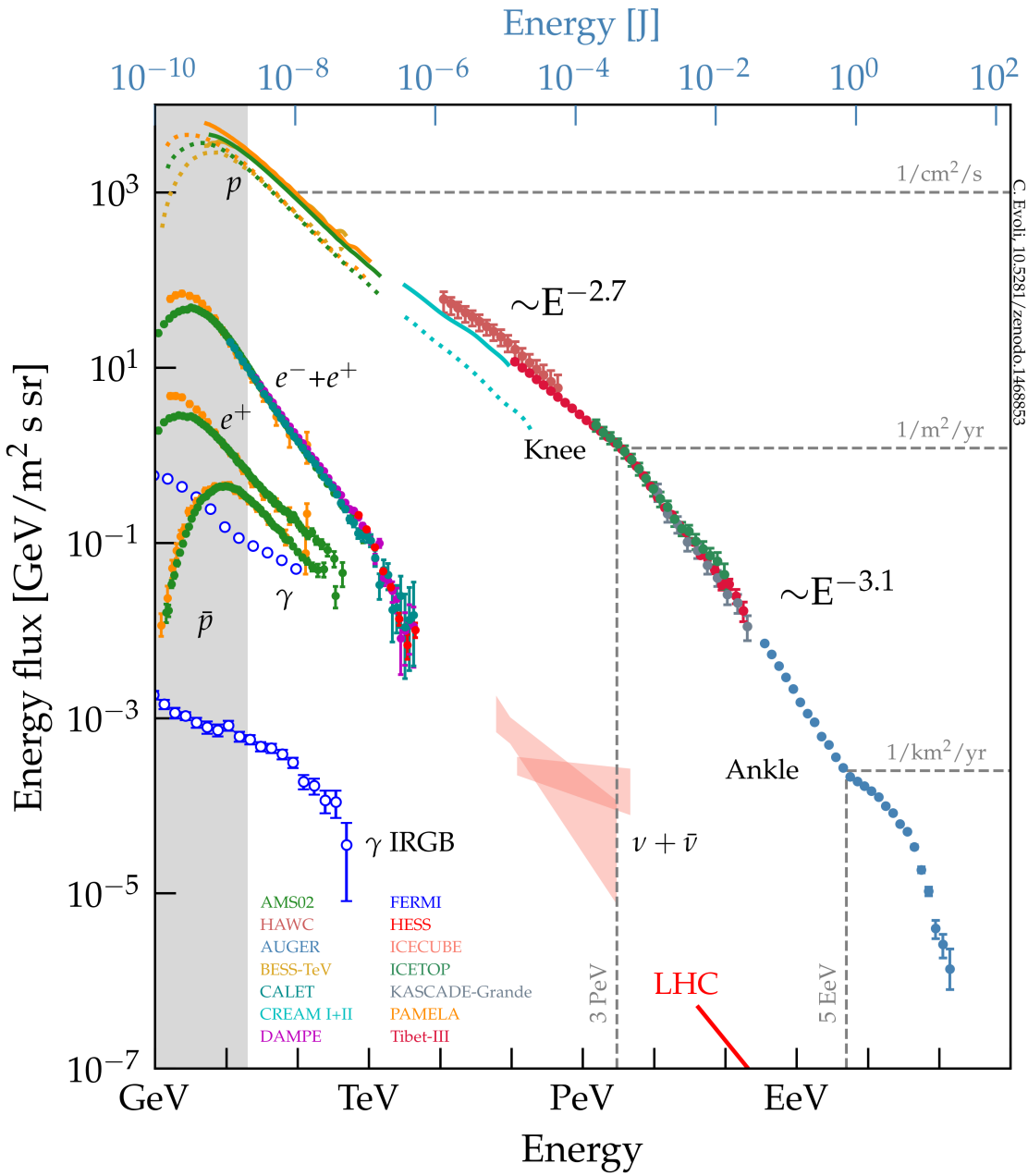

Figure I.2. Measured cosmic-ray energy flux of all particles as function of the energy of the particles. The y-axis represents the flux of particles per unit energy times the energy squared: $\frac{dN}{dE}E^{-2}$ to put in evidence the features of the flux. In particular the following constituents are shown: protons p, anti-protons $\bar{p}$, electrons e^-, positrons e^+, gamma-rays from the Isotropic Gamma-Ray Background (IGRB) and from the Diffuse Galactic gamma-ray Emission (DGE); neutrinos ν and anti-neutrinos $\bar{\nu}$. The colors indicate the experiment which measured the spectrum. Taken from [12].

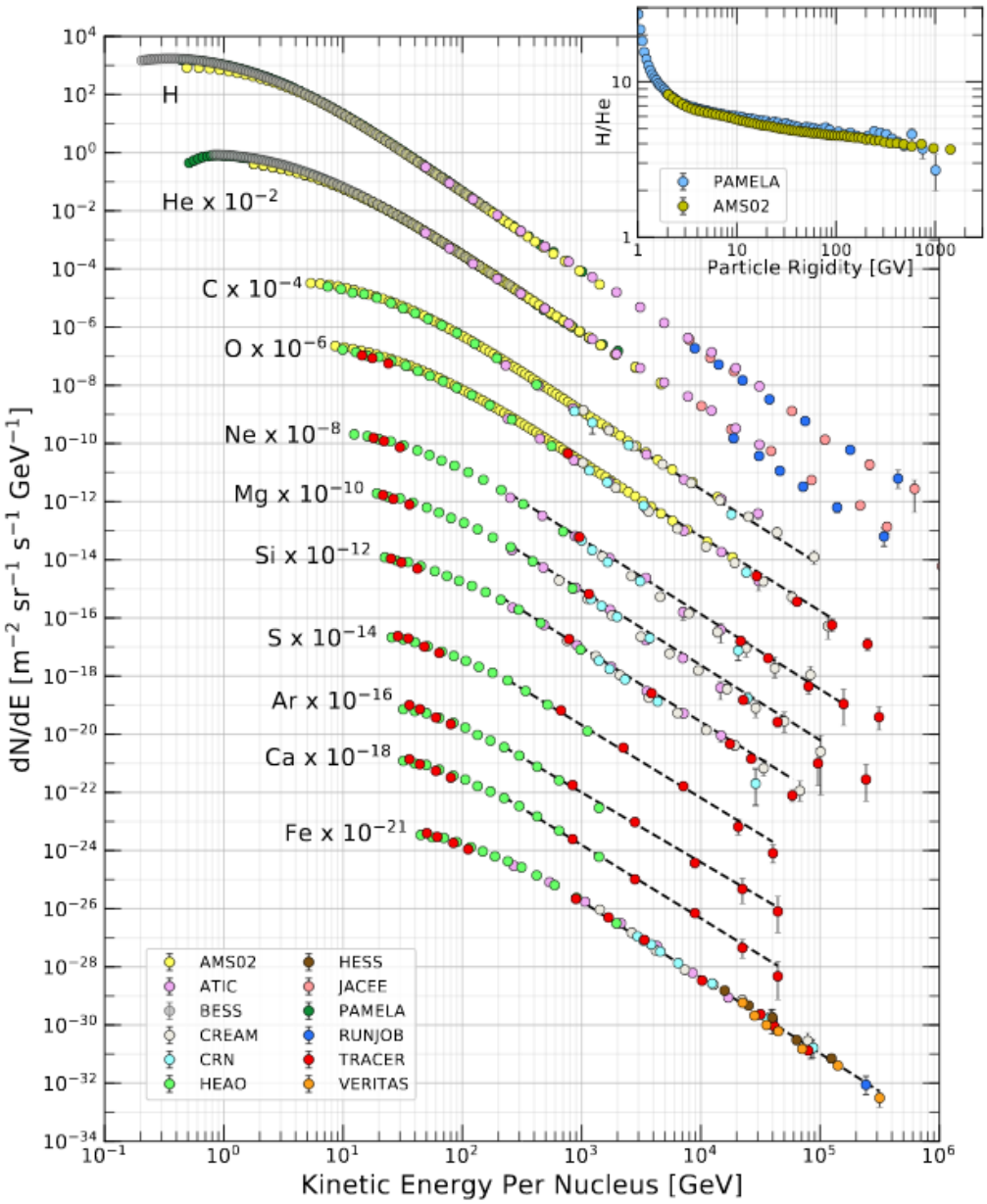

Figure I.3. Measured cosmic-ray spectra for nuclei from hydrogen to iron as function of the kinetic energy per nucleus. The insert shows the ratio of hydrogen to He flux as function of the particle rigidity. Taken from [11].

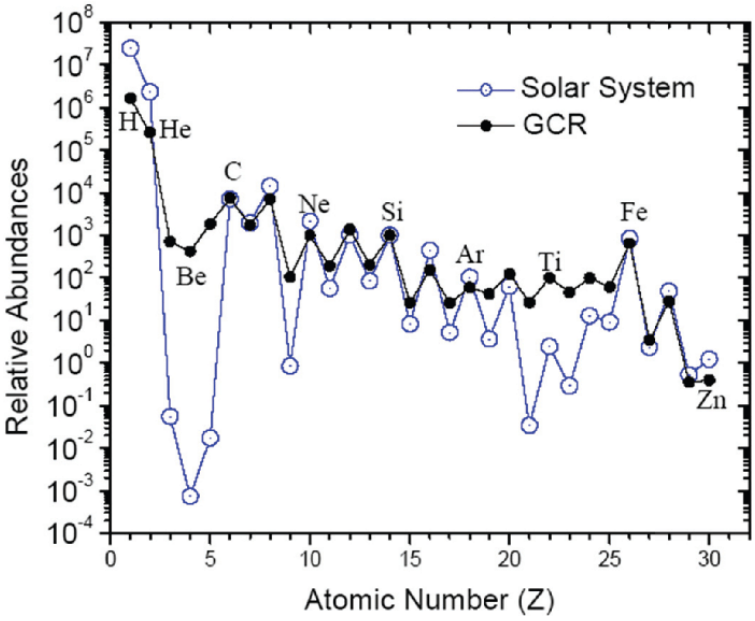

Figure I.4. Galactic cosmic-ray abundance compared to solar particles. The curves are normalized such that the abundance of silicon is 10^3. Taken from [13].

nism along the trajectory of propagation or the leakage from the volume where they can be detected. Nowadays, it is believed that the cosmic-rays found up to the knee originate in the Galaxy. The maximum reached galactic cosmic-rays energy would be around the knee. Nonetheless, it is problematic that the supernova remnants, hypothesized by Baade and Zwicky as most probable sources due to energy conservation reasons, SNRs seem not able, in standard models, to accelerate particles above 10^{15} eV.

One can also identify a "second knee" around 10^{18} eV, before the ankle. The second knee would find its origin similarly as for the "first knee". It could be interpreted as the knee of heavier nuclei such as iron, due to the fact that they would leak out of the galaxy at higher energies than protons by a factor equal to Z (their composition or number of protons). Hence, the first knee is attributed to protons ($Z_p = 1$) and second knees to Fe ($Z_{Fe} = 26$) at $E_{knee,Fe} = Z_{Fe} \times E_{knee,p}$.

The increase of spectral index above the ankle is usually attributed to the flux of extra-galactic sources. Supposedly, the highly energetic extra-galactic cosmic-ray particles escape their host galaxies. Above the ankle the extra-galactic population dominates the galactic ones. The region between the knee and the ankle could be a transition region from galactic to extra-galactic cosmic-rays.

As illustrated in fig. I.2, many experiments are involved in the detection of cosmic-rays. The fact that the flux decreases with increased energy requires to enlarge the detection surface with increased energy. Ground-based instruments detecting cosmic-rays protons and gamma-rays from few GeV to hundreds of TeV as well as PeV-scale neutrinos are described in chapters III and IV.

I.2.1 Greisen-Kuzmin-Zatsepin cut-off

The fact that the observed cosmic-ray spectrum starts at few GeV is attributed to a detection limit induced by geomagnetic and heliomagnetic interactions of the low energy

cosmic-rays. On the opposite side of the spectrum, at the highest energies, the spectrum rapidly steepens. The extinction of cosmic-rays can be attributed to the Greisen-Kuzmin-Zatsepin (GZK) interaction.

Under the assumption that cosmic-ray particles above the ankle originate from other galaxies, ultra-high energy cosmic-rays (UHECs) would interact with the cosmic microwave background (CMB) radiation. The CMB is a remnant radiation of the Big Bang with a black-body spectrum with a temperature of 2.7 K. The interaction of UHECR protons with CMB photons produce pions via the Δ^+ resonance:

$$p + \gamma_{CMB} \longrightarrow \Delta^+ \longrightarrow p + \pi^0 \tag{I.3}$$

$$p + \gamma_{CMB} \longrightarrow \Delta^+ \longrightarrow n + \pi^+. \tag{I.4}$$

Thus part of the proton energy is transferred to the pions and consequently the energy of the proton is diminished. About 20% of the proton energy is transferred to the pion.

The proton energy threshold for this process is expressed as:

$$E_p = \frac{m_\pi}{2E_{\gamma_{CMB}}}(2m_p + m_\pi) \simeq 2 \times 10^{20}\ \text{eV}. \tag{I.5}$$

This energy threshold indeed corresponds to the cut-off observed at the end of the cosmic-ray spectrum.

The GZK interaction creates pions which will inevitably decay before reaching us. The neutral pions will dominantly decay into two gamma-rays. The charged pion will also decay producing a muon μ and a muon neutrino ν_μ. Ultimately, the muon will also decay into an electron e, an electron neutrino ν_e and a muon neutrino ν_μ. At the end of the GZK process only the stable particles are left. Those can, in principle, be observed by gamma-ray and neutrino telescopes. Observing the secondaries of the GZK process could confirm its existence. To this day, no GZK secondaries have been observed.

I.2.2 Flux parameterization

In the following, parameterization of the cosmic-ray and of the electron flux are given as they will be used latter in chapter VI.

Diffuse proton spectrum below the knee Between 10 GeV and the knee, the energy spectrum for protons can be parameterized as [14]:

$$\Phi^p(E) = \Phi_0 \left(\frac{E}{TeV}\right)^{-\gamma} \tag{I.6}$$

$$\Phi_0 = 9.6 \times 10^{-2}\ \text{TeV}^{-1} \cdot \text{m}^{-2} \cdot \text{s}^{-1} \cdot \text{sr}^{-1}. \tag{I.7}$$

Diffuse electron spectrum The electron spectrum above few GeV can be expressed as [14]:

$$\Phi^e(E) = \Phi_0 \left(\frac{E}{TeV}\right)^{-\gamma} + \frac{L}{Ew\sqrt{2\pi}} \exp\left(-\left(\frac{\ln \frac{E}{E_p}}{\sqrt{2}w}\right)^2\right) \tag{I.8}$$

$$\Phi_0 = 6.85 \times 10^{-5}\ TeV^{-1} \cdot m^{-2} \cdot s^{-1} \cdot sr^{-1} \tag{I.9}$$

$$\gamma = 3.21 \tag{I.10}$$

$$L = 3.19 \times 10^{-3}\ m^{-2}s^{-1}sr^{-1} \tag{I.11}$$

$$w = 0.776 \tag{I.12}$$

$$E_p = 0.107\ TeV \tag{I.13}$$

I.3 Acceleration mechanism of cosmic-rays

The presence of high-energy particles in the Universe is an observational fact. While this can be taken for granted, the origin, the mechanism of production, the interaction with matter and on the way towards of us are still a matter of speculation.

The observation of the cosmic-rays on Earth has raised several questions:

- Where are the cosmic-rays produced?
- What mechanisms allows to accelerate them up to EeV energies with a power law spectrum?
- What kind of processes are responsible of the production of gamma-rays and neutrinos ?
- How do the cosmic-ray propagate in the Universe before reaching us?

In the following, possible explanations of the acceleration mechanism will be given (see section I.3.1). In sections I.4.1 and I.4.2, interaction processes of cosmic-rays within their source of acceleration will be presented.

I.3.1 Acceleration mechanism

It is well known to physicists that a particle of charge q moving at velocity $\vec{v}$ in an electric field $\vec{E}$ and a magnetic field $\vec{B}$ experiences the Lorentz force:

$$\vec{F} = q\left(\vec{E} + \vec{v} \times \vec{B}\right). \tag{I.14}$$

The work of the Lorentz force only depends on the electric field: $W = q\int \vec{E} \cdot d\vec{l}$ as the cross product of the magnetic field and the velocity the particle is perpendicular to the direction of motion. Thus, the particle velocity changes in module only due to electric fields. The magnetic field creates a force perpendicular to the direction of motion. Consequently, the trajectory of the particle is along a circle of radius:

$$R_l = \frac{mv_\perp}{|q|B}, \tag{I.15}$$

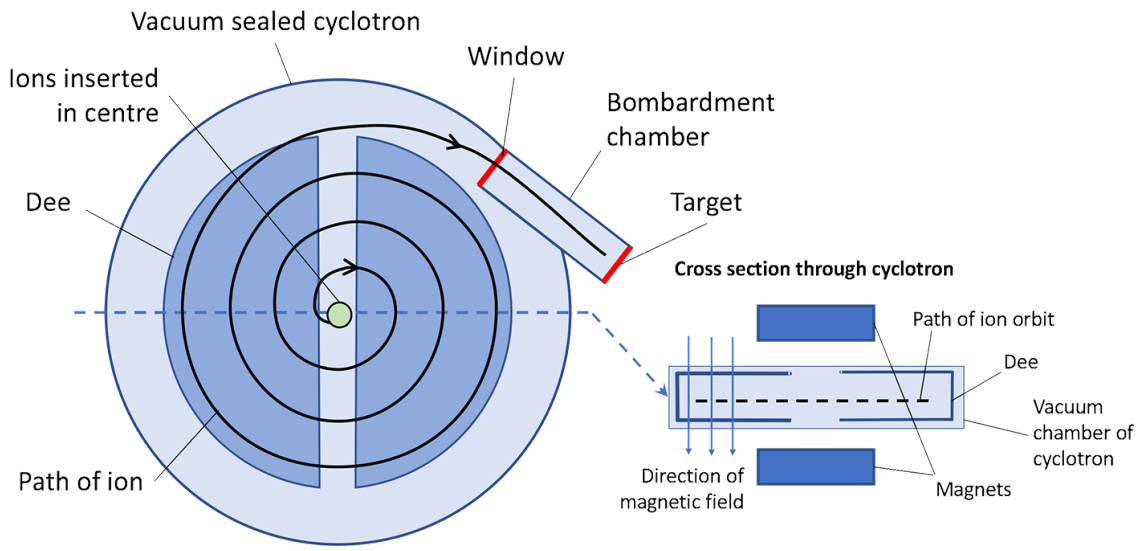

Figure I.5. Schematic of the cyclotron. A charged particle is freed at the center, two D-shaped electrodes (dark blue) create an alternating electric field between the two. The particle energy is increased when passing between the electrodes. A perpendicular magnetic field is keeping the particle on a spiral trajectory. The particle escapes the cyclotron after reaching a certain energy given by eq. (I.16). Taken from [15].

the Larmor radius.

To accelerate particles in an astrophysical object up to PeV energies the electric field potential would need to reach PV. In laboratory experiments, charged particles are accelerated by energy increments of ΔE when passing into electric fields along their trajectory. In a cyclotron (see fig. I.5), the particle is kept along a circular trajectory by using a magnetic field. After each half rotation the particle passes through an electric field increasing its energy. After each energy gain ΔE the particle will increase its Larmor radius. Therefore the maximum energy that can be reached is given by the size of the accelerator R and the magnetic field B in the accelerator:

$$E_{max} = qBR\beta, \tag{I.16}$$

with $\beta = \frac{v_\perp}{c}$.

More sophisticated machines, like synchrotron, adjust the magnetic field intensity to keep the trajectory of the particle within the same circular orbit. This has been successful for accelerator particle physics experiments such as the Large Hadron Collider (LHC) that reached up to TeV scale energies for a radius of about 10 km and magnetic field of about 10 kG.

One can understand, from eq. (I.16), that the size of the accelerator and the magnetic field intensity at the acceleration site limits the maximum observable cosmic-ray energy. This conditions in eq. (I.16), known as the Hillas condition, can be visualized as in fig. I.6. It can be seen that only a few candidates can explain the highest energy cosmic-ray protons observed.

I.3.1.1 Fermi mechanism

As seen in section I.3 from accelerator physics experiments, two observations can be applied to astrophysical particle accelerators:

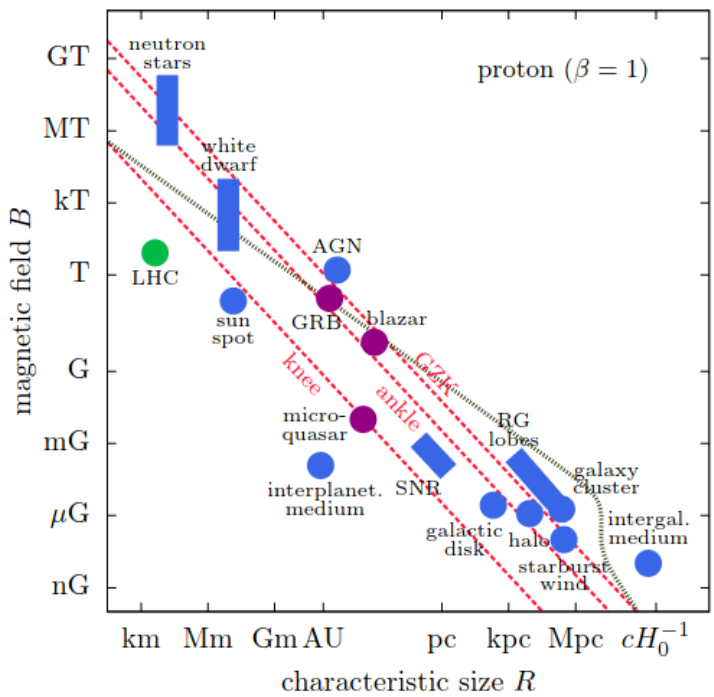

Figure I.6. "Hillas' plot". The plot shows some astrophysical objects as a function of their size and magnetic field strength. The dashed diagonal lines represent maximum energies achievable with protons with ($\beta = 1$) to achieve the knee, ankle and the GZK energies. These dashed lines do not take into account synchrotron energy losses in the source which are instead accounted for by the gray line. Taken from from [16].

- the size of the object and its magnetic field strength limits the maximum energy of the accelerated cosmic-rays;
- incremental increase of energy is a successful mechanism in accelerating particles.

However, the power law energy spectra observed for cosmic-rays is not explained. The second and first order Fermi mechanisms can accelerate particles with non-thermal energy spectra. The first mechanism proposed by Fermi [17] concerned particles accelerated in collisions with clouds of magnetized plasma. The second one concerned non-relativistic shocks, such as the ones observed by astronomers in supernovae. In both cases, the collision increases the particle energy by the increment $\Delta E = \langle \xi \rangle E$, proportional to the energy of the particle E[10]. Therefore, after n collision the energy E_n of the particle is:

$$E_n = E_0(1 + \langle \xi \rangle)^n, \tag{I.17}$$

with E_0 the injection energy in the accelerator. To reach an energy E, the particle has to undergo n interactions:

$$n = \frac{\ln\left(\frac{E}{E_0}\right)}{\ln\left(1 + \langle \xi \rangle\right)}. \tag{I.18}$$

Considering that after each interaction the particle as a probability p to escape. The number of particles reaching an energy E or greater is given by:

[10] where $\langle \xi \rangle$ represents the average value of the relative energy gain $\frac{\Delta E}{E}$.

$$N(\geq E) = N_{tot} \sum_{m=n}^{\infty} (1-p)^m = \frac{(1-p)^n}{p}, \tag{I.19}$$

with N_{tot} the total number of particles in the accelerator.
Substituting eq. (I.18) into eq. (I.19) gives the following:

$$N(\geq E) = N_{tot} \frac{1}{p} \left(\frac{E}{E_0}\right)^{-\delta} \Rightarrow \frac{dN}{dE} \propto \left(\frac{E}{E_0}\right)^{-\delta-1}, \tag{I.20}$$

where

$$\delta = \frac{\ln\left(\frac{1}{1-p}\right)}{\ln\left(1+\langle\xi\rangle\right)} \simeq \frac{p}{\langle\xi\rangle}. \tag{I.21}$$

From eq. (I.20) one can see that the Fermi mechanism, with an incremental increase of energy of $\Delta E = \langle\xi\rangle E$, leads to an energy power-law spectrum. Moreover, the escape probability p can be expressed in terms of the characteristic acceleration times T_{cyle} (the time it takes for a particle to be in the single acceleration cycle, e.g. traversing an accelerating shock and back) and the escape time T_{esc} (the time during which the acceleration process is efficient) as: $p = \frac{T_{cycle}}{T_{esc}}$. Thus, the number of collisions after a time t is $n = t/T_{cycle}$ and the corresponding energy is [18] :

$$E \leq E_0(1+\langle\xi\rangle)^{\frac{t}{T_{cycle}}}. \tag{I.22}$$

I.3.1.2 First and second order Fermi mechanism

Let's consider the collision of a charged particle entering a moving plasma cloud of velocity V at an angle θ_1 (see fig. I.7 left). The particle enters the magnetized cloud with energy E_1. Which in the rest frame of the moving gas is:

$$E_1' = \gamma E_1(1-\beta\cos\theta_1), \tag{I.23}$$

with γ the Lorentz factor and $\beta = V/c$ the velocity of the cloud.
The particle escapes the gas with energy E_2 and angle θ_2. The energy is given by the Lorentz transformation:

$$E_2 = \gamma E_2'(1+\beta\cos\theta_2'), \tag{I.24}$$

with θ_2' the escape angle in the cloud rest frame. Scattering within the cloud is due to magnetic deflection and thus do not imply a change of energy. Therefore the energy of the particle in the frame of the cloud is conserved $E_1' = E_2'$. Thus, using the previous results, the relative gain in energy per each magnetic cloud collision is:

$$\xi = \frac{\Delta E}{E_1} = \frac{E_2 - E_1}{E_1} = \frac{1-\beta\cos\theta_1+\beta\cos\theta_2'-\beta^2\cos\theta_1\cos\theta_2'}{1-\beta^2} - 1. \tag{I.25}$$

As many incident angle θ_1 and outgoing angle θ_2' are possible, averages of the terms $\cos\theta_1$ and $\cos\theta_2'$. Doing so the average energy gain $\langle\xi\rangle$ can be computed.
The second and first order Fermi mechanisms consider two scenarios. The second was just described. The first (see fig. I.7 right), supposes a large plane shock wave moving

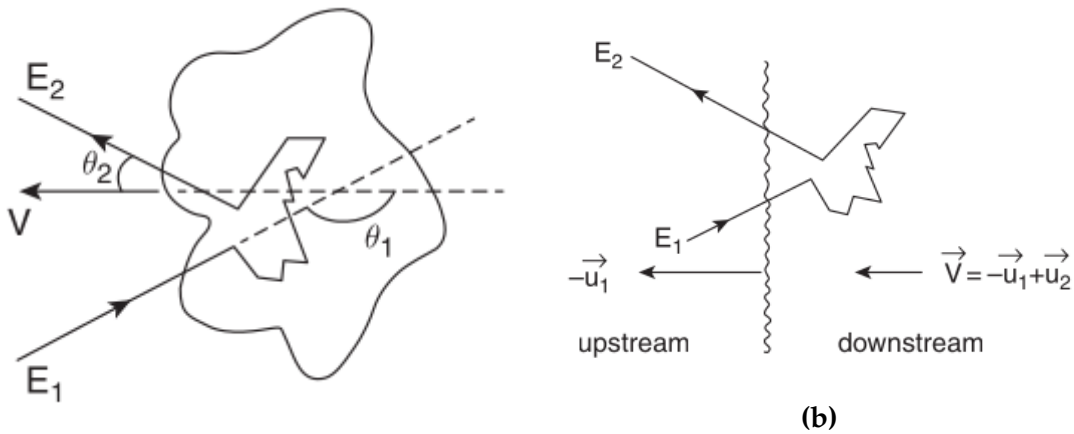

Figure I.7. Illustration of the first (right) and second (left) order Fermi mechanisms. Taken from [18].

with velocity $-\vec{u}_1$, e.g. after a supernova explosion. The shocked gas flows with a velocity $\vec{V} = -\vec{u}_1 + \vec{u}_2$, with $\vec{u}_2$ the relative velocity of the shocked gas by the shock front. In both the second and first order Fermi mechanisms, the relative energy gain can be described by eq. (I.25). However the difference arises from the different averaging of the cosine terms in eq. (I.25) which are:

$$\langle \cos\theta_1 \rangle = -\frac{\beta}{3} \qquad \langle \cos\theta_2' \rangle = 0 \qquad \text{Second order} \tag{I.26}$$

$$\langle \cos\theta_1 \rangle = -\frac{2}{3} \qquad \langle \cos\theta_2' \rangle = \frac{2}{3} \qquad \text{First order.} \tag{I.27}$$

These yield to the following average energy gain for each Fermi mechanism:

$$\langle \xi \rangle \sim \frac{4}{3}\beta^2 \qquad \text{Second order} \tag{I.28}$$

$$\langle \xi \rangle \sim \frac{4}{3}\beta \qquad \text{First order.} \tag{I.29}$$

As the energy gain in the second order Fermi mechanism is proportional to β^2 it makes it an inefficient acceleration mechanism when compared to the first order Fermi mechanism, since $\beta << 1$. To achieve high energies with the second order mechanism, the cloud velocity or the number of collisions would need to be high. This does not corresponds to the observations, as the cloud velocities are not ultra-relativistic and the number of collisions in the Galaxy is expected to be low.

It can be shown that, the escape probability of the first order Fermi mechanism depends on the compression ratio of the shock. For an ideal gas, this leads to an energy spectrum with a power-law spectral index of $\gamma = 2$. Such mechanism of acceleration could apply to supernova remnant shells [19].

I.4 Interactions in a cosmic-ray sources

The presence of cosmic-ray primaries in the Galaxy, such as electrons, protons, heavy nuclei can be attributed to stellar nucleosynthesis. The acceleration of those up to ultra-high energies can be explained by the first and/or the second order mechanisms.

In this section, a generic source and the mechanisms which produce gamma-rays and neutrinos is described. The mechanisms explaining the deep relationship between gamma-ray and neutrino astronomy addressed is explained in section I.4.1. Additionally, the mechanisms yielding the acceleration of high-energy gamma-rays through leptonic interaction are described in section I.4.2.

I.4.1 Hadronic processes

At cosmic acceleration site, hadronic cosmic-rays interact with the surrounding matter and radiation. For instance, the interaction of accelerated protons with hydrogen nuclei results in the following interaction:

$$p + p \longrightarrow N\left(\pi^+ + \pi^- + \pi^0\right) + X, \tag{I.30}$$

where X is a nuclei and N is the number of pions produced. Similar interactions happen for accelerated nuclei, where the nuclei can be treated by the superposition model (a nucleus of energy E_0 and atomic number A can be treated as a nucleus of energy E_0/A).

The interaction of cosmic-rays with the surrounding radiation in a source is characterized by the reaction:

$$p + \gamma \longrightarrow \Delta^+ \longrightarrow \pi^0 + p, \tag{I.31}$$
$$\longrightarrow \pi^+ + n. \tag{I.32}$$

The pp and $p\gamma$ interactions produce pions which are unstable particles and therefore decay via these dominant channels:

$$\pi^0 \longrightarrow \gamma + \gamma, \tag{I.33}$$
$$\pi^+ \longrightarrow \mu^+ + \nu_\mu \longrightarrow e^+ + \nu_e + \nu_\mu + \bar{\nu}_\mu, \tag{I.34}$$
$$\pi^- \longrightarrow \mu^- + \bar{\nu}_\mu \longrightarrow e^- + \bar{\nu}_e + \bar{\nu}_\mu + \nu_\mu. \tag{I.35}$$

The decay of neutral pions produce two gamma-rays. The decay of charged pions produce muons and associated neutrinos. The muons will inevitably also decay into electrons and neutrinos, unless its energy is very high so that its lifetime is augmented by a large Lorentz factor. Thus the end product of cosmic ray interactions through the pion decays are neutrinos of electron and muon flavors, electrons, together with other nucleons.

The secondary electrons resulting from the pp interactions can be further accelerated by the mechanism described in section I.3 or interact further with the surrounding media. However, the neutral secondaries produced from the pp and $p\gamma$ interactions: neutrinos and gamma-rays are free to escape the acceleration site. Being neutral, they

travel in straight lines. Therefore, they can be traced back to the acceleration site. Several gamma-ray sources have been detected by space and ground based telescopes, such as the ones described in section III.1. Nonetheless, astrophysical sources of neutrinos are yet to be identified. Efforts are being conducted in this direction by neutrino telescopes (see chapter IV for a description of a neutrino telescope). The low interaction probability of neutrinos makes them hard to detect. Nevertheless, their low interaction cross-section is also an advantage for astronomers. Neutrino messengers can travel over cosmological distances while being unaffected by the matter or radiation along their trajectories. See section I.7 for further information on the horizon of the cosmic-rays.

I.4.2 Leptonic processes

Leptonic processes concern interactions of charged leptons, especially electrons, and their energy losses. Electrons undergo two interactions in accelerators: the synchrotron radiation and the inverse Compton scattering. These two interactions produce detectable gamma-rays over a wide range of energy. They are responsible for great loss of energy of electrons and positrons.

I.4.2.1 Synchrotron radiation

In eq. (I.14), the Lorentz force applied on a moving charged particle in electric and magnetic field is given. This shows that an electron follows a helical trajectory along the magnetic direction. The rotational frequency of the electron is given by:

$$f = \frac{Be}{2\pi\gamma m_e}, \tag{I.36}$$

with B the magnetic field strength, e the electron charge, γ the Lorentz factor of the electron and m_e the electron mass. The bending of the electron trajectory on a circular path by the magnetic field creates a radiation called the synchrotron radiation. The synchrotron radiation forms a spectrum peaked at the synchrotron frequency (as seen by the observer):

$$f_s = \gamma^3 f. \tag{I.37}$$

In the process of radiating, the energy loss rate for the electron is given by:

$$-\frac{dE}{dt} = \frac{4e^4}{9m_e^4c^7}E^2B^2, \tag{I.38}$$

with E the electron energy.

From eq. (I.38), one can see that the energy loss rate increases with the square of the energy of the particle. This limits the acceleration of charged particles in particular of low mass charged particles as the energy loss rate is inversely proportional to the mass to the power four. Therefore synchrotron radiation for protons only becomes important if they reach energies above TeV range. As already mentioned, synchrotron radiation is emitted mainly by electrons. The electron synchrotron radiation spectrum of astrophysical sources is found from radio to soft X-ray [18].

I.4.2.2 Inverse-Compton scattering

In order to reach higher gamma-ray energies than the ones obtained from electron synchrotron radiation, ultra-relativistic electron can interact with surrounding photons (synchrotron photons or ambient photons). The photon gains energy from the electron by the so-called inverse-Compton (IC) scattering. This Compton effect is described in section II.1.1.2. In that case, the electron gains energy from the photon.

After each interaction the photon energy is increased by a factor γ^2. The Lorentz factor of electrons is thought to be between $\gamma = 100$ and $\gamma = 1000$. Moreover the gain of energy of the photon can be significant after multiple scattering. Depending on the initial energy of the photons and the Lorentz factor of electrons, the spectra of the inverse-Compton process varies significantly.

The energy loss rate of the electron for inverse-Compton scattering resembles the one of the synchrotron radiation (see eq. (I.38)). Moreover, the two can be put in relation by:

$$\frac{\left(\frac{dE}{dt}\right)_{syn.}}{\left(\frac{dE}{dt}\right)_{IC}} = \frac{B^2}{2\mu_0 U_{rad}}, \tag{I.39}$$

with U_{rad} the energy density of photons and μ_0 the vacuum permeability. This last equation is a great example of broad band multi-wavelength astronomy. Observing astrophysical objects from radio to high-energy gamma-rays allows to constrain the magnetic field strength assuming the radiation density U_{rad} is known. The energy spectrum of the Crab nebula, one of the most powerful gamma-ray emitter, can be seen in fig. I.9. The model of synchrotron and IC spectra are superimposed.

I.5 Astrophysical accelerators

The general theory behind the acceleration of primary cosmic-rays and the productions of the secondaries have been introduced in the previous section. In section I.5.1, the Crab Nebula a galactic cosmic-ray accelerator is presented. Then in section I.5.2, the Active Galactic Nuclei (AGNs) an example of extra-galactic sources of cosmic-ray is presented.

I.5.1 The Crab Nebula a galactic cosmic-ray accelerator

The Crab Nebula is a celestial object found in the Taurus constellation ($RA = 5\,h\,34.5\,min$, $Dec = +22°\,01'$). It is a supernova remnant (SNR) of apparent magnitude +8.4. The nebula spans over about 5 arcmin. It is the first object of the Messier catalog hence named M1. It is also sometimes designated as NGC 1952 or Taurus A. The SNR is thought to date from 1054, therefore named SN 1054, when Chinese astronomers observed it in the sky. M1 is located about 2 kpc from the Earth. Its diameter is estimated to be 3.4 pc wide and it is expanding at a rate of about 1500 km per second. A photograph of the Crab Nebula from the Hubble space telescope is shown in fig. I.8.

At the center of the nebula lies the remnant of the star that exploded in 1054, a neutron star. The neutron stars magnetic field beams its radiation. The neutron star is rapidly rotating (about 30 revolution per second). This rotating neutron star is known as the Crab Pulsar. The pulsar emits radiation spanning over a wide range of the light spectrum: from radio waves to gamma-rays.

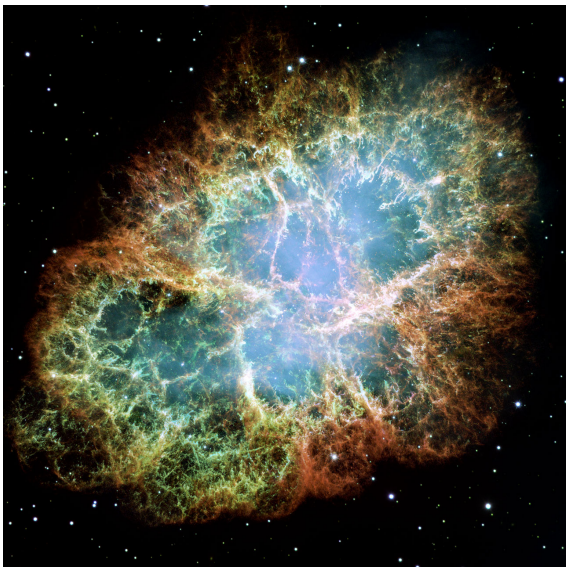

Figure I.8. The Crab Nebula captured by the Hubble Space Telescope. Credit: NASA, ESA.

The Crab Nebula is one of the brightest source of photons beyond the X-ray energies and its spectrum has been well studied by many telescopes. The Spectral Energy Distribution (SED) of the Crab Nebula from 10^{-5} eV up to 10^{13} eV is shown in fig. I.9 (top). Models for the synchrotron and IC radiations are shown.

Since M1 is a bright source of gamma-rays and its spectrum is well characterized up to 1 TeV it is used as a standard candle in gamma-ray astronomy.

The Crab nebula spectrum from 6 GeV up to 20 TeV has been measured by the MAGIC telescope. The measured spectrum is illustrated in fig. I.9 (bottom). A well suited parameterization, in this range, is given by [21]:

$$\Phi^{\gamma}(E) = 3.23 \times 10^{-7} \left(\frac{E}{TeV}\right)^{-\alpha-\beta \log_{10}\left(\frac{E}{TeV}\right)} \; TeV^{-1} \cdot m^{-2} \cdot s^{-1}, \tag{I.40}$$

$$\alpha = 2.47, \tag{I.41}$$

$$\beta = 0.24. \tag{I.42}$$

This parameterization will be used later in chapter VI.

The SED allows to constrain the magnetic field strength in the Crab Nebula. The analysis in [20] reported a magnetic field strength $B \simeq 124$ μG. Using the Hillas' condition in eq. (I.16), one can understand that the Crab Nebula has surely not a strong enough magnetic field to accelerate cosmic-rays above the ankle. However if the SNRs are the sources of galactic cosmic-rays they must be able to accelerate particle up to the knee. It is a puzzle if most SNRs can or not accelerate cosmic rays to the knee energies. As a matter of fact, the typical energy achieved for a SNR before the shock becomes inefficient ($t = T_{shock} \sim 1000$ yrs, see eq. (I.22)) is $E_{max} \sim Z \times 100$ TeV, hence an order of magnitude in energy is missing to explain the knee. For such high magnetic fields, one can evoke non-linear Fermi shock acceleration mechanisms, which can produce maximum energies compatible with the knee. Additionally, for SNRs softer spectra than what predicted by the Fermi acceleration mechanism (E^{-2}) are observed in the GeV-TeV region. This is still a puzzle and the slope and maximum energy seems to be connected to the age of the SNR

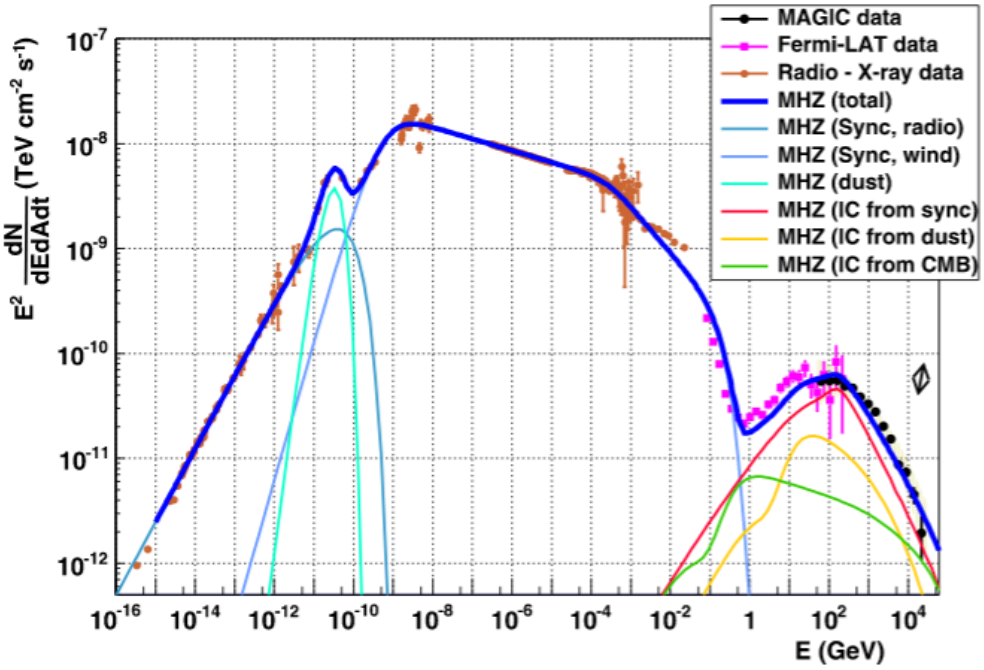

(a)

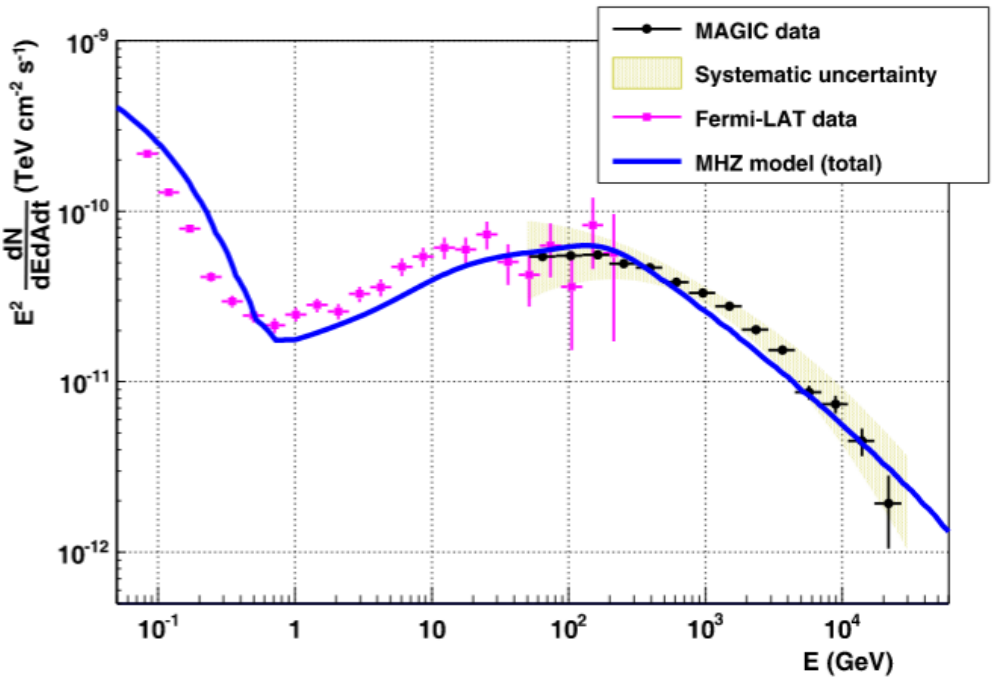

(b)

Figure I.9. Top: Crab Nebula energy spectrum from radio waves up to high energy gamma-rays. The data is fitted by the model in [20]. Bottom: Crab nebula energy spectrum in gamma-ray energies measured by the Fermi-LAT telescope and the MAGIC telescope. Taken from [21].

so to a time-dependent efficiency of the accelerator [22]. Thus other sources of cosmic-rays are needed to explain the observed flux above the ankle.

I.5.2 Active galactic nuclei

It is estimated that about one percent of galaxies are Active Galactic Nucleus (AGN), hosting at its centre an active black hole. AGNs are extremely bright sources covering the electromagnetic spectrum from radio up to TeV gamma-rays. The total energy radiated per seconds for AGNs can reach up to 10^{47} $\mathrm{ergs} \cdot \mathrm{s}^{-1}$ [18].

Such radiating power is reached by the accretion of matter around a supermassive black hole (see fig. I.10). The black hole is surrounded by a disk of matter. The fall of the matter towards the black hole liberates energy in the form of radiation. The radiation emitted pushes the matter outwards. Thus there is an equilibrium between the "feeding" of the black hole and its luminosity. Such equilibrium is found by equating the gravitational force on a hydrogen atom (supposedly the disk is composed of hydrogen mainly) and the radiation force on the atomic electrons:

$$\frac{L\sigma_T}{4\pi R^2 c} = \frac{GM(m_p + m_e)}{R^2} \simeq \frac{GMm_p}{R^2}, \tag{I.43}$$

with L the luminosity of the AGN, σ_T the Thomson cross section, R the radial distance, c the speed of light in vacuum, G the gravitational constant, M the black-hole mass, m_e the electron mass and m_p the proton mass [23]. The equilibrium in eq. (I.43) yields the so-called Eddington luminosity:

$$L_{edd} = L = 4\pi \frac{GMm_p c}{\sigma_T} \simeq 1.4 \times 10^{38} \left(\frac{M}{M_\odot}\right) \mathrm{erg} \cdot \mathrm{s}^{-1}. \tag{I.44}$$

The Eddington luminosity offers an upper limit for the radiation power of AGNs. If this limit would be surpassed the radiation would blow the accumulated matter thus no "food" would "feed" the black hole. This limit is however sometimes surpassed, for instance during short bursts of radiation.

The radiation from the jet is aligned with the rotational axis. AGNs have been classified in different categories. They correspond to a certain observation angle with respect to the jet. The categories of AGNs are schematically represented in fig. I.10.

The SED of AGNs allows for both leptonic and hadronic processes. The detection of high-energy neutrino secondaries from AGNs could confirm the existence of hadronic processes. If the existence of hadronic interaction in AGNs is confirmed, then AGNs could be at the origin of the UHECRs observed above the ankle of the cosmic-ray spectrum.

I.6 Neutrinos in the Universe

In section I.4.1, it was shown that the hadronic interaction of primary cosmic-rays with the surrounding media produces charged pions. In turn, the charged pions decay into leptons and neutrinos. From the interaction cross sections, it can be estimated that about 20% of the proton energy is transferred to the charged pions, and in the relevant energy region this number is constant with energy. The fraction of the pion energy transferred to its decay products is shown in fig. I.11. The charged pion decay produces neutrinos with

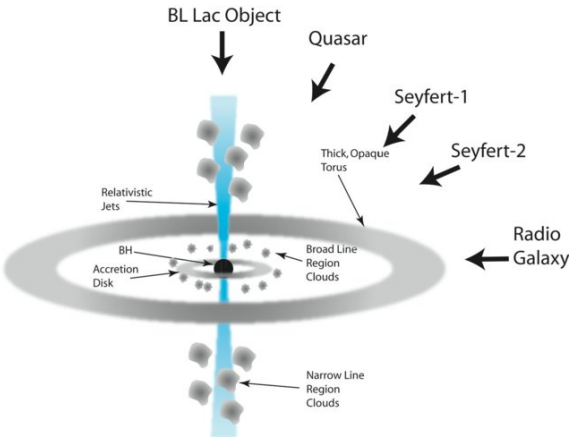

Figure I.10. Schematic of an AGN. At the center is a black hole (BH) surrounded by an accretion disk. The jet is emitted parallel to the rotational axis. AGNs observed at different angles correspond to different categories of AGNs. Taken from [24].

energy, on average, ~ 25% of the pion energy. Thus the energy of the neutrino is about 5% of the proton energy on average.

.

The decay of the charged pions and the following decay of the muon indicates that the flavor composition $(\nu_e : 1, \nu_\mu : 2, \nu_\tau : 0)$. Over cosmological distances, due to neutrino flavor oscillation, an equal composition of $(\nu_e : 1, \nu_\mu : 1, \nu_\tau : 1)$ is expected. In the end, this reduces the detected flux of muon neutrinos. The muon neutrinos are preferred for detection since they produce long muon tracks in the detection volume and thus allow for better angular resolution. A neutrino telescope is presented in chapter IV.

In fig. I.12, it is shown the neutrino spectrum as function of energy. Astrophysical neutrinos are found among the highest energy neutrinos because up to about 50 TeV they are submersed by the flux of atmospheric neutrinos produced by cosmic ray interactions in the atmosphere. The detection of neutrinos form astrophysical sources would be the proof of hadronic interaction in cosmic-ray accelerators, because they are produced by proton interactions and meson decay.

Neutrinos leave their production site and reach us without being deflected. Therefore, they should point back to their sources. On the contrary, charged cosmic-rays are deflected by magnetic fields. Nonetheless, the higher the energy of the charged cosmic-rays the lower the deflection. Following this, a study on the cross-correlation between astrophysical neutrinos and UHECRs has been conducted in chapter VII.

I.7 Propagation of cosmic-rays in the Universe

Once produced, accelerated and released, cosmic-rays undergo interactions with the media (radiation, interstellar matter) between the production site and the Earth. The interactions of cosmic-rays with matter surrounding the acceleration site have already been discussed. Here the interaction of particles when travelling over extra-galactic distance is discussed. Between galaxies one can consider that the prominent target for cosmic-rays are cosmic microwave background (CMB) photons [18]. As can be seen in fig. I.13, this is the most abundant radiation in the universe, with density of about 400 CMB photons per cubic centimeter left-over of the Big Bang. It was discussed in section I.2.1 that this

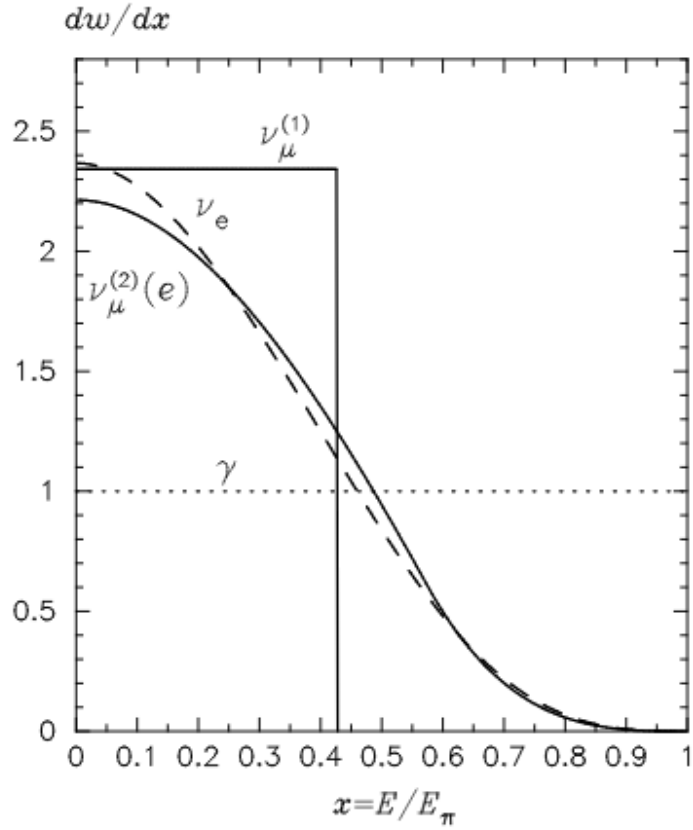

Figure I.11. Energy distribution as function of the fraction of the pion energy of the pion decay products. The figure shows: the electronic neutrino ν_e, the muonic neutrino ν_μ of the pion decay (1) and the muonic neutrino from the muon decay (2), the gamma-ray from the neutral pion decay. Taken from [25].

interaction with the CMB yields the so-called GZK limit at the end of the cosmic-ray spectrum. One can understand, that the interaction of cosmic-rays with CMB photons limits the horizon of cosmic-rays. For the highest energies the source would need to be close so that the CMB interaction probability would be small.

Analogously, the photons also have a horizon. The dominant interaction for the highest energy gamma-rays is the interaction with extra-galactic background light (EBL) producing an electron-positron pair:

$$\gamma + \gamma_{\mathrm{EBL}} \longrightarrow e^- + e^+. \tag{I.45}$$

The EBL comprises the diffuse background light of all wavelengths of the electromagnetic spectrum (see fig. I.13).

Comparing the integrated intensity of all known stars, galaxies, AGNs and other sources to the intensity of the EBL for each wavelength could allow to reveal new diffuse emission. Such emission could be associated to photon emission in dark matter annihilation [27].

From GeV-scale to TeV-scale gamma-rays, the interaction in eq. (I.45) happens with optical and near infrared EBL photons. This yields a horizon for gamma-rays. The horizon is given by the interaction length $\lambda = \frac{1}{n\sigma}$, with n the density of EBL photons and σ the cross-section. With the Cherenkov Telescope Array (see section III.2) in the

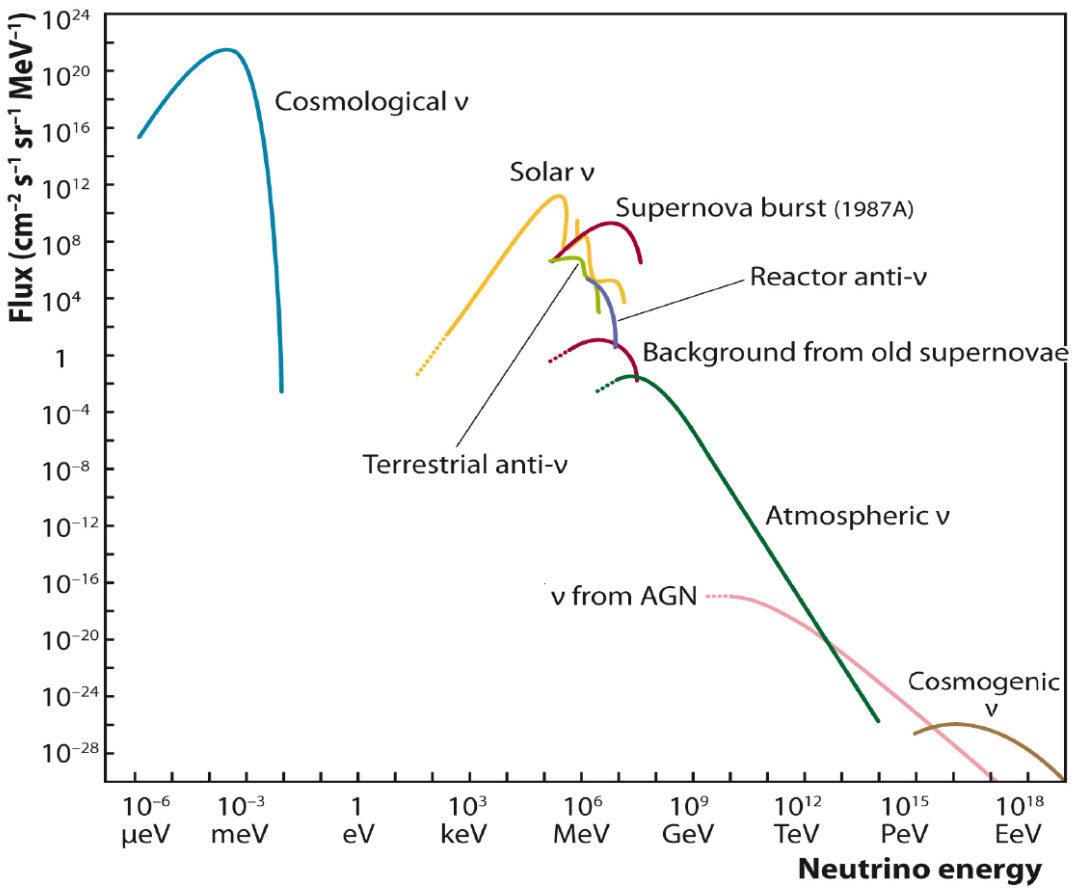

Figure I.12. Neutrino flux from natural phenomena and human activity. Are shown: the cosmological neutrinos from the neutrino cosmic background (blue); solar neutrino from nuclear fusion (yellow); neutrinos associated with the SN 1987A and over-all background from supernovae (red); neutrinos from β-decay in Earth and nuclear plant; atmospheric neutrinos produced in atmospheric showers initiated by cosmic-rays (green); expected neutrinos from extra-galactic sources such as AGNs (pink); cosmogenic neutrinos from the GZK process (brown). Taken from [26].

future, and currently with gamma-ray data from Fermi-LAT [28] and other existing IACTs (see section III.1), the limit on the highest observable gamma-ray fluxes as a function of the emitting source distances can be used to infer the EBL spectrum at optical and near infrared wavelengths. By measuring the spectra of a large population of distant blazars (for several redshifts), the absorption of gamma-rays due to EBL interactions can be determined, thus yielding an indirect measurement of the EBL. Such measurement have been performed for instance by the MAGIC and the H.E.S.S collaborations [29, 30] in the optical and near infrared regions. The direct measurement of the EBL is strongly affected by Zodiacal light (see section II.2.3.1) emission, which is difficult to suppress. Indirect measurements performed by the next generation of gamma-ray telescopes (such as the one presented in section III.2) will allow to constraint further the EBL spectrum in the optical and the near infrared wavelength band.

The proton and gamma-ray horizon are shown in fig. I.14. Above the GZK limit the observable Universe is about 10 Mpc, which is about the distance to nearby clusters. Similarly for gamma-rays the limit is at about 10 Mpc.

In addition to CMB interactions, charged cosmic-rays suffer from interactions with

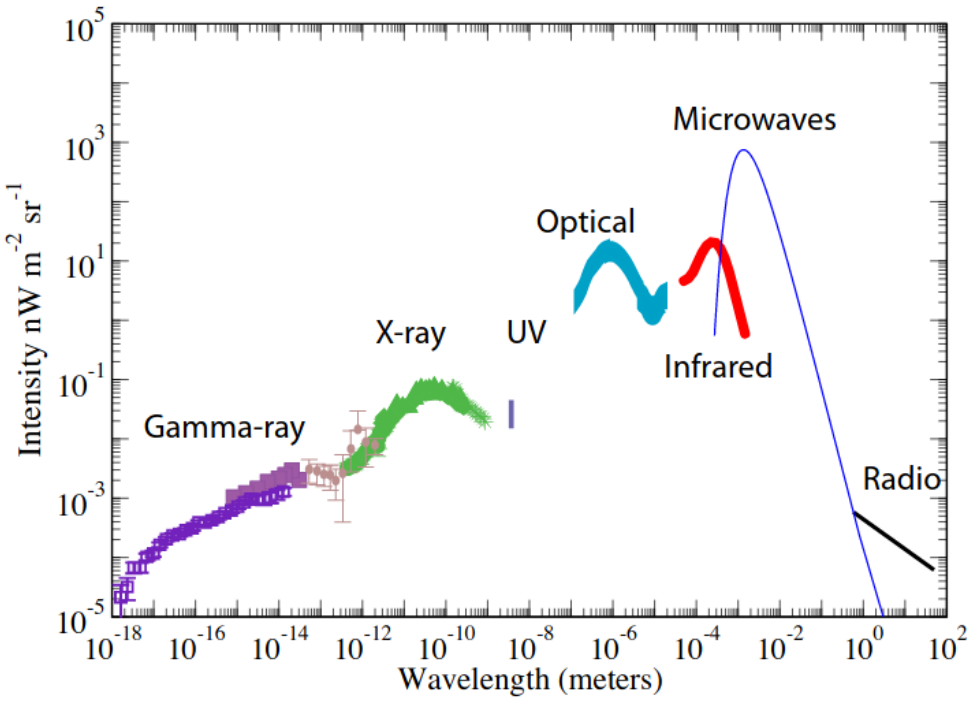

Figure I.13. Measured EBL intensity as a function of wavelength. Taken from [27].

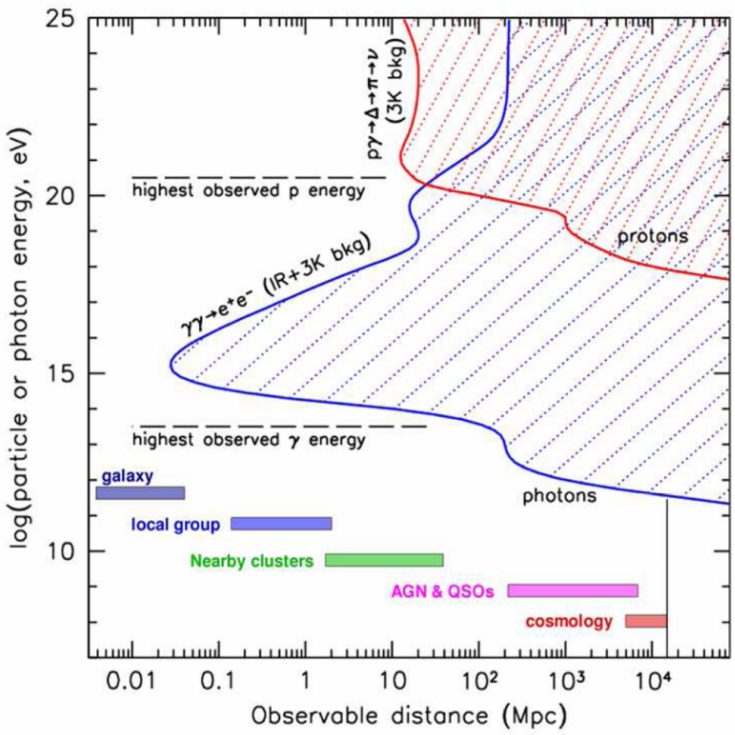

Figure I.14. The horizon (which is the interaction length) of protons (red) and gamma-rays (blue) from CMB and EBL interactions. Distances are compared to typical astrophysical sizes. Taken from [31]

magnetic fields found along their journey to us. In particular, they are affected by terrestrial, galactic and extra-galactic magnetic fields. The terrestrial field only affects the cosmic-rays flux below few GeV. Charged cosmic-rays undergo several deflections due to the regular and turbulent component of the galactic magnetic field. Models of the galactic magnetic fields are given in [32, 33]. The regular component of the galactic magnetic field is about 3 μG The turbulent component is about the same strength [18]. Simulated particles trajectories of charge Z and energy E over the galaxy model a deflection angle of about:

$$\theta_{RMS} \simeq 3^\circ Z \left(\frac{10^{20}\ \mathrm{eV}}{E}\right). \tag{I.46}$$

Thus the deflection angle is about 3° for the highest energy cosmic-rays of about 10^{20} eV. This led to a cross-correlation study between ultra-high energy cosmic-rays and neutrinos that is presented in chapter VII. Supposedly, the hadronic interactions of UHECRs, presented in section I.4.1, create neutrinos thus the two should be correlated. It is important to add, that although the deflection of UHECRs is low in absolute value, given the large distances the deflections with respect to the observer on Earth can make it impossible to detect the source of origin. As a matter of fact. To this day no source of UHECRs has been observed. However, a correlation is observed between the highest energy events of the Pierre Auger Observatory (PAO) [34] and a catalog of extra-galactic gamma-ray sources [35]. In particular, PAO observed a 4σ significance of correlation with a starburst galaxy (galaxies with high star formation rate) catalog (above 39 EeV) and a significance of 2.7σ for the AGN catalog (above 60 EeV). The detection of UHECR sources is the subject of extensive searches by the Telescope Array (TA) [36] and the PAO [37].

Less is known on extra-galactic deflection but one can estimate that extra-galactic deflection is about [18]:

$$\theta_{RMS} \simeq 3.5^\circ Z \left(\frac{B}{10^{-9}\ \mathrm{nG}}\right)\left(\frac{10^{20}\ \mathrm{eV}}{E}\right)\left(\frac{d}{100\ \mathrm{Mpc}}\right)^{1/2}\left(\frac{l}{1\ \mathrm{Mpc}}\right)^{1/2}, \tag{I.47}$$

with d the distance traveled by the cosmic-ray and l the coherence length.

The neutrinos are essentially free to travel. Therefore astrophysical neutrinos should provide deep insights to the cosmological distances far beyond the gamma-ray and cosmic-ray horizons.

Chapter II

Detection principle of astrophysical gamma-rays

Since the discovery of cosmic-rays, various techniques were aimed at detecting high-energy cosmic particles. Depending on the energy of the particle, it is detected directly or indirectly.

Additionally to cosmic-rays, the gamma-ray particles are of particular interest since their neutral charge makes them travel freely of galactic and extra-galactic magnetic fields. Thus their incoming direction traces back to the source of emission.

For the very low energy events, their progression towards us is rapidly stopped by the atmosphere or it is easily deflected by the dipolar Earth's magnetic field. Thus the lowest energy events are usually detected with space-based instruments. As the flux is higher at low energies it is not mandatory to have a large detection surface to have a sufficient event rate.

On the contrary, for the highest energy events, ground-based detectors are the preferred solution. The rate of high-energy events is low. Therefore the detectors effective surface area needs to be large. For this reason high-energy cosmic-ray detectors are ground based. Ground-based detectors detect the secondary particles produced from the interaction of cosmic-rays with the upper atmosphere. The interaction of high-energy cosmic-rays with the atmosphere produce an extensive air shower (EAS). Simulated extensive air showers are shown in fig. II.1. In section II.1 the interactions of photons and charged particles produced in air showers are explained. In particular, in section II.1.1 the dominant photon interactions with matter of high energy gamma-rays entering the atmosphere are described. Furthermore, in section II.1.2 the interaction of the charged secondaries produced in EASs are also explained. In section II.1.3 a model illustrating the air shower cascade mechanism for both hadronic and electromagnetic showers is presented.

Finally section II.2, an EAS detection technique from the emission of Cherenkov light form charged secondaries is described.

II.1 Interaction of cascade particles with the atmosphere

The interaction of high-energy particles with atmospheric molecules initiate a cascade of lower energy particles. These lower energy particles further create cascades of even lower energy particles. The cascade process stops once the sub-particles reach a certain

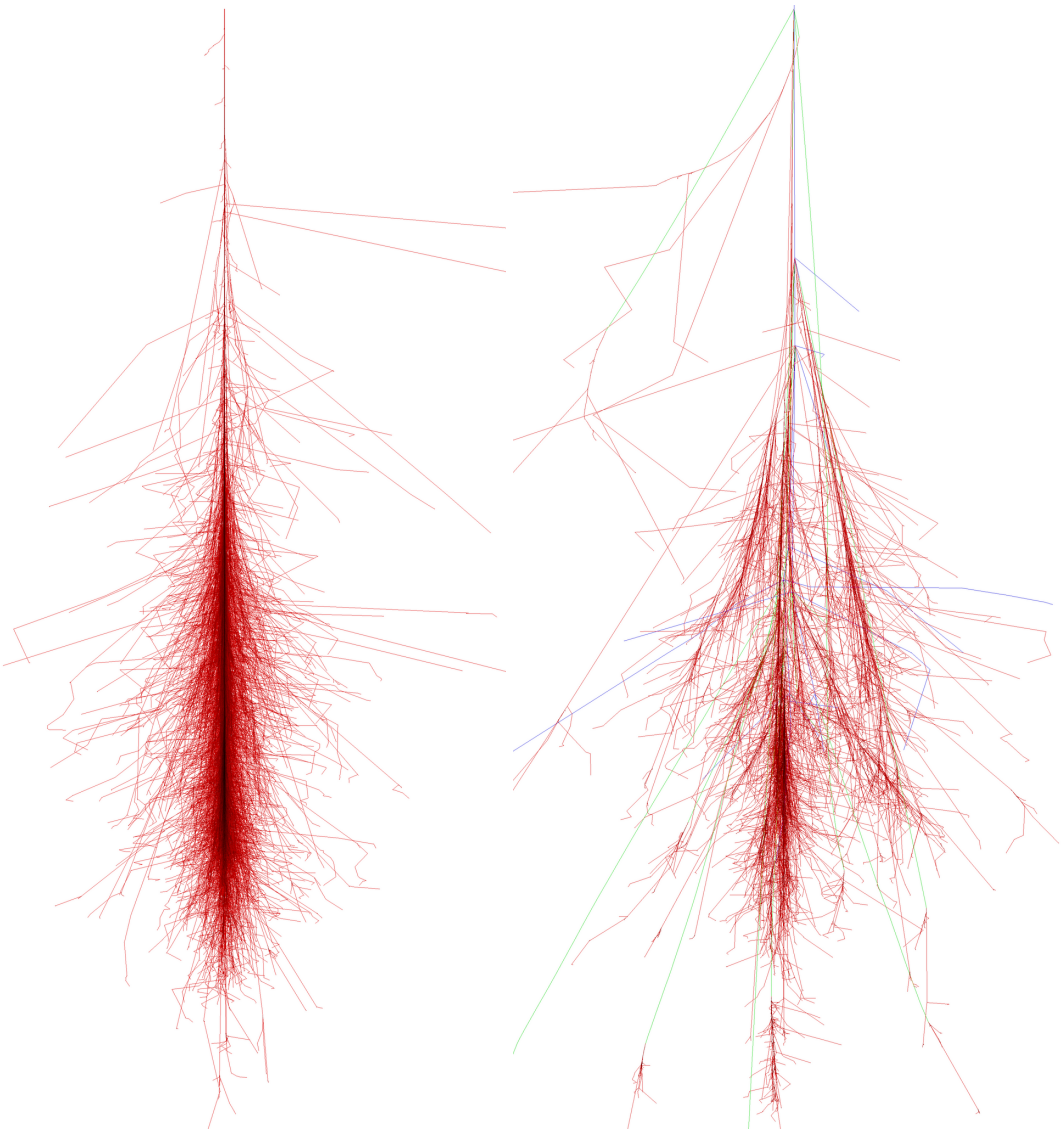

Figure II.1. Left: CORSIKA simulation of a 100 GeV gamma-ray EAS. Right: CORSIKA simulation of a 100 GeV proton EAS. The particle tracks in red correspond to electrons, positrons and gammas, the tracks in green correspond to muons and the tracks in blue to hadrons. The black color represents a high density of tracks. Taken from [38]

energy threshold stopping the cascade mechanism. This phenomenon is called extensive air showers.

In the following, the interaction of the primary particle (hadronic or photonic) with the upper atmosphere as well as the interaction and creation of the secondary particles are described.

II.1.1 Photon interaction with matter

The interaction of photons with matter can be reduced to three main interaction mechanisms: the photo-electric effect, the Compton effect and the electron positron pair production. The photo-electric effect dominates at low energies while the Compton scattering is dominant at mid-energies and the pair production is dominating at the highest energies.

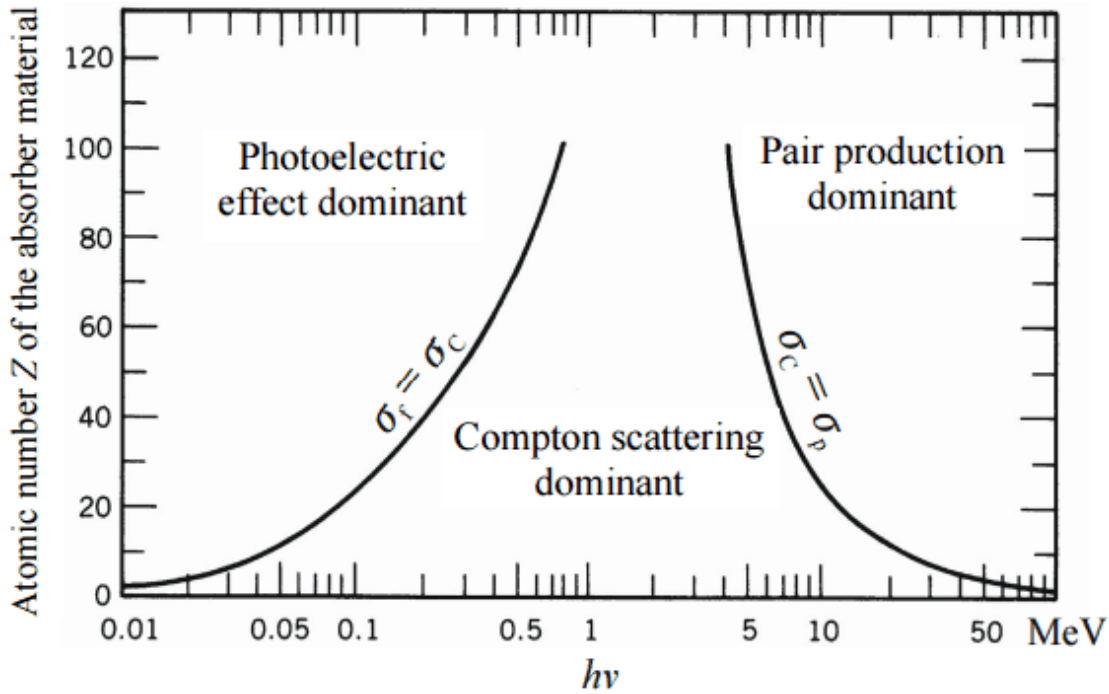

Figure II.2. Importance of gamma-ray interactions with matter as function of the energy of the photon and the atomic number of the atom. The solid lines indicates equal probabilities of interaction. Taken from [39].

The interaction probabilities depend on the atomic number as well (see fig. II.2).

II.1.1.1 The photo-electric effect

The photo-electric effect is the dominant interaction at low energies. The photon ejects an electron of an atom of atomic number Z. The photon disappears and the electron gains an energy $E = h\nu$ which is the energy of the incoming photon. The kinetic energy of the ejected electron is thus given by the difference between the photon energy and the binding energy of the electron E_b in the atom:

$$E_{kin} = h\nu - E_b. \tag{II.1}$$

The electron is ejected (i.e the photo-electric effect occurs) only if the energy of the photon is greater or equal to the binding energy of the electron.

This effect is used in low light photo-detectors such as photo-multiplier tubes (PMTs), see section III.3.1.

II.1.1.2 The Compton scattering

The Compton scattering is the dominating interaction of photons with matter in the mid-energy range. At these energies the photon interacts with an electron of an atom and is deflected by an angle θ (see fig. II.3).

Supposing that the electron is at rest, the following formula is obtained by applying momentum and energy conservation:

$$\lambda' - \lambda = \frac{h}{m_e c}(1 - \cos\theta) \tag{II.2}$$

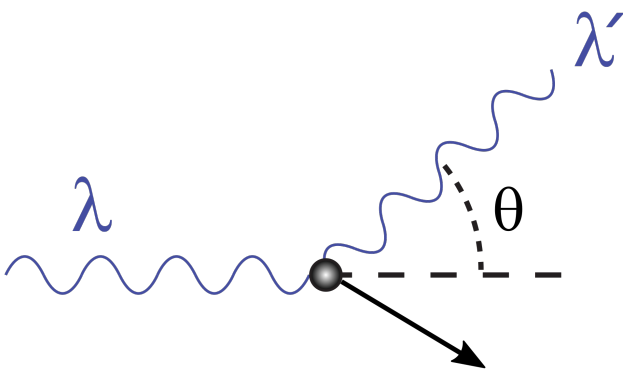

Figure II.3. Illustration of the Compton scattering.

where λ is the wavelength of the incoming photon, λ' is the wavelength of the scattered photon and m_e the electron mass. It can be seen from eq. (II.2), that no energy exchange occurs for $\theta = 0$. In addition a maximum energy exchange occurs for $\theta = \pi$. In this case the photon recoils with a wavelength change:

$$\Delta\lambda = \frac{2h}{m_e c} \simeq 4.86\ \mathrm{pm}. \tag{II.3}$$

The inverse effect of the Compton scattering: the Inverse Compton (IC) scattering is described in section I.4.2.2. In this case the electron increases the photon energy.

II.1.1.3 Electron positron pair production

The electron-positron pair production is the leading mechanism for photon interaction with matter at the highest energies. The process as its name suggests creates a pair of electron and position by, a photon:

$$\gamma \longrightarrow e^+ + e^-. \tag{II.4}$$

Such process cannot occur in vacuum as the energy and the momentum cannot be conserved. The process usually occurs near a nucleus. The nucleus is recoiled by the process. The minimum energy of the photon for electron-positron pair creation is $2m_e \simeq$ 1 MeV.

II.1.2 Interaction of charged particles with matter

Fast travelling charged particles interact with atomic nuclei and atoms. In EASs most charged particles are electrons. Their energy is typically higher than 85 MeV. In such case, two interaction processes are important to describe: the emission of Bremsstrahlung radiation (see section II.1.2.1 and the Cherenkov radiation (see section II.1.2.2). The first is responsible of the shower development from the electrons while the second enables the detection of the charged secondaries from the ground.

II.1.2.1 Bremsstrahlung radiation

Bremsstrahlung is a German word that can be translated as "braking radiation". It is the emission of photon by a decelerating charged particle. Typically the deceleration happens

when a free charged particle meets an atomic nucleus. The atomic nucleus deflects the charged particle trajectory. The loss of kinetic energy on the charged particle is emitted in the form of a photon.

The energy spectrum for Bremsstrahlung radiation is continuous. The maximum energy of the emitted photon corresponds to the energy of the electron.

The average energy loss per unit length for Bremsstrahlung radiation can be expressed as:

$$-\left\langle \frac{dE}{dx} \right\rangle \simeq \frac{4N_a Z^2 \alpha^3 (\hbar c)^2}{m_e^2 c^4} E \ln \frac{183}{Z^{1/3}}, \tag{II.5}$$

with N_a the density of atoms, Z the atomic number of the nucleus, m_e the electron mass, E the energy of the electron, α the fine structure constant, $\hbar$ the reduced Planck constant and c the speed of light in vacuum.

It can be seen that the energy loss per unit length depends linearly on the energy E. Thus at high energy the loss becomes greater. Moreover higher mass charged particles experience less energy losses through braking radiation than lower mass ones. Additionally the effect is stronger for higher Z materials as the energy loss per unit length is proportional to Z^2.

II.1.2.2 The Cherenkov radiation

Extensive air showers produce many charged particles in the atmosphere. Those charged secondaries are travelling at super-luminous velocities in the air. A form of radiation, called Cherenkov radiation, results, which can be detected on ground by telescopes. Here are presented the fundamentals of the Cherenkov radiation.

Cherenkov condition The Cherenkov radiation is an electromagnetic radiation produced by a charged particle travelling in a dielectric medium of refractive index n at a velocity v faster than the speed of light in the medium. The Cherenkov condition is given by:

$$v > \frac{c}{n}, \tag{II.6}$$

where c is the speed of light in vacuum. As the charged particle travels through the dielectric medium it polarizes the medium dipoles (see figure II.4 left). During the passage of the charged particle, the poles (the ones with the opposite charge of the particle) are attracted by the charged particle. After the passage of the charged particle, the dipoles return to their ground state. Doing so, the de-excited dipoles emit electromagnetic radiation. If the Cherenkov condition, in equation II.6, is fulfilled the emission is coherent and forms a wave-front (see figure II.4 right).

Cherenkov emission angle It can be understood by considering the schematic in figure II.5. Consider that the charged particle travels along the line indicated by the red arrow at a velocity $v = \beta c$. At time $t = 0$ it is at the left corner of the triangle forming an angle θ. After some time t it moved to the right corner of the triangle. The light emitted at first has traveled a distance of $\frac{c}{n}t$ while the particle has travelled a distance βct. The wave front is formed by the opposite side of the vertex forming an angle θ. Thus the Cherenkov emission angle can be expressed as:

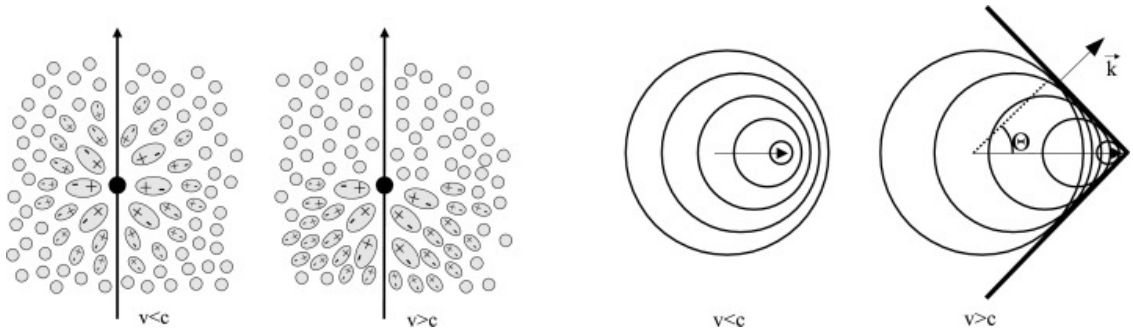

Figure II.4. Illustration of the Cherenkov effect. Left: Polarization of the dielectric medium (when the Cherenkov condition is satisfied and when it is not). Right: Construction of the wave-front of the Cherenkov light from a particle traveling to the right (when the Cherenkov condition is satisfied and when it is not). Taken from [40].

Dielectric	θ_{max} (deg)	Refractive index n	Minimum velocity β
Air (0 °C, 1 atm)	1.4	1.000293	0.9997
Water / Ice	41.4	1.333	0.75

Table II.1. Comparison of the maximum Cherenkov angle of emission θ_{max}, the refractive index n and the minimum velocity for different dielectric media.

$$\cos\theta = \frac{ct}{n\beta ct} = \frac{1}{n\beta}. \tag{II.7}$$

The Cherenkov effect is sometimes associated to the sonic boom created by super-sonic aircrafts. The build up mechanism of the wave-front is similar, but here the wave is created by electromagnetic radiation rather than sound waves.

As can be seen from equation II.7, the emission angle θ depends on the refractive index of the dielectric and the velocity of the charged particle β. The maximum velocity of the particle is $\beta = 1$ (the particle travels at the speed of light in vacuum c). Therefore the maximum angle of Cherenkov emission θ_{max} in a dielectric of refractive index n is given by:

$$\cos\theta_{max} = \frac{1}{n}. \tag{II.8}$$

In table II.1 are shown: the maximum emission angle θ_{max}, the refractive index and the minimum velocity of the charged particle satisfying the condition in equation II.6 for various dielectric media.

Cherenkov light spectrum The Frank-Tamm formula gives the number of Cherenkov photons emitted by a charged particle of charge Z per unit wavelength $d\lambda$ and per unit distance dx travelled in a radiator of index of refraction n:

$$\frac{d^2N}{dxd\lambda} = 2\pi\alpha Z^2\left(1 - \frac{1}{n^2\beta^2}\right)\frac{1}{\lambda^2}, \tag{II.9}$$

where $\alpha \sim \frac{1}{137}$ is the fine structure constant.

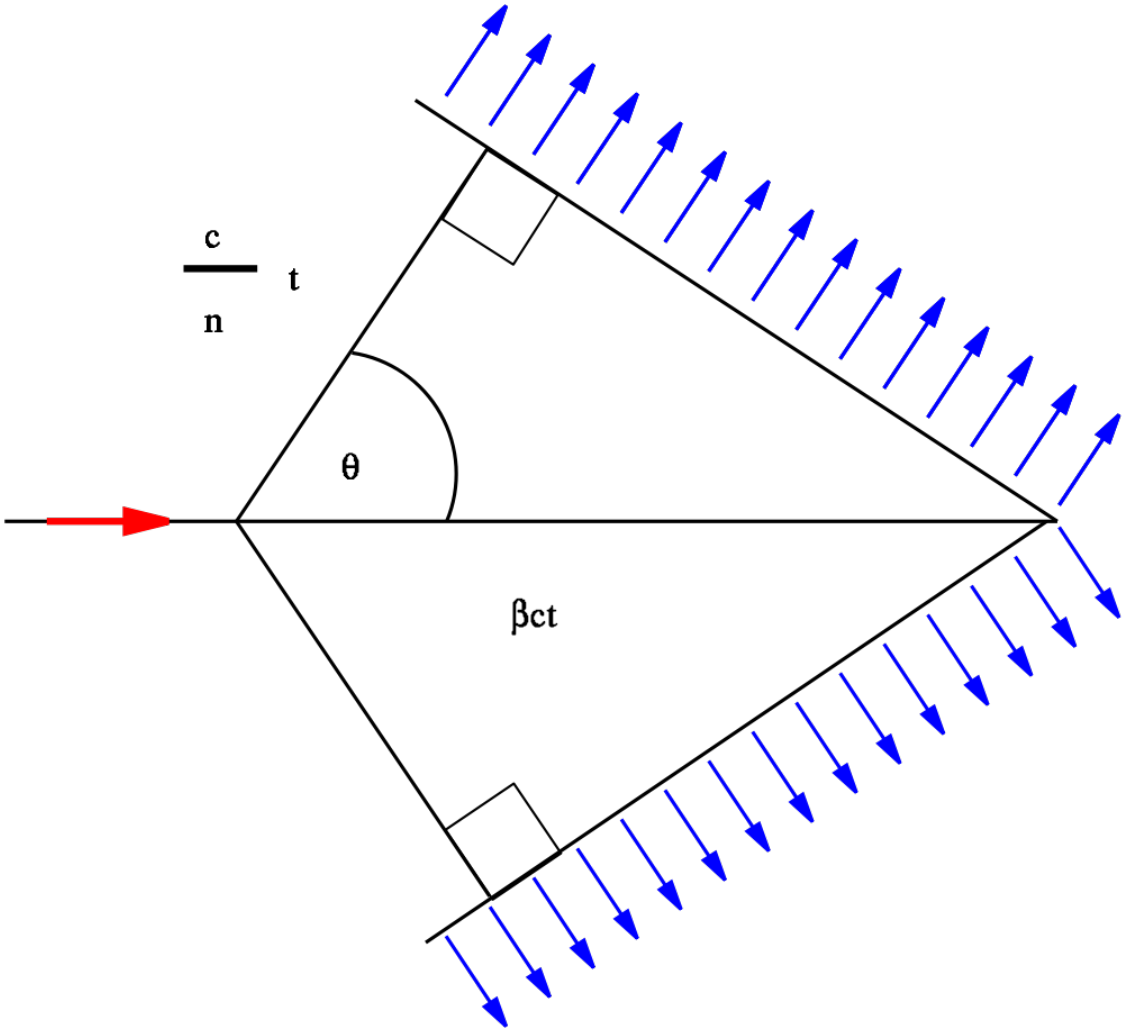

Figure II.5. Illustration of the Cherenkov emission angle. Credit: Arpad Horvath / CC BY-SA

P. Cherenkov, I. Frank and I. Tamm were jointly awarded the Nobel Prize in Physics in 1958 "for the discovery and the interpretation of the Cherenkov effect"[1].

II.1.3 A simplified model of extensive air showers

Extensive air showers are complex phenomena in which various interactions of hadronic and electromagnetic particles occur with the atmosphere. The complexity of the phenomenon imposes the use of detailed Monte Carlo simulations such as CORSIKA [38]. These simulations of EASs are latter used to simulate the detector response. As EASs produce many secondary particles the simulation can be very time consuming, in particular the higher the energy of the primary particle the longer the computation time. The interaction of hadronic and electromagnetic particles is described in sections II.1.1 and II.1.2. Here focus is given on the cascade process. Two types of EASs can be distinguished: electromagnetic showers and hadronic showers. The first is the result of a cascade process

[1] The Nobel Prize in Physics 1958. NobelPrize.org. Nobel Media AB 2020. Wed. 26 Aug 2020.

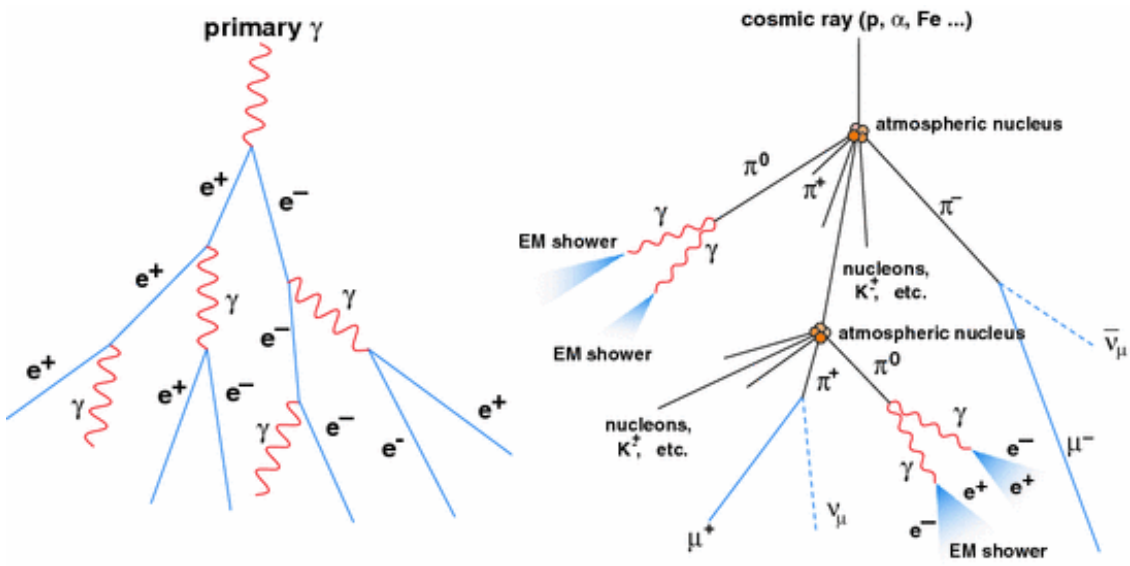

Figure II.6. Illustration of the particle interactions in electromagnetic (left) and hadronic (right) extensive air showers. Taken from [41].

initiated by a high-energy electromagnetic particle (an electron or a photon). The second is a shower initiated by an atomic nucleus [2].

II.1.3.1 Electromagnetic showers

A simplified model of extensive air showers, in particular of electromagnetic cascades, was introduced by Heitler [42]. This model is illustrated in fig. II.7a. The model supposes that electromagnetic interactions, which are electron-position pair production for photons and bremsstrahlung radiation for electrons and positrons (see section II.1.1), occur after a typical distance $d = \lambda \ln(2)$, with λ the radiation length[3]. Following this, after n steps, the number of particles is 2^n and the distance x is given by:

$$x = nd = n\lambda \ln(2). \tag{II.10}$$

The number of particles can be expressed in terms of the distance traveled x as:

$$N(x) = 2^{n(x)} = 2^{\frac{x}{\lambda \ln(2)}} = (e^{\ln 2})^{\frac{x}{\lambda \ln(2)}} = e^{\frac{x}{\lambda}} \tag{II.11}$$

The cascade process stops when the secondary particle energy reach a certain threshold. In the air this threshold corresponds to $E_c = 85$ MeV. Below this radiative energy losses become less important than collision losses. Supposing that at each split $n = 1, 2, \ldots, n_{max}$ the energy is equally partitioned between the two outgoing particles, the energy of the particle produced at step n is :

$$E_n = \frac{E_0}{N(n)} = \frac{E_0}{2^n}, \tag{II.12}$$

where E_0 is the energy of the primary particle. Thus the maximum number of steps n_{max} is given by:

[2] mostly hydrogen and helium see fig. I.3

[3] Notice that the bremmstrahlung radiation length is about 7/9 of the electron-position pair production radiation length [43]

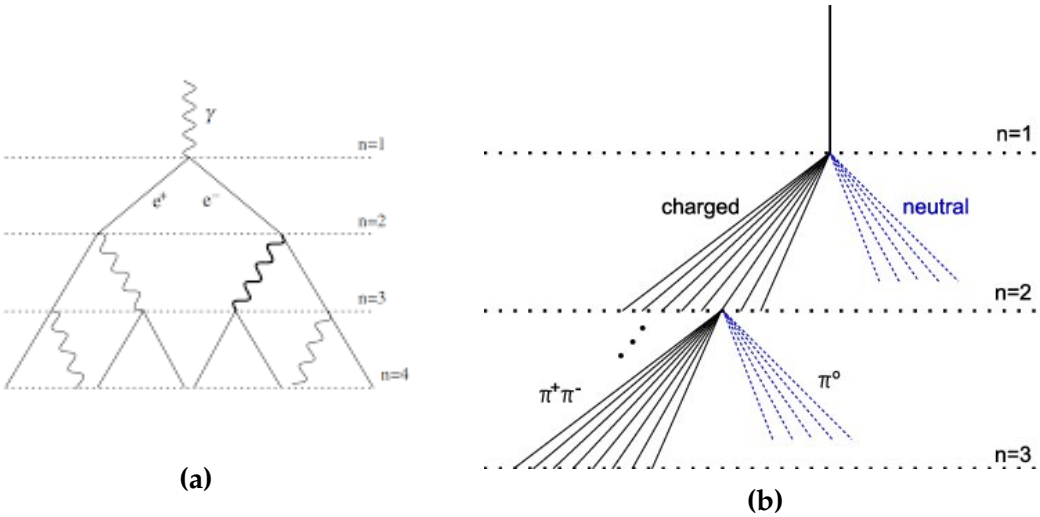

Figure II.7. Left: Illustration of the Heitler model for an electromagnetic shower initiated by a high-energy photon. The shower is divided several interaction steps n. Photons are drawn with wavy lines. Electrons and positrons are drawn with solid lines. Taken from [44]. Right: Illustration of a hadronic shower. Taken from [45].

$$E_{n_{max}} = E_c \Rightarrow n_{max} = \log_2\left(\frac{E_0}{E_c}\right). \tag{II.13}$$

The corresponding distance travelled x_{max} and number of particles N_{max} are thus:

$$x_{max} = n_{max}\lambda \ln(2) = \lambda \ln\left(\frac{E_0}{E_c}\right), \tag{II.14}$$

$$N_{max} = \frac{E_0}{E_c}. \tag{II.15}$$

It is important to note that the model is highly simplified. The attenuation of the particle is not taken into account. The model does not predict with great accuracy the total number of particle N_{max} (from eq. (II.15)) but the total length x_{max} (from eq. (II.14)) is more accurate. In addition the total number of electrons is overestimated in this model since bremsstrahlung of electrons produce more photons than assumed here. This is verified in Monte Carlo simulations. Two consequences of the Heitler model are verified [44] :

- The total number of particle N_{max} produced is proportional to the primary particle energy E_0.
- The elongation rate in air is $\Lambda = \frac{dx_{max}}{d\log_{10} E_0} = 2.3\lambda \sim 85\ \mathrm{g \cdot cm^{-2}}$ with $\lambda = 37\ \mathrm{g \cdot cm^{-2}}$. Which means that the maximum depth of the shower increases by $85\ \mathrm{g \cdot cm^{-2}}$ for an increase of one energy decade.

II.1.3.2 Hadronic showers

Hadronic showers are more complex to model than electromagnetic ones. However, the Heitler model reasoning can be applied to understand their development (see figs. II.6

and II.7b), as shown in [44]. In the following, hadronic showers initiated by protons are assumed. This simplifies the model and represents most of hadronic showers observed on Earth.

The primary particle, a proton, interacts with a nucleus at the top of the atmosphere. This interaction produces many charged and neutral pions:

$$p + N \longrightarrow N + \pi^+ + \pi^- + \pi^0 + \dots . \tag{II.16}$$

It is assumed that $N_{\pi^\pm}$ charged pions are produced and $N_{\pi^0} = \frac{N_{\pi^\pm}}{2}$ neutral pions are produced. Similarly as for electromagnetic showers, the cascades is divided in interactions steps n of length $\lambda_h \ln(2)$ with λ_h the interaction length.

The neutral pions rapidly decays into two photons (dominant decay mode):

$$\pi^0 \longrightarrow \gamma + \gamma, \tag{II.17}$$

thus creating two electromagnetic showers as described in section II.1.3.1.

The charged pions further interact with atomic nuclei in the atmosphere after producing more pions:

$$\pi^\pm + N \longrightarrow N + \pi^\pm + \pi^+ + \pi^- + \pi^0 + \dots . \tag{II.18}$$

The shower development of the charged pion branch stops when their energy reaches the energy threshold $E_c^{\pi^\pm}$ at which charged pions decays rather than interact with atmospheric nuclei. Charged pions decay into muons and muon neutrinos (dominant decay mode):

$$\pi^+ \longrightarrow \mu^+ + \nu_\mu, \tag{II.19}$$

$$\pi^- \longrightarrow \mu^- + \bar{\nu}_\mu. \tag{II.20}$$

Following Heitler's reasoning, the energy of the charged and neutral pions after n steps of the interactions are:

$$E_n^{\pi^\pm} = \frac{E_0}{\left(\frac{2}{3}N_{\pi^\pm}\right)^n}, \tag{II.21}$$

$$E_n^{\pi^0} = E_0 \left(1 - \frac{1}{\left(\frac{2}{3}N_{\pi^\pm}\right)^n}\right). \tag{II.22}$$

After reaching the critical energy $E_c^{\pi^\pm}$, the number interactions for the charged pions is given by:

$$n_{max}^{\pi^\pm} = \frac{\ln \frac{E_0}{E_c^{\pi^\pm}}}{\ln \frac{3}{2N_{\pi^\pm}}}. \tag{II.23}$$

The following parameters: $E_c^{\pi^\pm} = 20$ GeV; $N_{\pi^\pm} = 10$; $\lambda_h = 120\ g \cdot cm^{-2}$; $\lambda = 37\ g \cdot cm^{-2}$; $E_c = 85$ MeV are found to be reasonable choices for hadronic showers [44].

Primary particle energy Due to energy conservation, the primary energy of the particle is given by:

$$E_0 = E_c N_{max} + E_c^{\pi^\pm} N_{\pi^\pm}, \tag{II.24}$$

where $N_{\pi^\pm}$ is the total number of charged pions produced in the hadronic shower. From eqs. (II.19) and (II.20), it can be understood that the number of charged pions is equal to the total number of muons produced N_μ. Additionally, N_{max} corresponds to the total number of electrons N_e produces in the electromagnetic showers. Thus the primary particle energy can be estimated as:

$$E_0 \simeq 0.85\,\mathrm{GeV}(N_e + 24N_\mu). \tag{II.25}$$

From eqs. (II.15) and (II.25), it can be understood that the total number of particles (electron and muons) is proportional to the primary particle energy E_0 for electromagnetic showers and hadronic showers. Therefore, by detecting those particles the energy of the primary can be reconstructed. However, in practice it is impossible to detect all of the particles. Thus the energy estimation is a lower bound of the primary particle energy.

II.2 The imaging atmospheric Cherenkov technique

Direct and indirect detection techniques of the secondaries produced in extensive air showers are being used to reconstruct the primary particle energy, direction and type. An indirect detection technique of the charged secondaries based on the Cherenkov light emission they emit, the Imaging Atmospheric Cherenkov Technique (IACT) is presented here. Experiments such as HAWC [46] and Pierre Auger Observatory [34] are directly detecting the secondary muons and electrons. Such experiments, called air shower arrays, only detect the highest energy air showers since a great number of secondaries need to reach the ground. They have some advantages over IACTs detectors. Air shower arrays have a larger field of few and a greater duty cycle since they do not need to operate at night time. However, the energy threshold and energy resolution are much better for IACTs. In addition, the background rejection for IACTs is higher. The IACT technique images all charged particles from the first interaction point to the end of the cascade while the direct detection technique only collects the end particles.

II.2.1 Cherenkov emission from extensive air showers

As can be seen from table II.1, the minimum velocity required for charged particles to emit Cherenkov light in the atmosphere is about $\beta = 0.9997$, which corresponds to a Lorentz factor[4] of $\gamma \sim 40.83$. The minimum energy reached by each secondary charged particle can be estimated from the critical energies of electromagnetic and hadronic showers. One can estimate that the minimum electron energy at the end of the cascade is $E_c = 85\,\mathrm{MeV}$ while for charged pions it is $E_c^{\pi^\pm} = 20\,\mathrm{GeV}$. Thus the minimum Lorentz factor for both is high enough to guarantee that all secondaries meet the Cherenkov condition

[4]The Lorentz factor is $\gamma = \frac{1}{\sqrt{1-\beta^2}}$, where $\beta = \frac{v}{c}$ is the relative velocity of the particle to the speed of light in vacuum c.

Altitude (km)	Vertical depth (g/cm^2)	Cherenkov energy threshold (MeV)	Cherenkov angle θ (°)
40	3	386	0.076
30	11.8	176	0.17
20	55.8	80	0.36
15	123	54	0.54
10	269	37	0.79
5	550	28	1.05
3	715	25	1.17
1.5	862	23	1.26
0.5	974	22	1.33
0	1032	21	1.36

Table II.2. Cherenkov emission angle and energy threshold for electrons as function of the altitude (or vertical depth). Taken from [18].

Particle	Mass (MeV/c^2)	Minimum energy (MeV)	Minimum γ
$e^{\pm}$	0.51	85	166.7
$\pi^{\pm}$	139.57	2×10^4	143.3
$\mu^{\pm}$	105.66	$\leq 2 \times 10^4$	≤ 189.3

Table II.3. Mass, minimum energy and and corresponding minimum Lorentz factor γ for all charged secondaries produced in extensive air showers. The minimum γ values are above the minimum required Lorentz factor $\gamma = 40.83$ for Cherenkov light emission in the atmosphere. The muon minimum energy and minimum γ value is shown as upper bounds since in the charged pion decay (see eqs. (II.19) and (II.20)) some of its energy is passed to the neutrinos.

and thus radiate Cherenkov light in the atmosphere (see table II.3). However, the refractive index n, depends on the altitude. In table II.2, the Cherenkov energy threshold and angle as function of the altitude for electrons is shown.

As can be seen from eq. (II.7), the angle of emission of Cherenkov light θ depends on the refractive index. The refractive index of the air depends on the air density. Assuming a hydrostatic and isothermal atmosphere with density of the air being as function of the altitude z:

$$\rho(z) = \rho_0 \exp\left(-\frac{z}{z_0}\right), \; z_0 = 8.4 \text{ km}, \; \rho_0 = 1.2 \text{ kg} \cdot \text{m}^{-3}, \tag{II.26}$$

the refractive index as function of temperature T and pressure p in the atmosphere can be expressed as [40]:

$$n - 1 \simeq 2.92 \times 10^{-4} \times \frac{p}{p_0} \times \frac{288.15\ \mathrm{K}}{T}, \tag{II.27}$$

assuming that the atmosphere follows the ideal gas law. Since the Lorentz factor for charged particle is large thus the Cherenkov emission angle θ is small, the Cherenkov emission angle (see eq. (II.7)) becomes:

$$2(n - 1) \simeq \sin^2 \theta. \tag{II.28}$$

Following this, the Cherenkov light spectrum defined in eq. (II.9) can be simplified as:

$$\frac{d^2N}{dxd\lambda} \simeq 4\pi\alpha Z^2(n-1)\frac{1}{\lambda^2} \tag{II.29}$$

$$= \frac{4\pi\alpha Z^2}{\lambda^2} 2.92 \times 10^{-4} \times \frac{p}{p_0} \times \frac{288.15\ \mathrm{K}}{T}. \tag{II.30}$$

The total number of Cherenkov light per unit wavelength can be estimated by integrating the product of the simplified Frank-Tamm formula and the number of charged particles over the distance through which the EAS develops. Calculations show that between 10 GeV and 10 TeV the amount of Cherenkov light is proportional to the primary energy. This allows to use the induced Cherenkov photons by the EAS particles for a calorimetric measurements of the primary particle energy, where the calorimeter is the atmosphere. This observation is confirmed by simulations [40].

II.2.2 Cherenkov photons arriving on the ground

The cascade process develops in the atmosphere both longitudinally and laterally as can be seen from fig. II.1. The lateral development of the Cherenkov light is also observable from the ground, see fig. II.8 (top right). Most of the Cherenkov photons arrive in a circular region of about 120 m radius, this region is commonly referred as the Cherenkov light pool. Above this radius the density drops. The lateral spread of the Cherenkov light is the result of the conical direction of the Cherenkov emission added to the difference in Cherenkov angle from the top of the shower to the bottom. As a matter of fact, the angle increases from $\sim 0.1°$ at 40 km altitude to $\sim 1.4°$ at sea level (see table II.2). The consequence of such a change of angle with altitude is the formation of a light annulus. This process, illustrated in fig. II.8 (left), creates a peak of density of Cherenkov photons at the end of the Cherenkov light pool.

In addition, Cherenkov photon arrival time delays between the top and bottom of the shower are observed. These delays arise from the fact that the light emitted at the top of the shower travels slower than the shower develops (by definition of the Cherenkov condition). Consequently, the photons emitted at the bottom of the shower reach first the ground. However, when observing at a certain distance from the shower axis, the bottom photons can reach the detector latter than the top photons. The time duration of the Cherenkov signal as function of the impact parameter is shown in fig. II.8 (bottom right). Typically Cherenkov signals last up to 10 ns but can be longer for high impact distances.

Finally, the Cherenkov light emitted by the charged secondaries is subject to atmospheric absorption. It can be seen from eq. (II.9) that the Cherenkov light spectrum is dominated by high energy photons. The atmosphere absorbs lower wavelength photons.

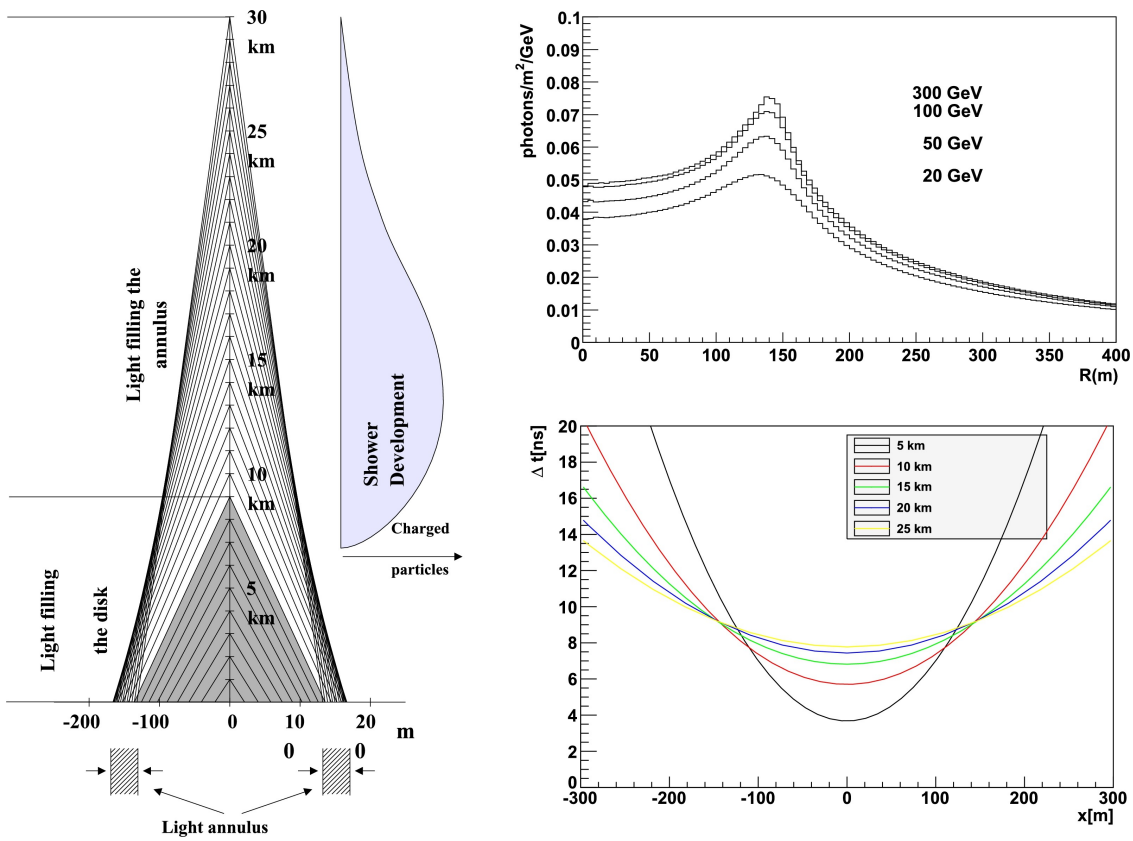

Figure II.8. Left: Illustration of the formation of the light annulus and number of charged particles as function of the altitude. Top right: Density of Cherenkov photons as a function of the impact distance for different energies (at sea level). Bottom right: Cherenkov photon time delays as function of the impact distance for different observation altitudes. Taken from [40].

Thus the Cherenkov light at the ground is dominated by UV and blue light. However, some lower wavelength photons can reach the detection level if emitted close to the detector [43]. The Cherenkov spectrum including atmospheric absorption is shown in fig. III.21.

II.2.3 Imaging and reconstruction technique

In order to detect the Cherenkov light emitted by EASs, light detectors can be placed on the ground. Placing light detectors facing upwards allows to detect the Cherenkov light. However, the small active area of the order of few cm^2 per detector or "pixel" implies that, to reach a detectable amount of Cherenkov light, the energy of the primary particle has to be high enough. For instance for gamma-ray energy of 1 TeV, the Cherenkov photon density within the light pool is about 100 $ph. \cdot m^{-2}$ [43]. Unfortunately, placing light detectors upwards, implies that they pick up stray light from all directions due to scattered photons rather than direct photons from EAS. Thus the direction of the incoming Cherenkov photons cannot be reconstructed using light detectors alone. Moreover, it increases the amount of background light collected.

A successful technique is being used to image the extensive air shower Cherenkov light in the atmosphere. It was pioneered by W. Galbraith and J. Jelley in 1952. They expected that a small fraction of the night-sky light was coming from Cherenkov light emitted by

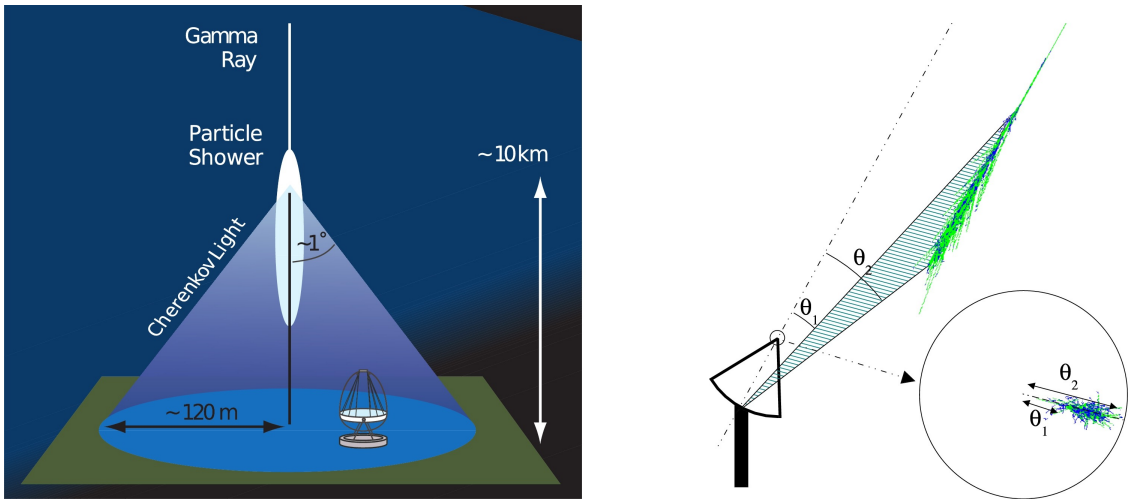

Figure II.9. Left: Drawing of a Cherenkov telescope placed within the light pool of a gamma-ray EAS. Right: Schematic of the EAS Cherenkov light projected to the camera focal plane. Taken from [40].

EASs. In the pursuance to detect the Cherenkov light from EAS, they built a simple set up consisting of a 25 cm-diameter light focusing mirror and a single 5 cm-diameter PMT to record the short light pulse. The PMT was connected to an amplifier and an oscilloscope from which they detected light pulses exceeding the night-sky background level every two minutes [47]. Their technique uses what is now called Imaging Atmospheric Cherenkov Telescopes (IACTs). Nowadays, the telescopes consist of a larger reflective dish with an area of the order of 100 m^2 and a camera that achieves field-of-views of few degrees with about 1000 pixels. The mirrors focus the Cherenkov light to the camera placed in its focal plane. The achieved field of view of Cherenkov telescopes is between 3° and 10° depending on the optics.

The use of a large area reflective dish allows to reach low energy threshold of about 70 GeV for a 100 m^2 reflective area. Furthermore, the reflective dish allows to image the EAS Cherenkov light as the angle of incidence is associated to a pixel of the camera (see fig. II.9 right). In addition, the fact that the Cherenkov light density is rather constant within a radius of about 120 m allows to detect showers with core distances (the distance between the telescope and the intersection of their direction and the ground) as far as 120 m, corresponding to an effective area of about 10^5 m^2 (depending on the energy of the EAS). However, such instruments can only operate during night times and moonless nights. Therefore the duty cycle is limited to about 10%.

Cherenkov telescopes face many technical challenges. In particular, the photo-sensors are required to respond to rapid flashes of light (of the order of 10 ns). Moreover these flashes can be faint (of about 10 photons) when compared to the night-sky background. In addition, the photo-sensors need to be sensitives in the UV/blue range. A detailed description of a prototype telescope, the SST-1M telescope designed for the Cherenkov Telescope Array (CTA) is presented section III.4.1.

The fact that the EASs are imaged is useful to reconstruct their direction, energy and to identify the primary particle type. The direction of the primary particle is found along the major axis of the primary particle. In practice using a single telescope to image the EAS is not enough to reconstruct the point of first interaction in the atmosphere. Nonetheless, using several telescopes allows to intersect directions and find the point

of first interaction. The precision is improved with increased number of telescope. For these reasons, stereoscopic reconstruction is widely used in current Cherenkov telescopes. The stereoscopic reconstruction is illustrated in fig. II.11. As seen in section II.1 the total collected Cherenkov light provides a calorimetric measurement of the energy of the primary particle. This is particularly true if the shower dies above the detection level. Cherenkov telescopes could be placed at sea level in order to guarantee that most EAS are extinct before reaching the ground. However, the atmosphere absorbs the Cherenkov light. A trade-off between atmospheric transparency and shower depth has to be found. Nowadays, Cherenkov telescopes are usually placed between 1300 m and 2300 m meter altitude. As can be seen from fig. II.8 (top right), the number of Cherenkov photons depends on the impact distance. Thus, a faint event could be attributed to a low energy event detected within the Cherenkov pool or a high energy event detected outside the Cherenkov light pool. This degeneracy is also difficult to solve when observing with a single telescope as the impact distance cannot be easily obtained from a unique image. As illustrated in fig. II.11 (right), the impact point is well defined when observing in stereoscopic mode. Therefore it improves the energy resolution as well.

The stereoscopic reconstruction requires more than one telescope to see the same EASs from different perspectives. Nearby telescopes would essentially see similarly oriented images thus offering poorer resolution on the crossing of the images. For this reason, the telescopes are usually placed in an equidistant array with inter-telescope distances of the order of 100 m. An example of the Cherenkov Telescope Array (CTA) layout is shown in fig. III.4 which was extensively studied through Monte Carlo simulations in [48].

The type of particle can also be identified from the image. In particular, Cherenkov telescopes aim at identifying gamma-ray events. About 1000 background events are observed for each gamma-ray event when looking at the Crab Nebula. The background is composed of (from the most dominant to the least dominant): diffuse hadronic cosmic-rays, diffuse electrons and positrons, diffuse gamma-rays. As can be seen from fig. I.2, the proton are overwhelmingly composing the background. The electron and positron background affects the lowest energies as its spectrum is steeper than the proton spectrum. The diffuse gamma-ray background is usually neglected. In order to reject background over signal, two features can be selected. First the background is diffuse, while the signal is coming from a point source, thus an excess comes from a particular sky direction. Second the proton events create hadronic showers that leave a different signature image in the camera. In particular, the lateral spread of hadronic showers is larger than of electromagnetic showers as can be seen in fig. II.10. In fig. II.10 (left), each of the circles represents the Cherenkov light cone emitted by each charged particle in the hadronic cascade. The electromagnetic part of the hadronic shower can be seen on the lower right of this image. The accumulation of the individual Cherenkov circles creates a "blob" of constant Cherenkov photon density. This is seen in fig. II.10 (right), where all the electron and positron Cherenkov rings are superimposed. A discrimination based on the image width allows to select gamma candidates from hadronic candidates (see section VI.3.2 for an example of machine learning based gamma/hadron separation). The discrimination allows to evaluate a hadroness score on the images. Nonetheless, the hadroness cannot distinguish electrons from gamma-rays as the two produce very similar electromagnetic showers. Only the first interaction differs, and so it was suggested that electrons could be discriminated over gamma-rays because of their different height of development of the showers. Nevertheless, the image resolution of current instruments and the performances of current reconstruction techniques do not allow to discriminate the electron induced

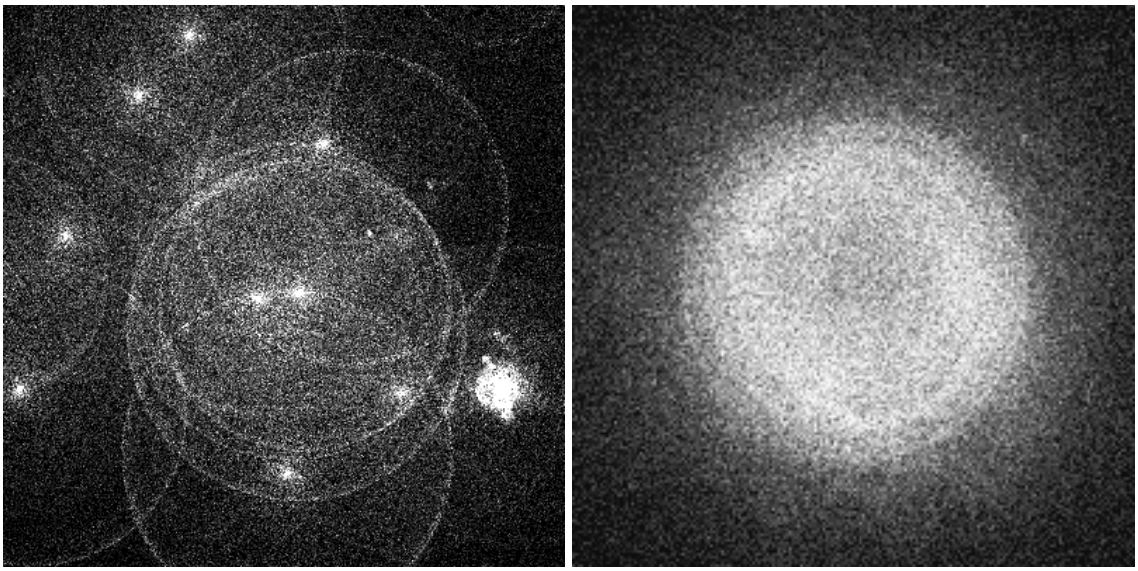

(a) (b)

Figure II.10. Left: CORSIKA simulations of the Cherenkov photon distribution on the ground for a 1 TeV proton (left) EAS and a 300 GeV gamma-ray (right) EAS. The simulation does not take the atmospheric absorption into account. Taken from [49].

EASs from the gamma-ray induced EASs.

In practice, the direction, the energy and the type of the primary are accessed through image parameters. Traditionally, the camera images are reduced into an ellipsoid parameterization: the Hillas' parameters [50]. This image parameters are used to train supervised machine learning models that predict the energy, the direction and the hadroness of the observed event. The Hillas' parameters are described in section VI.2.1.

A novel reconstruction technique exploiting more information than previously developed ones in the Cherenkov Telescope Array experiment. This method exploits the information on the pixel photo-electron resolution and the shower temporal development. This is presented in section VI.2.2.

Existing and future Cherenkov telescopes for gamma-ray astronomy are presented in sections III.1, III.2 and III.4.1.

II.2.3.1 The night-sky background light

As the cameras are exposed to the night-sky, light pollution affects the Cherenkov signal. This background is commonly referred to as night-sky background (NSB) light. This generic term comprises various sources of background light: air-glow; zodiacal light; star light; extra-galactic light; aurora light (only close to the geomagnetic poles); the Moon; human-activity light pollution. The strongest sources of natural background light are the air-glow and zodiacal light. [51]. By night time, sources of light such as: public lights; airplanes; satellites; roads are sources of background for astronomers. In practice, astronomical observatories are placed in remotes areas where the light pollution is reduced to its minimum. Such observational site ares unfortunately becoming rarer over the years as our society develops. However, the public is aware of this problem and efforts in reducing light pollution for both astronomers and environment enthusiasts are conducted.

The other sources of background light are natural sources of background that cannot be eliminated. In particular, the air-glow is emitted by atoms and molecules that were

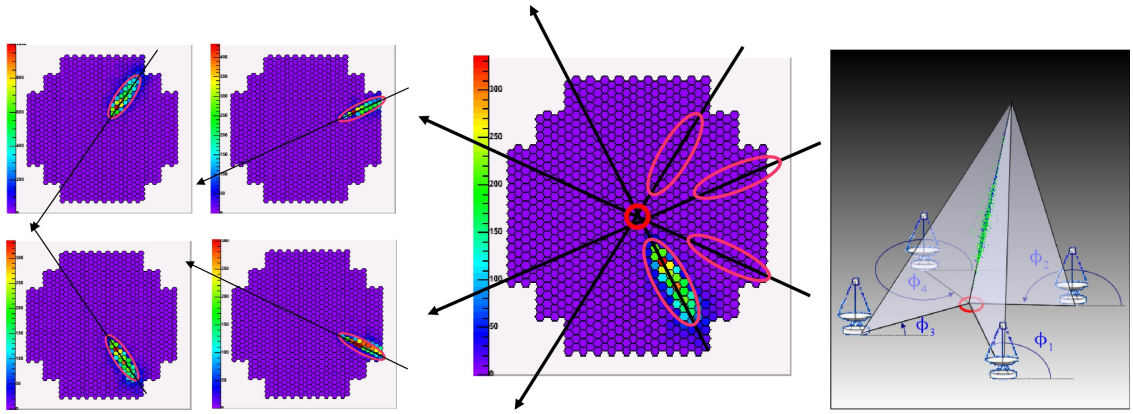

Figure II.11. Illustration of the stereoscopic reconstruction of the shower direction and impact point with Cherenkov telescopes. Left: 4 camera images of the same shower. Each shower main axis corresponds to a plane in the atmosphere. Center: Superposition of the images. The intersection of the main axes corresponds to the direction of the primary particle (red circle). Right: The intersection of the major axis planes provides the impact parameter on the ground (red circle). Taken from [40].

excited during day times by UV solar radiation. Zodiacal light is the Sun light reflected by interplanetary dust. Its spectrum resembles the one of the Sun. The zodiacal light is strongest within the ecliptic (orbital plane of the Earth). Star light is diffused by inter-stellar dust and creates a glow that is brightest in the galactic plane. Similarly, extra-galactic light is diffused by inter-stellar dust. Auroras are bright events occurring at latitudes close to the Earth's geomagnetic poles. The light emitted by the excitation of the atmospheric molecules produces a colorful glow of light. Nonetheless, this background can be avoided by placing the telescopes far from the poles. Direct star light also affects the atmospheric Cherenkov observations. Typically, the point spread function of Cherenkov telescopes is about the size of a pixel meaning that a star would illuminate a single pixel.

Finally, the Moon is a strong source of background light. It is usually avoided by observing during nights where the Moon is below the horizon. However, it reduces the duty cycle of the telescope drastically. In comparison, a half Moon night induces a photo-electron background rate about 15 times higher than for a moonless night (for SST-1M telescope, see chapter V). Additionally, the lifetime of photo-sensors used for Cherenkov telescope such as Photo-Multiplier Tubes (PMTs) is highly reduced by bright night-sky background.

The NSB spectrum in La Palma, Canary Island, is shown in fig. II.12 (left) for moonless and half Moon nights. Thankfully, the NSB spectrum is dominated by red light while the Cherenkov signal is dominated by blue and UV light. Thus the NSB can be reduced by choosing photo-sensors sensitive to low wavelength while being less sensitive to red light. Additionally, the NSB can be reduced by using filters cutting beyond red light.

The NSB produces fluctuations in the camera images. This fluctuations are not correlated. Thus they can be distinguished from clustered images due to hadronic and electromagnetic EAS. Cherenkov telescopes adopt a triggering logic based on the coincidence of neighboring pixels. This allows to efficiently reduce the NSB induced random triggers. However, this does not prevent triggers from a bright star. To avoid this, the pixels containing bright stars, which often saturate the electronic chain, can be eliminated from the trigger logic. A rate scan of the trigger rate as function of the night-sky background is shown in fig. II.12 (right) where one can see that the NSB induced trigger rate

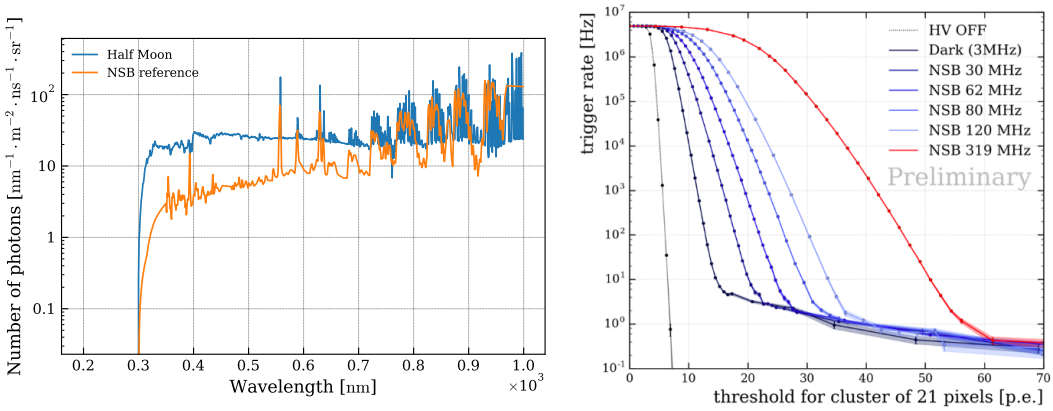

(a) **(b)**

Figure II.12. Left: Reference night-sky spectrum as function of the wavelength from 300 nm to 1000 nm. The reference CTA NSB spectrum (orange) for a moonless night, the spectrum is taken from [51]. The half Moon spectrum (blue) is taken from Cerro Paranal Advanced Sky Model [52]. It supposes a Moon elevation of 45° and observation at zenith. Right: NSB induced trigger rate as function the trigger threshold and for different night-sky background rate (in photo-electron per pixel) for the SST-1M telescope [53]. The measurements were taken with a calibrated light source illuminating the camera at different NSB equivalent rates. Taken from [54].

reduces rapidly with increased trigger threshold.

Chapter III

Gamma-ray Cherenkov telescopes

III.1 Current generation of air-imaging Cherenkov telescopes

The current generation of air-imaging Cherenkov telescopes using the IACT technique described in section II.2 is mainly composed of: the High Energy Stereoscopic System (H.E.S.S.) telescopes; the Very Energetic Radiation Imaging Telescope Array System (VERITAS) and the Major Atmospheric Gamma Imaging Cherenkov (MAGIC) telescopes (see fig. III.1 and table III.1 for a comparison of the three instruments). The differential flux sensitivities of these three arrays of telescopes are shown in fig. III.9. The angular resolution of the MAGIC and the VERITAS arrays are shown in fig. III.7.

The H.E.S.S array of telescopes is located in Namibia. The array is composed of 5 telescopes (4 H.E.S.S. I and 1 H.E.S.S. II). In summer 2002 the first H.E.S.S. was operated and in September 2004 the four H.E.S.S. I telescopes were inaugurated. The four telescopes are separated by about 120 m. They have a 12 m diameter mirror dish. The H.E.S.S. I cameras are made of 960 photo-multiplier tubes (PMTs) pixels for a field-of-view (FoV) of 5°. From July 2012, the H.E.S.S. II telescope is operated. It has a much larger reflective area than its predecessors (28 m diameter mirror dish). The H.E.S.S. II telescope is located at the center of the array. It extends the energy range of the array towards lower energies [55].

The VERITAS [56] is located in the Fred Lawrence Whipple Observatory, in southern Arizona, USA. It is in operation since 2007. It is composed of four telescopes separated by about 100 m. Each telescope has a 12 m diameter mirror dish and uses 499 PMTs for the camera. The field-of-view is 3.5° wide.

The MAGIC telescopes [57] are located in Roque de los Muchachos Observatory in La Palma, Canary Islands. There are two MAGIC telescopes (MAGIC I and MAGIC II) separated by 85 m. The mirror dishes have a diameter of 17 m. The two telescopes operate in stereoscopic mode since July 2009.

These three arrays of telescopes have revealed over the years more than 200 gamma-ray sources (see fig. III.2). The fact that the arrays are made of two to five telescope separated by about 100 m limits the effective area of these instruments to about 10^5 m^2. Thus being sensitive up to sources of about 10^{-2} Crab units. The next generation of ground-based gamma-ray observatory, the Cherenkov Telescope Array, aims at pushing the sensitivity by about a factor 10 lower than the sensitivity of the existing instruments (see section III.2).

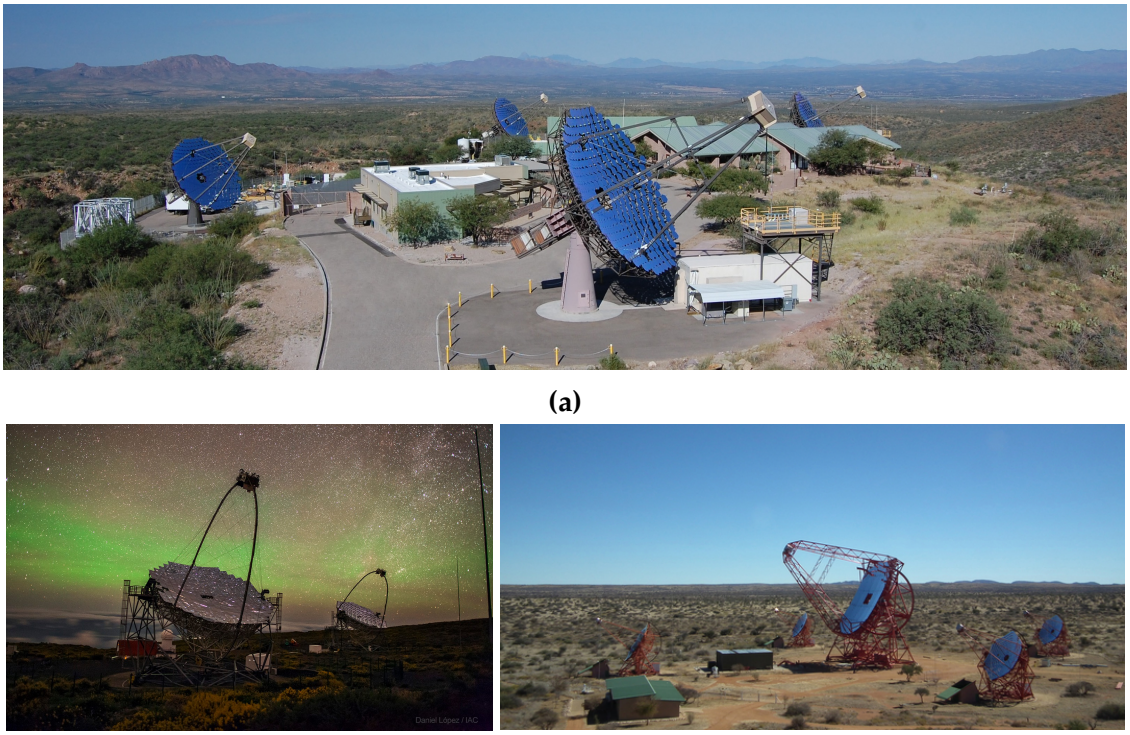

(a) (b) (c)

Figure III.1. Top: The VERITAS 4 telescopes in Arizona, United States of America. Taken from [58]. Left: The MAGIC I and II telescope in La Palma, Canary Islands. Taken from [59]. Right: the H.E.S.S. I and II telescopes in the Khomas Highland of Namibia. Taken from [55].

Telescope	Lat. (°)	Long. (◦)	Alt (m)	Number of tel.	Area (m^2)	Number of pixels	FoV (°)	Energy threshold (TeV)	Sensitivity (% Crab) > 1 TeV
H.E.S.S. I	-23	16	1800	4	107	960	5	0.1	0.7
H.E.S.S. II	-23	16	1800	1	614	2048	3.2	-	-
VERITAS	32	-111	1275	4	106	499	3.5	0.07	0.7
MAGIC I+II	29	-18	2225	2	234	1039	3.5	0.03	0.8
FACT	29	-18	2225	1	9.5	1440	4.5	1	-

Table III.1. Comparison of the current generation of Cherenkov telescopes. The sensitivity is defined as a 5-σ significance detection to a point-like source after 50 h of observation. Taken from [60].

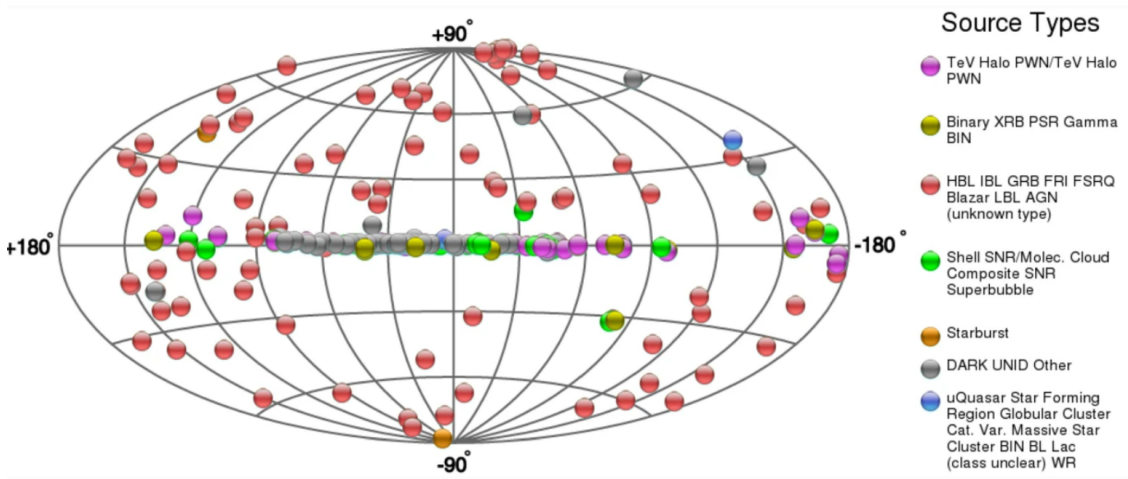

Figure III.2. The TeVCat [61] galactic and extra-galactic sources seen by: MAGIC, H.E.S.S and VERITAS. Taken from [62].

Additionally the duty cycle of these three instruments is limited by the Moon phases. In fact, operating when the Moon is present is damaging the PMTs of these instruments. However by lowering the operational voltage and/or by using NSB filtering windows the damages can be reduced [63, 64]. The First G-APD Cherenkov Telescope (FACT) [65] has demonstrated that the silicon photo-multipliers (SiPMs) can replace PMTs for Cherenkov telescopes while being able to operate under bright moon-light conditions. This telescope was built by ETHZ an is operated by an international collaboration including members from UNIGE. In particular the Département de Physique Nucléaire et Corpusculaire (DPNC), took part in the construction of the camera shutter.

The FACT, as its name suggests, is the first Cherenkov telescope using SiPMs as photo-detectors. It is located next to the MAGIC telescopes. The mirror dish has a surface of 9.51 m^2. It is a much smaller telescope than the ones mentioned above as its purpose was to demonstrate the possibility to use SiPMs for Cherenkov cameras. The camera is composed of 1440 SiPMs for a FoV of 4.5°. The telescope is in operation since October 2011 and completely remotely operable since the end of 2012. The telescope is monitoring a set of bright extra-galactic sources allowing to detect several flaring sources.

Following the steps of FACT and advancing the field in order to comply with the very demanding requirements of CTA, the small-sized single mirror (SST-1M) telescope (described in section III.4.1), is using SiPMs.

III.2 The Cherenkov Telescope array

The Cherenkov Telescope Array (CTA) is the next generation of ground-based gamma-ray observatory. The CTA consortium is composed of about 1500 people across 31 countries with more than 200 institutions. This developing array of telescopes will have two observations sites: a southern observatory near the European Southern Observatory (ESO) Paranal Observatory in the Atacama Desert in Chile and a northern observatory located at the Observatorio del Roque de los Muchachos (next to the MAGIC telescopes), in the Canary Islands. Both sites offer very good weather and night-sky conditions for astronomy as they are considered the best observational site in the world (southern) and in Europe

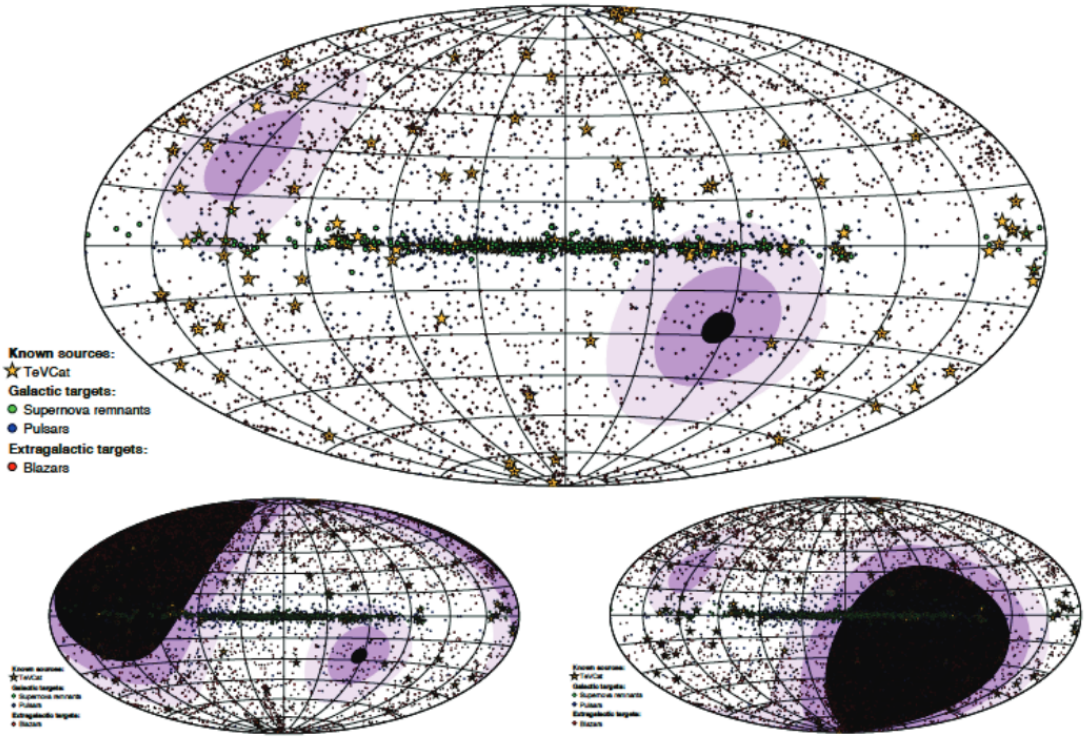

Figure III.3. Sky coverage of CTA southern site (bottom left), northern site (bottom right) and combined (top) in galactic coordinates. Known sources are indicated as points and stars. Taken from [66].

(northern). Having one observatory at each hemisphere allows to cover almost the full sky as can be seen from fig. III.3.

As the array is not constructed yet, the content that follows might change or already be outdated. For instance the exact number of telescopes in the southern array is still unknown. Some of the telescopes are at the prototyping stage and the selection of all best candidates is not yet done.

III.2.1 The northern and southern observatories

The southern site will outperform the northern site by more than one energy decade. It will cover the gamma-ray energies from 20 GeV up to 300 TeV. The array of telescopes will span over 4 km^2 with 99 telescopes. In order to meet the scientific requirements of CTA, a cost effective solution is found by placing the telescopes in a particular layout and with three categories of telescope sizes. These telescopes are the: Large-Sized Telescopes (LSTs); Medium-Sized Telescopes (MSTs) and Small-Sized Telescopes (SSTs). Each telescope type, when working in an array of telescopes, is designed to cover a specific energy range of the CTA sensitivity. The southern site will be composed of 4 LSTs, 25 MSTs and 70 SSTs. The layout of the southern array is shown in fig. III.4.

The northern site will cover the the gamma-ray energy range from 20 GeV up to 20 TeV. The array will be composed of 29 telescopes: 4 LSTs and 25 MSTs. The telescopes will be placed as shown in fig. III.4 within a circle of about 400 m radius. The site is on an extinct volcano thus it cannot accommodate for as many telescopes as in the southern site.

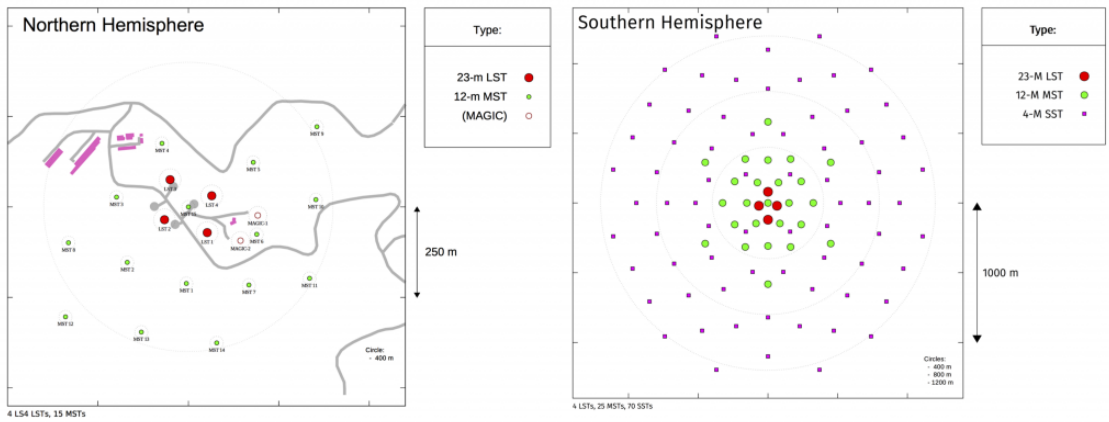

Figure III.4. Left: Layout of the CTA northern array. Right: Layout of the CTA southern array. Taken from [67].

Nonetheless the performance of the northern observatory will still outperform the ones of the existing ground-based gamma-ray instruments.

Currently, given that the total cost of the array was not fully covered, a baseline scenario was defined. It can start to be implemented from the start of the operations of the new legal entity of the observatory: the CTA Observatory (CTAO) ERIC. This scenario comprise reduced set ups of telescopes, still being discussed, for the moment being: in the north four LSTs + five MSTs and in the south 15 MSTs + 50 SSTs.

The Large-Sized Telescope The LST (see fig. III.5) is the largest telescope of CTA. Four LSTs will be placed at each CTA site in the center of the array. They are designed to cover the lowest energy part of the CTA sensitivity: from 20 GeV to 150 GeV. It is composed of a 23 m diameter parabolic mirror dish for an effective reflective surface of 370 m^2. The camera has 1855 PMTs. The first prototype is being commissioned in the northern site and construction of the second LST is undergoing. Currently, the UNIGE is involved in this project.

The Medium-Sized Telescopes The medium-sized telescopes (see fig. III.5) come in three variants: the Schwarzschild-Couder Telescope (SCT) [68]; the MST with the Flash-Cam [69] camera and the MST with the NectarCam [70] camera. The first is based on a dual mirror design and with 11328 SiPM pixels for the camera. The second and the third are based on the MST telescope structure which is a Davies-Cotton telescope. Only the cameras of the second and the third differ but they both use PMTs. A comparison of these three designs can be found in table III.2. The SCT design is at the moment not considered for the MST arrays. The Davies-Cotton MST has a 12 m diameter dish. The MSTs are aimed to cover the energy range from 150 GeV to 5 TeV. The MST telescope structure is being tested extensively since 2012 in Berlin. There the two camera prototypes were commissioned. Recently, the FlashCam has been subject to extensive test at the H.E.S.S. site.

The Small-Sized Telescopes 70 SSTs will be implemented in the southern array while in the northern array no SSTs will be placed. They will be spread over a large area of about

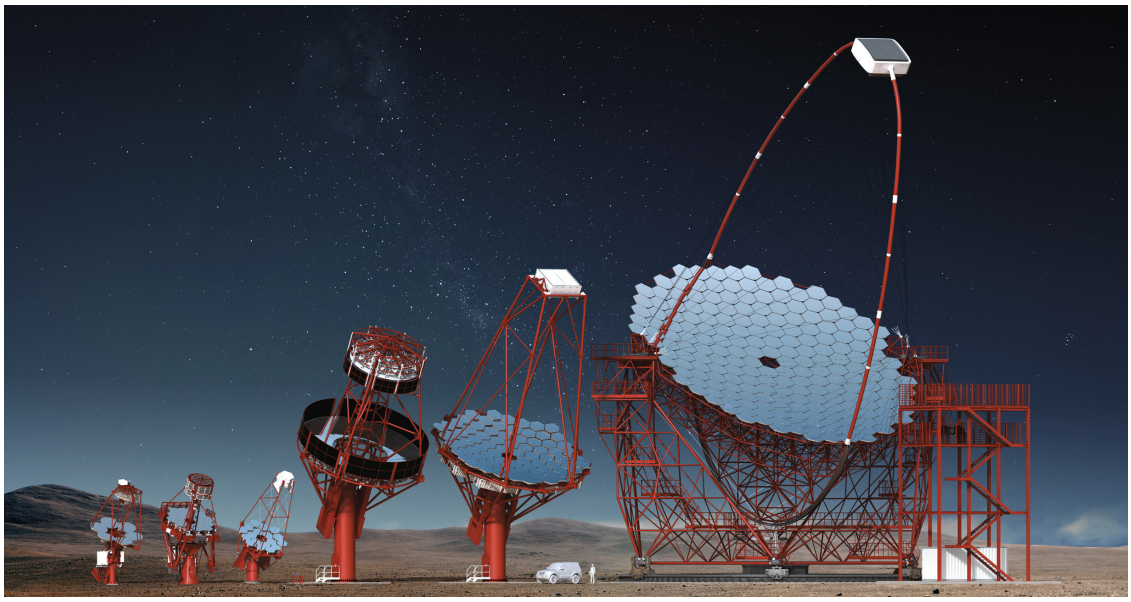

Figure III.5. Computer generated drawing of the CTA telescopes. From left to right: The GCT telescope; the ASTRI telescope; the SST-1M telescope; the SCT telescope; the MST telescope and the LST telescope. Taken from [67].

4 km^2. This will allow to detect the highest energy gamma-rays seen by CTA. The SSTs will cover the energy range from few TeV up to 300 TeV.

Three SST designs (see fig. III.5) were originally proposed for CTA: the ASTRI-Horn telescope [71], the Gamma-ray Cherenkov Telescope (GCT) [72] and the SST-1M [53]. The first two use a dual mirror Schwarzschild-Couder design while the SST-1M uses a Davies-Cotton design. The effective reflective area of the SSTs is about 8 m^2. They have a FoV of about 9° and a pixel angular size of about 0.2°. The three designs use SiPMs as photo-sensors for their respective cameras. A comparison of the SST designs can be found in table III.2. In June 2019, CTA decided to select a unique design for the SSTs in order to reduce the complexity of the array implementation, the maintenance costs and the production costs. A design based on the ASTRI-Horn structure and the CHEC-S camera [73], the original camera proposed for the GCT, was selected.

III.2.2 Array performances

CTA will out-perform the existing gamma-ray arrays in several aspects. The improvements in performances of CTA compared to in-operation Cherenkov telescopes can be mainly attributed to the high number of telescopes within the arrays. Additionally, the wide FoV optics, the large number of pixels and the use of latest photo-detection technology improves the overall performance of the array. The northern array will reach a maximum effective area of about 10^6 m^2 while the southern array will reach a maximum effective area of about 10^7 m^2 for energies above 10 TeV (see fig. III.6). When compared to the VERITAS this corresponds to an effective area from 10 up to 100 times greater. The boost in effective area will allow to increase the gamma-ray rate and provide sensitivity to transient phenomena.

The northern and southern arrays reach an angular resolution of about 0.05° at 1 TeV with a plateau for the northern array avove 1 TeV. The southern array, thanks to the

Telescope	LST	MSTs			SSTs		
Variant	-	SCT	NectarCam	FlashCam	ASTRI	GCT	SST-1M
Required energy range	20 GeV - 3 TeV	80 GeV - 50 TeV			1 TeV - 300 TeV		
Energy range of sensitivity	20 GeV - 150 GeV	150 GeV - 5 TeV			5 TeV - 300 TeV		
Number of telescopes (South)	4	25			70		
Number of telescopes (North)	4	15			0		
Optical design	Parabolic	Schwarzschild-Couder	Modified Davies-Cotton		Schwarzschild-Couder		Davies-Cotton
Primary reflector diameter	23 m	9.7 m	11.5 m		4.3 m	4 m	4 m
Secondary reflector diameter	-	5.4 m	-		1.8 m	2 m	-
Effective mirror area	370 m^2	41 m^2	88 m^2		8 m^2	8.9 m^2	7.5 m^2
Focal length	28 m	5.6 m	16 m		2.15 m	2.28 m	5.6 m
Total weight	103 t	80 t	82 t		19 t	11 t	8.6 t
Field of view	4.3°	7.6°	7.7°	7.5°	10.5°	8.3°	8.8°
Number of pixels	1855	11328	1855	1764	2368	2048	1296
Pixel angular size	0.1°	0.067°	0.17°	0.17°	0.19°	0.17°	0.24°
Photo-detector type	PMT	SiPM	PMT	PMT	SiPM	SiPM	SiPM
Sampling frequency	1 GHz	1 GHz	1 GHz	250 MHz	-	1 GHz	250 MHz

Table III.2. Comparison of the CTA telescopes key parameters. Adapted from [67].

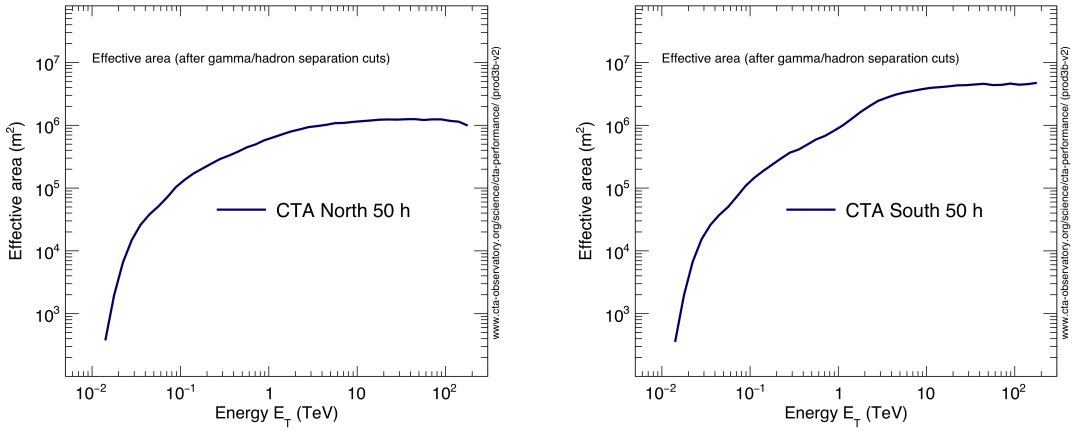

Figure III.6. Energy resolution of CTA as function of energy for the northern (left) and southern (right) arrays. The source elevation is considered at 20° zenith angle. Taken from [67].

additional SSTs, reaches a lower angular resolution of about 0.02° at 10 TeV (see fig. III.7). The enhancement in angular resolution as well as the widening of the FoV will allow to image extended sources of gamma-rays.

Both arrays will reach outstanding minimum energy resolution of about 6% at 1 TeV with a better resolution for the southern array at energies above 2 TeV below 10% (see fig. III.8).

In fig. III.9 is shown the sensitivity of CTA as function of energy compared to other gamma-ray instruments. It can be seen that the gamma-ray sensitivity is improved by a factor 10 in most energy bins. For instance, for energies of the order of 1 TeV CTA is sensitive to a source that is 10^{-3} fainter than the Crab Nebula. In comparison, the VERITAS is sensitive to about 10^{-2} C.U. at 1 TeV.

As the number of telescopes is large the array can survey or monitor a great fraction of the sky thus detecting transient phenomena and alert other instruments for multi-messenger studies.

III.2.3 The science with the Cherenkov Telescope Array

As seen above, CTA is designed to improve by a factor 10 our sensitivity to the gamma-ray sources. Additionally, the CTA consortium is also aiming at answering astro-particle physics most important questions [74]. These questions are grouped in three science themes: the origin and role of cosmic-rays; probing the extreme environments; exploring the frontiers of physics.

Understanding the origin and role of relativistic cosmic particles Relativistic cosmic particles are associated with astrophysical objects such as: supernovae and active galactic nuclei. The impact of the cosmic-rays on star formation is still not established. CTA will give insights on the production mechanism, acceleration mechanism and propagation within the interstellar medium. The following questions will be addressed by CTA, as reported in its science book [74]:

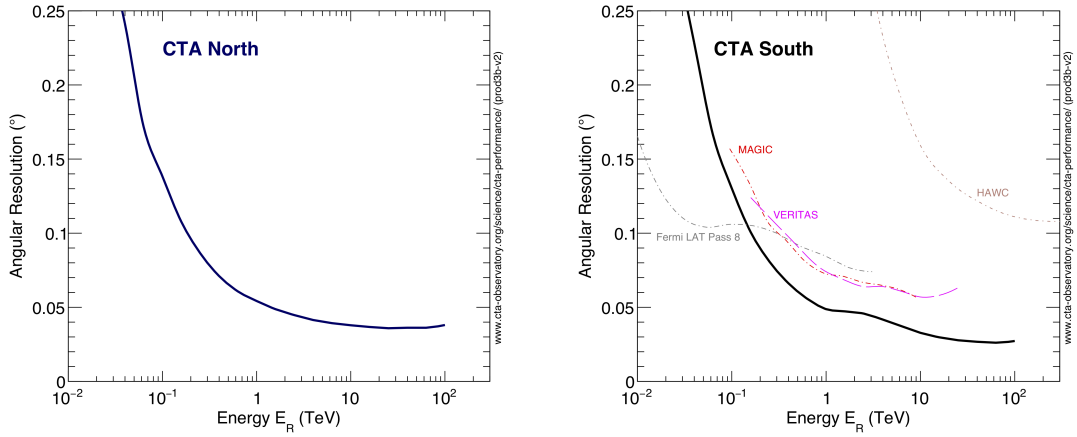

Figure III.7. Angular resolution as function of energy of CTA for the northern (left) and southern (right) arrays. The southern array angular resolution is compared to in-operation gamma-ray detectors. The source elevation is considered at 20° zenith angle. Taken from [67].

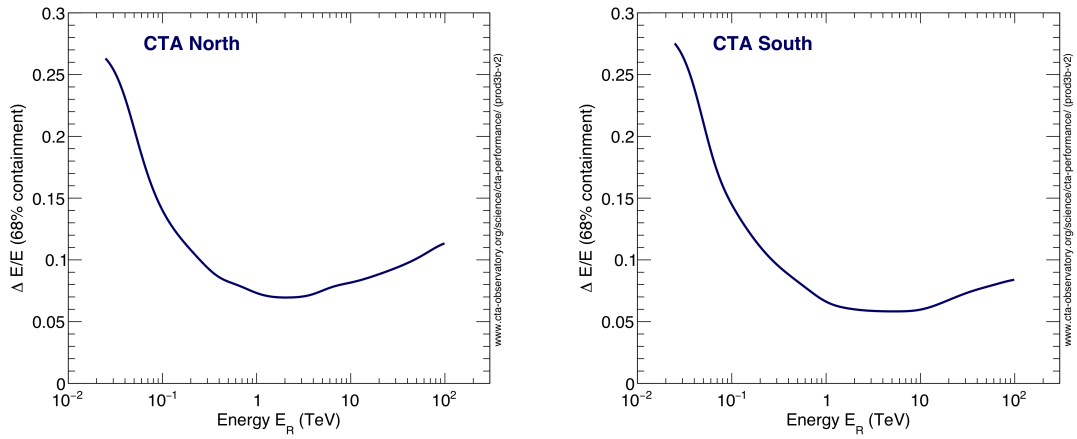

Figure III.8. Energy resolution of CTA as function of energy for the northern (left) and southern (right) arrays. The source elevation is considered at 20° zenith angle. Taken from [67].

- Are supernova remnants the only major contributor to the galactic cosmic rays?
- Where in our galaxy are particles accelerated up to PeV energies?
- What are the sources of high-energy cosmic electrons?
- What are the sources of the ultra-high energy cosmic rays (UHECRs)?

Probing extreme environments Production and acceleration of very-high energy (VHE) gamma-rays is associated with extreme environments such as: super-massive black holes and neutron stars. Merging binary systems of neutron stars or black holes are believed to emit bursts of gamma radiation and gravitational waves. CTA will be able to respond to triggers of other multi-messenger instruments such as IceCube (see chapter IV) or LIGO [75]. The measurement of the gamma-ray spectra of distant source will allow to constrain the extra-galactic background light (EBL) to great details. In particular, CTA

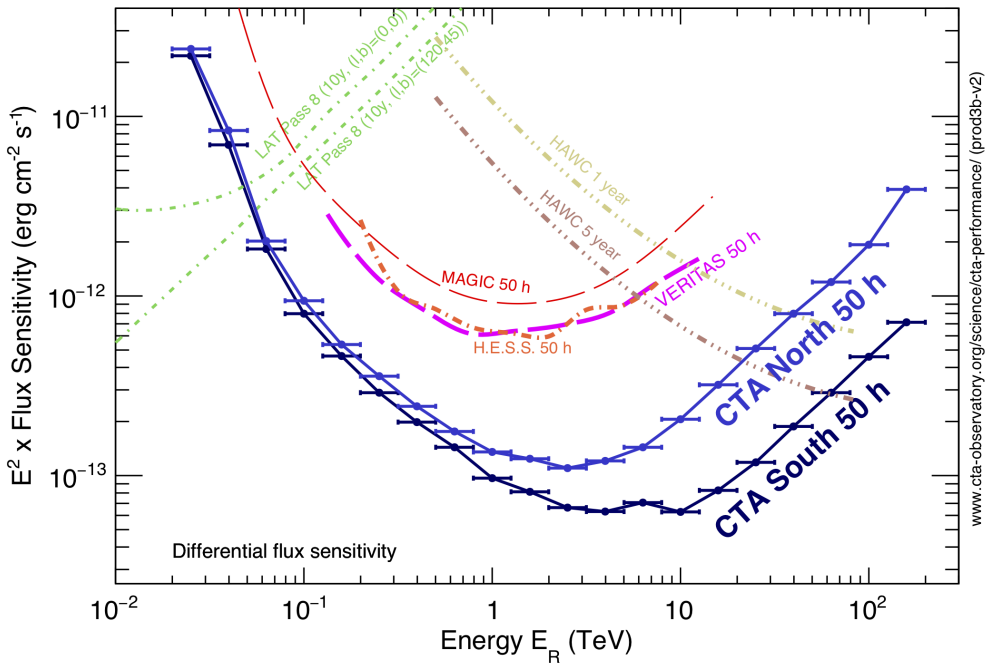

Figure III.9. Differential sensitivity of different gamma-ray instruments in bins of energy. The source elevation is considered at 20° zenith angle. Taken from [67].

will be able to study the evolution of the EBL with time. The following questions will be addressed by CTA [74]:

- What physical processes are at work close to neutron stars and black holes?
- What are the characteristics of relativistic jets, winds and explosions?
- How intense are radiation fields and magnetic fields in cosmic voids, and how do these evolve over cosmic time?

Exploring frontiers in physics CTA will explore the frontiers of physics and will try to bring answers to the dark matter puzzle. It will search for Weakly Interacting Massive Particles (WIMPs) annihilation or decay in the Galactic Center, where the dark matter concentration is expected to be the highest of the galaxy. CTA might reveal the existence of axion-like particles. These particles are proposed solutions for existing problems in particle physics and constitute good candidates for cold dark matter. The propagation of gamma-ray is limited by its interaction with the EBL (see section I.7). Recent observations suggest that the attenuation (from EBL interaction) of high energy gamma-rays from distance sources is lower than expected. Presumably, these photons would be converted to axion-like particle on their journey to us and be reconverted to photons. Such oscillation mechanism would occur in the inter-galactic magnetic field and counteract the absorption from EBL interactions [76]. Measuring the gamma-ray spectra from extra-galactic sources at different redshifts could allow to further study the axion-like particle gamma-ray oscillation [77]. Quantum gravity effects could introduce time delays in the arrival of high energy photons depending on their energy. The CTA sensitivity to faint distant extra-galactic gamma-ray emitters will allow to probe these quantum gravity effects. CTA will try to answer these questions at the frontier of known physics [74]:

- What is the nature of dark matter? How is it distributed?
- Are there quantum gravitational affects on photon propagation?
- Do axion-like particles exist?

III.2.4 The CTA astrophysical targets

In order to answer these questions, CTA has defined astrophysical targets that will be extensively studied [74].

The Galactic Center Within one degree of the Galactic Center, various high-energy gamma-ray emitters are found. It is the most studied region in the sky. CTA will complete the Galactic Center measurements with outstanding precision at the highest energies. Additionally, the Galactic Center will probe annihilation of dark matter particle in this region of the galaxy as it is believed to be host most of the galactic dark matter.

Large Magellanic cloud The Large Magellanic Cloud (LMC) is a galaxy which hosts several gamma-ray emitters. Its high star forming activity makes it a good candidate for gamma-ray astronomy. The nature of some sources in the LMC are still to be identified. The study of the LMC and its gamma-ray emitters will allow to understand the connection of galaxies and gamma-ray sources.

The galactic plane The study of the galactic plane will allow to discover new phenomena or classes of sources and transient behaviours. The predicted hundreds of new sources identified by CTA in the galactic plane will allow to study sources population with higher statistics.

Galaxy clusters Clusters of galaxies are expected to host cosmic-ray protons and electrons. The presence of electrons in galaxy clusters was identified by the observation of diffuse synchrotron radiation. Theses clusters could produce high-energy gamma-ray from proton interaction with the gas in the clusters via pion decays. The study of gamma-rays in galaxy clusters might constrain its cosmic-ray proton content. As the galaxy clusters host a large amount of dark matter they are also good candidates for dark matter investigation as for the galactic center.

Cosmic-ray PeVatrons Cosmic-ray particles of energies beyond PeV-scale have been detected by ground-based detectors. The super-massive black hole at the center of the galaxy cannot explain alone all the PeV cosmic-rays observed. More source of PeV-scale particles: PeVatrons are to be identified. CTA will extend the energy range of detectable gamma-ray sources beyond the one of the existing instruments allowing to detect PeVatrons.

Star forming systems It is believed that the cosmic-rays regulate the star-formation process. Understanding the: acceleration, propagation and interaction of the cosmic-rays in star forming regions might reveal the role the cosmic-rays play in the star forming regions.

Active galactic nuclei Super-massive black holes with orbiting matter on a accretion disk are among the brightest extra-galactic sources in a broad band of the electromagnetic spectrum. Such objects are referred as Active Galactic Nuclei (AGNs). Their emission in the TeV range is highly variable. CTA will allow to understand the physics behind AGNs. A large extra-galactic sky survey by CTA is aimed at constructing a large extra-galactic catalog of sources for which AGNs are expected to be the main class.

Transient phenomena Among the sources of gamma-rays in the universe some are identified as having time varying fluxes. The time variation can last from milliseconds up to years. These sources are commonly named: transient sources. The time variability indicates changes in the activity of the source. The change in activity can be associated with other messengers of the Universe such as: neutrinos and gravitational waves. CTA with its large field-of-view will be able to monitor the gamma-ray sky and respond in short timescales to alerts of other instruments. The be more precise, the CTA array is required to change target in less than 90 s. Among the transient phenomena, there are gamma-ray bursts (GRBs) for which the lower energy coverage of the LSTs is important. The LST will be able to reposition itself to any position in the sky in less than 50 s. Additionally among the transient phenomena there are: galactic transients; neutrino and gravitational wave alerts and optical/radio transients.

III.3 Photo-detectors for IACTs

In this section, the working principle of photo-multiplier tubes is briefly explained in section III.3.1. Then in section III.3.2, a more extensive description of silicon photo-multipliers is given.

III.3.1 Photo-multiplier tubes

Photo-multiplier tubes (PMTs) are designed to convert photons to a detectable amount of electrons. The working principle of these devices is shown in fig. III.10. The incident photon is converted into an electron when reaching the photo-cathode. The ejected electron is directed to a dynode designed to eject more electrons. Several dynodes are placed in series in order to multiply the number of electrons therefore reaching a detectable amount of electrons. A more recent technology of low light photo-detectors: silicon photo-multipliers (SiPMs) is present in section III.3.2.

III.3.2 Silicon Photo-Multipliers

In this section, the working principle and the characteristics of silicon photo-multipliers (SiPMs) are explained. These silicon-based solid state sensors are used in the detection of low light levels. In the context of this work, they are used to detect the Cherenkov light emitted by EASs (see section II.2.2). In particular, in chapter V the calibration of the SiPMs used for the SST-1M camera is presented.

Photons passing through silicon interact with the atomic electrons. The leading interaction at $\mathcal{O}(1\text{ eV})$ photon energies (UV to red light) is the photo-electric effect (see sec-

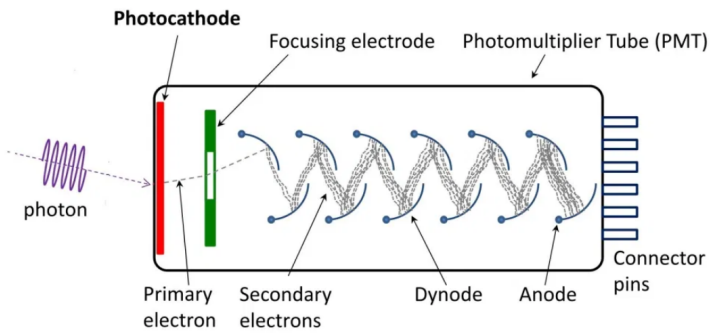

Figure III.10. Schematic of a photo-multiplier tube. A photon reaches the photo-cathode which ejects an electron. The ejected electron is beamed (by the focusing electrode) towards the first dynode ejecting more electrons. The ejected electrons create further electrons by reaching a succession of dynodes. The signal is collected on the anode. Taken from [78].

tion II.1.1.1). The energy gained by the electron allows it to pass from the valence band to the conduction band. This, creates an electron-hole pair. The electron (and hole) is free to move and can be collected through a wire to detect a signal. However the current generated by a single electron cannot be detected. The produced electron needs to be multiplied.

III.3.2.1 Single photon avalanche diodes

The multiplication of electrons (to about 10^6 electrons) allows to reach a detectable amount being recorded by for instance an ADC. The avalanche process is created by creating a high electric field ($> 5 \times 10^5$ V/cm) in the depletion region of a p-n junction. The electric field is created by applying a reverse bias voltage. The electric field allows to drift the free charge carrier towards the anode (for holes) and cathode (for electrons). When the bias voltage reaches a threshold the silicon will become conductive. This threshold is called the breakdown voltage. At this threshold the electron produced by the original photon is multiplied in a cascade. Above the breakdown voltage, the free carriers liberate secondary charge carriers. This triggers a cascade of charge carriers multiplying the number of charges [79]. Such device operating above the breakdown voltage are called Single Photon Avalanche Diodes (SPADs).

The avalanche process is stopped by the use of a quenching resistor in series with the SPAD. The current flowing through the resistor reduces the effective voltage of the SPAD which when passing below the breakdown ends the avalanche. The SPAD returns to its original bias voltage and is able to detect photons again. This process is shown in fig. III.11 (left).

If the bias voltage of the SPAD is high enough the number of charge carriers produced in the avalanche process is the same regardless of the initial photon energy. This is referred as the Geiger-mode. In the Geiger-mode the gain is high enough to detect low energy photons but no distinction between photon energy can be done. Additionally, one can only determine if at least one photon was detected.

To count the photons, SPADs are arranged in a small dense (100 to 1000 per mm^2) array (see fig. III.11 right). The SPADs output are summed. Therefore, provided that the gain of each SPA is more or less equal, the signal output is proportional to the number

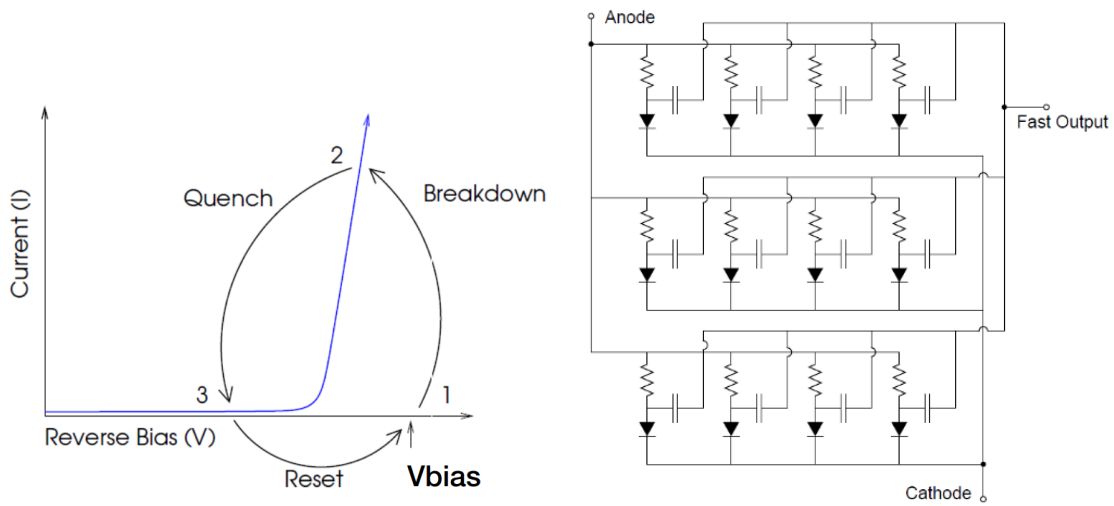

Figure III.11. Left: Cycle of breakdown, quench and reset of SPAD. Right: An array of SPADs forming a SiPM. Taken from [79].

of discharged SPADs thus the number of photons detected. Such devices form a SiPM. The SPAD units are sometimes called microcells. As a side remark, a photon is not always detected as it has to interact with an electron. A photon triggering an avalanche in a SPAD is called a photo-electron.

III.3.2.2 Performance parameters

Gain The proportionality of SiPMs is well illustrated by the multiple photo-electrons spectrum. Example of those are given in fig. V.7. The spectra show the reconstructed charge for an average incoming amount of photo-electron. The photo peaks illustrate the photo counting capabilities of SiPMs. In fig. V.7 the gain is represented by the photo-peak distances. The total charge generated in a SiPM is given by:

$$Q_{tot} = eN_{fired}G, \tag{III.1}$$

where N_{fired} is the number of fired cells, G is the gain of the SiPM and e the electron charge. The gain of a SiPM depends on the overvoltage ΔV (voltage above breakdown) applied to the sensor. It is given by:

$$G = \frac{C\Delta V}{e}, \tag{III.2}$$

with C the microcell capacitance. The gain is subject to fluctuations. These fluctuations arise mainly from the differences of gain within the SPADs composing the SiPM and from the statistical fluctuation of the number of charge carriers produced in an avalanche. Therefore, in addition to the gain, the gain smearing is also an important parameter of the SiPM. On the photo-electron spectra illustrated in fig. V.7 the gain smearing affects the width of the photo-peaks.

Photo-detection efficiency The photo-detection efficiency (PDE) of SiPMs is the measure of the efficiency to detect photons for different wavelength. It is the convolution of different effects. First the quantum efficiency of silicon, the probability of the photon to convert an

electron. Second the avalanche probability, the probability to initiate an avalanche in the silicon. Last, the sensor fill factor which is the ratio of active area to the device area. The PDE as function of wavelength λ is therefore expressed as:

$$PDE(\lambda) = \eta(\lambda)\epsilon(\lambda)F, \tag{III.3}$$

where η is the quantum efficiency, ϵ the avalanche probability and F the fill factor. The PDE for the SST-1M camera pixels is shown in fig. III.24 (right). The PDE increases with increased over-voltage.

Dark count Thermal electrons can reach a sufficient energy to initiate a cascade within a SiPM microcell. The signal induced by thermal electrons or photons is identical. Such source of noise is referred as dark photons.

This thermal noise is expressed in units of counts per second. Sometimes also in counts per second per surface area as this phenomenon increases with increased active area. Moreover, the dark count rate (DCR) increases with temperature and over-voltage.

Besides being a source of noise, the dark photons are useful to calibrate SiPMs in the absence of a light source. The photo-electron spectra of dark counts is used to evaluate the gain, the gain smearing, the dark count rate and the optical cross-talk. An example of this measurement is shown in section V.2.1.3.

Optical cross-talk In the avalanche, the charged carriers produced emit photons. These photons might initiate an other avalanche in a neighboring cell. As a consequence, it creates an excess count of photon-electrons. These secondary photons are near infrared photons able to travel long distances in the active volume. Different scenarios for optical cross-talk are shown in fig. III.13. The cross-talk photon travels directly to the neighbor cell (a). The cross-talk photon is reflected off the protective layer (b). The cross-talk photon is reflected off the bottom silicon substrate (c).

Optical cross-talk is usually limited by the use of trenches between microcells.

The optical cross-talk is usually quantified in terms of probability p_{XT} of a primary microcell triggers a secondary microcell. One other definition consist of counting the average number of microcells discharged μ_{XT} from a primary discharge. This is the case for instance in [80]. In section V.2.1.3, the model introduced in [80] is used to measure the SiPM parameters among which the optical cross-talk. In fig. III.12, the different statistical cross-talk processes are illustrated for two cases: a single primary event and a Poisson number of primary events. The model used in this work corresponds to the one on the lower right.

The optical cross-talk increases with increased over-voltage. Usually, one defines the operational over-voltage applied to the SiPM by compromising between optical-cross talk probability and PDE.

After-pulsing The defects in the silicon lattice might trap charged carriers released during the avalanche. The trapped charged carries are released with short delay (typically 1 ns) thus creating a secondary avalanche (after pulses).

Linearity The SPAD array in SiPM offers photo counting capacities. However, the number of microcells limits the linearity of the device. The saturation occurs when the number of photo-electrons if comparable to the number of microcells: $N_\gamma PDE/(1-\mu_{XT})) \simeq N_{cells}$.

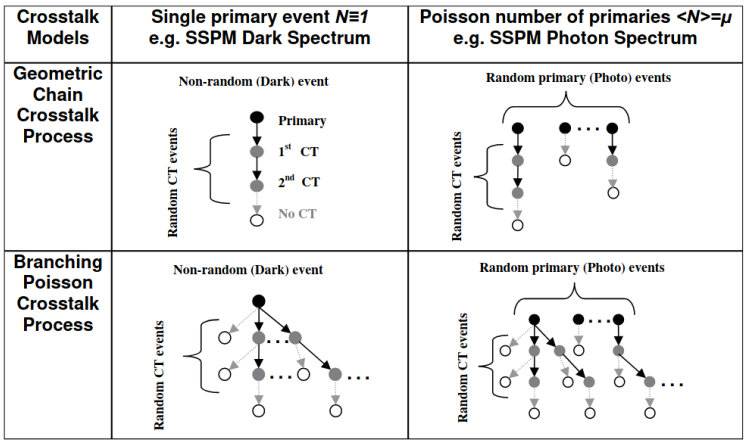

Figure III.12. Illustration of the optical-cross talk statistical processes. Taken from [80].

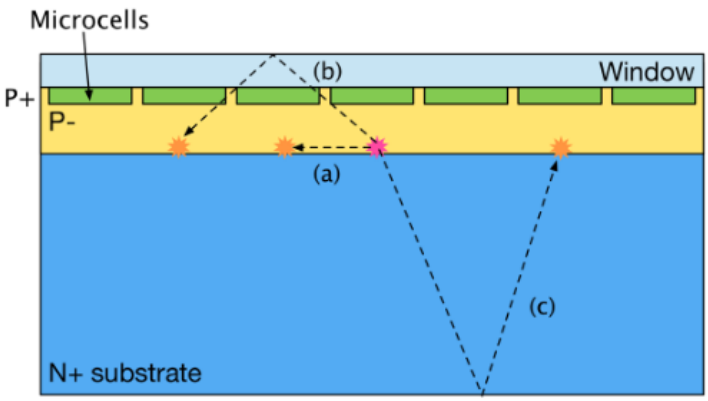

Figure III.13. Illustration of the optical cross-talk phenomenon in a SiPM. Taken from [79].

In this case, the device has not enough cells to guarantee that each photon will enter a free cell. Multiple photons reaching the same microcell within a time comparable to the recovery time of a SPAD will produce a unique discharge. Probabilistic considerations yields that the number of fired cells is:

$$N_{fired} = N_{cells}\left(1 - \exp\left(-\frac{N_\gamma PDE}{N_{cells}(1-\mu_{XT})}\right)\right), \tag{III.4}$$

The device works in the linear regime when $N_\gamma PDE/(1-\mu_{XT}) \simeq N_{fired}$. Linearity is achieved by having enough microcells for the range of required sensitivity.

Temperature dependence It was mentioned that the dark count rate depends on the temperature on the SiPM. Additionally, thermal changes affect the breakdown voltage of the SiPMS. Thus to ensure stable operation of the sensor, cooling of the device are sometimes used in particular when the temperature varies significantly. For instance, the SST-1M camera is constantly cooled and the bias voltage is adjusted to compensate for change of the breakdown voltage with temperature (see section III.4.2.4).

Figure III.14. Photograph (in 2018) of the SST-1M telescope installed at IFJ PAN in Kraków.

III.4 The single mirror small sized telescope

The single mirror small sized telescope (SST-1M) is a 4 m mirror diameter Davies-Cotton Cherenkov telescope (see figure III.14). It has been conceived to operate in an array of about 70 other telescopes to cover the highest energy of CTA (from 1 TeV to 300 TeV). The SST-1M project involves 60 people from 16 different institutions across Europe: from Switzerland, Poland, Czech Republic, Ireland and Ukraine. The key parameters of the SST-1M telescope are given in table III.3.

The telescope structure is mainly composed of steel for a total weight of 8.6 tons. It has been designed to sustain the environmental conditions of the CTA southern site. The structure is described in section III.4.1.1.

The mirror dish is composed of 18 hexagonal facets for a total effective area of 9.42 m^2. The mirrors and their performances are described in section III.4.1.2.

The camera of the SST-1M telescope is equipped with a filtering window designed to cut night-sky background light, described in section III.4.2.1. The rays reflected by the mirrors are collected by hexagonal hollow light cones, described in section III.4.2.2, which are redirecting it towards a smaller photo-detection sensors. The photo-detection devices, described in section III.4.2.3, are large area hexagonal SiPMs from Hamamatsu (S10943(X)). The analog signal of the SiPMs are amplified and shaped by the front-end electronics, described in section III.4.2.4. The amplified signals are then digitized by the trigger and readout system: DigiCam, described in section III.4.2.5.

The technical design report of the SST-1M telescope can be found in [53].

The first prototype has been commissioned at IFJ PAN in Kraków in 2018.

In the future, two telescopes will be installed at the Ondřejov Observatory in the Czech Republic.

Telescope properties		Optical properties		Camera properties	
Number of mirrors	18	Focal length f	5600 ± 5 mm	Number of pixels	1296
Elevation range	−16° to +97°	Dish diameter D	4 m	Pixel linear size (side-to-side)	23.2 mm
Azimuth range	±280°	Reflective area	9.42 m^2	Pixel angular size	0.24°
Total weight	8.6 t	Effective reflective area	6.47 m^2	Sampling frequency	250 MHz
		On-axis D_{80}	0.1°	Maximum trigger frequency	250 MHz
		4° off-axis D_{80}	0.21°	Read-out window	200 ns
		Field-of-View (FoV)	9.1°	Maximum read-out rate	~ 10 kHz
		Optical time spread	1.5 ns	FADC range	12-bit

Table III.3. Key numbers for the SST-1M telescope.

III.4.1 The SST-1M telescope structure

III.4.1.1 Supporting structure

The SST-1M telescope structure, shown in figure III.15, is composed of several sub-systems. The telescope is fixed on the ground by the reinforced concrete foundation (0). The foundation measures 3.5 m wide and go down to a depth of about 1.2 m. Attached to the foundation is the telescope tower (1). A counterweight (2) is found at the back of the mirror dish support structure (4). The 18 hexagonal facets mirrors (3) are reflecting the light towards the camera (7) which is attached to the mirror dish support structure by four masts (8). The telescope structure includes the docking station (6) which allows to park the telescope in a locked position. The docking station is fixed on the ground by means of reinforce concrete foundations (5).

Within the tower is found a slew drive allowing to rotate the telescope in the azimuth axis over 280° in both rotation directions. At the top of the tower, the elevation slew drive allows to elevate or descend the telescope within −16° to +97°.

The mirrors are placed on the dish support, a welded steel structure to fix the mirrors. At the back of the mirror dish, cast-iron counterweights are fixed to balance the camera weight. The mirrors are glued on a fixing structure which is then mounted to the mirror dish. This fixing structure allows to keep the mirrors in a steady position. Two actuators for each mirror facet allow to orientate the mirrors such that the reflected light is focused on the center of the camera.

The docking station allows to park the telescope when it is not operating. In parking position, the telescope can sustain seismic activities, temperature gradients (from −45 °C to +45 °C), wind (mean 200 km/h and 1.7 higher gust wind), snow and ice accumulation.

III.4.1.2 Mirrors and optical system

The mirrors (see figure III.17 left) are redirecting the Cherenkov light, emitted in the atmosphere by the EASs, onto the camera. The mirror dish hosts 18 hexagonal mirrors facets as can be seen in figure III.14. The central mirror being not necessary as it is shadowed by the camera, is removed to place the telescope pointing related equipment. The orientation of each mirror can be controlled individually by two actuators.

A mirror facet measures 780 mm flat-to-flat. The dish of 18 mirrors is 4 m diameter wide for a total surface of 9.42 m^2 and an effective reflective surface of 6.47 m^2 when taking

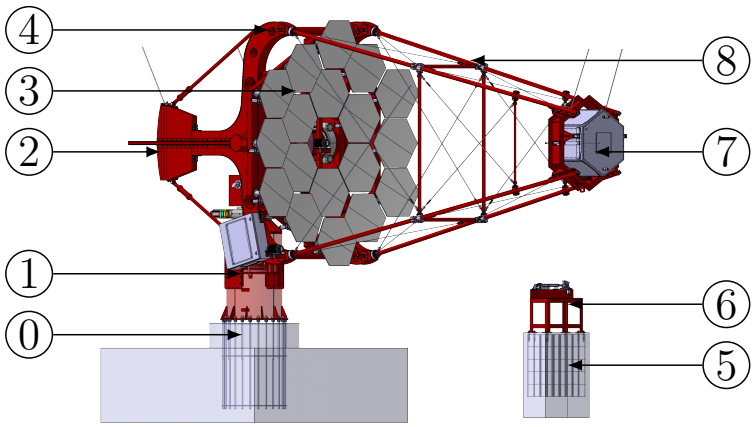

Figure III.15. Structure drawing of the SST-1M telescope. (0) Foundation of the telescope support. (1) The telescope tower. (2) The counterweight. (3) Hexagonal mirrors. (4) Dish support structure. (5) Foundation of the docking station. (6) Docking station. (7) Camera. (8) Mast. Taken from [53].

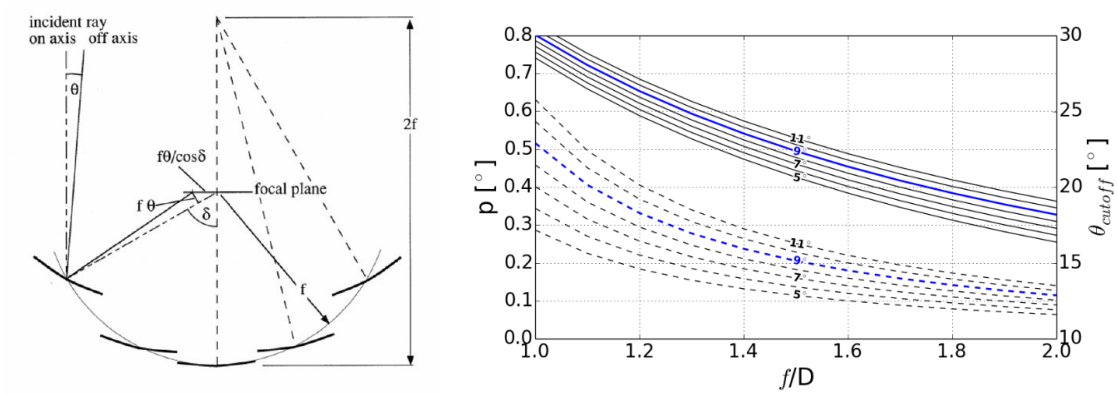

Figure III.16. Left: Schematic of the Davies-Cotton optical design. Taken from [81]. Right: Pixel angular size (dashed and left y-axis scale), defined as 4 times the standard deviation of the PSF, and required cut-off angle of the light guides (solid and right y-axis scale) as a function of the ratio of the focal length and of the mirror dish diameter: f/D. Each curve corresponds to a different field-of-view. The blue curve shows the field of view selected for the SST-1M telescope (9°). The SST-1M has a f/D = 1.4. Taken from [82].

into account the reflectivity and the shadowing of the structure. The dish hosting the mirrors is spherical with a curvature radius f = 5.6 m. Each mirror facet is spherical with a curvature radius 2f = 11.2 m (from the definition of Davies-Cotton itself, see fig. III.16 (left)).

As the reflectance of the mirrors has to be high in the UV range, aluminum coated mirrors are used. The mirrors are made of a glass substrate which is coated with aluminum. The aluminum coating is protected by a silicon dioxide layer. As the mirrors are exposed

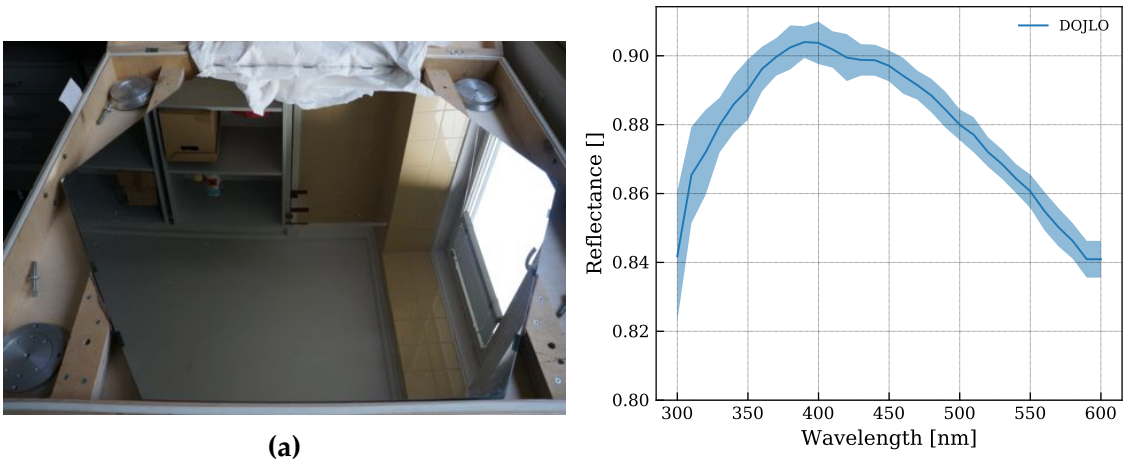

(a) **(b)**

Figure III.17. Left: Photograph of a SST-1M mirror. Taken from [53]. Right: Average reflectance of the mirrors of the SST-1M telescope as function of the wavelength measured from a batch of 8 mirrors. The shaded area represents the standard deviation. Courtesy of D. Mandat.

to an open environment, damages and thus degradation of the specular reflectance is expected over the years (from the experience of previous IACTs a 2% drop in specular reflectance per year is expected). This overall drop of reflectance is even larger for dual mirror designs since the light has to be reflected twice. In order to recover the nominal reflectance, the coating can be removed chemically and then the glass substrate can be re-coated. This operation should be repeated every 6 to 7 years. The reflectance of the mirrors as function of the wavelength is shown in figure III.17. The reflectance of the mirrors is above 0.84 from 300 nm to 600 nm with a maximum reflectance of 0.9 at 400 nm.

The mirrors can be properly aligned with the actuators. The alignment procedure consists of pointing the telescope towards a source of light that is far enough, so that the incoming rays can be considered parallel (e.g. a star). As the spherical mirrors have a radius of curvature of 2f their focal point is located at f. Thus parallel rays will focus the light on a point f = 5.6 m away from the mirrors. The focal length f is the distance between the mirror dish and the camera. The alignment procedure orientates each of the 18 mirrors such that their focal points are all at the center of the camera. To align the telescope mirrors, images of the point spread function (PSF) are taken. The images are recorded by a CCD camera (Lid CCD Camera) placed at the center of the mirror dish. The camera records the PSF and the image is used to align the mirrors. After a few iterations the mirrors are aligned. In figure III.18 the PSF (simulated and measured) of the SST-1M telescope for several off-axis angles from the camera center is shown. In figure III.19 the 80% containment diameter as a function of the off-axis angle is shown. The 80% containment diameter is 0.1° at the center and about 0.3° at the edge of the field-of-view (FoV). In comparison the pixel angular size is 0.24°.

III.4.2 The SST-1M camera

The SST-1M camera is the camera developed for the SST-1M project by the UNIGE. Its calibration and characterization can be found in chapter V. It comprises various sub-

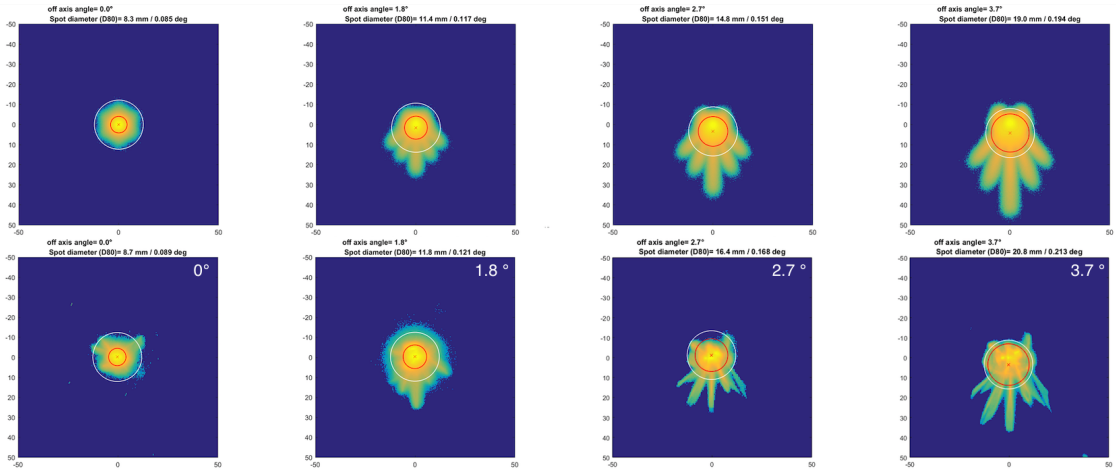

Figure III.18. Optical point spread function of the telescope for different off-axis angles (0°, 1.8°, 2.7° and 3.7°). The red circles indicate the 80% containment of the image and the white circle the required maximum 80% containment circle at 4° by CTA. The images are log-scaled. The top row shows simulations of the PSF with the Zeemax software while the bottom row shows the measured PSF. Taken from [83].

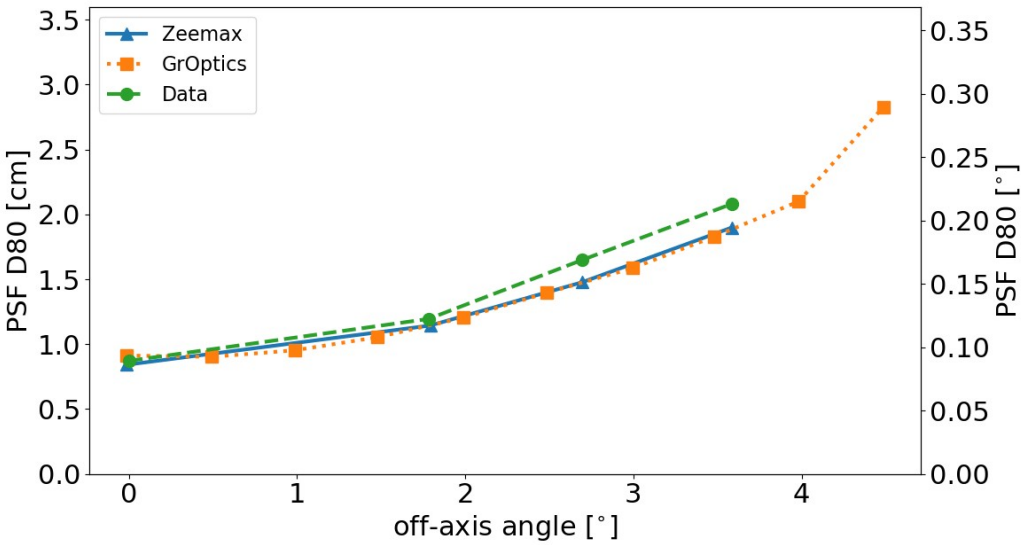

(a)

Figure III.19. Point spread function as a function of the off-axis angle. The measured PSF is shown in green while two simulation of the telescope PSF are plotted in orange (GrOptics) and blue (Zeemax). Taken from [53].

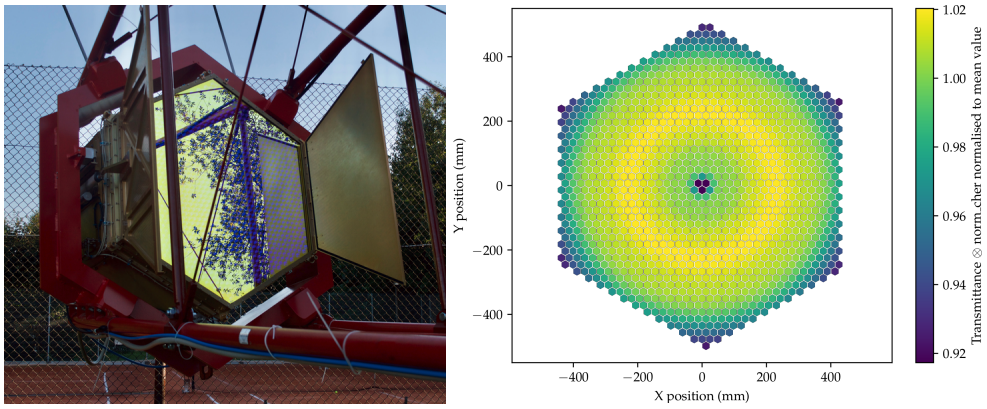

Figure III.20. Left: The SST-1M camera equipped with its filtering window on the telescope structure in Krakow. The entrance window appears yellowish as the majority of the light above 540 nm is reflected by the window coating. The filter is optimized for transmission in the blue. It also reduces Fresnel losses with an anti-reflective layer. Taken from [85]. Right: Relative efficiency of transmission of the window for the Cherenkov light spectrum from 300 nm to 550 nm per camera pixel with respect to the average value over all pixels. Taken from [85].

elements: a filtering window, described in section III.4.2.1; light guides, described in section III.4.2.2; photo-detection sensors, described in section III.4.2.3; front-end electronic boards, described in section III.4.2.4; digitizing and trigger electronics, described in section III.4.2.5 and a cooling system, described in section III.4.2.6. Other sub-systems such as, the camera shutter or the house keeping board are not described here. Additional information on the camera can be found in [84].

III.4.2.1 Filtering window

As explained in section II.2.3.1, the telescope is exposed to background light from the night sky. In particular, the NSB spectrum is higher in the red than in the blue wavelength range. The Cherenkov light spectrum has its maximum in the UV range. Thus the photo-detection efficiency of all optical elements is optimized for efficiency in the UV range. However, it is still efficient above 550 nm, where the NSB spectrum is high (see fig. II.12). In order to maximize the signal to noise ratio a filtering entrance window was designed to cut wavelengths above 510 nm. The window also protects the camera component from the environmental conditions (rain, dust, etc.).

The window (see fig. III.20) is an hexagonal 3.3 mm thick Borofloat 33 borosilicate glass from Schott. It is coated on both sides with a combination of dichroic filters, to reduce the amount of NSB light. It is also coated with an anti-reflecting layer, which allows to reduce the Fresnel losses. The coating process limits the uniformity of the transmittance. This can be seen in fig. III.20 (right). The average transmittance of the window as function of the wavelength is show in fig. III.21. The window has an average transmittance of about 0.9 between 330 nm and 510 nm. As can be seen from fig. III.21 the window is transparent, in the region where the Cherenkov signal is the highest, and opaque above 520 nm where the NSB becomes more intense.

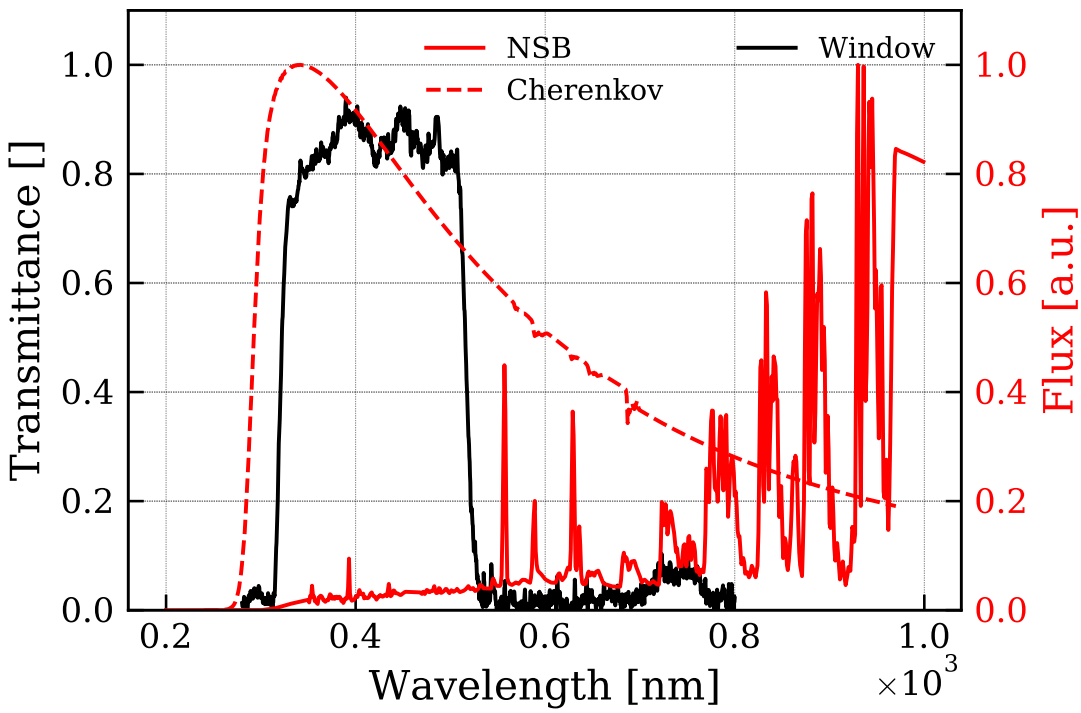

Figure III.21. Transmittance of the SST-1M filtering window (black) as function of the wavelength. The CTA reference Cherenkov spectrum (dashed red) and the CTA reference NSB spectrum are shown.

III.4.2.2 Light guides

Each of the 1296 camera pixels is equipped with a light guide (see fig. III.22). The light guides serve three purposes: reduce the photo-sensor surface by a factor ~ 6 thus limiting the dead spaces; remove background stray-light from large incident angles and reduce cross-talk between pixels. The light guide has a hexagonal entrance area of 466.5 mm^2 and a hexagonal exit area of 78.6 mm^2. A hexagonal entrance shape allows to have equidistant neighboring pixels. thus the shower image orientation is geometrically unbiased [82]. The light guides are made of a plastic substrate coated with aluminum superimposed with dichroic layer which protects the aluminum from oxidation.

The light guides collect the light that comes from the sky and that are reflected by the mirrors to the camera. These rays of light have an angle of incidence on the camera $\theta \leq 24°$. Thus any ray that has an incident angle greater than this value is background light. The light guides are designed to veto the stray light with $\theta > 24°$ by reflecting it back outside of the funnel. The transmittance of the light guides as function of the incidence angle θ is shown in fig. III.22. The collection efficiency drops sharply at 20° with a 50% collection efficiency at 24° and reaches zero above 30°. The optical efficiency as function of the wavelength is shown in fig. III.22 for incidence angles smaller than 24°. The efficiency is almost independent of wavelength (from 300 nm to 650 nm). The light guides angular size (thus the pixel angular size) and their angular cut-off were chosen under the constraints set by CTA. The CTA requires a mirror dish diameter of about 4 m and a telescope field-of-view of about 9° for the SSTs. In addition, a cost effective solution for the 70 foreseen SSTs is found with cameras composed of about 1300 pixels. Moreover the ratio f/D of the focal length f to the mirror diameter D needs to stay in the range

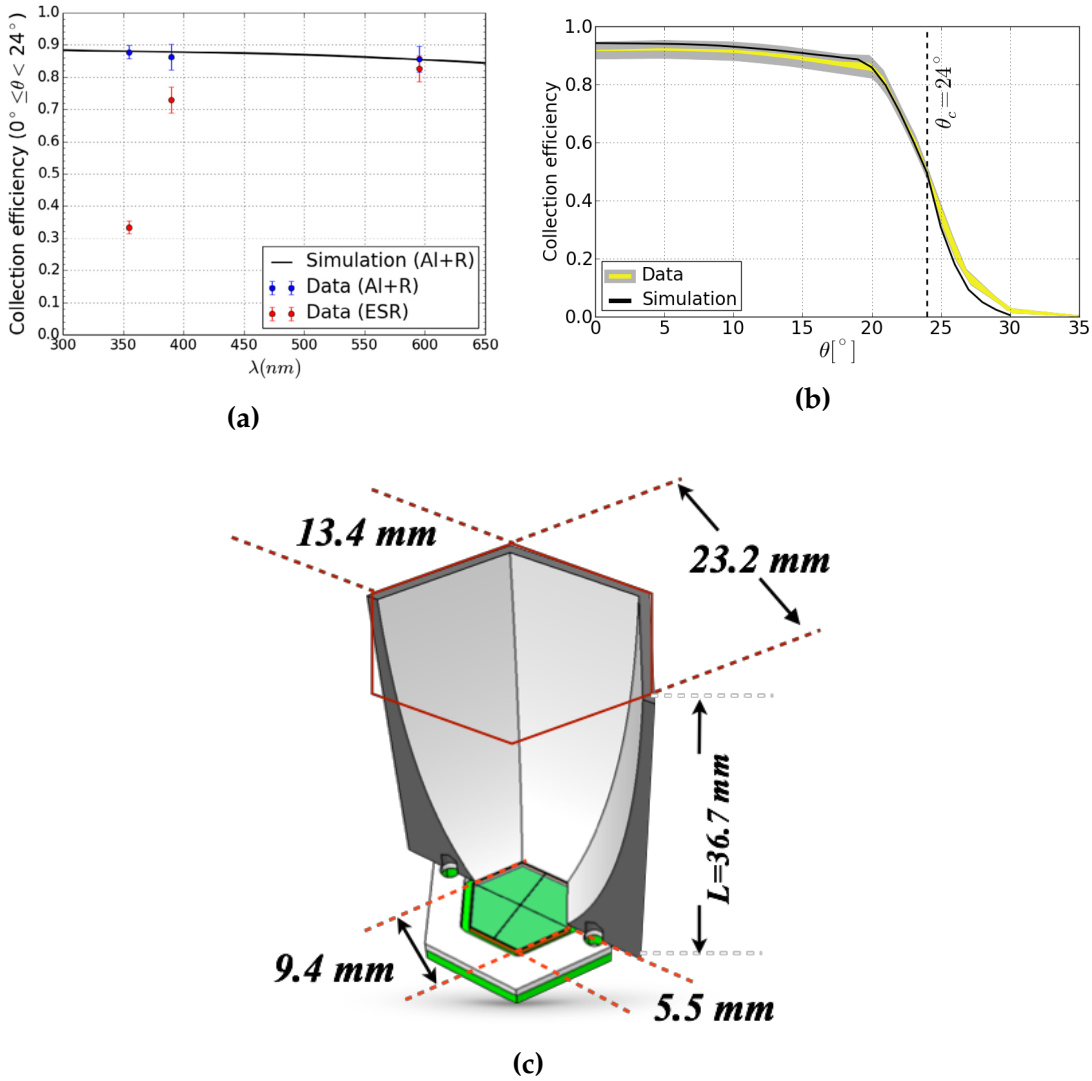

Figure III.22. Left: Average collection efficiency of the light guides for angle of incidences smaller than 24°. The data points show two coatings measured at 3 wavelengths. The simulated data is used to extrapolate the efficiency. The Al + R (blue) coating is the one chosen for the SST-1M light guides. Taken from [82]. Right: Collection efficiency of the light guides as function of the incidence angle θ. The measured data is shown is yellow and gray including the systematic and statistics error, while the Zeemax ray-tracing simulation is shown in black. Taken from [82]. Bottom: Drawing of a light guide mounted on a SiPM. The light guide is cut in half to see its interior. Taken from [53].

from 1.2 to 1.4 to keep the optical aberration low [82]. The angular size of the pixels and the required cut-off angle as function of f/D is shown in fig. III.16 (right). This figure is obtained from geometrical considerations of the Davies-Cotton design.

More information on the SST-1M light guides is found in [82].

III.4.2.3 Photo-detection sensors

Most of in-operation IACTs use Photo-Multiplier Tubes (PMTs) as photo-detectors. They offer great sensitivity in the UV range and good signal-to-noise ratio. Nowadays IACTs

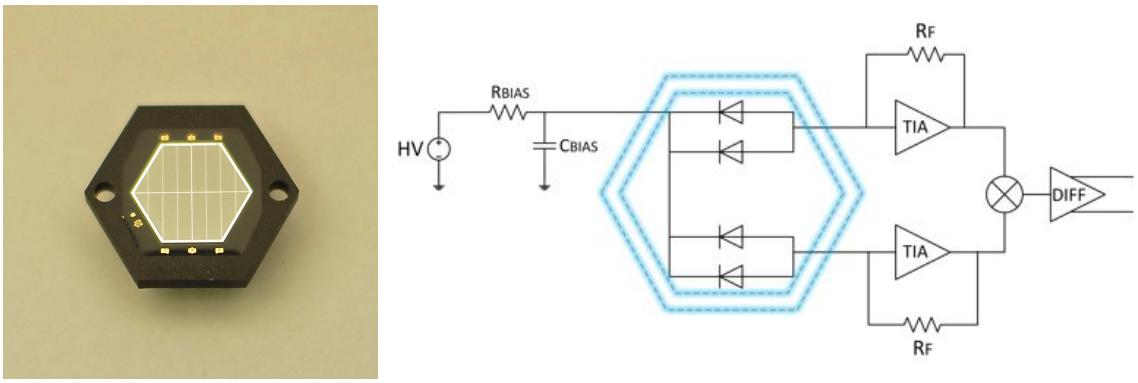

(a) (b)

Figure III.23. Left: Image of a SST-1M SiPM (S10943(X)) from Hamamatsu. Right: Pre-amplification scheme of the SiPM signal. Taken from [87].

use them as low light detection devices but the newest generation of Cherenkov telescope are considering to use Silicon Photo-Multipliers (SiPMs) as photo-detection devices (see section III.3.2 for a brief introduction on SiPMs). The progress made in SiPM technology, especially the improved photo-detection efficiency towards UV light, which depends mostly on their coatings, and the capability to distinguish single photon signals. Additionally, the reduction of optical cross-talk and the decrease of dark noise makes them suitable for ground based gamma-ray astronomy experiments such as CTA. The SST cameras of CTA are following the steps of the FACT [65], the first telescope demonstrating that SiPMs can be used for Cherenkov cameras.

SiPMs offer the advantage of being operable in high night-sky background conditions, for instance in the presence of moonlight [86]. On the contrary, PMTs cannot be operated in such conditions without risking to damage them. In fact, observations in the presence of the Moon with PMTs requires to lower the operation voltage or to mount a filtering window [63, 64].

The SST-1M camera is composed of 1296 large-area hexagonal SiPMs (S10943(X)) from Hamamatsu (see fig. III.23). The active area is divided in 4 channels, sharing the same cathode. Two channels are analogously summed and amplified by a trans-impedance amplifier (see fig. III.23). The output of two amplifiers are further summed in a differential amplifier. This signal is passed to the digitizing electronic (see section III.4.2.5).

The SiPM has an active area of 93.6 mm^2. Such large area (when compared to other SiPMs) creates high dark count noise of the order of 3 MHz per SiPM. In some applications, where the background light is well under control, such dark count rate is dominating the background light. However for the SST-1M telescope the NSB is dominating over the dark noise. In comparison a NSB rate of about 40 MHz is expected for the darkest night sky conditions. Moreover dark counts can be used for calibration without an external light source.

The reverse IV curve of the SiPM is shown in fig. III.24 (left) where the breakdown voltage (54.7 V) is indicated. The SiPM is operated in Geiger regime at 2.8 V above the breakdown voltage. At this bias voltage the gain of the SiPM, meaning the average number of electrons a single photo-electron produces, is 1.49×10^6. In fig. III.24 (right) the photo-detection efficiency of the SiPM is shown as function of wavelength. As can be seen, the SiPM is sensitive in the near UV ($\geq$ 350 nm) up to the near infrared ($\leq$ 1000 nm) with a maximum photo-detection efficiency of 0.36 at 472 nm. The wavelength range of

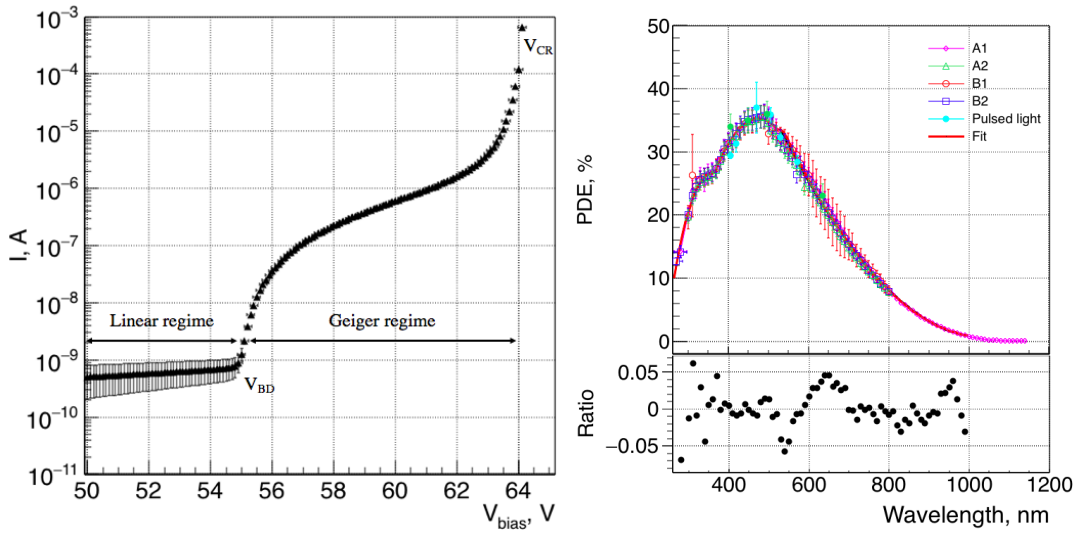

(a) **(b)**

Figure III.24. Left: Reverse IV curve of the SST-1M SiPM. The breakdown voltage is found at 54.7 V and the sensor is operated at 57.5 V. Taken from [87]. Right: Photo-detection efficiency of the SST-1M SiPM as function of the wavelength. The data points A1, A2, B1, B2 correspond to the 4 channels of the SiPMs measured individually. The ratio between the data and the fit is shown below. Taken from [87].

photo-detection efficiency overlaps nicely with the reference Cherenkov spectrum in the atmosphere shown in fig. III.21. However the fact that it is still sensitive above ~ 550 nm is not desired, since the NSB spectrum is dominant in this region (see fig. III.21). The filtering window cuts wavelengths above 540 nm therefore reducing the NSB rate.

III.4.2.4 Front-end electronics

The SST-1M camera pixels are grouped into hardware modules. These photo-detection (PDP) modules comprises 12 pixels, for a total of 108 modules in the camera. A PDP module is composed of 12 light guides, 12 SiPMs, a pre-amplification board and a slow-control board (SCB) (see fig. III.25).

The pre-amplification board amplifies the signal from the SiPMs individually. The amplification circuit (see fig. III.23 right) sums the four channels of the SiPMs into a single output. The summation is done by first summing two channels together and amplify them with low-noise trans-impedance amplification stages then the two amplified outputs are summed with a differential output stage. This configuration allows to have a fast response after the pre-amplification stage. In fig. III.26 the pulse shape as a function of time for different light level intensity (in units of photo-electron) is shown. The saturation of the amplification stage occurs for signals above 600 p.e. Above the 600 p.e. the response of the amplifiers is not linear anymore. Although the signal is saturated, the integral of the pulse can be used to recover the number of p.e. above the saturation threshold (see section V.3.1).

At the back of the pre-amplification board (see fig. III.25) is the slow-control board (SCB). This board routes the pre-amplified signals to the digitizing electronics but its main goal is to read the temperature and adjust the bias voltages of the PDP module SiPMs to ensure stable operation. Each SiPM is equipped with a Negative Temperature

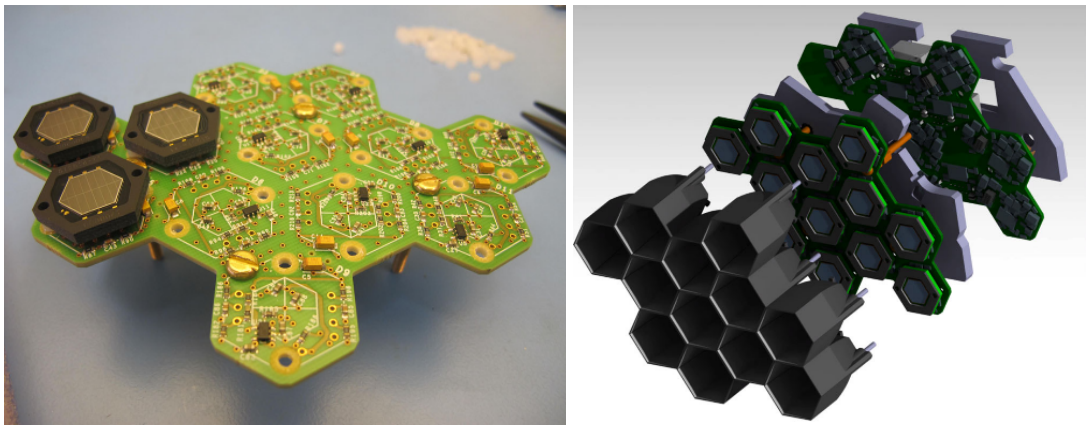

(a) (b)

Figure III.25. Left: Picture of a pre-amplification board with three SiPMs mounted on it. Taken from [84]. Right: CAD drawing of a PDP module. A PDP module is composed of: 12 hollow light guides, 12 SiPMs, a pre-amplification board and a slow control board. Taken from [84].

Coefficient (NTC) thermistor to measure its temperature. The temperature read-out is used by the SCB to adjust the operational voltage of the SiPMs at a frequency of 10 Hz. This is done in a micro-controller. This adjustment is necessary in order to keep the operational over-voltage of the SiPM constant as it varies with temperature. Thus the gain of the SiPM is kept constant although temperature is varying. This adjustment is called the compensation loop. The temperature within the camera is kept constant by a water cooling (see section III.4.2.6) but the individual pixel temperature variations are coped for with the SCB compensation loop. More information on the front-end and the compensation loop is found in [88].

III.4.2.5 Back-end electronics

The electronic signals produced by the SiPMs, amplified by the front-end electronics and routed by the SCB are then digitized by the back-end electronics. In the SST-1M camera the digitizing and triggering system is called DigiCam (Digital Camera). The DigiCam is divided into three crates (see III.27). Each crate contains nine Flash ADC (FADC) boards and a trigger board. A crate is associated with a sector of the camera which represents one third of it. The FADCs board collect the analog signal from the PDP modules via RJ45 cables (three per PDP module). These signals are digitized by 12-bit FADCs at a frequency of 250 MHz. The particularity of the DigiCam is that these signals are continuously digitized and memorized thanks to the ring buffer which allows to store 2048 samples (8.192 µs) per pixel and to the fast digitizing technology. The trigger board is responsible of triggering decision. This decision is based on the digitized sample of the FADCs. This allows to reduce the complexity of calibrating trigger and readout, as both are identical. In order to not overload the trigger boards the baseline subtracted 12-bit samples are summed in groups of three neighboring pixels called triplets and are clipped to 8-bit unsigned integers. This data volume reduction allows to reach a dead-time free trigger rate, thus at each cycle of 4 ns. Thus the trigger decision can be taken at each clock cycle of 4 ns. Then from these triplet digits a cluster value, made of 7 or 19 neighboring triplets, is formed by summing all the triplets values. The DigiCams

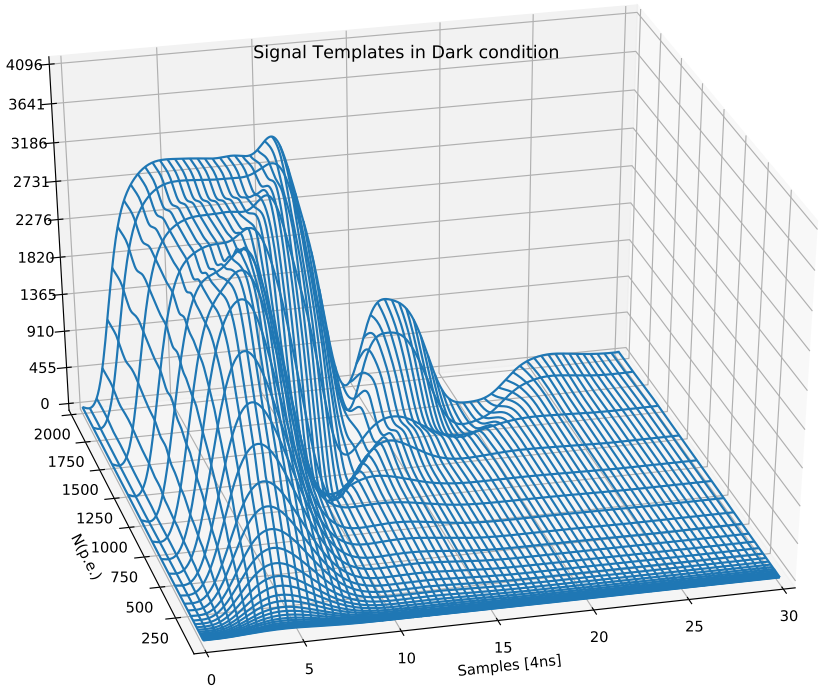

Figure III.26. Pulse shape as function of the number of photo-electrons and the time after the pre-amplification and digitization stage. Taken from [85].

exchange triplet values from the overlapping regions of the camera sectors they cover. The trigger topology based on neighboring pixels, allows to identify signal which is clustered in an almost circular region of the camera. The EAS Cherenkov images are expected to produce images clustered in space and time while the NSB fluctuations are not clustered. Additional triggers can be configured thanks to the high flexibility of the DigiCam. For instance a muon ring trigger is implemented and allows to trigger signals based on their ring structure. Also an internal clocked trigger is available in order to take snapshots of the night-sky for calibration purposes and trigger other sub-systems. The clocked trigger signal can also be passed to other sub-systems, for instance those of the calibration. Additionally, the DigiCam can trigger on external signals.

For each triggered event, 1296 12-bit waveforms of 50 samples (programmable value) are sent to the camera server via a 10 Gb/s optical fiber link. Additionally to these waveforms, trigger waveforms, trigger tagging, pedestals and time stamps are also sent. The camera server receives also slow-control data from the SCBs. The slow-control data are routed by the DigiCams and transported to the camera server via a 1 Gb/s optical fiber link. Additionally, slow-control data of the DigiCam are sent to the camera server. The camera server stores the data from the camera into *zfits* files [89]. These data can be read with the *protozfits* Python package [90].

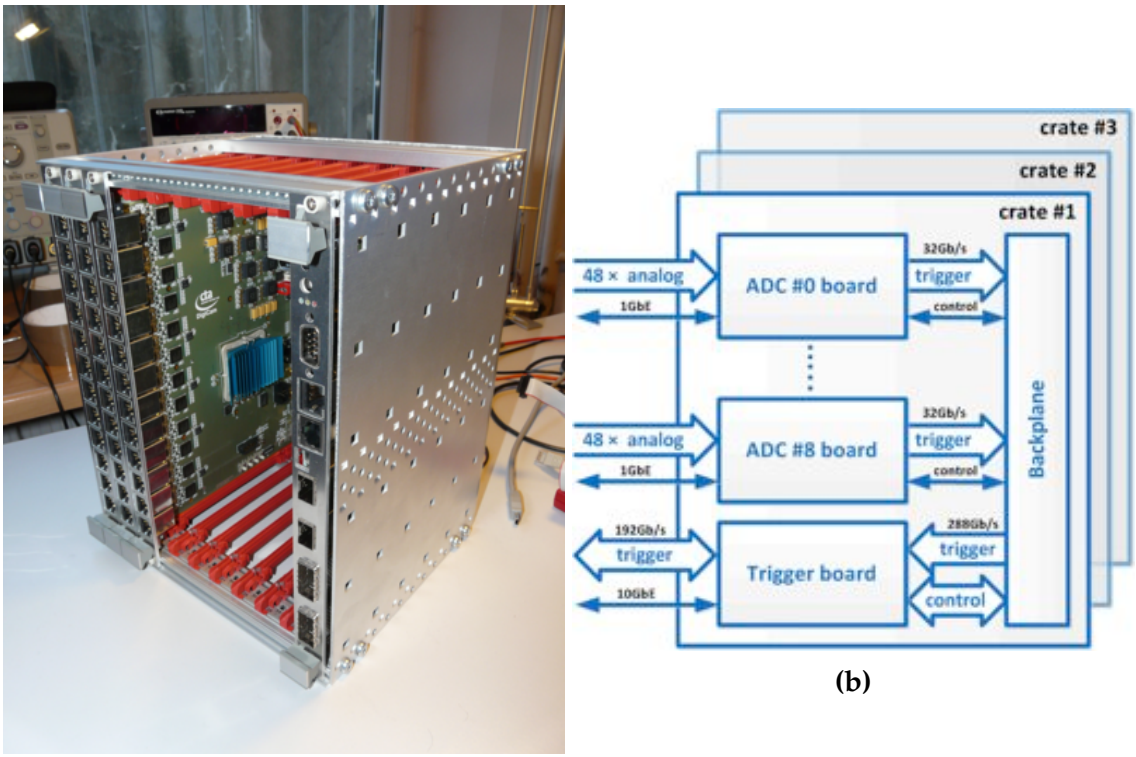

(a) (b)

Figure III.27. Left: Picture of a DigiCam crate with three FADC boards and a trigger board mounted. Taken from [53]. Right: Schematic of the DigiCam crates in the SST-1M camera. Taken from [53].

III.4.2.6 Cooling

The camera needs a cooling power of about 2 kW. The PDP is responsible for about 25% of the heat produced in the camera. Due to its high-frequency digitizing system, the DigiCam is responsible for about 60% of the heat produced. The 15% left can be attributed to the other auxiliary systems [84]. In order to extract the heat out of the camera, a water cooling solution is adopted. The water is mixed with glycol to lower the freezing temperature.

Aluminium pipes are used to distribute the water flow to the PDP and the DigiCam crates (see fig. III.28). The PDP modules exchange heat via their connection to the aluminum back-plate. The copper layers in the printed circuit board were made thicker for better heat distribution and extraction. The use of a ceramic thermal paste offers an optimal contact with the electronics components. For the DigiCam crates, heat pipes are connected to the FADC and trigger boards via an interface plate to exchange the heat with the water cooling.

The other subsystems exchange heat by air circulation within the camera. The air circulation is provided by the DigiCam fans.

In fig. III.28 the temperature for each of the camera pixels is shown. As can be seen, the cooling is capable of keeping the temperature of the pixels at 22.6 ± 0.9 °C (mean and standard deviation) within a range of 20 °C to 26 °C. As the camera plane was placed vertically, a vertical temperature gradient is observed.

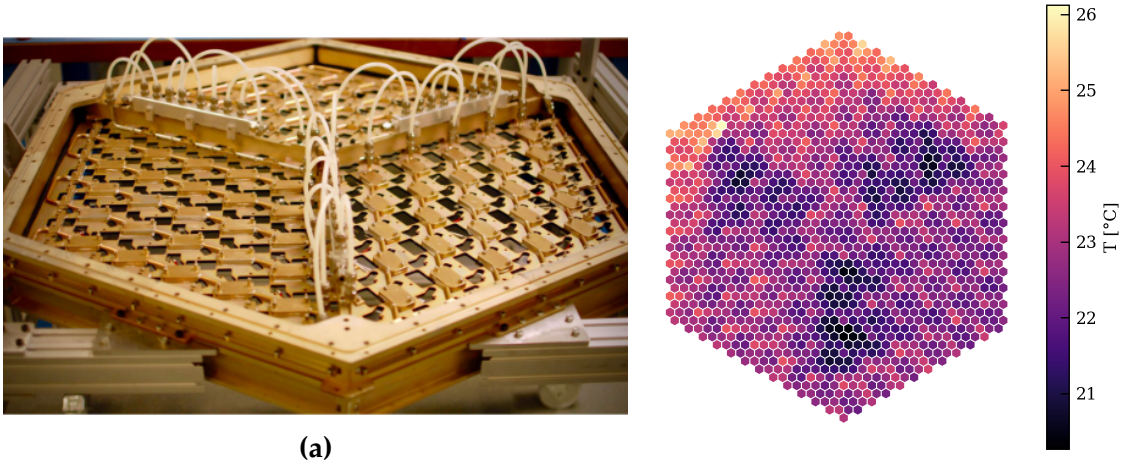

(a) **(b)**

Figure III.28. Left: Picture of the back of the PDP with the aluminium back-plates and the cooling pipes. Taken from [84]. Right: Temperature of the camera pixels as measured during commissioning of the camera. The camera is positioned in vertically.

Chapter IV

Neutrino Cherenkov telescopes

IV.1 The IceCube neutrino telescope

As discussed in section I.4.1, the interaction of cosmic-rays with its surrounding produces neutral and charged pions. This pions further decay into neutrinos and gamma-rays. Therefore the sources of cosmic-rays are expected to emit both neutrinos and gamma-rays (see eqs. (I.33) to (I.35)). The detection of neutrinos from a source would unambiguously confirm hadronic interaction. The IACTs presented in chapter III are detecting the gamma-rays. The IceCube neutrino telescope aims at detecting astrophysical sources of neutrinos from the decay of charged pions produced in hadronic interactions. Hence, gamma-ray and neutrino Cherenkov detector science is intimately connected, and this is at the core of the 'multi-messenger' high-energy astrophysics.

Both gamma-rays and neutrinos are neutral particle thus being insensitive to magnetic deflections. This ensures that the arrival direction of these messengers of the Universe correspond to the direction of the source.

In the pursuance to detect astrophysical neutrinos, several neutrino detectors have been built. The neutrino telescope community achieved to detect atmospheric neutrinos (neutrinos produced in the atmosphere), solar neutrinos (and their oscillations towards us [91]) and neutrinos emitted from Supernova 1987A [92]. However, due to the low interaction probability of neutrinos and the high level of atmospheric background, an astrophysical origin of neutrinos could not be established before the km^3-scale detector IceCube would be attained.

The IceCube detector is a kilometer-scale detector submerged deep in the ice of Antarctica. The detector is located at the South Pole and is in operation since 2011 in its completed configuration. In 2013, the collaboration published evidence of extraterrestrial neutrinos [16]. The detector is also used for other purposes than cosmic accelerator searches, such as: dark matter indirect detection; search of exotic particles; neutrino oscillation study; detection of transient $\sim$ MeV neutrino emission such as in the case of supernovae. The collaboration is also investigating correlation of neutrinos with other messengers of the universe, such as X-ray and gamma-ray photons; ultra-high energy cosmic-rays and gravitational waves.

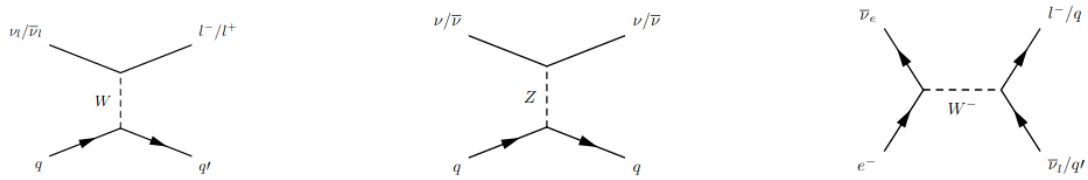

(a) charged-current (b) neutral-current (c) Glashow resonance

Figure IV.1. Feynman diagrams of the charged current interaction (left), neutral current interaction (middle) and the Glashow resonance (right). Taken from [93].

IV.1.1 Neutrino detection principle

As neutrinos are neutral particles, they cannot be detected directly. Moreover they can only interact via the weak force. Only the interaction of a neutrino with the matter in which it travels can be detected. This interaction comes in two kinds: neutral current (NC) and charged current (CC). The neutral current interactions are carried by the Z boson, while the charged current is an interaction mediated by the W bosons. The NC and CC interactions can be represented as:

$$\nu_l(\bar{\nu}_l) + N \longrightarrow \nu_l(\bar{\nu}_l) + X \quad \text{(NC)} \tag{IV.1}$$

$$\nu_l(\bar{\nu}_l) + N \longrightarrow l^-(l^+) + X \quad \text{(CC)}, \tag{IV.2}$$

where $l^- = (e^-, \mu^-, \tau^-)$ is a lepton, $l^+ = (e^+, \mu^+, \tau^+)$ is an anti-lepton, ν_l is a neutrino of leptonic flavor l, $\bar{\nu}_l$ is an anti-neutrino of leptonic flavor l, N is a nucleon (proton or neutron) and X is either a proton or a neutron. The corresponding Feynman diagrams are shown in fig. IV.1.

As can be seen from eqs. (IV.1) and (IV.2), neutral current interactions do not produce charged leptons but a neutrino of lower energy of the incident one. This process is called deep inelastic scattering. Part of the incoming neutrino energy is passed to the nucleon N. The energy passed to the nucleon triggers a hadronic cascade that can be detected by IceCube (depending on the energy transferred). The charged current interactions produce charged leptons. Depending on its flavor and its energy, the produced charged lepton will either: travel a short distance before loosing all its energy; travel through the detector; or decay.

All the the charged particles produced in the NC and CC interactions will emit Cherenkov light (see section II.1.2.2) when satisfying the condition in eq. (II.6). This light is collected by the optical modules (see section IV.1.3) and is used to reconstruct the energy and direction of the neutrino.

The charged lepton $l^\pm$ is of the same flavor as the neutrino because the leptonic number is conserved. Thus by identifying the flavor of the charged lepton, the flavor of incoming neutrino can be determined (see section IV.1.4 for more information on the event categories). It is important to point out that in IceCube the charge of the lepton cannot be identified from CC and NC interactions. To do this a magnetic field would be needed, and on a volume of a cubic-kilometer cost would be prohibitive. Therefore, one cannot say if the incoming neutrino is a neutrino or an anti-neutrino. In fig. IV.2 the neutrino nucleon scattering cross-section as a function of the neutrino energy for neutral and charged current interactions is shown. The Glashow resonance is also shown. The Glashow resonance

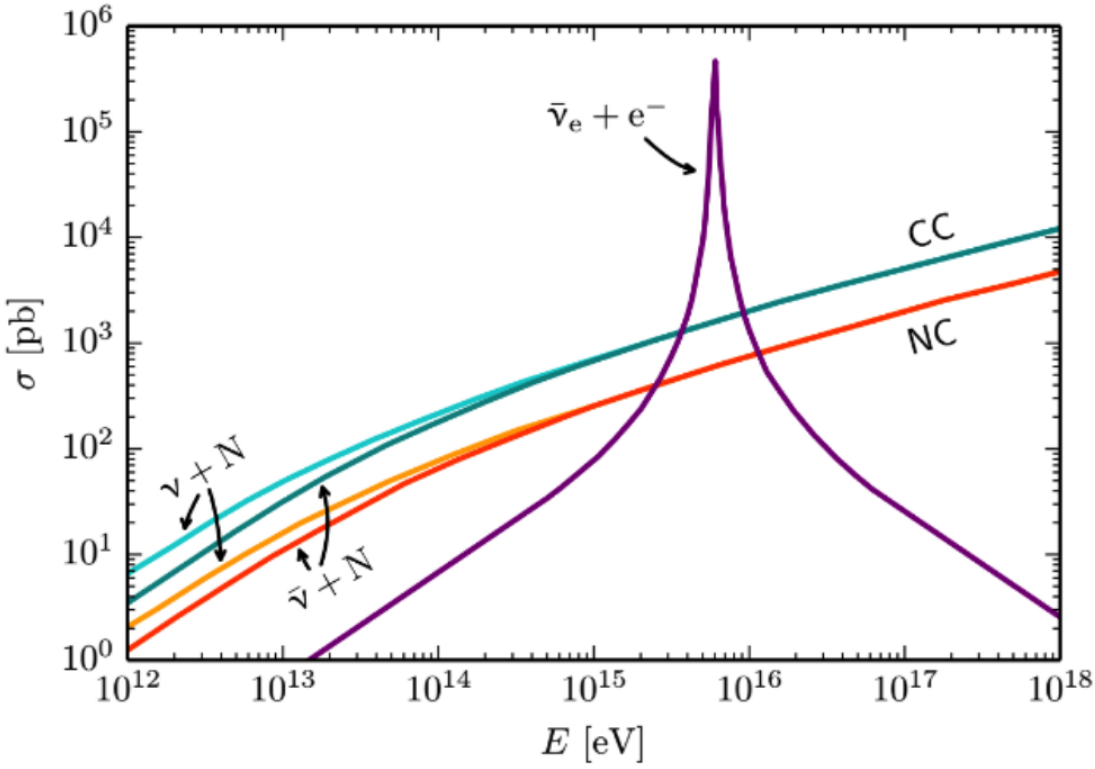

Figure IV.2. Neutrino nucleon scattering cross-section as a function of the neutrino energy. The cross-section for charged (turquoise and blue) and neutral current (orange and red) are shown. The cross-section for anti-neutrino is smaller than for neutrinos at energies below 10^{14} eV. The Glashow interaction cross-section is shown in purple. Taken from [94].

comes from the interaction of an electronic anti-neutrino with an electron (see fig. IV.1 right):

$$\bar{\nu}_e + e^- \longrightarrow W^- \longrightarrow l^- + \bar{\nu}_l \ (33\%) \tag{IV.3}$$

$$\longrightarrow q + \bar{q} \ (67\%), \tag{IV.4}$$

with q and $\bar{q}$ being quarks and anti-quarks. This interaction creates a negative *W*-boson which decays into a charged lepton and the associated neutrino or hadronically. This process can be detected by IceCube and is the only interaction for which one can distinguish an anti-neutrino $\bar{\nu}_e$ from a ν_e. This is due to the fact that the only charged lepton present in matter is the electron. Therefore, in order to conserve the leptonic number, only an electronic anti-neutrino $\bar{\nu}_e$ is allowed for this interaction. It happens at neutrino energies of about $E_{\bar{\nu}_e} = \frac{m_W^2 - m_e^2}{2m_e} \simeq 6.3$ PeV, with $m_W = 80.4$ GeV/c^2 the mass of the *W*-boson.

IV.1.2 The in-ice array

To detect the Cherenkov light emitted by the charged particles produced during the interaction of a neutrino, the IceCube detector uses Digital Optical Modules (DOMs). 5160 DOMs are placed under the ice of Antarctica along 86 vertical strings. The DOMs

are deployed between 1450 m and 2450 m meter deep (see fig. IV.3). To each string 60 DOMs, spaced by 17 m, are attached. The strings are deployed within an hexagon and placed triangularly with spacing of 125 m. The total volume corresponds to about one kilometer-cube [95].

The detector is submerged deep in the ice for two main reasons. First, the ice offers a great volume target of matter. Such large volume is needed when considering that the interaction probability of neutrinos is very low when compared to other fundamental particles.

Second, natural ice is transparent to Cherenkov light. In particular the antarctic ice has a high purity. Moreover, at a depth of more that 1450 m the pressure is high enough to remove air bubbles that might increase the scattering of the light and purity increases further so that light is seen propagate several hundred meters. LED flashers attached to the PMTs allowed to measure the ice optical properties. These properties are used for the reconstruction of the neutrino events [95].

Within the in-ice array, a sub-array is located at its center: DeepCore. DeepCore is essentially a denser version of the in-ice array in the deepest layer of the array, which is the most transparent. It consists of 8 strings together with 7 strings of the standard array, separated by mutual distances ranging from 41 m to 105 m. The DeepCore strings have 60 DOMs with inter-DOM distance of 7 m to 10 m depending on the depth of the DOMs. Additionally, 6 out of the 8 DeepCore string DOMs are equipped with more sensitive PMTs (about 35% higher quantum efficiency). The increase in quantum efficiency, the smaller spacing between strings and between the DOMs allow to extend the sensitivity of IceCube to lower energies of the order of 5 GeV, extending IceCube scope to the physics of atmospheric neutrino oscillations, indirect searches of WIMP dark matter from neutrino annihilation and improves the sensitivity for supernovae explosion bursts of $\sim$ 10 MeV neutrinos [95].

At the top of array, the IceTop detector is located. IceTop is a cosmic-ray detector at an altitude of about 2835 m. IceTop is composed of 162 detectors made of ice equipped with 2 PMTs (high gain and low gain) to detect the Cherenkov light emitted by the charged secondaries produced in EASs. The IceTop array layout is similar to the one of the in-ice array. Additionally, a denser core is found about where the DeepCore strings are located. The IceTop detector is sensitive from PeV-energies to 1 EeV-energies of cosmic-rays. The IceTop detector is also used to veto events for down-going neutrinos [95].

IV.1.3 Digital optical modules

The Digital Optical Modules (DOMs) (see fig. IV.4) are standalone modules responsible for: the detection the Cherenkov light, the signal shaping, the digitization and the calibration. The module embeds in a spherical glass: a 10″ PMT looking downwards; a board responsible of data acquisition, calibration, communication and voltage conversion; boards responsible of applying the high-voltage to the PMT, collect the PMT signal, and generate light pulses with a LED.

The PMTs are able to detect the Cherenkov light of charged particles from 10 GeV to 10 PeV energy which can be as far as 500 m from the DOM. The PMTs produce about 10^7 electron per photo-electron for about 1 mV pulse amplitude. The PMTs response is linear over a dynamic range of 2 V. Several digitizers are used to record the pulse signals. The DOMs individually detect the photons and are able to store waveform signals up to

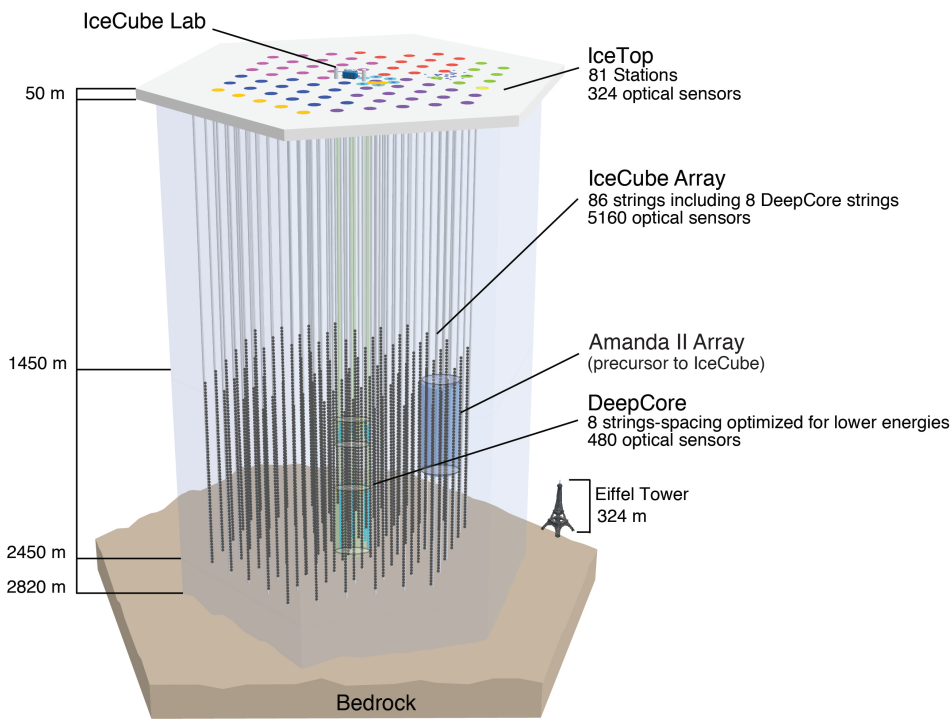

Figure IV.3. Drawing of the IceCube observatory with its laboratory, the cosmic-ray detector: IceTop and the in-ice array. The Eiffel tower is drawn for size comparison. Taken from [96].

6.4 µs following the initial photon. Together with the waveforms are stored the individual arrival times of detected photons (hit times). The PMT hit rate is recorded as well. This allows to propagate the information about burst of hits. Bursts could occur when many low-energy (about 10 MeV) supernova-neutrino interact in the detector.

IV.1.4 Event categories

The IceCube events can be classified in three categories. Depending on the type of interaction (charged or neutral current) and the flavor of the incoming neutrino, the signature shape left by the charged particles in terms of Cherenkov light is different. The three categories are track-like events, cascade-like events and double-bang events. In fig. IV.5 are shown typical examples of these event types.

Track-like events A track-like event (see fig. IV.5a) leaves in the detector a long track. The DOMs that detected the Cherenkov photons are placed on a linear track which extends from the first interaction point to the edge of the detector. These tracks are created by a muonic neutrino interacting via the charged current interaction producing a muon or muons produced in the atmosphere that travel through the ice layer. The long-surviving muons travel distances that can go beyond the detector limits before decaying thus leaving its signature Cherenkov track. The atmospheric muons are at the origin of a large source of noise for IceCube (see section IV.1.5).

The energy deposited by the muons is used to estimate the neutrino energy. The

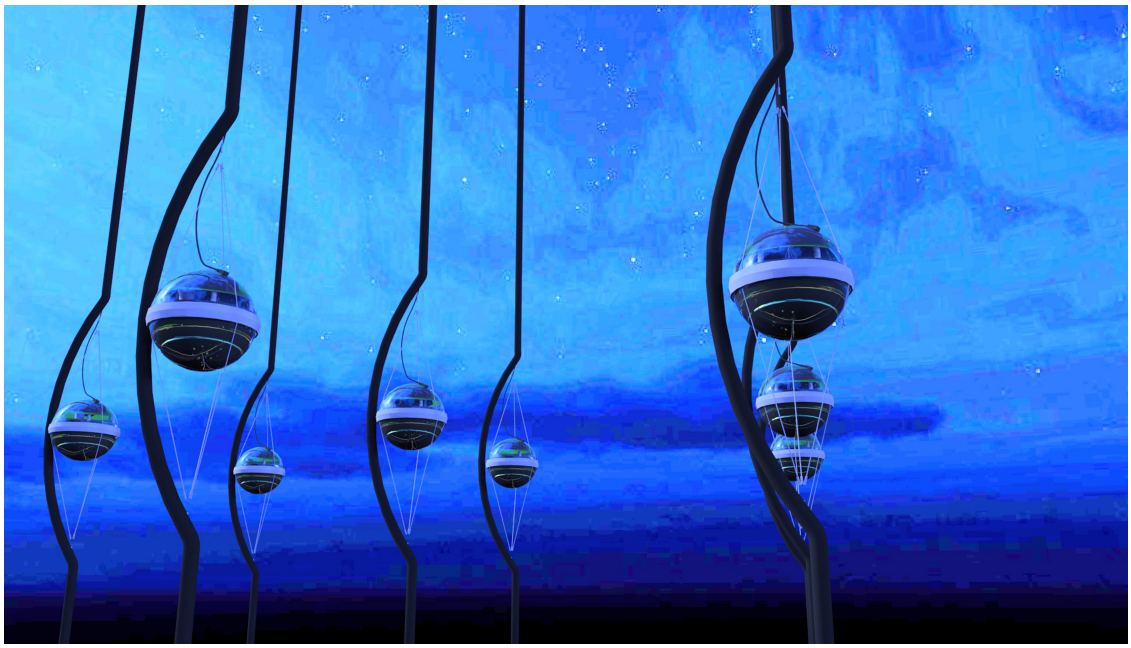

(a)

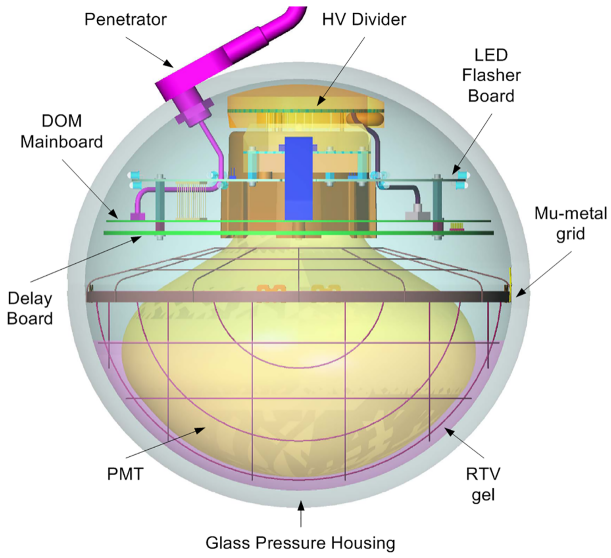

(b)

Figure IV.4. Top: Computer image of the DOMs attached to the strings in the ice. Bottom: Schematic of a DOM. Taken from [96].

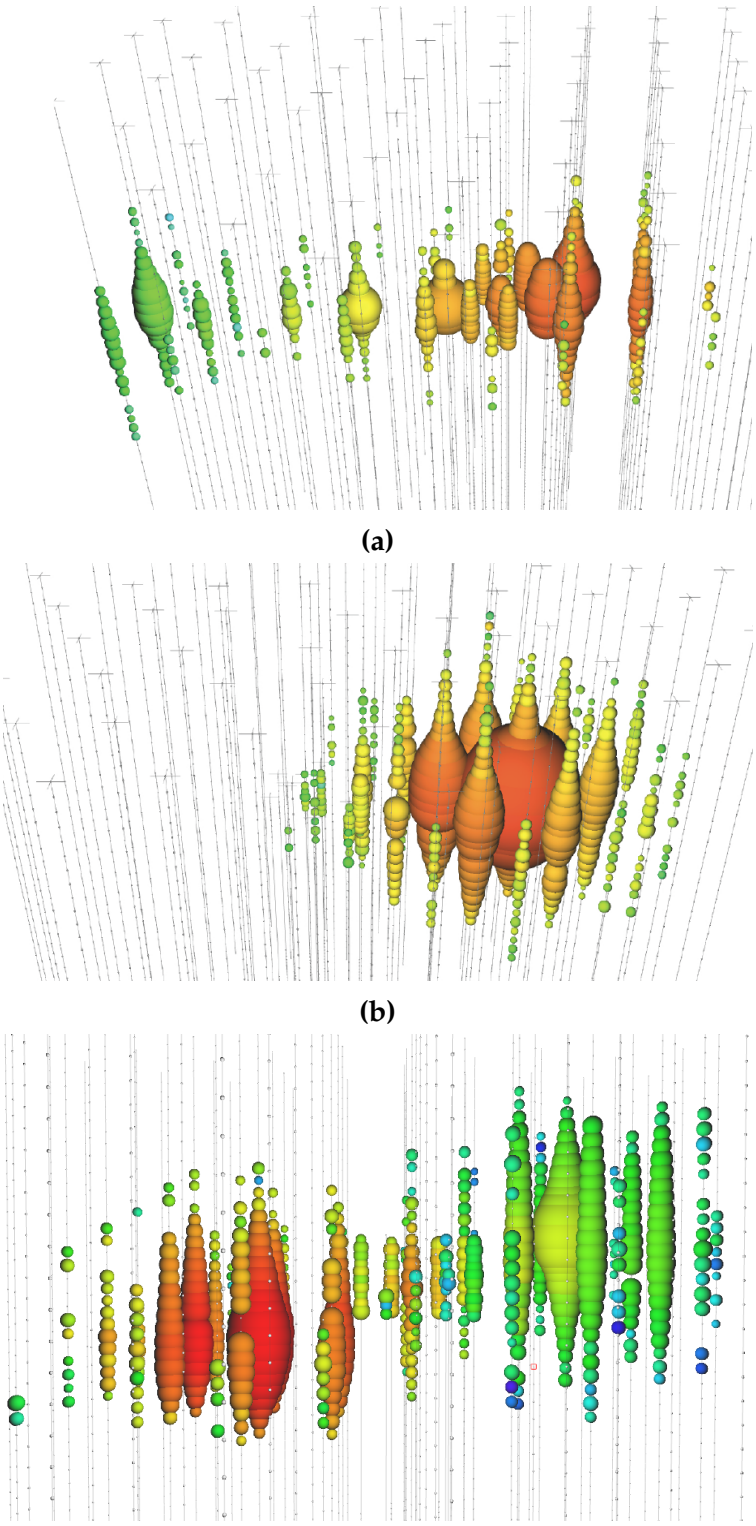

(a)

(b)

(c)

Figure IV.5. Typical track-like event (top), cascade-like event (middle) and double-bang event (bottom) in the IceCube detector. Each DOM is represented as a sphere its volume is proportional to the total number of photons detected. The color scale indicates the time of arrival of the light. Red denotes earliest hits will green denotes latest hits. Taken from [96].

muons loses energy via ionization, bremsstrahlung, photo-nuclear interaction and pair production. The observed energy loss within the sensitive ice volume of the muon offers a good estimate of its energy.

Due to their elongated shape, the muon event offer great angular resolution when compared to cascade-like events. The angular resolution for a track-like event is typically below 1°.

A muon neutrino can interact outside the IceCube detector and the produced muon could travel through the detector, leaving a track starting at the edged of the detector. This has the advantage of extending the effective volume of IceCube for track-like events. However, the distance travelled by the muon before reaching the detector is unknown which limits its energy estimation.

Cascade-like events Unlike the track-like events, the cascade-like events (see fig. IV.5b) leave a spherical signature that is contained in a region of the detector. Cascade-like events originate from NC interaction of all flavor of neutrinos and CC interaction of electron neutrino ν_e and tau neutrino ν_τ.

These events, being contained in the detector, offer a good energy resolution of about 10%. Moreover for the charged current interactions of ν_e and ν_τ nearly all the neutrino energy is deposited in the detector. Thus the energy deposited offers a good estimate of the neutrino energy. However for NC interactions of all flavors, part of the neutrino energy is passed to the undetected outgoing neutrino. Therefore, the deposited energy gives a lower limit of the incoming neutrino energy. IceCube cannot distinguish between NC cascades and CC cascades. Consequently, the energy deposited is always a lower limit of the incoming neutrino energy.

Due to their spherical shape, the angular resolution of cascade-like events is about 15°.

Double-bang events The CC interaction of ν_τ can be distinguish from the CC interaction of ν_e at energies beyond 1 PeV. Above this threshold, the tau lepton produced has enough energy to travel a long distance before decaying into a lower mass lepton. At the interaction point, the tau neutrino initiate a hadronic cascade and the tau produced travels a distance greater than the inter-string separation before decaying. While travelling the tau leaves a track. The decay of the tau lepton leaves a second cascade in the detector. These events are referred as double-bang events (see fig. IV.5c) for there two distinct cascades.

The neutrino tau are of particular interest for IceCube because they are less present in the atmospheric background and thought to originate from astrophysical sources.

IV.1.5 Atmospheric background

Being able to detect neutrinos with energy above 100 GeV, the IceCube detector is sensitive to atmospheric neutrinos produced in cosmic-ray showers (see fig. I.12). Moreover, the hadronic extensive air showers produce secondary muons that can be miss-identified as muon neutrino from astrophysical origin. In fact, the atmospheric background is the main source of background observed by IceCube. In fig. IV.6, the different sources of neutrinos seen by IceCube are illustrated.

Several techniques are in place to discriminate atmospheric events from astrophysical events. The astrophysical-ness of the events is established based on: the reconstructed energy; the type of event; the point of first interaction and the reconstructed direction.

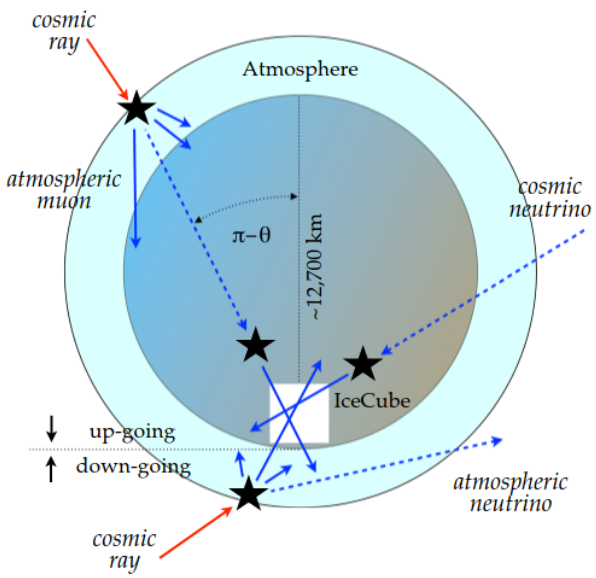

Figure IV.6. Illustration of the neutrinos seen with the IceCube telescope from up-going and down-going directions. The IceCube detects atmospheric muons and neutrinos as well as cosmic neutrinos. The up-going region corresponds to the northern sky while the down-going region corresponds to the southern sky. Taken from [97].

It can be seen in fig. I.12 that above a certain energy the astrophysical neutrinos are dominating the atmospheric background. This threshold depends on the supposed spectral index of the astrophysical neutrino sources.

Additionally, the fact that a track-like event is starting within the detector volume rules out the possibility that it is an atmospheric muon. An atmospheric muon would, as its name suggests, be produced outside of the ice. The fact that the detector is placed between 1450 m and 2450 m depth under the ice, offers a natural shielding for atmospheric muons to some extent.

Cascade-like events rule out the atmospheric muon hypothesis as its signature shape is significantly different from a muon track. However cascade-like events can originate from atmospheric electron neutrinos or atmospheric tau neutrinos and all-flavour NC interactions. However the flavor composition of atmospheric neutrinos is about $(\nu_e : 1, \nu_\mu : 2, \nu_\tau : 0)$. This means that two third of the atmospheric neutrinos are muon neutrinos and about one third are electronic neutrinos. The proportion of tau neutrino is very small.

The detector is able to reconstruct events coming in all directions. IceCube distinguishes two event directions: down-going and up-going. Down-going events are events that traverse the detector from the surface of the ice to the bottom of the ice. Up-going events are events that traverse in the opposite direction (see fig. IV.6). As the detector is located at the Geographic South Pole, down-going events correspond to events coming from the southern sky while up-going events come from the northern sky. In the northern sky, almost no atmospheric muon can reach the detector. This is particularly true at declination $\delta \sim +90°$ where Earth's crust absorbs almost all atmospheric muons. However in the northern sky, part of the neutrino flux at high energy is absorbed by the Earth.

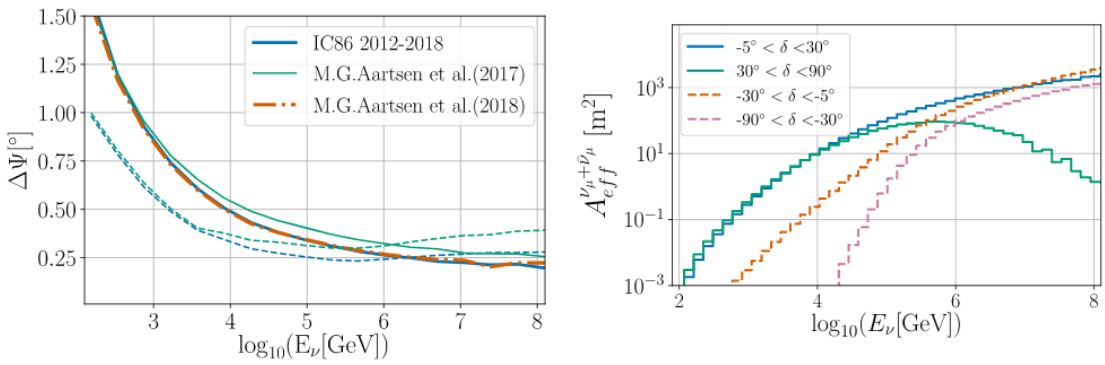

(a) **(b)**

Figure IV.7. Left: Median angular distance between the reconstructed muon and the neutrino direction as a function of the neutrino energy. The dashed lines represent the median bias for the 10 year analysis in [100] for the northern sky (blue) and southern sky (green). Right: Effective area for muon neutrinos as function of the neutrino energy and for different declination angles δ. Taken from [100] .

IV.1.6 Performance

IceCube has shown evidence for astrophysical neutrinos by showing an excess of the observed neutrino flux at energies above 50 TeV incompatible with the expected atmospheric background [98]. Several searches are conducted to cross-correlate known source of gamma-rays with neutrinos or to cross-correlate transient phenomena with neutrinos. A flaring gamma-ray source: the blazar TXS 0506+056 initiated a multi-wavelength search. IceCube identified an excess of neutrino events at the blazar location over several years. It showed that blazars are sources of neutrinos [99].

The search for sources of neutrino is still an on-going activity for the collaboration. IceCube published recently an all-sky scan in the aim to detect neutrino sources with 10 years of track-like events [100]. Here are reported the median angular bias and effective area (see fig. IV.7). The neutrino source sensitivity flux is shown in fig. IV.8.

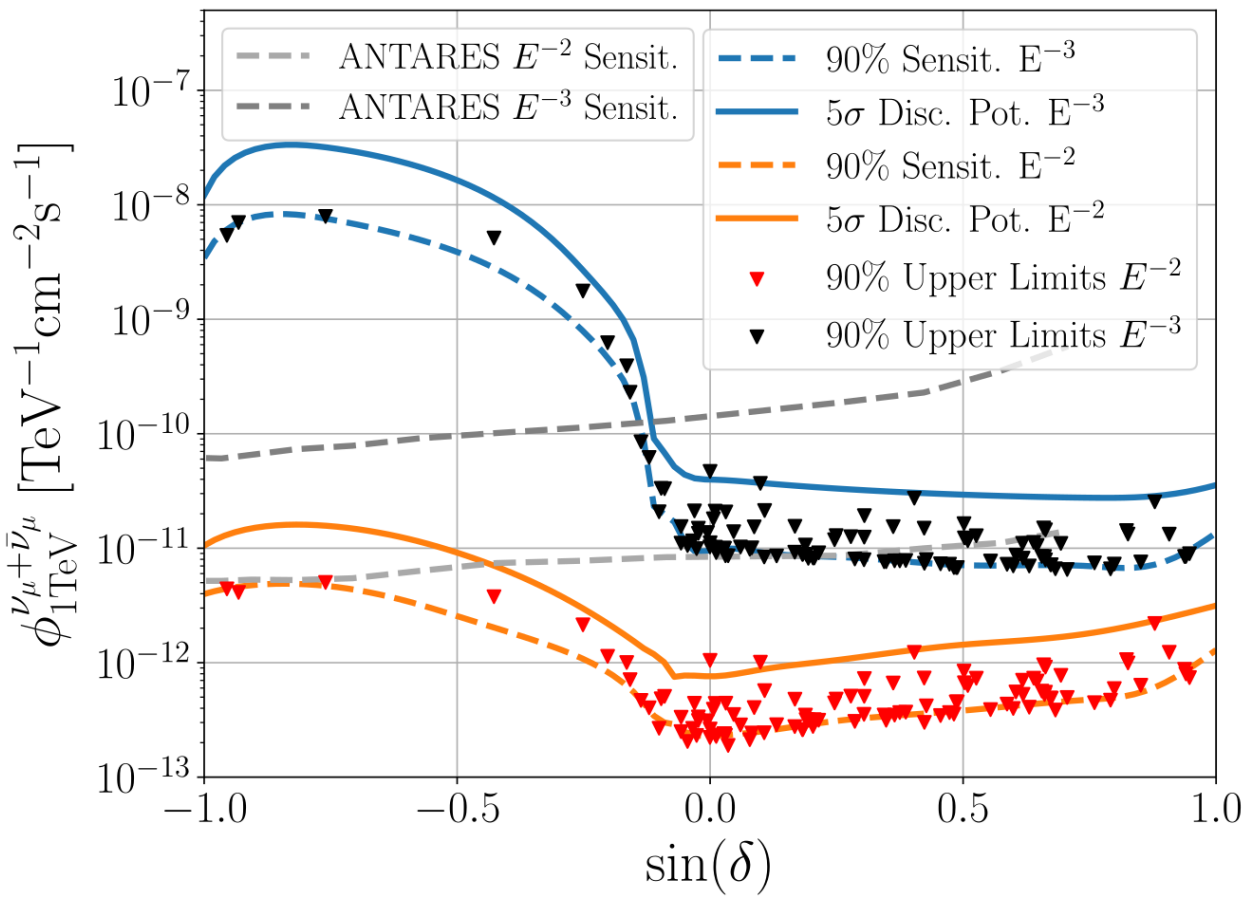

Figure IV.8. IceCube neutrino source flux sensitivity (dashed) and 5σ discovery potential (solid) as function of the declination angle δ. Two neutrino source fluxes hypothesis are drawn: spectral index $\gamma = -2$ (orange) and $\gamma = -3$ (blue). The sensitivity is shown for track-like events. Taken from [100] .

Chapter V

Calibration of a Cherenkov telescope camera using Silicon Photo-Multipliers

Silicon Photo-Multipliers (SiPMs) are becoming a standard for low light level detection in nuclear and particle physics experiments. Presently, the majority of Cherenkov cameras used in gamma-ray astronomy on imaging air Cherenkov Telescopes (IACTs) are equipped with photo-multiplier tubes (PMTs). Their operation in the presence of moonlight is possible, but it requires either lowering the high-voltage applied to the PMTs or the use of UV-pass filters [63, 64]. The FACT telescope [65] has shown that SiPMs can replace PMTs for Cherenkov cameras allowing to observe during strong moonlight and even with the Moon in the field of view (FoV), therefore, increasing the duty cycle [86], i.e. the observation time. Over the years, SiPMs have shown to have many advantages when compared to PMTs. As example their insensitivity to magnetic fields, the absence of ageing or the high level of reproducibility, being solid state devices, and their progressively lower cost. In terms of performance, SiPMs show consistent improvements of the photo-detection efficiency towards ultra-violet light, while reducing the correlated noise probability and dark noise rate. For these reasons, SiPMs are taking over PMTs in many fields of particle and nuclear physics. As mentionened in section III.2, the new generation of gamma-ray observatory, the Cherenkov Telescope Array (CTA), adopts SiPMs for the small size telescope (SST) cameras [101]. Also the LHAASO experiment adopted SiPM for the cameras of the fluorescence/Cherenkov array of telescopes [102] and the TAIGA experiment is also considering them for their IACTs [103].

This work defines the methods to measure the relevant calibration parameters in the laboratory and monitoring during operation on the field of a SiPM-based camera for gamma-ray astronomy. Here, the precision at which the calibration parameters are measured together with the methods and the calibration devices used for their determination are described. Through the measurement of these parameters, the camera performance can be fully assessed. The delivery schedule for the CTA southern observatory imposes a production and delivery of two telescopes per month for a total of up to 70 SSTs. The CTA project imposes strict requirements on the performances of its instruments. These are verified during the production phase. Therefore, emphasis has been put on the automation of the calibration (see section V.2) and validation (see section V.3) processes for large scale production of cameras.

In section V.1 I present the reconstruction of the arrival time and the number of photons

from the waveform signals. In section V.2, I describe the mandatory characterization, in the laboratory, of the different camera elements and of the full assembled camera. The characterization is performed using a likelihood maximization of the multiple photo-electron spectra of each pixel and for various light intensity. Compared to previous work, here the likelihood includes the optical cross-talk as modeled in [80]. It also combines the multiple photo-electron spectra of various light intensity to achieve better precision. The characterization of the camera elements is essential to understand the camera performance and define the methods and strategy to calibrate the signals at the site. For the calibration in the laboratory, the camera test setup (CTS) is a key element, therefore a brief description is also given there. The precision achieved for the measurement of the critical parameters is presented. Finally, the optical efficiencies of the camera elements are presented. In particular, the optical efficiency of the filtering window has been determined as function of wavelength and on its entire surface. In section V.3, I present two of the most important parameters to assess the camera performance, the charge and time resolution of the camera as a function of the impinging light intensity for different NSB levels. Finally, in section V.4, we describe the calibration and monitoring strategy envisaged to be performed on-site. The on-site calibration provides information about the trigger stability, the aging of the PDP components and the correction of the sensor bias voltage drop induced by the NSB.

The following work was published in the Journal of Instrumentation and can be found in [85]. The parts for which I mainly contributed are extracted.

V.1 Signal reconstruction

The main scope of the calibration of a SiPM based gamma-ray camera is to convert raw data expressed in Least Significant Bit (LSB) units into a number of photons per pixel and a respective arrival time. Ultimately, the number of photons and the reconstructed arrival time profile of an extensive air-shower event are used to determine the energy and direction of the primary particle. The precision at which they are measured is linked to the energy and angular resolution of the detector, respectively. The determination of the characterizing parameters of the camera is also relevant to accurately simulate the response of the camera to Cherenkov light. This is particularly relevant to estimate the performance of the telescope and properly infer the fluxes of gamma-ray sources. It is also relevant when energy and direction of the primary particle are reconstructed with machine learning algorithms, trained on Monte Carlo simulated images of extensive air-showers.

V.1.1 Reconstruction of the number of photons

The DigiCam FPGA features a ring buffer capable of storing up to 2048 samples at $f = 250$ MHz. Each sample is a 12-bit integer marked as W_k, with $k \in [0, 2047]$. When a trigger (internal or external) is satisfied, the raw signal waveform per pixel, which is composed by an ensemble of ring-buffer samples W_k, is acquired in a readout window, as it is shown in figure V.1. To reconstruct the number of photons, the raw waveform needs to be converted into a photon signal. The first step is to extract the number of photo-electrons $N_{p.e.}$ from the waveform of the pixel. The signal baseline is mainly due to the average uncorrelated noise, such as the dark noise or NSB. Therefore, it needs to be subtracted from each waveform, to extract the signal contribution. The baseline B is computed by

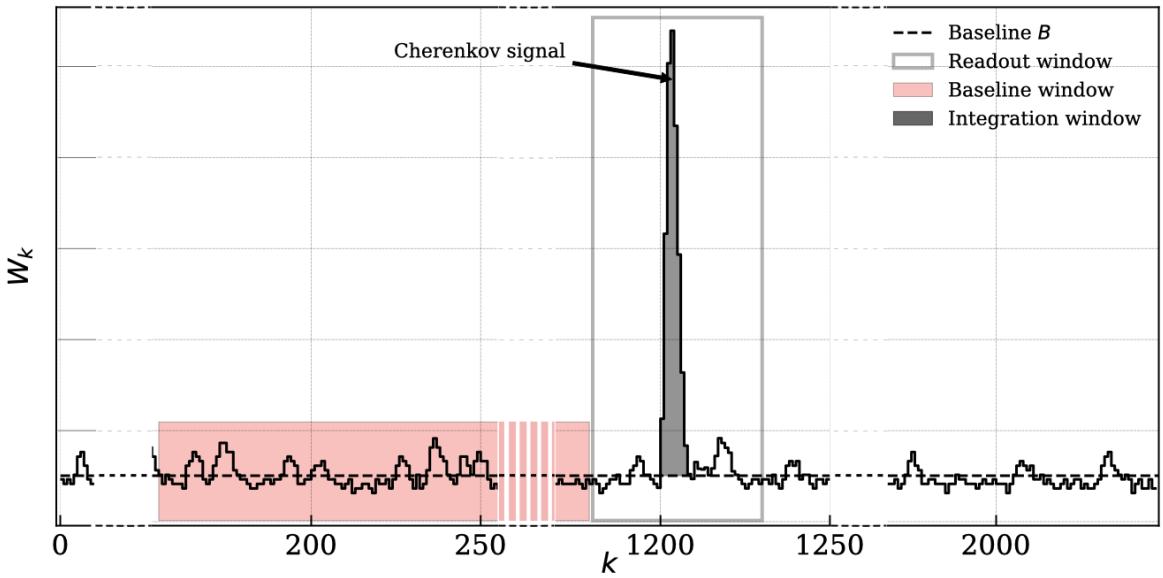

Figure V.1. Waveform scheme as seen in the ring buffer of DigiCam FPGA. The readout window contains between 50 and 91 samples depending on the used configuration. The charge is computed as the sum of the samples around the Cherenkov signal after the baseline subtraction (as in equation V.2). To be able to represent the full buffer size the waveform is truncated.

the DigiCam FPGA for each pixel as the average of the 1024 samples (4.096 µs) preceding the readout window of the triggered event (see equation V.1).

$$B = \frac{1}{1024} \sum_{k=i}^{i+1023} W_k; \tag{V.1}$$

$$N_{p.e.} = \frac{1-\mu_{XT}}{G} \sum_{k=j}^{j+f\Delta t} (W_k - B), \tag{V.2}$$

where i is an adjustable parameters of the DigiCam. It allows to adjust from which ring buffer sample k the baseline is calculated. This parameter is set such that the baseline is computed before the start of the readout window.

The baseline-subtracted waveforms are then integrated within the readout window over a duration Δt from the sample j, where j is the start of the integration window. The resulting value is converted into photo-electrons using the gain, G, and corrected for the average excess of photo-electrons induced by optical cross-talk μ_{XT}, as in equation V.2.[1] In order to maximize the signal-to-noise ratio, an optimal integration window of $\Delta t = 28$ ns was found.

Finally, the number of photons arriving at the camera photo-detection plane N_γ is obtained by correcting also for the window transmittance η_{window}, the cone collection efficiency η_{cones} (this includes the coating reflectance and geometrical fill factor) and the

[1] μ_{XT} represents the average number of total cross-talk avalanches initiated by a primary avalanche, while $\sum_{i=0}^{\infty} \mu_{XT}^i = \frac{1}{1-\mu_{XT}}$ is the total number of discharged micro-cells resulting from a primary avalanche.

photo-detection efficiency (PDE) of the SiPM sensor, η_{SiPM}:

$$N_\gamma = \frac{N_{p.e.}}{\eta_{window} \times \eta_{cones} \times \eta_{SiPM}}. \tag{V.3}$$

Since the PDP efficiency depends on the photon's wavelength, we refer to the efficiency of the various camera components η_{window}, η_{cones} and η_{SiPM} as their wavelength dependent efficiencies folded with the Cherenkov signal light spectrum.[2]

Among the calibration parameters defined above, the gain G, the baseline B and the optical cross-talk μ_{XT} are measured for each camera pixel. Therefore the number of photo-electrons $N_{p.e.}$ can be computed per pixel. On the contrary, the overall photo-detection plane efficiency η_{total} cannot be calculated for each pixel individually. As a matter of fact, the determination of N_γ requires to measure individually the SiPM photo-detection efficiency and the cone collection efficiency, which are quite time consuming procedures. However the transmittance of the camera window is determined on its entire surface (see section V.2.2.1). On the other hand, the relative pixel-to-pixel PDE can be determined using a diffuse light source, with a known irradiance profile (see section V.4.3), by comparing the reconstructed number of photo-electrons in each pixel. This relative efficiency is converted in an absolute efficiency, using a set of 12 reference-calibrated pixels (corresponding to a PDP module), whose optical efficiencies have been precisely measured.

It is important to stress that the SiPM gain, and therefore the overall gain G, the optical cross-talk μ_{XT} and the photo-detection efficiency of the SiPM, η_{SiPM}, depend on the operation voltage of the SiPM.[3] To prevent a high current to flow through the SiPM, which increases its temperature and in the long term might damage it, it is necessary to have a resistor at its bias stage which acts as a current limiter. The steady current produced by NSB light induces a voltage drop across the resistor, which reduces the operational voltage of the SiPM [104]. As a consequence, these parameters vary for different NSB levels. This voltage drop effect has been both modeled and measured [105] and it is corrected for in this analysis. For simplicity, the reported values in this work for G and μ_{XT} are given in the absence of any background light. Nonetheless, the necessary corrections are applied in the presence of background light.

V.1.2 Reconstruction of the arrival time of photon light pulse

For atmospheric showers, the typical time spread of the Cherenkov signal within a single pixel (on average $\sim$ 1.7 ns for diffuse cosmic ray protons with a spectrum of $E^{-2.7}$) is much shorter than the duration of the SiPM response signal (full width at half maximum $\sim$ 20 ns). Thus, the Cherenkov flashes collected in each pixel can be viewed as an instantaneous flash of light. Moreover, the flash of light produces a waveform with the same shape as a typical single photo-electron pulse, but with an amplitude and integral proportional to the number of photo-electrons producing it (in the linear range of the amplification chain). As a consequence, a typical normalized SiPM pulse or pulse template, $h(t)$, fitted to the waveform is used to determine the arrival time of the

[2]The efficiency of an optical component is $\eta = \frac{\int_0^\infty g(\lambda)\frac{dN}{d\lambda}\,d\lambda}{\int_0^\infty \frac{dN}{d\lambda}\,d\lambda}$, where $g(\lambda)$ is the transfer function of the optical component and $\frac{dN}{d\lambda}$ is the number of photons emitted by the source per unit wavelength λ.

[3]The overall gain G corresponds to the average signal charge produced by the full readout chain (SiPM, front-end pre-amplifying electronics, and back-end digitizing electronics) for one photo-electron.

photons. The procedure to derive the pulse template from measurements is illustrated in section V.2.1.3.

To extract the photon arrival time t', the waveforms (composed of $N_{samples}$ samples) and the template are normalized to their integrals around their maximum. One defines $k_{max} = \underset{k}{\text{argmax}}\, W_k$ as the sample where the waveform is maximum and $\hat{k}_{max} = \underset{k}{\text{argmax}}\, h(k/f+dt)$ as the sample of the maximum of the pulse template, sampled with the time offset dt with respect to the kth sample (sampled at $t_k = k/f$, where f is the sampling frequency of FADCs). The normalization coefficients A_W and $A_h(dt)$ are obtained with the sum over eight consecutive samples (three before the maximum and four after) for the waveform, once the baseline has been subtracted, as

$$A_W = \sum_{k=-3}^{4} (W_{k+k_{max}} - B) \tag{V.4}$$

and for the template as

$$A_h(dt) = \sum_{k=-3}^{4} h(t_k + \hat{k}_{max}/f + dt)\,. \tag{V.5}$$

The residual $r_k(dt)$ of the comparison of the normalized waveform with the normalized template is:

$$r_k(dt) = \frac{W_k - B}{A_W} - \frac{h(t_k + dt)}{A_h(dt)}\,, \tag{V.6}$$

while the estimated error is the normalized combination of the electronic noise σ_e and the uncertainty on the template $\sigma_{h(t)}$ with:

$$\sigma_k(dt) = \sqrt{\left(\frac{\sigma_e}{A_W}\right)^2 + \left(\frac{\sigma_{h(t_k+dt)}}{A_h(dt)}\right)^2}\,. \tag{V.7}$$

The $\chi^2(dt)$ obtained comparing the normalized pulse template and the normalized waveform is computed for different offsets dt of the template in time according to :

$$\chi^2(dt) = \frac{1}{N_{samples}} \sum_{k=1}^{N_{samples}} \frac{r_k^2(dt)}{\sigma_k^2(dt)}, \tag{V.8}$$

and the photon arrival time t', defined as the time where the fitted amplitude is maximum, is calculated as:

$$t' = \frac{k_{max}}{f} - \underset{dt}{\text{argmin}}\, \chi^2(dt)\,. \tag{V.9}$$

V.2 Off-site calibration strategy

V.2.1 Photo-sensor and electronics properties

V.2.1.1 The Camera Test Setup and its LED calibration

To assess the camera performance and extract all the relevant parameters of its calibration, the Camera Test Setup (CTS), shown in figure V.2, has been developed. The CTS is a

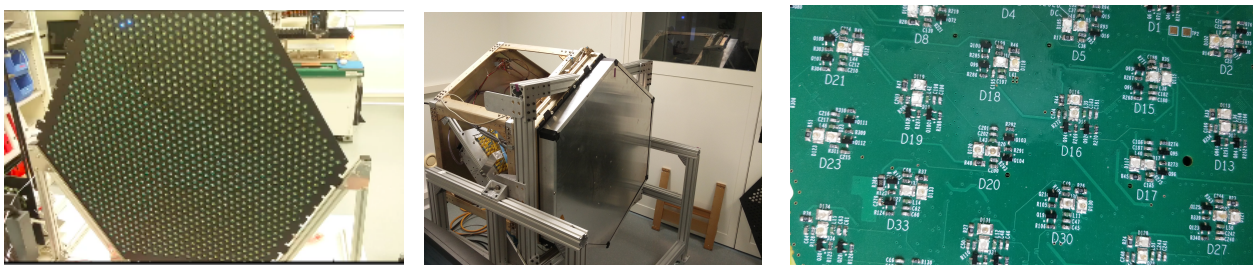

Figure V.2. From left to right: CTS seen from the LED side, from the back and details of the LED placement.

hexagonal structure that can be mounted in front of the PDP. It has been conceived to have each pixel of the camera facing two nearby LEDs, one operated in pulsed mode (AC LED), while the other in continuous mode (DC LED). For each pixel, the AC LED is meant to emulate the prompt Cherenkov signal produced by atmospheric showers, while the continuous DC LED emulates the NSB. The intensity of the AC LED can be controlled for patches of three neighboring pixels, while the continuous DC LED intensity is adjustable by groups of 24 pixels. The light intensity of the LED is controlled by a 10 bit DAC. The AC and DC LEDs have both a peak wavelength of $\lambda = 470$ nm (Broadcom / Avago ASMT-BB20-NS000). The AC LED is operated from 0 up to $\sim$ 8000 photons (about 2000 p.e.), while the DC LED is operated to emulate a NSB with frequency up to 1 GHz per pixel.

The CTS is fully programmable and controllable via an OPC-UA server controlled by scripts written in the ALMA Control Software [106] (ACS) framework. Its programmable feature allows injecting different kinds of patterns; therefore also simulated images of showers or muon rings can be injected in the CTS to test the camera performance and trigger algorithms.

The trigger signal and the communication bridge are provided to the CTS by DigiCam. Its mechanics have been optimized such that the CTS can be mounted on the camera without removing the shutter doors nor the protection window and still providing light tightness. The light tightness of the CTS allows to re-calibrate the camera on-site without needing to remove it from the telescope structure, thus saving on the maintenance time.

V.2.1.2 Acquisition and processing

The data are acquired as if the camera was mounted onto the telescope during standard observations: The camera is connected via the two 10 Gbps optical fibers (one for the data, one for the slow-control) to the camera server, where the acquisition software runs. All data acquisition components are controlled via ACS by the use of ACS scripts. This feature allows programming all steps of the measurement, from the light generation to the data recording. All measurements performed with the CTS use DigiCam as a trigger source that offers stable synchronization (estimated to be $\leq$ 100 ps) between the light pulses and the data acquisition. In addition to the event number, timestamp, and 1296 waveforms, each event contains:

1. 16 bit unsigned integers providing the baseline for each pixel computed as the average of the 1024 samples preceding the trigger decision (see equation V.1);

2. the sum of the baseline-subtracted waveforms from three neighboring pixels clipped at 8 bit;

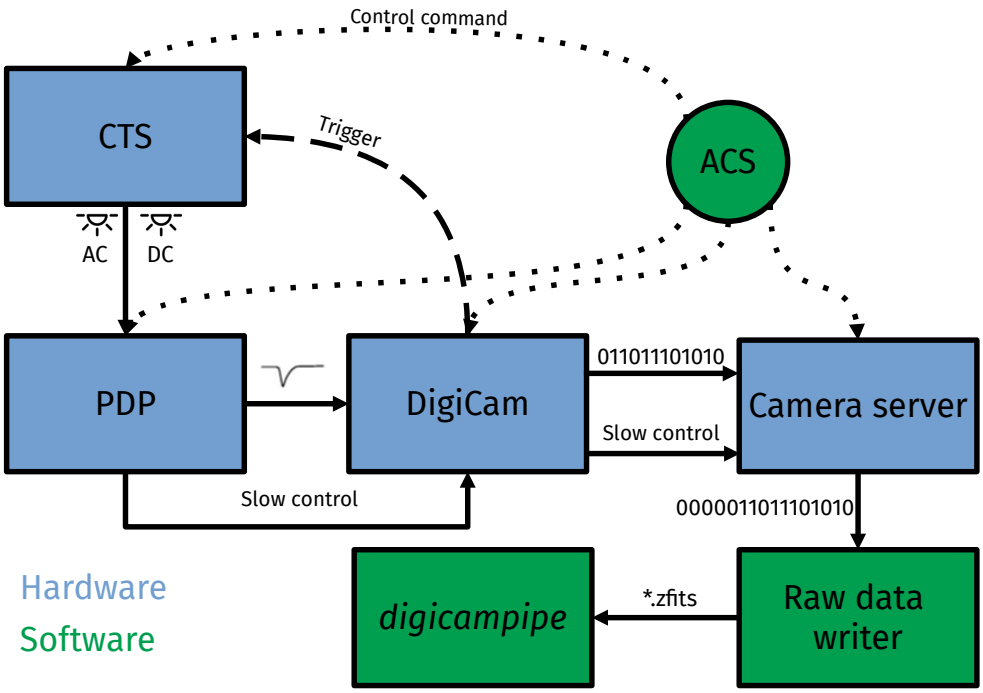

Figure V.3. Schematic of the CTS data acquisition setup.

3. 1 bit waveforms per cluster (a group of 7 triplets or 19) and per trigger algorithm, identifying when in the readout window the trigger condition was satisfied.

The first item provides a precise measurement of the baseline while the second and third allow studying the trigger. For example, they allow to measure the trigger efficiency as both external and internal triggers can be flagged as true for the same event.

The data analysis is performed using a dedicated software package *digicampipe* [107] developed by the SST-1M team.[4] The code contains calibration scripts, reconstruction and data quality pipelines for the SST-1M telescope. A schematic of this acquisition setup is shown in figure V.3.

AC/DC scan A scan of pulsed and continuous light-level is realized to infer the photo-sensor properties. A set (referred to as AC/DC scan in the following) of $N_w = 10^4$ waveforms, per pixel, for each level of pulsed and continuous light (AC and DC light) is acquired with the CTS. The AC light ranges from 0 up to $\sim 2 \times 10^4$ photons in $N_{AC} = 50$ levels, while the DC light ranges from 0 up to ~ 1 GHz equivalent night-sky background rate in $N_{DC} = 10$ levels. The scan without continuous light is used to determine the reference SiPM characteristic parameters. Using the single photon-counting capabilities of SiPMs, the average number of photo-electrons μ_j for the jth pulsed-light level can be determined allowing to calibrate the AC LEDs at the same time. The LEDs have been calibrated using the SiPM sensors in the pre-amplifier linear range ($N_{p.e.} \leq 600$ p.e.). In the non-linear range, the calibration of the LEDs is extrapolated using a calibrated photo-diode as described in [84]. Figure V.4 shows the calibration of a pair of LEDs.

[4]It has been constructed to be based on the core components of *ctapipe* [108], the reconstruction pipeline

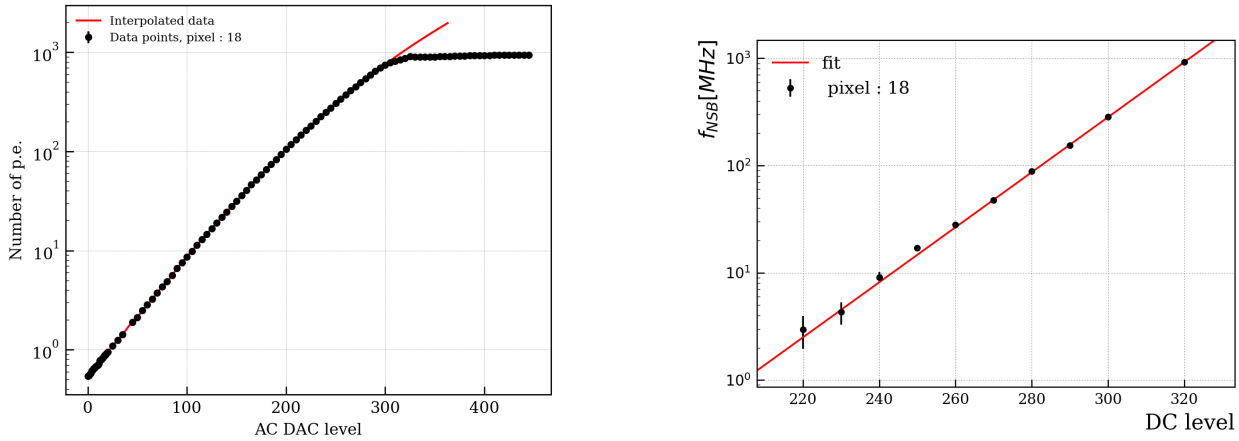

Figure V.4. Left: Pulsed CTS LED (AC LED) calibration curve for the LED pair numbered 18. The number of photo-electrons is obtained from the pulse amplitude in the linear regime of the amplification chain. They were extrapolated using a forth degree polynomial above saturation. Right: Continuous CTS LED (DC LED) calibration curve for the LED pair numbered 18.

Time delay scan Compared to the sampling frequency f = 250 MHz of the FADCs, the full width at half-maximum of the photo-electron pulse of ~ 20 ns is quite short, meaning that the rising and falling edges of the pulse typically fall within 5 samples (each of 4 ns). Therefore, for a given time delay between the flash of light and the readout window, the pulse waveform might not be sampled at its maximum. To artificially obtain a higher sampling frequency, the delay between the trigger and the readout window can be adjusted in DigiCam by steps of 77 ps over 32 steps. This allows to shift up to 2.464 ns (32×77 ps) the readout and trigger windows within the 4 ns sample of the FADC, therefore capturing nearly all features of the waveform. Low jitter and stable light source are required to be able to combine the waveforms for the different delays and obtain a precise pulse template for each pixel. This scan is referred to as the time delay scan in the following.

V.2.1.3 Analysis and results

Single photo-electron spectrum The single photo-electron spectrum (SPE) is derived from the charge distribution within the readout window in absence of external light source, therefore containing only thermal pulses. It is obtained in dark conditions, namely in the absence of AC and DC light. An example of a SPE is shown in figure V.5.

From the SPE, the number of events N_0, corresponding to the number of times no dark pulses were observed within the readout window, is obtained by fitting the SPE with equally spaced Gaussians. Using Poisson statistics the dark count rate (DCR) is given by (as in [87]):

$$DCR = \frac{< N_{pulses} >}{T_{window}} = \frac{-\ln\left(\frac{N_w}{N_0}\right)}{\frac{N_{samples}}{f}}, \tag{V.10}$$

software for CTA.

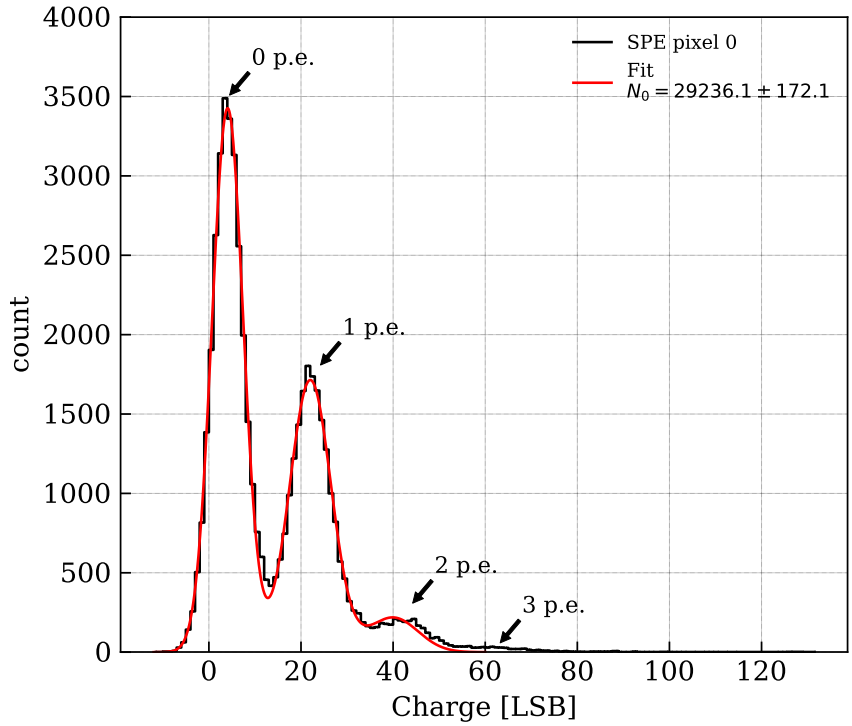

Figure V.5. Example of a single photo-electron spectrum fitted with equally spaced Gaussians.

where $< N_{pulses} >$ is the average number of dark pulses in a duration T_{window}, N_w is the number of waveforms acquired and $N_{samples}$ is the number of time samples recorded in each waveform. An average dark count rate of 3.08 MHz per pixel is observed (see figure V.6 (left)).[5] On the right of this figure, the dark count map over the plane of the camera is shown. A lower dark count rate can be noticed at the lower left edge of the camera, corresponding to a different batch production of the SiPMs. As expected, the dark count rate is correlated with temperature, as can be seen from figure V.9 (bottom right) and figure V.6 (right).

It should be noted that the dark count rate, as defined above, actually measures the number of thermal pulses above 0.5 p.e. Thus this value also includes after-pulses induced by dark counts with amplitude higher than 0.5 p.e. As the after-pulse probability is of the order of 2% [87] and the readout window used is long enough (T_{window} = 364 ns) the dark count rate is only slightly overestimated as can be seen from figure 15 in [87]. Since the dark count rate is about 13 times lower than the expected NSB rate at a high-quality observational site (e.g. the NSB rate in a moon-less night is about 40 MHz in Paranal, Chile), it is not relevant to obtain an DCR measurement unbiased by afterpulses. Moreover, the results are compatible with the ones reported in [87].

The rather high dark count rate observed in the SiPM, due to its large active surface of 93.6 mm^2, makes it difficult to extract with high precision the optical cross-talk and the gain. This is due to the high probability of having coincident uncorrelated dark count events. Therefore, to extract the calibration parameters the multiple photo-electron spectrum (MPE) is used as presented in the following section.

[5]Corresponding to 32.9 kHz/mm^2 at 26.5 °C

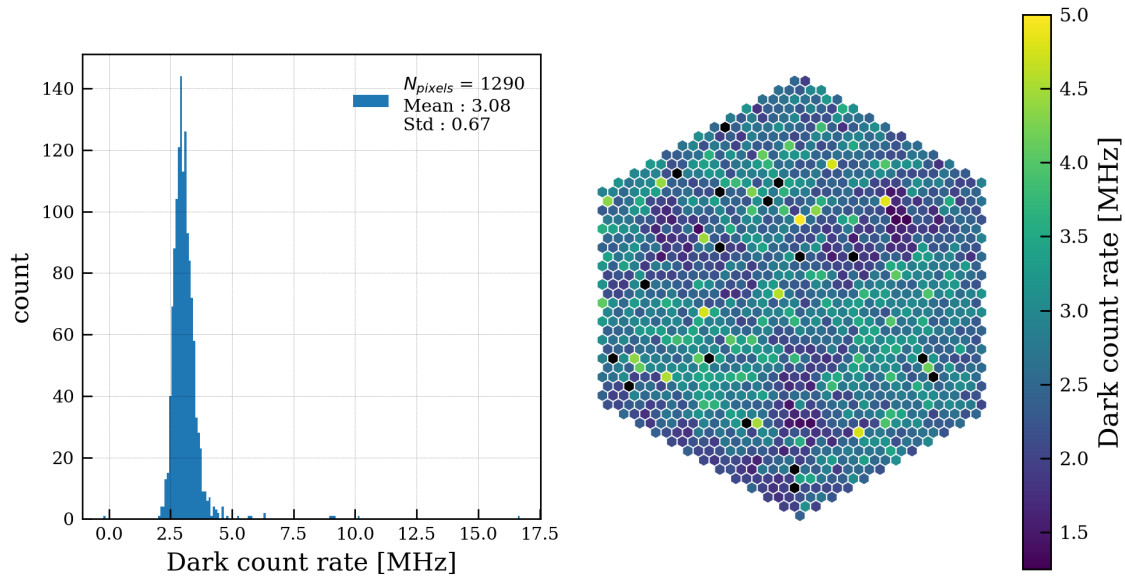

Figure V.6. Left: Dark count rate distribution over the camera pixels. Right: Dark count rate viewed for each pixel.

Multiple photo-electron spectrum To extract the gain G, the optical cross-talk μ_{XT}, the SiPM gain smearing σ_s and the mean number of photo-electrons μ_j of the jth pulsed light level for each pixel, the single photon counting capability of the SiPM is used. The reconstructed charge C distribution of prompt signals from the AC LED can be expressed with a smeared generalized Poisson distribution as in [80]:

$$P(C_j = x) = \sum_{k=0}^{\infty} \frac{\mu_j(\mu_j + k\mu_{XT})^{k-1}}{k!} e^{-\mu_j - k\mu_{XT}} \frac{1}{\sqrt{2\pi}\sigma_k} e^{-\frac{(x-kG-\bar{B})^2}{2\sigma_k^2}} \tag{V.11}$$

$$\text{with} \quad G = \bar{G}\int_0^{\Delta t} h(t)dt, \tag{V.12}$$

$$\sigma_k^2 = f\Delta t\sigma_e^2 + kG\sigma_s^2, \tag{V.13}$$

where σ_e is the electronic noise per time slice, $\bar{G}$ is the amplitude of a single photo-electron signal and $\bar{B}$ is a free parameter allowing to center the first photo-electron peak to a null value, that can be interpreted as the residual charge after baseline subtraction as defined in section V.1.1.

A maximum log-likelihood estimation (MLE) on a smeared generalized Poisson distribution is applied to the charge spectrum (or multiple photo-electron spectrum) of each pulsed light level j acquired, where the log-likelihood is defined as:

$$\ln \mathcal{L}(\vec{\theta}) = \frac{1}{N_w}\sum_{i=1}^{N_w} \ln P(\vec{\theta}; C_{ij}), \tag{V.14}$$

with $P(\vec{\theta}; C_{ij})$ defined from equation V.11 and represents the likelihood of the parameters $\vec{\theta}$ given the observed charge C_{ij} of the ith waveform and the jth AC light level. All fit parameters $\vec{\theta}$, except the mean number of photo-electrons μ_j, are not changing with the amount of light emitted by the LEDs. Therefore the fit results for each input pulsed light

level should be consistent. To achieve that the log-likelihood $\ln \mathcal{L}$ is further reduced by summing over the pulsed light level j:

$$\ln \hat{\mathcal{L}}(\vec{\theta}) = \frac{1}{N_w N_{AC}} \sum_{j=1}^{N_{AC}} \sum_{i=1}^{N_w} \ln P(\vec{\theta}; C_{ij}). \tag{V.15}$$

By combining the MLE of each light level, the number of fit procedures is reduced from N_{AC} to 1 and the number of independent fit parameters from $6 \times N_{AC}$ to $N_{AC} + 5$. The number of fit parameters can be again drastically reduced by imposing that the sample mean $< C_{ij} >_i$ and the mean number of photo-electrons μ_j follow the relation derived from the mean of the smeared generalized Poisson distribution (in equation V.11):

$$\mu_j = \frac{< C_{ij} >_i - \bar{B}}{G}(1 - \mu_{XT}) \tag{V.16}$$

The overall reduction and simplification of the MLE increases the robustness of the fit and reduces the chances of falling into local minima. The number of independent fit parameters is, in the end, reduced to 5 (the gain G, the optical cross-talk μ_{XT}, the electronic noise σ_e, the gain smearing σ_s and the residual baseline $\bar{B}$). It allows to fit consistently the MPE from the lowest light levels, where the photo-electron peaks are clearly distinguishable, up to the highest light level, where one cannot resolve single photo-electrons.

Figure V.7 shows four distinct light levels of the same pixel together with the fit results. Only the mean light level μ_j differs from one distribution to the other, all other parameters being common.

This method has been applied to all the camera pixels individually. The distributions of the fit parameters are shown in figure V.8 and V.9 and summarized in table V.2. The results were obtained after the first round of gain equalization of the full readout chain using the FADCs variable gain (described in section V.2.1.3). We observe an average optical cross-talk of 0.08 p.e. (this value corresponds to the average number of cross-talk photo-electrons induced by a single avalanche) which is comparable to the measurements performed in [87] (10% optical cross-talk at the operational voltage). A higher optical cross-talk is observed on the left edge of the camera. This part corresponds to the second batch of production of SiPMs. The differences observed are within the producer specifications (typical value 8% optical cross-talk, maximum value 15% optical cross-talk). It also highlights the precision at which the optical cross-talk can be determined ($\leq$ 0.01 p.e.). A similar pattern is observed for the SiPM gain smearing on the same part of the camera. In that case, the gain smearing is lower, consequently the photo-electron resolution ($\sim$ 0.09 p.e. on average) is improved. Lower values of gain smearing can be also observed at the camera center because the SiPM with the best photo-electron resolution were mounted on purpose at the camera center for better image resolution. An average electronic noise of 16% of a single photo-electron signal is observed. The baseline residual, on average, is of the order of 1.17 LSB, which translates to a systematic underestimation of the baseline evaluated by the DigiCam FPGAs of 5.7% of the photo-electron amplitude. This can be explained by the 16 bit limitation of the baseline computation and rounding effects. Nevertheless the systematic baseline offset can be coped off-line by adjusting the baseline value provided by DigiCam accordingly.

The systematic biases of the parameters measured from multiple photo-electron spectra, described in this section, is determined using a Monte Carlo simulation. The Monte

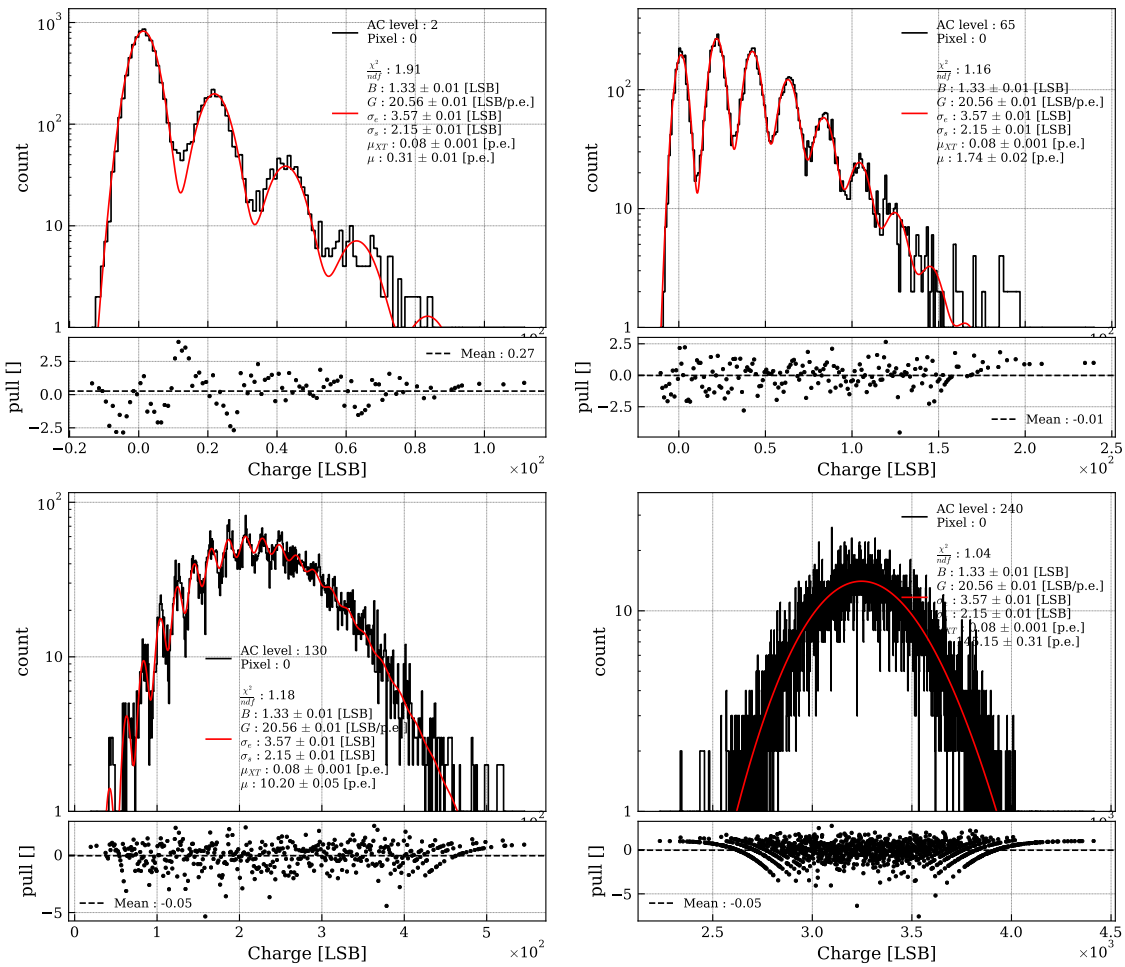

Figure V.7. Multiple photo-electron distributions, of pixel 0, acquired with different light levels. It shows four distinct light levels: 0.31 p.e. (top left), 1.74 p.e (top right), 10.2 p.e. (bottom left) and 145.15 p.e. (bottom right) fitted with the probability density function defined in equation V.11. The fit for these light levels is performed in a combined way by maximizing the log-likelihood defined in equation V.14. The reduced chi-squared for each fitted spectra is reported individually as an estimate of the goodness of fit.

Carlo is designed to reproduce the PDP response to a prompt light-source and a continuous background light-source. The Monte Carlo simulates the baseline and its fluctuations due to NSB, dark count rate and electronic noise. It simulates also the amplification chain gain and gain smearing. The Poisson fluctuations and optical cross-talk are also simulated. It is similar to the one described in [84] but it includes optical cross-talk as modeled in [80]. The result shows that the bias increases with an increased thermal noise rate. In particular, the relative differences between the true and reconstructed parameters for a dark count rate of 3.08 MHz (observed average dark count rate for the off-site calibration) shows negligible systematic error and good resolution in the reconstructed parameters (see table V.1). Moreover, the bias induced in the reconstructed number of photo-electrons, from equation V.2, is of the order of 1% (assuming a typical value for optical cross-talk of 0.08 p.e.).

The distributions of the calibration parameters can be used to identify outlier pixels. Pixels for which at least one of the six calibration parameter values shows a 5 standard deviation from the camera-averaged value are flagged. In figure V.9 the identified outlier

Table V.1. Results of the systematic study of the calibration parameters for a dark count rate of 3.08 MHz

	G	σ_e	σ_s	μ_{XT}	μ
Relative resolution [%]	≤ 0.1	1	7	9	1
Relative systematic error [%]	≤ 0.1	1	2	4	1

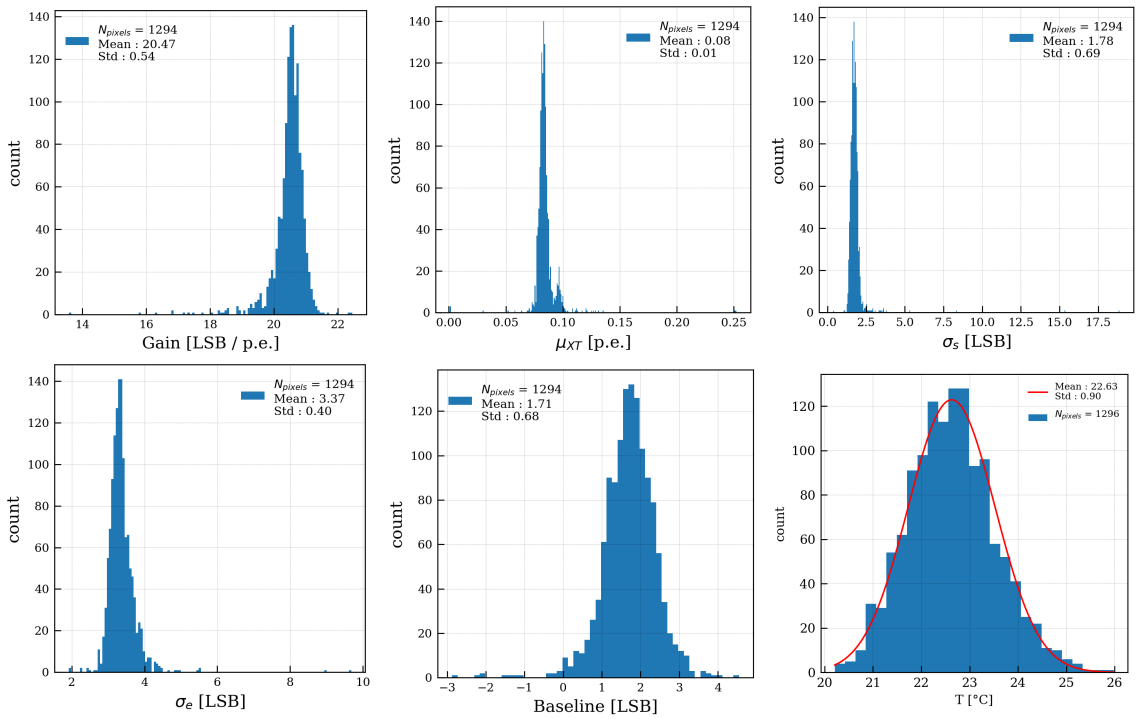

Figure V.8. Measured fit parameter distributions for all the 1296 pixels. In reading order, the gain G, the optical cross-talk μ_{XT}, the gain smearing σ_s, the electronic noise σ_e, the baseline residual $\bar{B}$ and the average temperature of the SiPMs during the measurements are shown.

pixels are drawn in black. It can be seen that two outlier pixels are identified for each calibration parameter. For these pixels the MPE spectrum cannot be obtained, because the corresponding AC LEDs on the CTS are damaged. Furthermore, among the 1296 pixels, none showed to be inoperable. A few pixels have a lower gain than the central value or poor photo-electron resolution. But these out-off-spec pixels have been characterized ensuring raw data to photo-electron conversion.

Gain equalization To reach a uniform signal response of the camera, each one of the 1296 read-out channel are equalized in gain. Each SiPM is provided with its operating voltage and a compensation loop on the slow control boards is implemented to cope with breakdown voltage changes with temperature, as described in [88]. To further improve signal uniformity the DigiCam allows to adjust the FADC gain by steps of 0.01% for each readout channel within ±5% (see [84, 109] and [110] for more details) .

A gain uniformity of 2.6% is achieved after one round of equalization as can be seen in figure V.8. The gain is measured as described in section V.2.1.3. The updated gains are

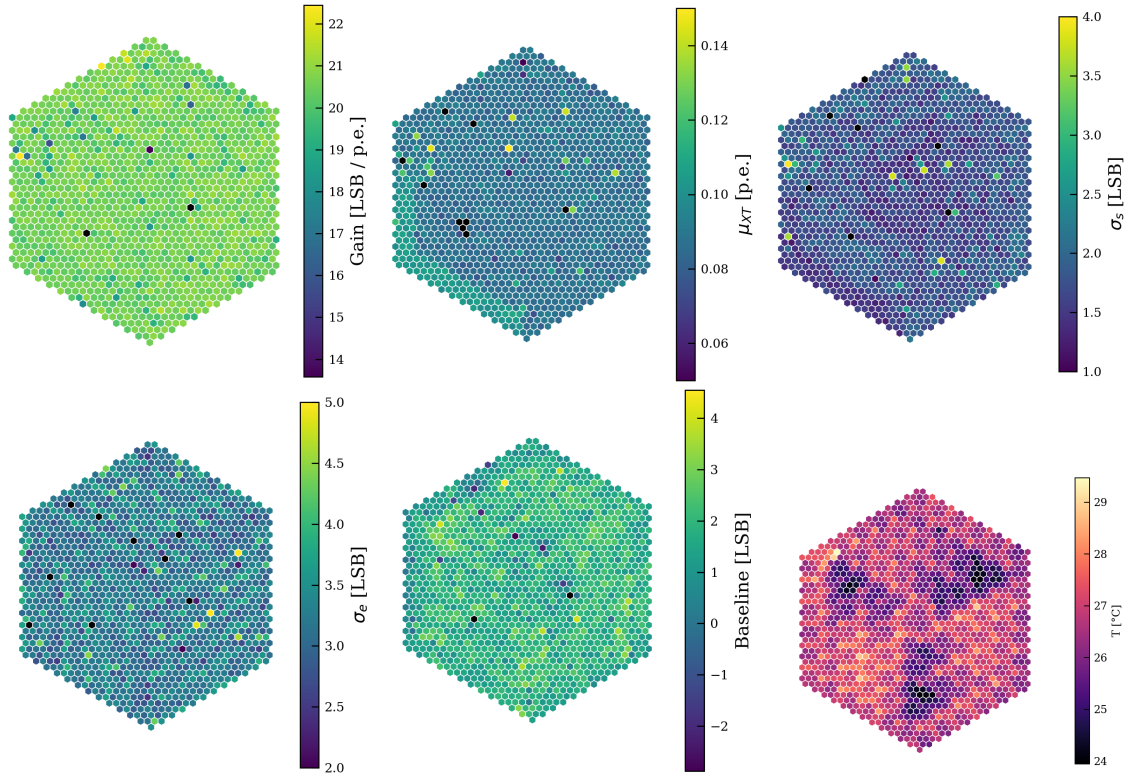

Figure V.9. Measured fit parameter maps across the camera. In reading order, the gain G, the optical cross-talk μ_{XT}, the gain smearing σ_s, the electronic noise σ_e, the baseline residual $\bar{B}$ and the average temperature of the SiPMs during the measurements are shown. The pixels appearing in black are considered as outliers.

Table V.2. Summary of the fit results.

Parameters	Units	Mean	Std	Spread [%]
Gain	[LSB/pe]	20.47	0.54	2.6
μ_{XT}	[p.e.]	0.08	0.01	12.5
σ_s	[LSB]	1.78	0.69	38.8
σ_e	[LSB]	3.37	0.40	11.81
Baseline residual	[LSB]	1.17	0.68	58.12
Dark count rate	[MHz]	3.08	0.67	21.7
T	[°C]	26.45	0.82	3.1

equalized to the previously measured camera average gain. The uniformity can be further improved with many iterations, but a larger data sample is needed to achieve a precision below the percent level. The gain correction coefficients are loaded at each boot of the camera. This equalization process can also be regularly performed on-site, with the CTS mounted in front of the camera.

DigiCam also permits to equalize the baseline of each FADC within ±138 LSB.

The method is similar to the one applied for the gain equalization. The baselines were measured in dark conditions with the SiPMs at their operational voltage over a collection of ten thousand waveforms of 50 samples each.

Pulse template As can be seen in section V.1.2, the pulse template $h(t)$ is used to reconstruct the timing information of the signal. It is also used for Monte Carlo simulations of the telescope as it describes the typical signal response to a single photo-electron signal. In addition, it provides a conversion factor between a single photo-electron amplitude $\bar{G}$ and single photo-electron integrated charge G, as can be seen from equation V.12. Moreover, to be able to extract charge and timing information the pulse template characterisation in the saturation region of the pre-amplifier and of the FADC is important.

The time delay scan, discussed in section V.2.1.2, is used to evaluate the pulse template. The flashes of the CTS are triggered by the camera and a delay is adjusted by steps of 77 ps to vary the position of the light pulse in the sampling window. Given that each LED has a different response to a given DAC value and that the DACs control groups of neighboring pixels, the homogeneity of the light is not guaranteed with the CTS. Therefore, the timing scan is done by scanning the AC DAC level to ensure that most of the pixels are illuminated between 50 and 400 p.e. This light level range ensures a good signal-to-noise ratio and no saturation.

For each camera pixel and each flash of light, a charge estimation is done summing up the FADC samples in a large enough window to fully contain the pulses for all LEDs, despite the offset in time between LEDs of the CTS. A large number of samples allows also to detect saturation when the pulse amplitude flattens, but the pulse width increases as shown in figure V.10.

Pulses whose estimated charges are between 50 and 400 p.e are added to a single 2D histogram (combining all pixels). The histogram is binned as a function of the time of half maximum amplitude and as a function of the normalized amplitude (normalized by the estimated integral charge). The template value and its uncertainty are taken as the mean and standard deviation of the normalized amplitude of each bin of time with significant number of entries. Figure V.10 shows the obtained average template.

V.2.2 Optical element properties

The efficiencies η_i of the different optical components (namely the light funnels, the SiPMs and the entrance window) have been measured for the wavelengths in the range of the spectrum of Cherenkov emission in the atmosphere. The efficiencies as a function of the wavelength are shown in figure V.11 (left) together with the product of the efficiencies (in red). Their measurements provide the photo-electron to photon conversion factor, as illustrated in equation V.3. The average efficiencies for all elements, convoluted with the Cherenkov spectrum over the wavelength range 300 nm to 550 nm (as defined in the

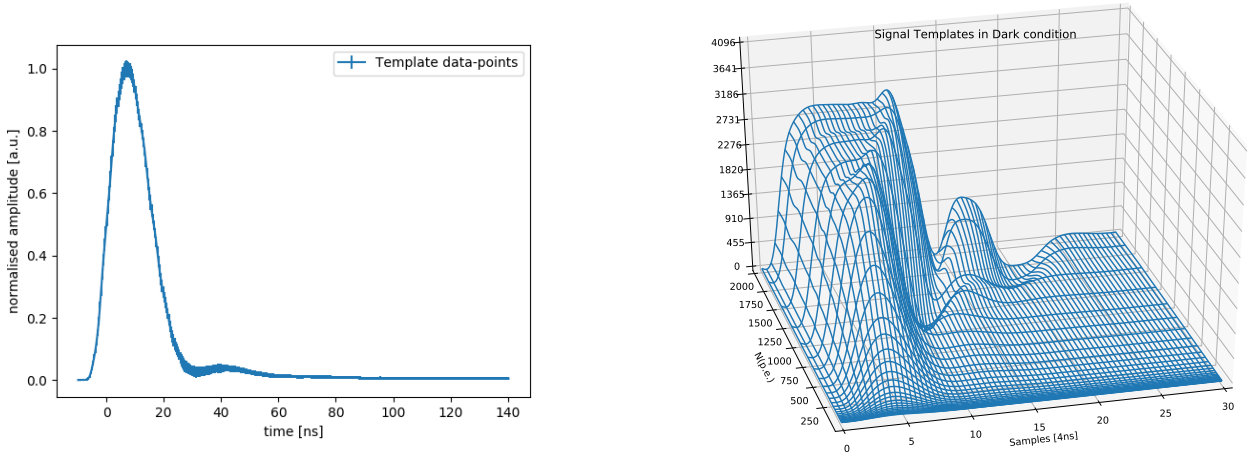

Figure V.10. Left: Average normalized pulse template for the whole camera between 50 and 400 p.e. The error bar width corresponds to the standard deviation of the measurement for all pixels and all flashes. Right: Pulse template as a function of the number of photo-electrons.

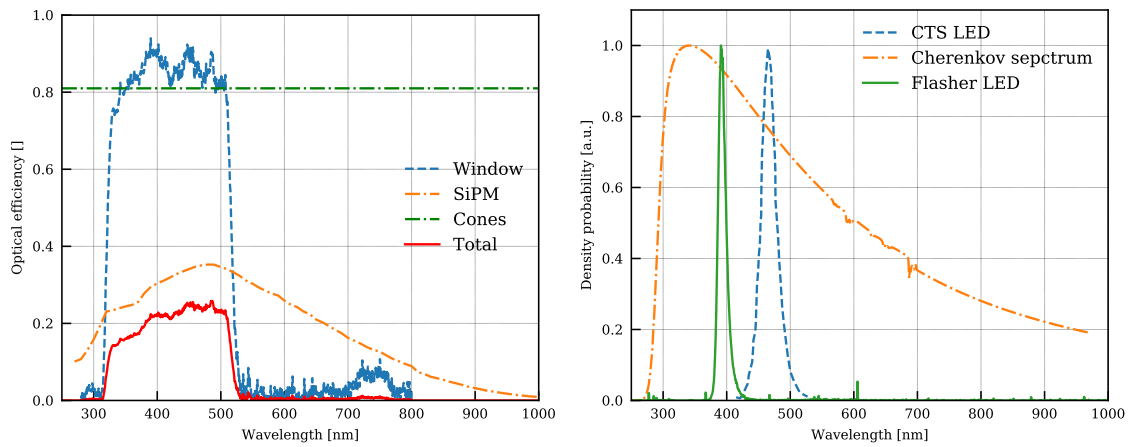

Figure V.11. Left: Transmittance of the filtering window (blue), photo-detection efficiency of the SiPM (orange), the collection efficiency of the cones (green) and the overall efficiency (red) as a function of the wavelength. Right: Spectra of the calibration devices measured with a spectro-photometer (AvaSpec-ULS3648) and the CTA reference Cherenkov light spectrum in the atmosphere.

CTA requirement B-TEL-1170), are provided in table V.3. Also the total PDP efficiency, $\eta_{total} = \eta_{window} \times \eta_{cones} \times \eta_{SiPM} = 17\%$, is indicated.

The average optical collection efficiency for the light concentrators below the cut-off angle corresponds to 0.88 for the Cherenkov light spectrum. Taking into account a geometrical fill factor of 0.92 the average collection efficiency of the cones reduces to $\eta_{cones} = 0.81$. The verification of the cone performance cannot be done for each individual camera cone, being too time consuming. For this, in the validation phase of the technique (described in [82]), the uniformity of the quality over a batch of production has been verified allowing to qualify a batch just measuring few samples. The photo-detection efficiency (PDE) for SiPM is very uniform across each silicon wafer and overall for SiPMs of the same type, being solid state device produced with well controlled and reproducible

Table V.3. Window transmittance η_{window}, cone collection efficiency η_{cones}, SiPM efficiency η_{SiPM} and total efficiency η_{total} for the Cherenkov light spectrum from 300 nm to 550 nm (as defined in the CTA requirement B-TEL-1170). In this range the CTA requires $\eta_{total} \geq$ 20%).

	Cherenkov Spectrum (300-550 nm)
η_{window}	0.68
η_{cones}	0.81
η_{SiPM}	0.29
η_{total}	0.17

techniques over the same batch of production. In addition, the manufacturer has to comply with precise specification on the spread in breakdown voltage between the four channels of a single SiPM (< 0.3 V). The PDE measurement done to characterize our sensor are described in detail in [87].

Table V.3 gives the average efficiencies, but as shown in figure V.12 (right), the optical efficiency varies from pixel to pixel. These differences need to be evaluated to properly reconstruct the number of photons in each pixel (flat-fielding). The flat-fielding correction is one of the main goals of the on-site calibrations (see section V.4). This operation can be done at the site using an external light source, mounted at the center of the mirror dish, which illuminates the camera with a given known photon intensity. The number of photo-electrons in each camera pixel is measured and corrected for the light in-homogeneity. This in-homogeneity was measured in the laboratory using a calibrated photo-diode (see section [85]). Therefore, the relative differences in the number of reconstructed photo-electrons between the camera pixel gives a flat-fielding correction. The flat-fielding correction comprises the window transmittance, the cone collection efficiency and the SiPM PDE.

V.2.2.1 Window transmittance

N.B The work presented in this section was the work of the master thesis of N. de Angelis which can be found in [111]. Here the results are reminded and discussed in the context of the overall camera efficiency.

Coataing the window is a complex process for such large optical elements as the window ($\simeq$ 0.81 m^2), given the scarce availability of large coating facilities. Additionally, it is extremely challenging to produce uniform coating layers over large surfaces, in order to guarantee uniform transmittance. To correct the images for disuniformities, the measured transmittance as a function of the wavelength and position across the window can be used. Figure V.12 (left) shows the camera with the window installed on it.

To optimize the coating uniformity, the window rotates in the coating chamber around its center and therefore, the coating profile has a radial symmetry. Consequently, in principle it is sufficient to measure the transmittance only from one corner to the center, given the rotation symmetry. However, in [41], this hypothesis was verified by measuring the 6 diagonals of the hexagonal window.

The window transmittance as a function of the wavelength is illustrated in figure V.11 (left) and it is consistent with the expected design specifications. Further details on the

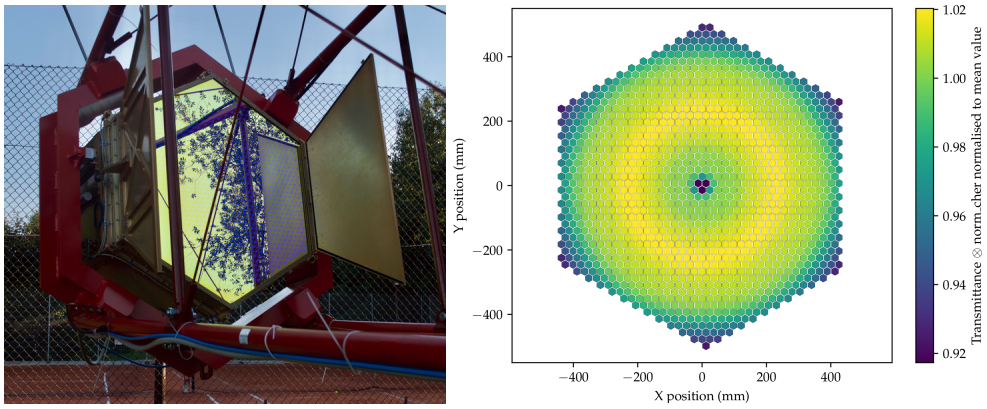

Figure V.12. Left: The SST-1M camera equipped with its filtering window on the telescope structure in Krakow. The yellowish color of the reflected image is due to the window coating, which cuts off light beyond 540 nm, which is then reflected out of the camera. The filter is optimized for transmission in the blue. It also reduces Fresnel losses with an anti-reflective layer. Right: Relative efficiency of transmission for the Cherenkov light spectrum from 300 nm to 550 nm per camera pixel with respect to the average value over all pixels.

window transmittance can be found in [111]. The multi-layer coating optical transmittance property depends on the light incidence angle. However, the maximal incidence angle of the light on the window is 25° and the wavelength transmittance shift is negligible. The window is effective in reducing the NSB as the expected rate, for a dark night, in each pixel is about 40 MHz (from 200 nm to 1000 nm) thanks to the low pass filter coating. As a matter of fact, with a simple window without any filter, even with a more UV transparent material as PMMA, the NSB would have been about 3.75 times bigger. The non-uniformity among the six diagonals as a function of the distance to the center was measured to be lower than 2%. Therefore, the average radial profile was used to generate the window transmittance map. From this map, the relative per-pixel correction was derived and is shown in figure V.12 (right). These corrections can be used to derive the per-pixel $\eta_{\mathrm{SiPM}} \times \eta_{\mathrm{cones}}$ value from a measurement with uniform illumination or using muon ring images on-site (as described in [112]).

V.3 Characterization of the camera performance

V.3.1 Charge resolution

The charge resolution plays a crucial role for the energy resolution of the telescope. The number of photons impinging on the camera and the density of photons at ground are directly related to the primary gamma-ray energy starting the electromagnetic shower. It is therefore fundamental to assess the error in reconstructing the number of photons and that this estimate is not affected by any systematic effect. The charge resolution is ultimately limited by the nature of the source, which has Poisson fluctuations in the emitted number of photons. It also takes into account the resolution of the camera photo-sensors, pre-amplifying electronics and data acquisition chain.

The data analysis performed here is similar to the one described in [84], but we

now perform the measurement for each of the 1296 camera pixels and express results in photon units rather than photo-electrons. The results are also compared against the CTA requirements.

The charge resolution CR is defined as the ratio between the variance and expected value of the reconstructed charge in units of photons:

$$CR(N_\gamma) = \frac{Var(N_\gamma)}{\mathbb{E}(N_\gamma)} \tag{V.17}$$

where, the variance and expected value are computed as standard deviation and mean of the acquired sample. The charge resolution presented here takes into account: Poisson fluctuations of the LED source, electronic noise from the photo-detection plane, SiPM gain smearing, optical cross-talk, precision of the computed baseline, and non-linearity of the amplification chain.

In order to meet the requirements on the dynamic range (0-2000 p.e.) and on the charge resolution (see figure V.13) and in order to have a single amplifying channel per pixel, which is mandatory to keep the cost and the power consumption reasonable, the analogue stage has to saturate. The saturation of the response allows to reach the required charge resolution across the whole dynamic range, while the signal shape remains within the 12-bits range of the FADCs. This feature allows to retrieve as much information as possible from the digital pulse, which would be lost in the case of a digital saturation. For this reason, the measurements of the gain G obtained from the MPE fit are reliable only in the linear regime. In figure V.13 (left), the pulse integral as a function of the number of p.e. was extracted. As can be seen in figure V.10, the pulse shape is conserved up to saturation. A saturation threshold of 600 p.e. (respectively 3500 LSB) on average for all pixels is obtained. It is defined as a deviation from $> 20\%$ of a linear extrapolation of the slope G, which is determined in section V.2.1.3. To cope with the saturation of the readout chain the waveform integration window is extended, as the pulse width increases with increased light intensity.

The estimated number of photons sent by the LED is obtained from the number of photo-electrons μ_{ij} extracted from the MPE spectrum fit described in section V.2.1.3. The number of photons is then assessed by correcting for the efficiencies of the SiPMs, the filter window transmittance and the light concentrators as in equation V.3. The effect of voltage drop from the NSB (see [105]) is also taken into account in the correction of the number of photons.

The charge resolution, presented in figure V.13 (right), has been measured with the AC/DC scan data. The solid lines represent the average resolution over the camera pixels and the contoured area represents its 1-σ deviation. The theoretical Poisson limit (fluctuations of the light source) is shown as a black dashed line. The charge resolution is given for two distinct NSB rate levels, given as a rate of photo-electrons per pixel in MHz. The effects of the saturation can be seen at around four thousand photons but are well coped with as the resolution does not drastically worsen.

V.3.2 Time resolution

The AC/DC scan data are also used to evaluate the time resolution of the camera pixels. The CTS LEDs were triggered by the camera in order to have the light pulse always in the same position within the sampling window. The reconstructed time t′ is obtained

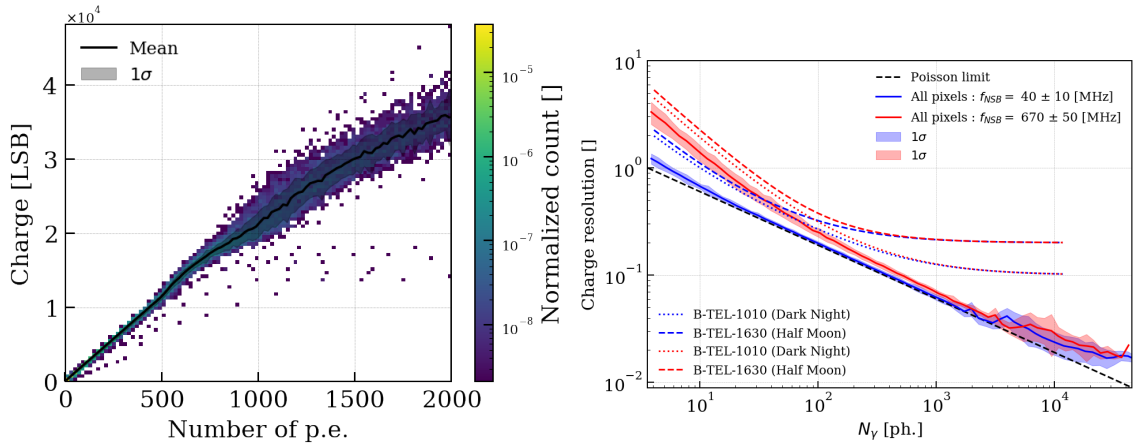

Figure V.13. Left: Charge linearity of all pixels. Right: Charge resolution in photons for all pixels and for two distinct NSB rates per pixel. The ranges of NSB rate correspond to dark sky conditions at 40 MHz, and a half Moon night at 670 MHz in Paranal, Chile. The CTA requirement curves, B-TEL-1010 and B-TEL-1630, for the small-sized telescopes of CTA are also drawn with dotted and dashed lines, which correspond to two data processing levels .

from the χ^2 minimization as defined in equation V.9. It is calculated over the time window every $dt = 0.1$ ns (as smaller steps did not improve the results), for each pixel and each flash of light. The time with the lowest χ^2 is chosen as the reconstructed time t' for the event. The time resolution for each pixel is obtained as the standard deviation of the sample. Flashes of light whose measured amplitude are below 2.5 p.e. are not used in order not to affect the estimate of the time resolution with thermal noise and NSB.

This measurement is repeated for several LEDs pulse amplitudes and the corresponding number of p.e. is derived using the LED calibrations (see figure V.4). Figure V.14 shows, for the whole camera, the evolution of the time resolution as function of the charge ($N_{p.e.}$) for 0 and 125 MHz NSB rate. As can be seen, the time resolution, without any NSB, is always below 1 ns and reaches 0.1 ns at 400 p.e. At 125 MHz of NSB, the resolution is mainly affected below 50 p.e. and goes above 1 ns only for pulse amplitudes below 7 p.e. (30 photons).

V.4 On-site calibration strategy

During the summer 2018, the SST-1M camera was mounted on the SST-1M telescope at IFJ PAN in Kraków. This period allowed to commission the telescope and perform preliminary science observations. The site conditions are, however, not adequate to perform gamma-ray astronomy nor calibration tasks. In fact the telescope is located within the institution area and is exposed to many sources of background light: street lights; office lights; nearby airport; nearby national road. The NSB light rate per pixel was estimated to range between 0.5 GHz and 1.5 GHz depending on the cloudiness of the sky [83]. When compared to the darkest nights, at the foreseen CTA southern site, this is at least 12.5 times higher. Additionally, the external light source was not yet mounted on the telescope structure. For these reasons most of the calibration tasks at the site could not be performed. In 2021, the telescope will be installed at the Ondřejov Observatory in

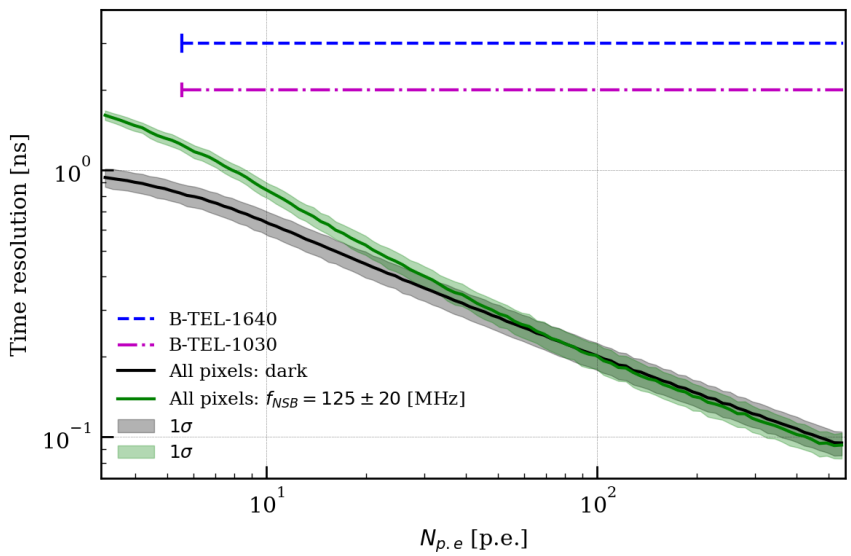

Figure V.14. Time resolution of all pixels as a function of the number of photo-electrons in dark conditions (black) and with 125 MHz NSB (green). The time resolutions are compared to the CTA requirements as a reference for 125 MHz NSB and two data processing levels (B-TEL-1640 and B-TEL-1030).

Czech Republic. Following this, the on-site calibration tasks, described in the following, will be performed there.

The goal of the on-site calibration activities is to monitor that the calibration parameters, listed in table V.2 and table V.3, extracted off-site and used for the image reconstruction still apply when operating at the site. Moreover, it also allows to determine the flat-field coefficients. To do so, three event types can be used for each observation night, i.e. muon events, dark count events and external light source events.

Muon events (see section V.4.1) allow to monitor the stability over time of the optical throughput of the telescope, providing an overall correction factor for telescope shadowing, mirror reflectivity, window transmittance, cone collection efficiency and sensor PDE.

The dark count events (see section V.4.2) allow to reproduce data that were acquired in the laboratory and can, therefore, be directly compared to it. If a significant discrepancy between on-site and laboratory results is observed, the parameters in equation V.2, used to reconstruct the number of photo-electrons, have to be re-evaluated to ensure unbiased photo-electron reconstruction.

The external light source events (see section V.4.3) are affected by the ambient background light (typically 40 MHz night-sky background for a moon-less night), which means that SiPM parameters cannot be extracted as done in section V.2.1.3. However, provided that the light source has been thoroughly characterized, it allows the monitoring of the model presented in [104] and the extraction of the flat-field coefficients to equalize the trigger among the pixels as presented in section V.4.3.2.

Additionally, as mentioned in section V.2.1.1, the CTS can be used on-site for a re-calibration or to identify components that need replacement. The re-calibration can also be performed yearly independently of any corrective maintenance activities.

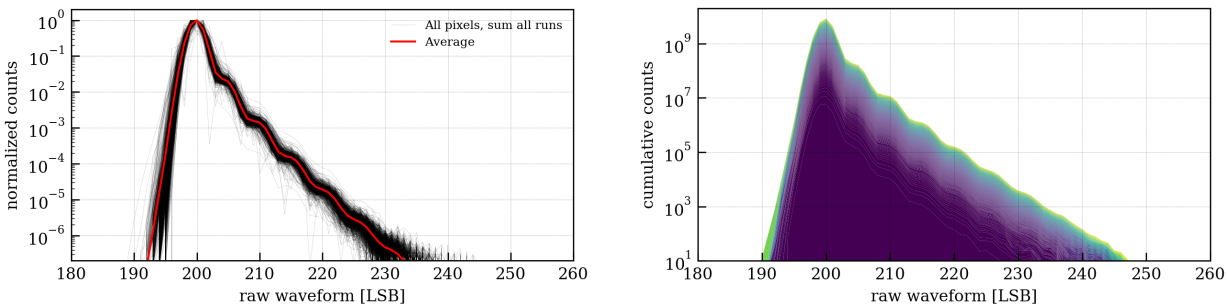

Figure V.15. Left: Normalized distribution of the projection of the raw waveform in LSB for all the pixels and one run. Right: Merged distribution of all pixels and all nights.

V.4.1 Muon events

Muon events, which produce ring images or arc images in the camera plane, are expected to be triggered with the same trigger configuration as the one used for the atmospheric showers. Dedicated muon triggers, more adapted to the ring-like structure, are possible to tag the muons on-line without requiring any data processing. The overall optical efficiency of the telescope can be assessed by comparing the expected number of photons within a muon image (assessed from Monte Carlo simulations) to the reconstructed number of photo-electrons within the muon image. The method is widely used in the current generation of IACTs as can be found in [113, 114, 115]. A dedicated study for the SST-1M telescope was carried on and is presented in [112].

V.4.2 Dark count events

The dark counts events are acquired at a fixed rate of 1 kHz using the internal clock of the digital readout. Dedicated dark runs are envisaged each night before and after sky observation, while the lid is closed. During each dark run ten thousand waveforms for each pixel are registered. The charge spectra can be used to evaluate the SiPM parameters. Even though the SiPM parameters cannot be measured with the same precision as presented in section V.2.1.3, it is a useful procedure to track their evolution with temperature. It is worth noting that the dark count events also probe the camera component aging, such as the front-end and digital electronics aging. Figure V.15 shows the projection of the raw waveform in LSB for each camera pixel. Up to 6 p.e., the sensor parameters are easily measurable on a per night basis and can be extracted with satisfactory precision. Additionally, merging all the dark runs and/or merging all the pixels allows building up the necessary statistics to correct the optical cross-talk model, as shown in [116].

The dark count runs are also used to measure the baseline in the absence of NSB. This is used to determine the baseline shift per pixel induced by the NSB. The baseline shift is used to correct the pixel gain, photo-detection efficiency and crosstalk as described in [105]. The baseline shift is also used to evaluate the NSB.

V.4.3 External light source events

The external light source, which will be referred to as the flasher in the following sections, is mounted at the focal distance of the telescope, in the middle of the mirror dish but not exactly on the optical axis as this position is occupied by the lid CCD camera used for the telescope pointing. Short light flashes (few nanoseconds) will be emitted during the science data taking at a rate of 100 Hz. This rate is low enough not to affect the physics data taking. Events are acquired using the flasher which acts as a trigger source. Upon reception of a trigger signal emitted by the light source, the readout of the entire camera is started and the event is tagged with a specific trigger type.

The flasher (LUMP Calibration box), has been designed and built by the astroparticle group at the University of Montpellier for the CTA medium-sized telescope (MST) [117] and having in mind the CTA requirements. It consists of an IP65 box containing an array of 13 LEDs whose peak wavelength is 390 mn (see figure V.11-right) to resemble the Cherenkov spectrum, followed by a diffuser which is transparent to wavelength from 350 to 800 nm and whose diffusion angle is equal to 10°. The FWHM of the pulsed light is between 4 to 5 ns, similar to Cherenkov flashes. In addition, the user can turn on and off individual LEDs, vary their intensity and adjust the frequency of the flashes from 100 Hz to 10 kHz. The flasher temperature characteristics, light stability and spatial light profile have been characterized. The characterization can be found in [85].

V.4.3.1 Monitoring of optical efficiencies with muon and flasher events

The degradation of the mirrors performance is expected due to dust deposition or degradation induced by environmental condition, e.g. acid rain, bird feces, etc. In particular, dust sedimentation has the tendency to increase diffuse reflectivity [118] but can be recovered by cleaning the mirrors regularly. From the experience of current generation of IACTs, we can expect a decrease of specular reflectivity of about 2% per year due to: dust deposition, mechanical damage of the upper protective layer and oxidation of the aluminium coating. The window is also exposed to an open environment and damages on its surface are expected as well. However it is much less exposed as it is sheltered by the lid when not observing. Concerning the cones, we expect minimal degradation of their reflecting coating with time, as they are in the sealed environment of the camera. The same applies to the SiPM sensors, which are not subject to significant aging even when exposed to high light level.

The total optical efficiency to the muon event η^{muon} and to the flasher events $\eta^{flasher}$ are probing different optical elements as can be seen from equations V.18 and V.19.

$$\eta^{muon} = \eta_{shadowing} \times \eta_{mirror} \times \eta_{window} \times \eta_{cones} \times \eta_{SiPM} \tag{V.18}$$

$$\eta^{flasher} = \eta'_{window} \times \eta'_{cones} \times \eta'_{SiPM} \tag{V.19}$$

The difference between η and η' comes from the spectrum of the light source: the Cherenkov spectrum for the muons and the LED spectrum for the flasher (see figure V.11 right).

An efficiency drop cannot be attributed to a given element as only the product is measured. Using both muon and flasher events, the contribution from the mirrors from the camera can be disentangled where the wavelengths of the Cherenkov and flasher

spectra overlap. For instance a relative drop of the optical efficiency measured with muon events indicates a degradation of the mirrors reflectance or/and of the window transmittance. In particular, if no relative drop of optical efficiency is observed with the flasher events, the drop can only be attributed to the mirrors. As both muon and flasher events are acquired during observations, this measurement can be performed on a per night basis.

As the SiPM response depends on the voltage drop, as described in section V.1.1, the η_{SiPM} has to be corrected according to the level of NSB. This effect is assumed to be corrected in equations V.18 and V.19, meaning that the drop in photo-detection efficiency, gain and optical cross-talk are accounted in the efficiency drop.

V.4.3.2 Flat-fielding

To get a uniform trigger rate across the camera field of view, the SiPM bias voltage could be tuned individually. While achieving the desired goal, this would complicate the photon reconstruction as the parameters of the SiPMs reported in section V.2 are given for a nominal bias voltage. The same goal can be achieved with a different strategy, which is applying different trigger thresholds in different camera regions, called clusters.

For the standard triggering scheme (see [119] for more information on the trigger), the camera is divided into 432 clusters. Each cluster (except for the ones located at the camera border) comprises 7 neighboring triplets, where each triplets is composed by 3 pixels, for a total of 21 pixels (one pixel belongs to multiple clusters). The signal of each pixel is baseline subtracted (the baseline is computed as described in equation V.1 by the DigiCam FPGAs). The signal of each triplet (sum of baseline subtracted triplet pixel signals) is clipped to form a 8 bit-integer and added to the one of the 6 other triplets. The resulting signal sum is compared to a threshold which can be adjusted for each cluster independently and dynamically. This last point is critical to be able to flat-field the trigger response. A global threshold T is determined from validated Monte Carlo simulation for a given NSB level. Then the individual cluster thresholds $T^j_{cluster}$ are applied accounting for the possible non-uniformities of the pixel responses, i.e. the flat-field coefficients. The flasher events are used to compute these coefficients. The coefficient F_i for the pixel i is the ratio between the pulse amplitude A_i measured in this pixel corrected for the light profile and the camera average pulse amplitude:

$$F_i = \frac{A_i}{\langle A \rangle} \tag{V.20}$$

These coefficients not only account for different optical efficiencies between pixels but also for different electronic responses, including the effect of the voltage drop. For each cluster j, the threshold is computed as in equation V.21.

$$T^j_{cluster} = \frac{T}{21} \sum_{i=1}^{21} F_i. \tag{V.21}$$

V.5 Conclusion

The method to reconstruct the number and arrival times of photons for a gamma-ray telescope camera has been presented. In addition, the methods to extract the relevant

calibration parameters have been presented and illustrated using the SST-1M camera prototype with its calibration devices. Moreover, the model of SiPM optical cross-talk described in [80] has been applied and has shown that it can be reliably used with a large number of sensors to extract the photo-sensors properties. It has been applied to various light levels (up to 200 p.e., i.e. well below the sensor saturation) reducing the number of free parameters, while increasing the sample size allowing to achieve competitive precision. Furthermore, the systematic effects induced by dark count rate on the measurement have been calculated. It was found that it is negligible. Since the optical cross-talk affects mainly neighboring cells [120] (the number of which is limited to 8) and the generalized Poisson model does not take into account this fact, we might expect systematic problems for higher cross-talk probability than the one reported for our sensor. The photo-sensor typical properties have to be injected in the Monte-Carlo to enable reliable predictions of the camera response.

The full calibration procedure is automatized thanks to the integration of the various sub-systems being controlled by the telescope control software. The data have been processed with the open-source pipeline of the SST-1M telescope *digicampipe* that relies on widely-used python libraries.

The results of the off-site calibration show reliable performances for gamma-ray astronomy when compared to the requirements of the next-generation gamma-ray observatory. In particular: A gain uniformity of the entire readout chain of 2.6% was observed. By adjusting the trigger delays a precise determination of the pulse template in steps of 77 ps is obtained even with a 4 ns FADC sampling period. The template has been characterized above the linear range allowing to use its features for the charge and arrival time reconstruction for saturated pulses. The efficiencies of the optical elements have been presented. In this work, the window transmittance as a function of wavelength was shown. The measurement showed irregularities of the coating on a surface as large as 0.81 m^2. However, the irregularities have been characterized and are comparable in all radial directions. Thus they can be accounted for in the photo-electron to photon conversion. Moreover, we show that even on large Cherenkov cameras a filtering window can be used to reduce night-sky background light without losing too much of the Cherenkov light. The overall optical efficiency of the PDP of η_{total} = 17% was found for the Cherenkov light spectrum. To increase the PDP optical efficiency above 20% (in order to comply with the corresponding CTA requirement), a second window was designed extending the transmittance bandwidth to lower wavelength. Additionally, replacing the S10943(X) SiPMs with the latest low cross-talk technology from Hamamatsu, S13360(X), could be considered but this would require redesign of the front-end electronics. The reported charge and time resolution show excellent performances and satisfy highly demanding requirements, for instance those of CTA.

The results of the on-site calibration show that the SiPM degradation can be monitored by performing dark runs on a per-night basis before astronomical observations. The flasher will ensure a uniform trigger response of the camera over the night even in the presence of a highly fluctuating night-sky background level. In the future, we would like to show that the multiple photo-electron spectrum analysis performed off-site can be repeated on-site with the flasher. This would require the inclusion of a NSB rate parameter in the likelihood similarly as done in [121]. However, we expect it could only be performed during the darkest nights (with a night-sky background less than 60 MHz). Following this, an absolute calibration of the flasher would be interesting to allow for absolute monitoring of the optical efficiencies.

Chapter VI

Image reconstruction of a Cherenkov telescope camera using Silicon Photo-Multipliers

After the extraction of the relevant calibration parameters for charge reconstruction as described in chapter V, a method for reconstructing the Cherenkov event has been developed. The method consists of reducing the data waveforms into image parameters. The image parameters are used to reconstruct the energy of the primary, its direction and to identify gamma-ray events among background. In section VI.1, the Monte Carlo sample used to evaluate the performances of the reconstruction and to train the predictive models is described. In section VI.2, the parameterization algorithm of the images is presented. In section VI.3, the training and testing of the machine learning models is presented. Finally, in section VI.4, the sensitivity of the analysis to a Crab Nebula like source is presented.

VI.1 Monte Carlo simulations of the SST-1M telescope

The telescope performances are determined through instruments response functions such as: the effective area; the energy threshold to gamma-rays; the triggered event rates; the sensitivity to the Crab nebula spectrum. They are evaluated with Monte Carlo simulations of the EASs and of the telescope. The EASs are simulated with the *CORSIKA* software [38]. In particular the *CORSIKA* software is used to simulate the Cherenkov photons emitted by the charged secondaries of the EASs. The telescope response to Cherenkov light is simulated with *sim_telarray* [122]. The *sim_telarray* software simulates: the optical path of the light rays from the mirrors to the SiPMs, the electronic response of the SiPMs, the amplification chain, the digitization of the data and the trigger of the camera. Additionally, it is possible to simulate an array of telescopes for stereoscopic operation but here we used it to simulate the SST-1M telescope prototype in Kraków.

The simulation parameters were set with the latest available laboratory measurements of the telescope instrument response function such as the ones presented in section III.4.1. The laboratory parameters were fine-tuned to match the distribution of ADC counts and the trigger rate scan of the telescope. In addition a good matching of the number of photoelectron in the images is found between the data taken in Kraków and the simulation.

This comparison of Monte Carlo and data is presented in [123]. The corresponding NSB rate at the Kraków site was set at 290 MHz and a zenith angle of 20° is used.

VI.1.1 Simulated event samples

When simulating an EAS event, the energy E, the impact parameter r and the off-axis angle δ between the telescope pointing direction and the point of origin of the primary particle has to be randomly chosen according to a probability density function. The upper and lower bounds of these three parameters are taken large enough to cover the observable range of the telescope (meaning that the trigger probability of the telescope tends to zero beyond these ranges).

To simulate the Crab Nebula, its spectrum, in eq. (I.40), could be used as well as the diffuse proton spectrum in eq. (I.6) to simulate diffuse cosmic-rays. Nonetheless, these choices are not necessarily optimized for computational speed nor representing the need for high statistics in a certain range of energy, impact parameter or off-axis angle.

The distribution of the simulated events is given as follow. First, the energy is selected randomly from E_{min} to E_{max} following a power-law spectrum of index γ_{sim}:

$$\frac{dN_{sim}}{dE} = \begin{cases} \frac{N_{tot}}{\ln\left(\frac{E_{max}}{E_{min}}\right)} E^{-1}, & \text{if } \gamma_{sim} = -1 \\ \frac{1}{\gamma_{sim}+1} \frac{N_{tot}}{E_{max}^{\gamma_{sim}+1} - E_{min}^{\gamma_{sim}+1}} E^{\gamma_{sim}}, & \text{otherwise} \end{cases}, \tag{VI.1}$$

where N_{tot} is the total number of simulated events. Secondly, the impact parameter is selected such that the density of events in an impact area πr^2 is constant for all $r_{max} \geq r \geq 0$. Thus the number of simulated events per bin of impact parameter is:

$$\frac{dN_{sim}}{dr} = \frac{2N_{tot}}{r_{max}^2} r. \tag{VI.2}$$

Finally, the off-axis angle δ (for diffuse particles) is selected such that the density of simulated events in a solid angle Ω of aperture δ is constant for all $\delta_{max} \geq \delta \geq 0$. Thus number of simulated events per bin of off-axis angle is:

$$\frac{dN_{sim}}{d\delta} = \frac{N_{tot}}{1 - \cos\delta_{max}} \sin\delta, \ \delta_{max} \leq \pi. \tag{VI.3}$$

The parameters used for simulating the primary particle energy, impact distance and off-axis angle are summarized in table VI.1. In fig. VI.1 are shown the distribution of the simulated events in bins of energy, impact parameter and off-axis angle.

VI.1.2 Effective area

The effective area A represents a surface area on which the telescope is sensitive. It can be understood that this area is mostly limited by the Cherenkov light pool surface since the Cherenkov light density reduces after a distance R_{pool}, as can be seen from fig. II.8 (top-right). The Cherenkov light pool is imprinted on a surface of πR_{pool}^2. Thus the effective area can be interpreted as $A \simeq \pi R_{pool}^2$. However, the brightness of the event and consequently the energy of the primary particle, has an impact on the detection

Particle	N_{tot} (10^6)	N_{use}	γ_{sim}	E_{min} (TeV)	E_{max} (TeV)	r_{max} (km)	δ_{max} (deg)
Point γ	200	20	-2	0.1	1	0.4	0
	15.4	20	-2	1	10	0.6	0
	15.6	20	-2	10	100	0.8	0
	3.02	20	-2	100	300	1	0
Diffuse γ	314	40	-2	0.1	1	0.8	7
	62.8	40	-2	1	10	0.8	7
	16.56	40	-2	10	100	1	7
	2.36	40	-2	100	300	1.4	7
Diffuse p	682.25	50	-2	0.5	500	1.2	7

Table VI.1. Table of the simulated energy, impact parameter and off-axis angle range. For each particle (point gamma, diffuse gamma and diffuse proton): the total number of showers N_{tot} simulated; the number of times a simulated EAS is re-used N_{use}; the spectral index simulated γ_{sim}; the minimum E_{min} and maximum E_{max} energies; the maximum impact parameter r_{max} and the maximum off-axis angle δ_{max} are given.

probability. A faint event, although falling close to the detector, might not trigger. On the contrary a bright event, falling far from the telescope could be triggered even if the detector is outside the Cherenkov light pool. From this, it can be understood that the effective area depends on the energy of the primary particle. It comes therefore natural to define an effective area based on the trigger probability as:

$$A^{\gamma}(E) = 2\pi \int_0^{\infty} P(E, r) r dr, \tag{VI.4}$$

where E is the energy of the primary particle initiating the EAS, r is the radial distance and $P(E, r)$ is the trigger probability of an event of energy E with impact distance r.

It is important to point out that the effective area in eq. (VI.4), represents the effective area for a source located at center of the camera frame. For diffuse protons the effective area takes into account the off-axis angle δ. Thus the effective area for diffuse protons is:

$$A^{p}(E) = 2\pi \int_0^{\infty} \int_0^{4\pi} P(E, r, \Omega) r dr d\Omega, \tag{VI.5}$$

where $\Omega = 2\pi(1 - \cos\delta)$ is the solid angle of aperture δ. The triggering probabilities P are estimated by the ratio of triggered events $N_{trigger}$ to the number of simulated events $N_{simulated}$ in bins of energy E, impact distance r and off-axis angular distance δ:

$$P(E_i, r_j, \Omega_k) = \frac{N_{trigger}(E_i < E \leq E_{i+1},\ r_j < r \leq r_{j+1},\ \Omega_k < \Omega \leq \Omega_{k+1})}{N_{simulated}(E_i < E \leq E_{i+1},\ r_j < r \leq r_{j+1},\ \Omega_k < \Omega \leq \Omega_{k+1})}; \tag{VI.6}$$

$$\Delta E_i = E_{i+1} - E_i,\ \Delta r_j = r_{j+1} - r_j,\ \Delta\Omega_k = \Omega_{k+1} - \Omega_k; \tag{VI.7}$$

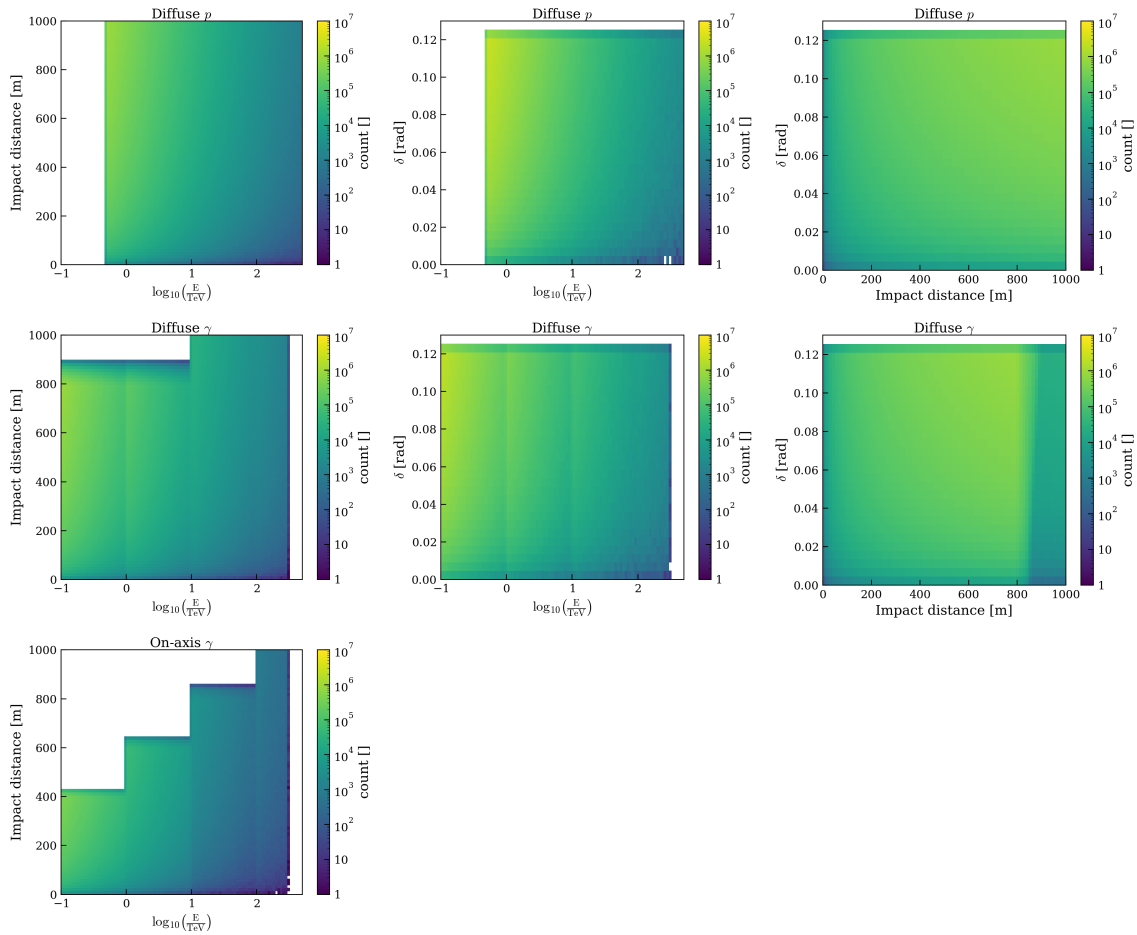

Figure VI.1. Number of simulated events as function of the primary particle energy, the impact distance and the off-axis angle δ. Top: Simulated diffuse proton events. Middle: simulated diffuse gamma events. Bottom: simulated on-axis gamma events.

with ΔE_i, Δr_j and $\Delta\Omega_k$ being small enough.

The trigger probabilities for diffuse protons, diffuse gamma-rays and on-axis gamma-rays are shown in fig. VI.2. In this figure, it is observed that the maximum triggering impact parameter depends on energy. It is observed that there is a minimum triggering energy at about $\sim$ 3 TeV for gamma-rays. For diffuse protons this minimum triggering energy is higher at about 7 TeV. This can be understood by the fact that hadrons, for the same energy, produce less Cherenkov light than gamma-ray particles. The trigger probability of the diffuse protons above the maximum impact distance parameter is higher than for gamma-rays (both diffuse and on-axis). This can be understood by the sub-showers created by the proton induced showers. For instance in fig. II.10, one can see that spread of Cherenkov light is larger for protons than for gamma-rays. These sub-showers, can propagate far from the main shower thus being able to trigger the telescope even if located outside the Cherenkov light pool. Finally, it can be observed that the energy threshold for the gamma-rays is lower at about $r \sim 180$ m than at $r < 180$ m. This is explained by the peak of the Cherenkov light density at about this distance, as can be seen from fig. II.8 (top right).

The effective areas as function of the primary particle energy are shown in fig. VI.20. The effective area are given at different selection cuts of the analysis: at trigger level; at cleaning level and after the reconstruction. The effective area for SST-1M reaches 10^6 m^2 at

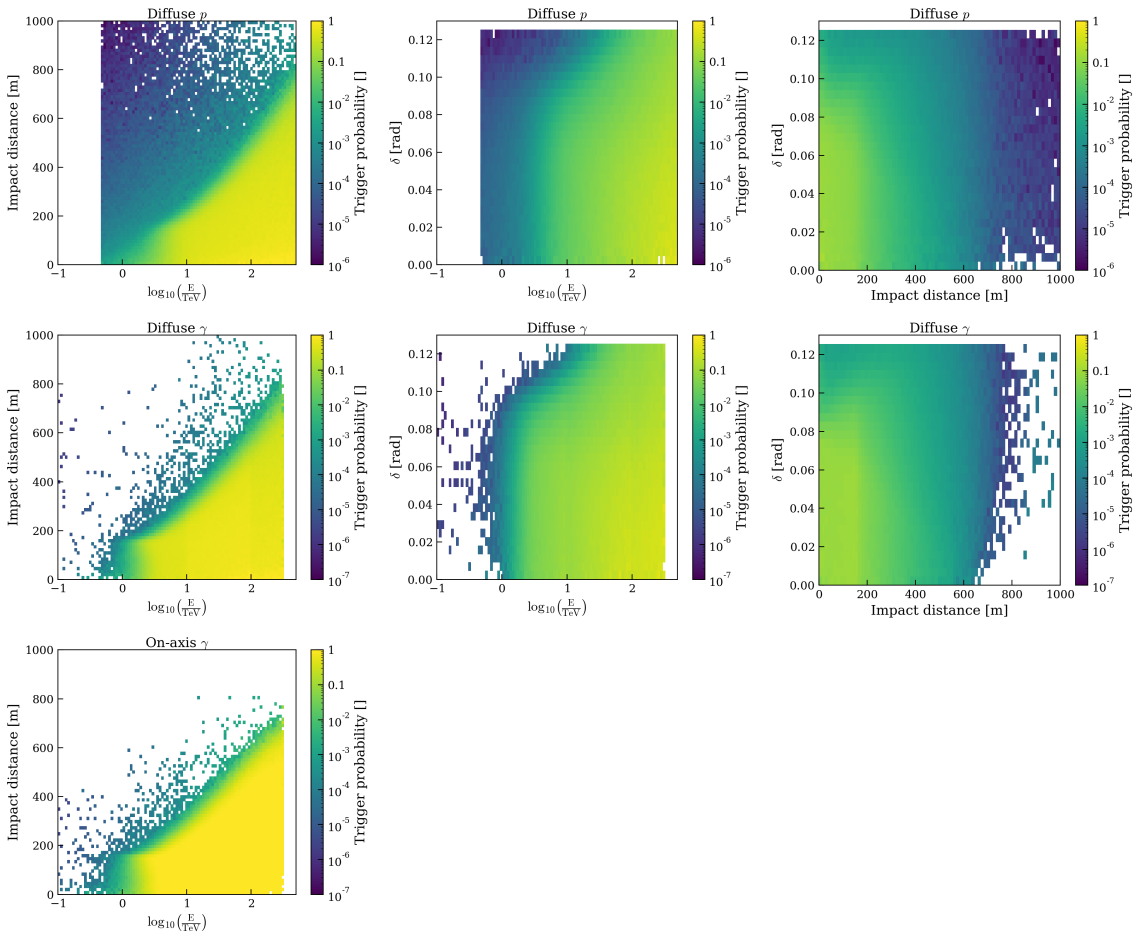

Figure VI.2. Trigger probabilities as function of simulated energy, impact parameter and angular offset δ for diffuse protons (top), diffuse gammas (middle) and on-axis gammas (bottom).

about 300 TeV for on-axis gamma-rays. A point of inflection at about 2 TeV is observed, it corresponds to the threshold energy at which the detection probability is close to 1 when the telescope is within the light pool.

VI.1.3 Differential trigger rate

The effective area allows to represent a complex Cherenkov telescope into a simple detector of surface A. This representation is used to determine the flux of the observed source (or the cosmic-ray flux). The observed rate of events after the event reconstruction has to be translated into a flux of the source. This is where the effective area comes handy. If the observer sees a rate of event per energy $\frac{dN}{dEdt}$ then the flux of the source is given by:

$$\Phi(E) = \frac{1}{A(E)} \frac{dN(E)}{dEdt}, \tag{VI.8}$$

where Φ is the number of gamma-ray per unit time per unit surface per unit energy.

Equation VI.8 can be used to predict the expected rates per energy bins for a given source spectra or for the cosmic-ray spectrum. In fig. VI.21, the differential trigger rates for

the Crab and the cosmic-ray spectra are shown. The Crab spectrum is defined in eq. (I.40) while the cosmic-ray spectrum is defined in eq. (I.6).

The total trigger rate $f_{trigger}$ is computed as:

$$f_{trigger} = \int_0^{\infty} \frac{dN(E)}{dEdt} dE. \tag{VI.9}$$

VI.1.4 Re-weighting of the simulated events

As can be seen from table VI.1 the simulation parameters do not reflect the spectra of cosmic-ray protons, in eq. (I.6) and of gamma-rays from the Crab Nebula, in eq. (I.40). In particular the spectral indices are different from the expected ones and the ratio of the total number of events between point gamma-rays and diffuse protons do not reflect the reality. In fact, the expected trigger rate of cosmic-ray protons is about 1000 times higher than for the gamma-rays from the Crab Nebula. In order to simulate that a weight is attributed to each simulated events. The weights are computed in bins of energy, impact parameter and off-axis angle as the ratio between the expected events per unit time and the simulated events. The weight w_{ijk} is defined as:

$$w_{ijk} = \frac{\frac{dN}{dt}(E_i < E \leq E_{i+1},\ r_j < r \leq r_{j+1},\ \Omega_k < \Omega \leq \Omega_{k+1})}{N_{sim}(E_i < E \leq E_{i+1},\ r_j < r \leq r_{j+1},\ \Omega_k < \Omega \leq \Omega_{k+1})}, \tag{VI.10}$$

where $\frac{dN}{dt}$ is computed from the flux of the particle Φ as:

$$\frac{dN}{dt}(E_i < E \leq E_{i+1},\ r_j < r \leq r_{j+1},\ \Omega_k < \Omega \leq \Omega_{k+1}) = \tag{VI.11}$$

$$= \Phi \Delta E_i (r_{j+1}^2 - r_j^2) \pi \Delta \Omega_k. \tag{VI.12}$$

The weights for the diffuse protons and the on-axis gamma-rays are shown in fig. VI.3.

VI.2 Image reconstruction with a calibrated camera

As the camera has been characterized, the raw data EAS images can be processed. The raw data, consisting of $N_{pixels} \times N_{samples}$ 12-bit unsigned integer, has to be translated into: an energy estimate, a direction in the sky and a particle identification. Intermediate steps to reconstruct these parameters are required. In particular, the waveforms of each pixel are integrated to reconstruct the number of photo-electrons in each pixel. Then the resulting camera image is used to compute image parameters sometimes referred as the Hillas [50] parameters. The parameters of the image are then used to reconstruct the end parameters. For this last stage various method have been investigated like look-up tables or semi-analytical formula[124, 125], but as in other science fields, supervised machine learning is becoming the standard. In particular, an analysis based on the Hillas parameters and using random forest models for the SST-1M telescope has been shown in [126].

In the following, the standard Hillas reconstruction method will be presented in section VI.2.1 and a new image parameterization technique, based on the results obtained for the camera calibration (in chapter V), will be compared to in section VI.2.2.

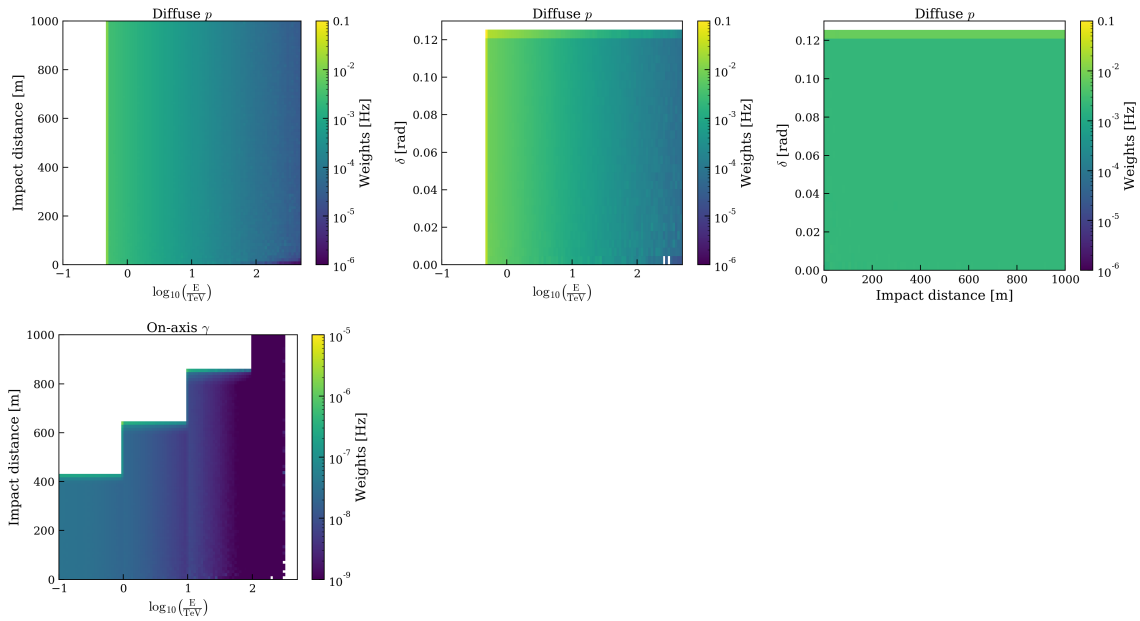

Figure VI.3. Weights of the simulated events as function of energy, impact parameter and off-axis angle. The weights are calculated as in eq. (VI.10). For diffuse protons (top), the proton cosmic-ray spectrum (in eq. (I.6)) is used. For point gamma-rays (bottom), the Crab Nebula spectrum (in eq. (I.40)) is used.

VI.2.1 EAS images standard parameterization

The Hillas parameters, introduced by A. M. Hillas in 1985 [50] have been used widely by the current and past generations of Cherenkov telescopes. It allows to compress the data volume to a much smaller amount while keeping the most important information of the EAS image. In his publication, Hillas showed that his parameters can be used to discriminate between EASs induced by gamma-rays and EASs induced by hadrons. As can been seen from simulations of EAS in the atmosphere (see fig. II.1), it is rather natural, at first order, to parameterize the observed Cherenkov image in terms of first and second order moments.

Charge reconstruction Prior to the parameterization of the image the $N_{pixels} \times N_{samples}$ 12-bit integer are reduced to a photo-electron image by summing each pixel waveform individually over a time period Δt:

$$C_i = \sum_{j=k}^{k+\Delta t f} W_{ij} - B_i, \tag{VI.13}$$

where k is the starting sample of the integration window and B_i the baseline of the pixel i. As a side remark, the starting sample from pixel to pixel might be different.

Photo-electron reconstruction The reconstructed charges C_i have to be equalized in terms of photon response. Meaning that the intensity in each pixel has to be corrected for non uniformity in the optical efficiency of the overall optical chain. Nonetheless, here it is assumed that the optical efficiency among pixels is the same and that corrections in

terms of photo-electrons are only required. To achieve that, the calibration of the camera offers the needed parameters to reconstruct the number of photo-electrons. The gain G of each SiPM is known allowing to translate the charge into a photo-electron scale. One of the disadvantage of SiPM is the fact that total amount of micro-cell discharge is overestimating (or exactly estimating, never underestimating) the number of photo-electrons. This is because of optical cross-talk within the SiPM. Therefore the optical cross-talk μ_{XT} has to be accounted for in the photo-electron reconstruction. Additionally, after-pulses might also induce an overestimation of the number of photo-electron however they are neglected since characterization of the SiPMs as shown that they were negligible. The number of photo-electron in each pixel is given by:

$$N_i^{p.e.} = \frac{C_i - \bar{B}_i}{G_i}\left(1 - \mu_{XT_i}\right), \tag{VI.14}$$

where $\bar{B}$ is a parameter to account for the baseline correction.

The photo-electron reconstruction allows to maximize the Cherenkov signal to NSB ratio. In fact, the signal-to-noise ratio depends on the duration of the integration Δt. A short time window would efficiently avoid integrating NSB pulses but would also weaken the Cherenkov signal. While a large Δt would ensure that most of the Cherenkov signal is collected at the cost of also integrating NSB pulses.

Image cleaning Additionally, to reduce background fluctuations induced by NSB in the reconstructed image it is common to apply an image cleaning. The cleaning method takes into account the fact that the EAS image is clustered within a region of the camera and its reconstructed number of photo-electron is expected to be above the NSB fluctuations. The cleaning method mostly used is commonly referred as "tail-cut cleaning". It consists of keeping all pixels i that satisfy at least one of the two following conditions:

$$\begin{aligned} &N_i^{p.e.} \geq T_{picture} \\ &N_i^{p.e.} \geq T_{boundary} \text{ and } \exists\, j \in S_i \mid N_j^{p.e.} \geq T_{picture}, \end{aligned} \tag{VI.15}$$

where $T_{picture}$ is referred as the picture threshold, $T_{boundary}$ the boundary threshold and S_i is the set of direct neighbor pixels of the pixel i. The picture threshold is the primary threshold. This threshold finds the core pixels of the Cherenkov signal image. Then the secondary threshold, the boundary threshold, allows to recover the signal from the direct neighbors of the primary cleaned pixels. As can be seen from eq. (VI.15), this two-thresholds cleaning method do not guarantee that all the pixels in the cleaned image are neighbors. In fact, it is common to have more than one island of pixels in the image especially for hadron showers which tend to have sub-showers that can be far from the dominant shower (see fig. II.10). A secondary island can find its origin in NSB fluctuations as well. For these reasons the number of island is sometimes computed and kept as an additional parameter of the event. In the following, only the brightest island is kept. The cleaning of the image can also be dilated by adding the direct neighbors of the initially cleaned pixels.

Image parameterization Once the charge has been reconstructed and the image cleaned, the photo-electron image is parameterized. The number of photo-electrons in the pixels

that did not pass the cleaning conditions is set to zero. The total charge in the event is given by:

$$size = \sum_{i=1}^{N_{pixels}} N^i_{p.e.} \tag{VI.16}$$

The centroid of the image is computed as the weighted mean of the x and y coordinates of the pixels:

$$x_{CM} = \frac{1}{size} \sum_{i=1}^{N_{pixels}} x_i N^i_{p.e.} \tag{VI.17}$$

$$y_{CM} = \frac{1}{size} \sum_{i=1}^{N_{pixels}} y_i N^i_{p.e.}, \tag{VI.18}$$

where x_i and y_i are the central coordinates of the pixel i.

The second order momenta offer a parameterization of the width σ_w, length σ_l and orientation angle of the image ψ. One defines a covariance matrix:

$$\Sigma^2 = \frac{1}{size} \sum_{i=1}^{N_{pixels}} N^i_{p.e.} \begin{pmatrix} (x_i - x_{CM})^2 & (x_i - x_{CM})(y_i - y_{CM}) \\ (x_i - x_{CM})(y_i - y_{CM}) & (y_i - y_{CM})^2 \end{pmatrix} \tag{VI.19}$$

The two eigenvectors $\vec{v}_1$ and $\vec{v}_2$ of the covariance matrix Σ^2 give a basis in the reference frame of the image. The orientation of this basis gives the orientation angle ψ of the image major axis with respect to camera coordinate system:

$$\psi = \arctan\left(\frac{v_{2y}}{v_{2x}}\right). \tag{VI.20}$$

The eigenvalues λ_1 and λ_2 (with $\lambda_1 \leq \lambda_2$) associated to the eigenvectors $\vec{v}_1$ and $\vec{v}_2$ represent the width and length of the image:

$$\sigma_w = \sqrt{\lambda_1} \tag{VI.21}$$

$$\sigma_l = \sqrt{\lambda_2}. \tag{VI.22}$$

Two additional parameters are added to measure the image asymmetry and if it is tailed or not. These two parameters are the *skewness* and *kurtosis*. They are measured along the major axis (along the axis of propagation of the EAS):

$$skewness = \frac{1}{size \times length^3} \sum_{i=1}^{N_{pixel}} \left((x_i - x_{CM})\cos\psi + (y_i - y_{CM})\sin\psi\right)^3 N^i_{p.e.} \tag{VI.23}$$

$$kurtosis = \frac{1}{size \times length^4} \sum_{i=1}^{N_{pixel}} \left((x_i - x_{CM})\cos\psi + (y_i - y_{CM})\sin\psi\right)^4 N^i_{p.e.} \tag{VI.24}$$

In fig. VI.6-left, an example of the reconstruction of the event is represented on the camera frame.

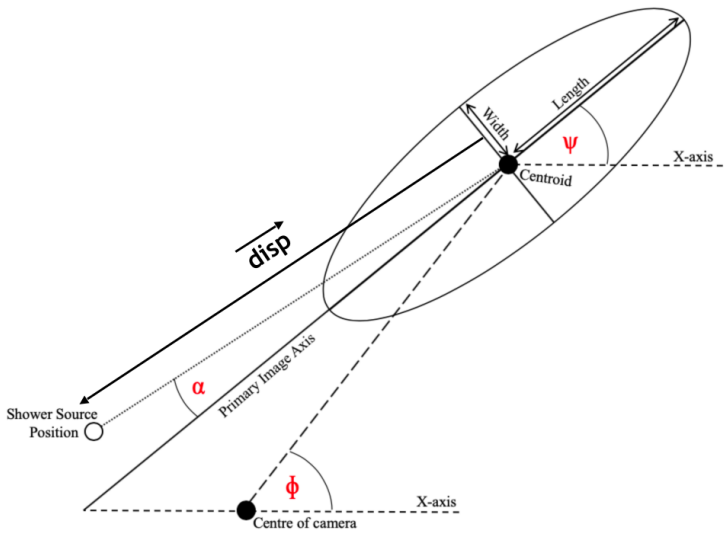

Figure VI.4. Schematic of the image parameters viewed in the camera frame coordinate system. The EAS image is approximated by a 2D Gaussian centered at (x_{CM}, y_{CM}) of given width σ_w and length σ_l. The orientation angle of the ellipse is ψ. The α angle represents the off-axis angle between the image major axis and the source position. The DISP is the vector between the image centroid and the source position. Taken from [127].

Additional image parameters As shown, the photo-electron image is finally reduced to a set of eight independent parameters $\vec{\theta} = (size, x_{CM}, y_{CM}, \psi, \sigma_w, \sigma_l, skewness, kurtosis)$. Since these parameters are used to reconstruct the event primary particle direction and energy by a supervised machine learning algorithm, an additional representation is also suited. In particular the centroid coordinates are represented in polar coordinates r_{CM} and ϕ:

$$r_{CM} = \sqrt{x_{CM}^2 + y_{CM}^2} \tag{VI.25}$$

$$\phi = \arctan\left(\frac{y_{CM}}{x_{CM}}\right). \tag{VI.26}$$

An other representation of the orientation of the EAS with respect to the source is the angle α. It measures the off-axis angle between the source position and the orientation angle of the EAS. If the source is expected to be at a position x_{source}, y_{source} in the camera field of view, the α angle is given by:

$$\alpha = \hat{\phi} - \psi, \alpha \in \left[0, \frac{\pi}{2}\right], \tag{VI.27}$$

where $\hat{\phi} = \arctan\left(\frac{y_{CM} - y_{source}}{x_{CM} - x_{source}}\right)$ is equal to ϕ in the case of the source being at the center of the camera (when the telescope is tracking the source). The angle α shows to be a useful parameter to detect sources of gamma-rays. In fact, over the many EAS background events which are diffuse (as the hadron flux is diffuse), hence showing a uniform distribution of the α parameter, the gamma-ray coming from a source located at the center of the camera should in principle have $\alpha \sim 0$. Which shows an excess of events

coming from the center of the field of view. A representation of the image parameter is shown in fig. VI.4.

Parameters reflecting the shape of the EAS reconstructed image like:

- width over length = $\frac{\sigma_w}{\sigma_l}$;
- area = $\pi \times \sigma_w \times \sigma_l$;
- density = $\frac{size}{area}$,

are also used.

As some of the events will inevitably fall at the camera edges, the image parameters of those might be miss-reconstructed. To reject those events a containment parameter is used. It computes the ratio of the area of the 3-σ ellipse to the area of the pixels contained in the same ellipse and is defined as:

$$\text{containment} = \frac{3 \times \text{area}}{A_{\text{pixels}}} \tag{VI.28}$$

$$A_{\text{pixels}} = \sum_{j \in S} A_i, \tag{VI.29}$$

where S is the set of pixels contained in the 3-σ ellipse. Analogously, one can define a leakage parameter. Usually it is defined as ratio of the image intensity of the last two rows of pixels to the total image intensity.

Timing reconstruction As for the charge contained in each pixel gives information on the EAS event direction, energy and primary particle, the timing information is also relevant for the reconstruction of the event. The reconstructed arrival time in each pixel $\hat{t}_i$ is computed as the arrival time of the pulse. The pulse arrival time can be reconstructed in different ways (see section V.1.2 for an other time reconstruction method). For simplicity we consider the arrival time of the pulse as the time sample of the maximum of the waveform W_{ij}:

$$\hat{t}_i = \frac{1}{f} \underset{j}{\text{argmax}}\, W_{ij}, \tag{VI.30}$$

where f is the sampling frequency of the FADCs. The timing information of each pixel are also cleaned to remove NSB fluctuations. The same pixels that survived the tail-cut cleaning (see eq. (VI.15)) are kept.

Timing parameters If one considers a vertical EAS falling onto the telescope and if we consider that the shower front moves at a constant velocity it can be understood that the Cherenkov light emitted at the top of the atmosphere will reach the telescope after the light emitted at the bottom of the atmosphere. This is the case because the Cherenkov light travels slower than the charged particles responsible for it. In reality, the situation is more complicated as the shower loses energy while propagating through the atmosphere. Moreover the delay observed between the top Cherenkov photons and the bottom Cherenkov photons depend on the orientation angle of the shower, the impact parameter (distance between impact point and the observer) and its energy. For instance,

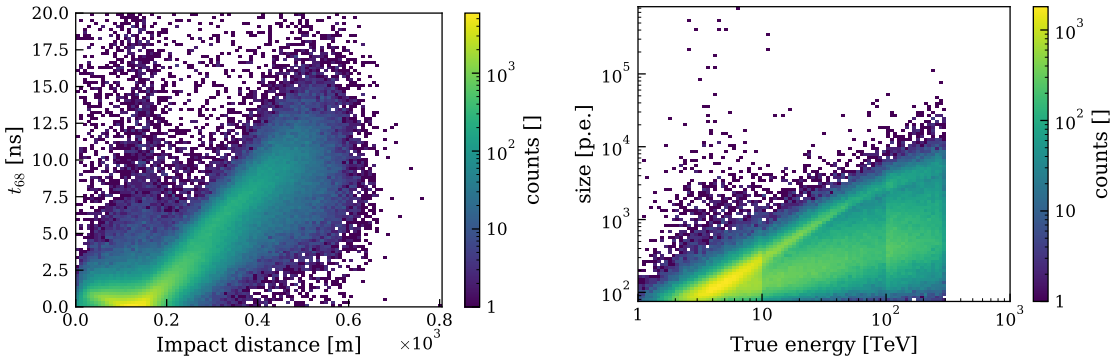

(a) **(b)**

Figure VI.5. Left: Time containment as a function of the impact parameter for on-axis gamma-ray. Left: Total charge μ in the reconstructed event as function of the simulated energy for on-axis gamma-rays.

in fig. VI.5 (left) one can see dependency of the duration of the signal with the impact parameter of the EAS. Finally, the delays are not only in the longitudinal direction (from top to bottom) but also in the lateral direction.

The time structure of gamma-ray and cosmic-ray showers have been studied in [128]. It is found that a first order polynomial can be used to represent the arrival times of the Cherenkov photons in the longitudinal direction while a second order polynomial is better suited in the lateral direction. Here a parameterization in the longitudinal direction is used, where the pixel coordinates are projected in the longitudinal direction $\hat{x}$:

$$\hat{t}_i = t_{CM} + v^{-1}(\vec{x}_i - \vec{x}_{CM}) \cdot \hat{x},\ \hat{x} = (\cos\psi, \sin\psi), \tag{VI.31}$$

where $\hat{t}_i$ is the expected arrival time in the pixel i, t_{CM} is the arrival time in the image center of mass $\vec{x}_{CM} = (x_{CM}, y_{CM})$ and $\vec{x}_i = (x_i, y_i)$ are the pixel coordinates of the pixel i.

The parameters t_{CM} and v^{-1} are computed by doing a linear regression with the reconstructed arrival times of the pulse $\hat{t}_i$. The first (sometimes referred as "intercept") represents the arrival time of the center of mass of the image relative to the readout window time. This parameter is of no particular interest as the relative time at which the event arrives carries no information on the primary particle. The second (sometimes referred as "time gradient") represents the velocity at which the image develops in the camera. It is an important parameter in order to reconstruct the impact parameter of the EAS. As can be seen from fig. VI.5 the impact parameter depends almost linearly on the time duration of 68% containment of the event ($t_{68} = \sigma_l v^{-1}$). Above 130 m impact distance the slope is about +30 $\mu s \cdot m^{-1}$. While for impact distances closer than 130 m the slope is negative and is about $-8\ \mu s \cdot m^{-1}$, it can be seen, that if the telescope is within the light pool (i.e impact distance $\leq$ 130 m) the event is almost instantaneous. On the contrary, if the telescope is outside the light pool the event lasts longer.

It is important to add that further time delays can be introduced by the telescope. As a matter of fact the delays introduced by the mirrors have to be taken into account if shown to be relevant. Moreover the electronic delays in the camera could also affect the measurement of the timing parameters.

An example of the timing parameter reconstruction is shown in fig. VI.6-right.

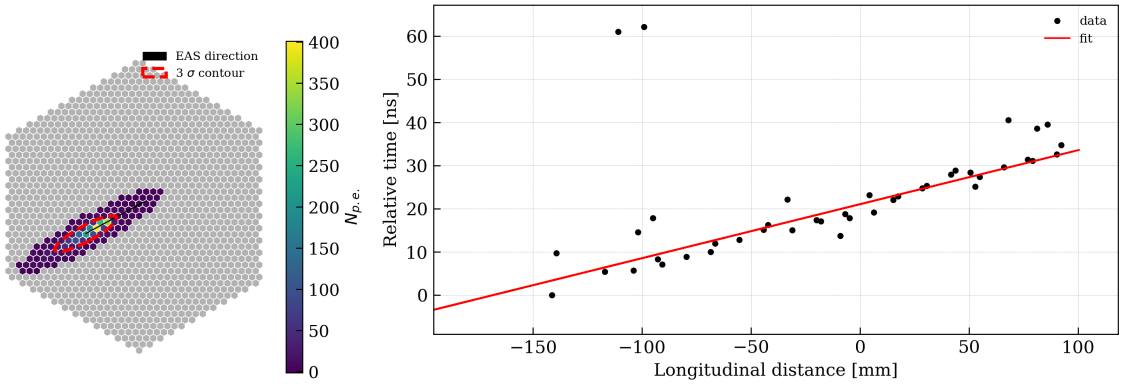

Figure VI.6. Example of a 107 TeV gamma-ray simulated event reconstructed with the standard analysis. Left: Reconstructed number of photo-electron $N_{p.e.}$ within each pixel as defined in eq. (VI.13). Pixels that do not satisfy the cleaning conditions, as defined in eq. (VI.15), are greyed. The 3-σ contour of the reconstructed ellipse is drawn in red. The arrow (in black) indicates the reconstructed orientation angle ψ of the EAS and its direction shows the time development direction. Right: Relative reconstructed time of each pixel (satisfying the cleaning condition) as function of the longitudinal coordinate of the pixel (black points). The red line represents the linear fit from eq. (VI.31).

VI.2.2 EAS images likelihood maximization

In section VI.2.1 the standard reconstruction for EAS images was presented. The standard reconstruction first reduces the waveforms into a charge and a time image of the event. The reconstruction of those is subject to the noise fluctuations (primarily NSB) therefore the tails of the EAS image might be miss-estimated. The image parameters are then reconstructed on these two images that require an image cleaning. The image cleaning introduces two additional parameters (picture and boundary thresholds) that need to be optimized for. Usually the analysis is performed with multiple cleaning threshold and the best configuration is used. Moreover, the charge image is described as a two dimensional normal distribution. It is well known that the longitudinal profile of an EAS is not symmetric [128] therefore the two dimensional normal distribution might not be well suited. Additionally, the time gradient ν^{-1} computation depends on the predetermined shower orientation ψ as can be seen from eq. (VI.31). On the other hand, the time gradient is not used to infer the shower orientation as the spatial and time images are separated. Finally, the reconstruction of the charge assumes that all pixels have identical charge resolution. While the per-pixel gain G, optical cross-talk μ_{XT} and baseline residual $\bar{B}$ are used, no information on the uncertainty of the reconstructed number of photo-electrons is used.

Here, an independent approach for reconstructing the image parameters while trying to solve some of the problems pointed above is described.

Pixel photo-electron likelihood In order to include the resolution of each pixel into the reconstruction we introduce a likelihood approach to reconstruct the number of photo-electrons. Instead of applying a linear transformation between the reconstructed charge C and the number of photo-electrons (as in eq. (VI.14)), the number of photo-electrons μ maximizing the likelihood:

$$\mathcal{L}_{p.e.}(\mu; C, \sigma_e, \sigma_s, \mu_{XT}, \bar{B}, G) = \sum_{k=0}^{\infty} \frac{\mu(\mu + k\mu_{XT})^{k-1}}{k!} e^{-\mu - k\mu_{XT}} \frac{1}{\sqrt{2\pi}\sigma_k} e^{-\frac{(C-kG-\bar{B})^2}{2\sigma_k^2}}, \quad \text{(VI.32)}$$

$$\sigma_k^2 = \sigma_e^2 + k\sigma_s^2 \quad \text{(VI.33)}$$

is found given that the pixel calibration parameters $(\sigma_e, \sigma_s, \mu_{XT}, \bar{B}, G)$ are known and that the observed reconstructed charge is C. The parameter σ_e represents the pedestal fluctuations. These fluctuations arises primarily from NSB but also from electronic noise and SiPM dark noise. The parameter σ_s is the single photo-electron resolution (or SiPM gain smearing). The likelihood given in eq. (VI.32) is obtained from the calibration of the camera pixels. Further information can be found in chapter V.

In fig. VI.7 a two dimensional likelihood map as function of the reconstructed charge and the number of photo-electronsis shown. It can be seen that for a given observed charge many true numbers of photo-electron are likely. This is mainly due to the Poisson fluctuations of the Cherenkov photon source. On the other side it can be also seen that for a given number of photo-electrons many reconstructed charges are likely as can be seen from the bottom figure. The approach for reconstructing the number of photo-electron as in eq. (VI.14) is represented with the solid white line. While the maximum likelihood approach is represented with the white dashed line. Both approaches give the same results on average. However the former tends to round the number of photo-electron toward integer values. For instance an observed charge of 10 LSB would result in a most probable value of 1 p.e. while the standard computation would reconstruct ~ 0.5 p.e.

Spatial modeling of an EAS Cherenkov image As seen before, the likelihood and the standard reconstruction approach do not drastically change the reconstructed number of p.e.. However, if a spatial model for the image profile is provided, the likelihood approach should tolerate Poisson and sensor fluctuations. Therefore the image maximizing the likelihood given the observed image is different from the image maximizing the individual pixel likelihoods. In order to be consistent with the standard image parameterization (described in section VI.2.1), a 2-dimensional Gaussian is used. For each camera pixel $i = 1, 2, \ldots, N_{pixel}$ the expected number of p.e. μ_i is given by:

$$\mu_i = \mu A_i \frac{1}{2\pi\sigma_w\sigma_l} \exp\left(-a(x_i - x_{CM})^2 - 2b(x_i - x_{CM})(y_i - y_{CM}) + c(y_i - y_{CM})^2\right), \quad \text{(VI.34)}$$

where μ represents the total number of p.e. in the image which is equivalent to the size parameter of the standard reconstruction from eq. (VI.16), A_i is the area of the pixel i, (x_i, y_i) are the pixel coordinates of the pixel i, (x_{CM}, y_{CM}) are the center coordinates of the 2-dimensional Gaussian, σ_w is the length of the minor axis and σ_l the length of the major axis. The a, b and c coefficients are function of the 2-dimensional Gaussian orientation angle ψ, the width σ_w and the length σ_l:

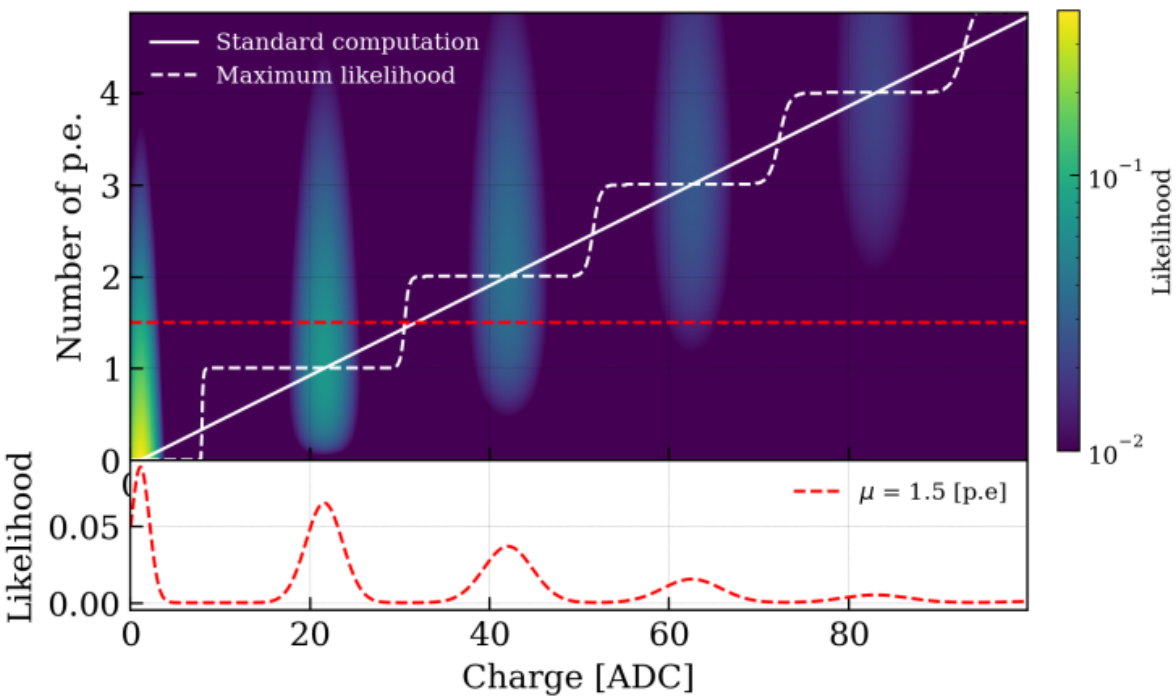

Figure VI.7. Example of a pixel likelihood (from eq. (VI.32)) as function of the reconstructed charge and of the number of photo-electrons. The white dashed line represents the number of photo-electrons maximizing the likelihood as function of the reconstructed charge. The white solid line represent the number of photo-electrons as function of the reconstructed charge as obtained from eq. (VI.14). Below is shown a profile of the likelihood for 1.5 p.e.. The following calibration parameters were assumed : $G = 20$ LSB/p.e., $\mu_{XT} = 0.1$ p.e., $\bar{B} = 1$ LSB, $\sigma_e = 1$ LSB and $\sigma_s = 2$ LSB.

$$a = \frac{\cos^2\psi}{2\sigma_l^2} + \frac{\sin^2\psi}{2\sigma_w^2} \tag{VI.35}$$

$$b = \frac{1}{4}\sin 2\psi\left(\frac{1}{\sigma_w^2} - \frac{1}{\sigma_l^2}\right) \tag{VI.36}$$

$$c = \frac{\sin^2\psi}{2\sigma_l^2} + \frac{\cos^2\psi}{2\sigma_w^2}. \tag{VI.37}$$

Time modeling of an EAS Cherenkov image The pixel likelihood from eq. (VI.32) and the 2-dimensional Gaussian of eq. (VI.34) can be combined in order to constrain the expected image. However doing so would require to integrate the waveforms W_{ij} into reconstructed charge C_i as in eq. (VI.13). The charge reconstruction requires to find an optimal integration window Δt and also to know where the Cherenkov signal falls into the readout window. There exists different integration methods to extract the maximum amount of signal. For instance it is common to search for the maximum reconstructed charge in a sub-window around the expected arrival time of the Cherenkov photons. Also the maximum reconstructed charge in each pixel can be searched individually without considering that neighbor pixels should have their maximum signal close in time. An other widely used method consists of using the time profile of the event to adjust dynamically

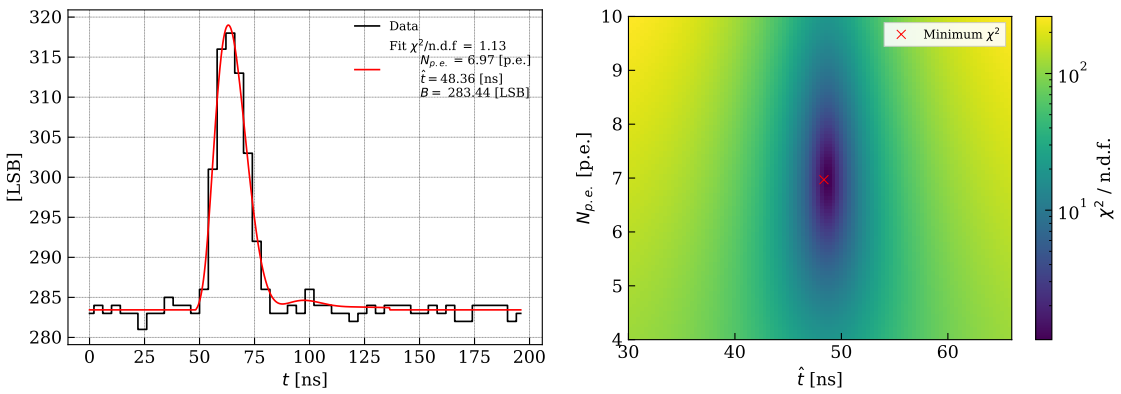

Figure VI.8. Left: Example of a waveform (black) fitted with a pulse template (red). Right: Reduced χ^2 as function of reconstructed time $\hat{t}$ and number of photo-electron $N_{p.e.}$ for the waveform presented in the left figure. The minimum is found at $N_{p.e.} = 6.97$ p.e. and $\hat{t} = 48.36$ ns.

the position of the integration window. This method requires to first integrate the signal with a static integration window in order to characterize the timing parameters as defined in section VI.2.1. Then using the timing parameters the integration window position is moved along the shower time propagation axis. Inclusion of the timing information in the reconstruction and especially in the image cleaning has shown to improve the performance of event reconstruction [129].

In order to avoid to find the optimal integration window Δt and the location of the integration window, the waveform W_i can be fitted to a typical pulse template $h_i(t)$ by minimizing the χ^2_i for each pixel i:

$$\chi^2_i(N^i_{p.e.}, \hat{t}_i; G_i, B_i, W_{ij}, \sigma_i) = \sum_{j=1}^{N_{samples}} \frac{1}{\sigma_i^2}\left(N^i_{p.e.} G_i h(t_j - \hat{t}_i) + B_i - W_{ij}\right)^2, \tag{VI.38}$$

$$i = 1,\ 2,\ \ldots,\ N_{pixels} \tag{VI.39}$$

where G is the gain, B the baseline and σ a parameter to account for baseline fluctuations (mainly composed of NSB fluctuations) are the calibration parameters. While $N_{p.e.}$, the number of photo-electron, and $\hat{t}$, the arrival time of the pulse, are the fit parameters.

An example of the time reconstruction minimizing the chi-square defined in eq. (VI.38) is represented in fig. VI.8. The time reconstruction obtained from the maximum of the waveform in section VI.2.1 has a resolution which depends on the sampling frequency f: $\frac{1}{\sqrt{12}f}$. While the time obtained from the chi-square minimization in eq. (VI.38) has a much finer resolution since the fit allows to scan for times less than $\frac{1}{f} = 4$ ns. This can be seen in fig. VI.9. However finding the minimum of all the χ^2_i of all the pixels can be computationally expensive. Moreover doing it in a independent way (each pixel independently of its neighbor pixels), could lead to fit thermal pulses as these pulses have the same shape of a Cherenkov light pulse.

Time and space linking of the photo-electron likelihood The time and space modeling of an EAS Cherenkov image can be combined into a single likelihood function. To achieve

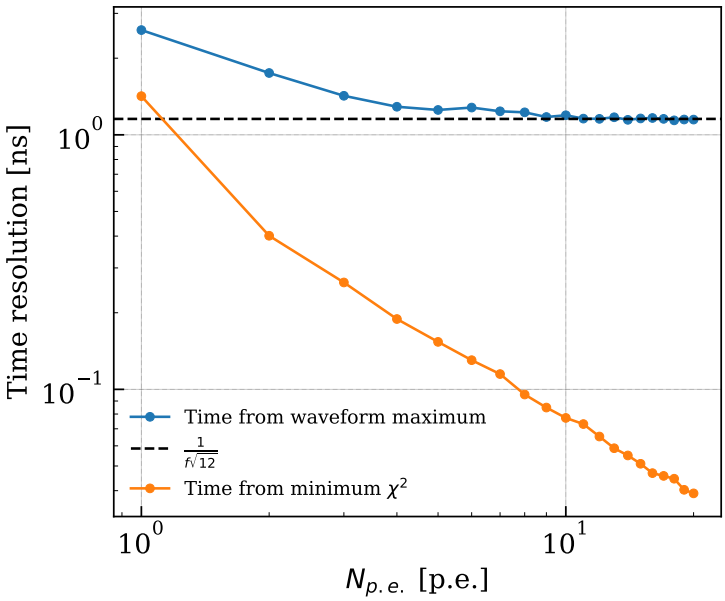

Figure VI.9. Time resolution of the time reconstruction using the maximum of the waveform as defined in section VI.2.1 (blue) and minimizing the chi-square in eq. (VI.38) (orange) as a function of the number of photo-electrons. The theoretical limit for the method using the maximum of the waveform is indicated with the dashed black line. The signal waveforms have been produced with a dedicated Monte Carlo simulation of the camera electronics. For simplicity the waveform have been simulated without thermal noise (no dark count nor night-sky background light).

this, the pixel photo-electron likelihood in eq. (VI.32) is used for each pixel i and each sample j. One defines the following log-likelihood:

$$\ln \mathcal{L} = \sum_{i=1}^{N_{pixels}} \sum_{j=1}^{N_{samples}} \ln \mathcal{L}_{p.e.}(\mu_i; W_{ij}, \sigma_{e_i}, \sigma_{s_{ij}}, \mu_{XT_i}, \bar{B}_i, G_{ij}), \tag{VI.40}$$

where μ_i is the expected number of photo-electrons in the pixel i defined as in eq. (VI.34) and W_{ij} is the observed digitized waveform value in pixel i and time sample j. As can be noticed, the calibration parameters $\vec{\theta}_c = (\sigma_e,\ \sigma_s,\ \mu_{XT},\ \bar{B},\ G)$ are used pixel-wise. This allows to take into account the resolution differences among the camera pixels. The gain and σ_s parameters are depending on the time sample j in order to take into account the pulse shape $h(t)$. For a Cherenkov light pulse arriving at time $\hat{t}_i$, with respect to the readout window, the gain G_{ij} and the gain smearing $\sigma_{s_{ij}}$ of the pixel i and the time sample j are given by:

$$G_{ij} = G_i h(t_j - \hat{t}_i) \tag{VI.41}$$

$$\sigma_{s_{ij}} = \sigma_{s_i} h(t_j - \hat{t}_i), \tag{VI.42}$$

where G_i and σ_{s_i} are the amplitude and fluctuations in LSB of a single photo-electron pulse and $t_j = j\frac{1}{f}$ the clock time cycles.

The time of arrival in the pixel i, $\hat{t}_i$, can be parameterized using eq. (VI.31). Using the constraints defined above the log-likelihood reads:

$$\ln \mathcal{L}(\vec{\theta};\, W_{ij},\, \vec{\theta}_c) = \sum_{i=1}^{N_{pixels}} \sum_{j=1}^{N_{samples}} \ln \sum_{k=0}^{\infty} \frac{\mu_i(\mu_i + k\mu_{XT_i})^{k-1}}{\sqrt{2\pi}\sigma_{k_{ij}} k!} e^{-\frac{(W_{ij}-kG_{ij}-\bar{B}_i)^2}{2\sigma^2_{k_{ij}}} - \mu_i - k\mu_{XT_i}} \tag{VI.43}$$

$$\vec{\theta} = (\mu,\, x_{CM},\, y_{CM},\, \sigma_w,\, \sigma_l,\, \psi,\, \nu,\, t_{CM}) \tag{VI.44}$$

$$\sigma^2_{k_{ij}} = \sigma^2_{e_i} + k\sigma^2_{s_{ij}} \tag{VI.45}$$

Approximation of the pixel photo-electron likelihood function As can be seen from eq. (VI.32), the pixel photo-electron likelihood function is a series. In practice such function cannot be computed. However it can be approximated. An approximation allows to reduce the computational time, which has to be kept low to be able to process observational data on a reasonable time scale. The computation time of the photo-electron likelihood function is particularly important as it will be evaluated many times by the maximization algorithm maximizing the likelihood of eq. (VI.43).

Three kinds of approximations are possible: neglect the least contributing terms; use the law of large numbers; neglect the gaussian photo-peaks.

First, by neglecting the least contributing k-terms, the computation time is kept finite. The sum can be performed from $k = k_{min}$ to $k = k_{max}$:

$$\mathcal{L}_{p.e.} \simeq \sum_{k=k_{min}}^{k_{max}} \frac{\mu(\mu + k\mu_{XT})^{k-1}}{k!} e^{-\mu - k\mu_{XT}} \frac{1}{\sqrt{2\pi}\sigma_k} e^{-\frac{(C-kG-\bar{B})^2}{2\sigma^2_k}}. \tag{VI.46}$$

The number of considered photo-peaks is directly linked to the expected number of photo-electrons in a single pixel μ. The values of k_{min} and k_{max} can be derived from the Generalized-Poisson probability mass function $P(X = k)$. The bounds of the sum can be computed by finding the k-terms for which the probability of observing k photo-electrons, given that the expected number of photo-electron is μ and the optical cross-talk is μ_{XT}, is smaller than $\epsilon > 0$:

$$P(X = k) = \frac{\mu(\mu + k\mu_{XT})^{k-1}}{k!} e^{-\mu - k\mu_{XT}},\; k = k_{min},\, k_{max} \tag{VI.47}$$

$$P(X = k_{min} + 1) \geq \epsilon > P(X = k_{min}) \tag{VI.48}$$

$$P(X = k_{max} - 1) \geq \epsilon > P(X = k_{max}) \tag{VI.49}$$

Examples of Generalized-Poisson probability mass distribution together with the corresponding k_{min} lower and k_{max} upper bounds, for $\epsilon = 10^{-6}$, are illustrated in fig. VI.10.

As can be noticed from fig. VI.10, the number of k-terms: $k_{max} - k_{min} + 1$ increases with the expected number of photo-electron μ. As a consequence the computational time increases with larger μ. However, by the nature of the source observed (following a spectrum which weakened with increased energy), a number of photo-electron per pixel higher than about 1000 p.e. rarely occurs. Therefore the increase of significant k-terms in series with increased μ should not drastically affect the overall data processing time.

Secondly, the law of large number can be applied to the pixel photo-electron likelihood to reduce the complexity of its computation. Therefore the likelihood is approximated as:

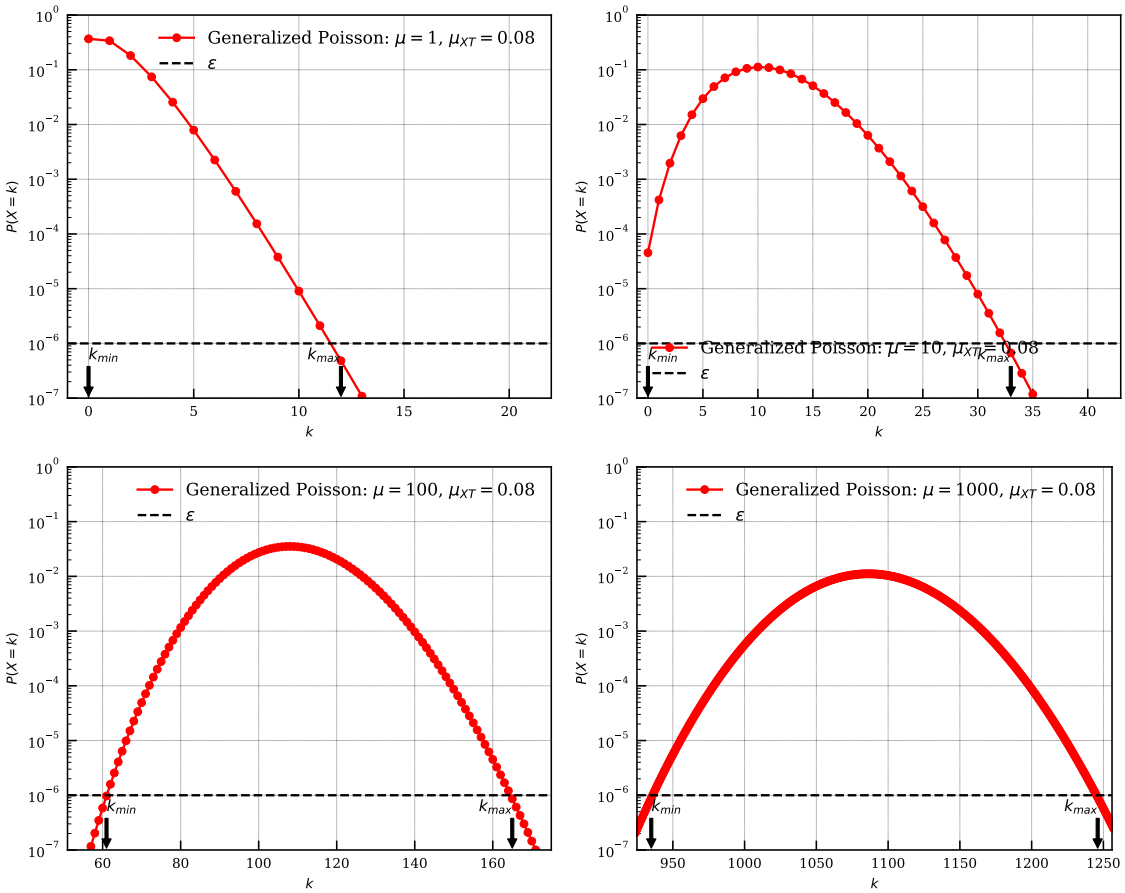

Figure VI.10. Examples of Generalized-Poisson probability mass $P(X = k)$ function (in red) as function of the number of photo-electron k assuming an optical cross-talk of $\mu_{XT} = 0.08$ p.e. In reading order are shown the Generalized-Poisson probability mass function for an expected number of photo-electron $\mu = 1$, 10, 100, 1000 p.e. The dashed line indicates the $\epsilon = 10^{-6}$ probability threshold as defined in eq. (VI.48) and eq. (VI.49). The lower (k_{min}) and upper (k_{max}) indices of the approximated series in the pixel photo-electron likelihood (defined in eq. (VI.32)) are indicated with arrows. If there exist no k_{min} satisfying the conditions in eq. (VI.48), $k_{min} = 0$ is chosen.

$$\mathcal{L}_{\text{p.e.}} \simeq \frac{1}{\sqrt{2\pi\hat{\sigma}^2}} \exp\left(\left(\frac{C - \hat{\mu}}{\sqrt{2}\hat{\sigma}}\right)^2\right), \tag{VI.50}$$

$$\hat{\mu} = \frac{\mu}{1 - \mu_{XT}} G + \bar{B}, \tag{VI.51}$$

$$\hat{\sigma} = \sqrt{\frac{\mu}{(1 - \mu_{XT})^3}} G. \tag{VI.52}$$

Finally, the photo-peaks of the likelihood $\mathcal{L}_{\text{p.e.}}$ can be neglected. This is achieved by transforming the discrete Generalized-Poisson probability mass function into a continuous Generalized-Poisson probability density function. It is equivalent to consider that the width of the photo-peaks σ_k to be infinite. The approximated likelihood reads:

$$\mathcal{L}_{p.e.} \simeq \frac{\mu(\mu + \hat{k}\mu_{XT})^{\hat{k}-1}}{G\Gamma(\hat{k}+1)} \exp\left(-\mu - \hat{k}\mu_{XT}\right), \tag{VI.53}$$

$$\hat{k} = \frac{C - \bar{B}}{G}, \tag{VI.54}$$

where $\Gamma(x)$ is the gamma function.[1]

The three approximation of the pixel photo-electron likelihood have been compared to the true one. The results are shown in fig. VI.11. As demonstrated by fig. VI.11 bottom-right, where the L^2 norm of the difference between the approximation and the true function as function of the expected number of p.e. μ is drawn, the first approximation is the most accurate.[2] However, as previously mentioned, this approximation is computationally expensive as μ increases. For small numbers of photo-electrons ($\mu \leq 20$) the two other approximations are not accurate since the photo-peaks are eliminated. For large number of photo-electron ($\mu \geq 100$), the photo-peaks are blurred and thus the continuous Generalized-Poisson and the Gaussian approximations are well suited. In this range, the continuous Generalized-Poisson approximation converges faster than the Gaussian approximation. This can be explained by the asymmetry, induced by optical cross-talk, of the true distribution .

To conclude, the three approximations presented offer a suited simplification of the pixel photo-electron likelihood which can reduce the computation time. However a increasing computation speed decreases the numerical precision. A trade off between the two is found by neglecting the least significant k-terms in the series for low number of expected photo-electron. At large number of photo-electron the continuous Generalized-Poisson approximation is well suited. It is important to point out that the threshold of transition between the two approximations depends on the calibration parameters $\vec{\theta}_c$. In particular if the photo-electron resolution σ_s is lower the threshold is shifted towards higher values. Here, typical calibration parameters of the SST-1M camera are assumed.

Initialization of the likelihood maximization The maximization of the log-likelihood defined in eq. (VI.43) is achieved by minimizing the negative log-likelihood with the minimization software *Minuit* [130]. In particular, the *python*-based interface software *iminuit* [131] is used. Most of minimization algorithms need to be initialized with parameters where the negative log-likelihood is already close to its minimum. As initialization parameters, the parameters reconstructed by the standard analysis are used. The standard reconstruction requires to set the cleaning thresholds in eq. (VI.15). The threshold are kept low in order to not discard the event. The values of the thresholds $T_{picture}$ and $T_{boundary}$ depend on the NSB light level. For a NSB rate of about 250 MHz, $T_{picture} = T_{boundary} = 10$ p.e. is chosen. In principle, the waveforms W_{ij} do not need to be cleaned when minimizing $-\ln\mathcal{L}$ since the spatial modeling of the EAS is included in the likelihood function. However, to reduce the number of summing terms in the log-likelihood (and therefore reduce the computation time), the pixels and time samples in which no Cherenkov light is expected can be removed. The set of pixels S that are

[1]The gamma function is defined as: $\Gamma(x) = \int_0^\infty z^{x-1}e^{-z}dz$, for all $x > 0$ and in particular $\Gamma(n) = (n-1)!$ for any positive integer n.

[2]The L^2 norm of a function $f(x)$ is defined as: $||f(x)||_2 = \sqrt{\int_{-\infty}^{\infty} f(x)^2 dx}$

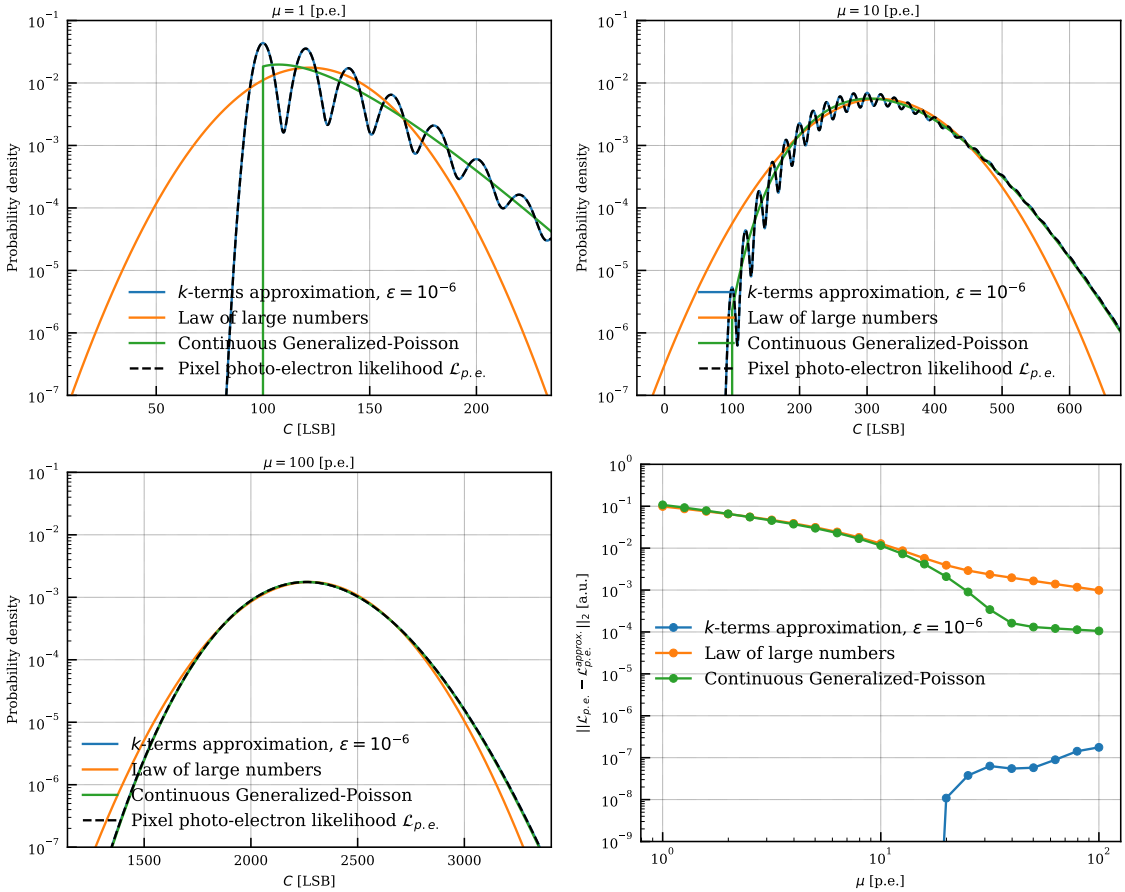

Figure VI.11. Pixel photo-electron likelihood (dashed black), as defined in eq. (VI.32), as function of the reconstructed charge C for different expected number of photo-electron: $\mu = 1$ p.e. (top left), $\mu = 10$ p.e. (top right) and $\mu = 100$ p.e. (bottom left). The following typical SST-1M calibration parameters are assumed: $\vec{\theta}_c = (\sigma_e = 3.37$ LSB, $\sigma_s = 1.78$ LSB, $G = 20$ LSB/p.e., $\mu_{XT} = 0.08$ p.e., $\bar{B} = 100$ LSB). The approximations are drawn for comparison: the k-terms approximation (blue) from eq. (VI.47); the approximation of the law of large numbers (orange) from eq. (VI.50); the continuous Generalized-Poisson approximation (green) from eq. (VI.53). The bottom right figure shows the L^2 norm of the difference between the pixel photo-electron likelihood $\mathcal{L}_{p.e.}$ and its approximation $\mathcal{L}_{p.e}^{approx.}$ as function of the expected number of photo-electron μ.

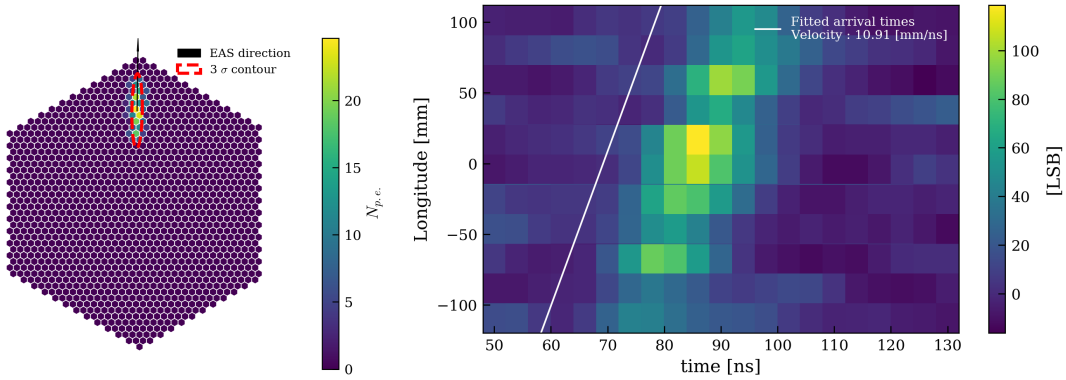

Figure VI.12. Example of a 107 TeV gamma-ray event reconstructed by minimizing the negative log-likelihood defined in eq. (VI.43). Left: Within each camera pixel is indicated the number of photo-electrons reconstructed from eq. (VI.14). The 3-σ contour of the reconstructed ellipse minimizing $-\ln\mathcal{L}$ is drawn in red. The black arrow indicates the time development direction of the image. The greyed pixels correspond to the set of pixels for which the cleaning condition from eq. (VI.55) is not satisfied (with $n_{space} = 5$). Right: Waveforms of the pixels, as function of time. Only the pixels and times samples satisfying eqs. (VI.55) and (VI.57) are drawn. The waveforms are placed in longitudinal coordinate order. The white-dashed line shows the reconstructed time development of the image. The corresponding likelihood profiles are illustrated in fig. VI.13.

contained within the n_{space}-σ initialization ellipse contour are kept. This set is defined as:

$$S = \left\{ i = 1,\ 2,\ \ldots,\ N_{pixels} \,\middle|\, \left(\frac{(\vec{x}_i - \vec{x}_{CM})\cdot\hat{x}}{\sigma_l}\right)^2 + \left(\frac{(\vec{x}_i - \vec{x}_{CM})\cdot\hat{y}}{\sigma_w}\right)^2 \leq n_{space}^2 \right\} \quad \text{(VI.55)}$$

$$\hat{x} = (\cos\psi, \sin\psi),\ \hat{y} = (\sin\psi, -\cos\psi). \quad \text{(VI.56)}$$

Similarly, the time samples prior and after the event expected arrival times are removed. The set T of time samples being in n_{time}-σ of the expected arrival times in the major-axis direction is defined as:

$$T = \left\{ j = 1,\ 2,\ \ldots,\ N_{samples} \,\middle|\, v^{-1}\sigma_l n_{time} \leq t_j - t_{CM} \leq v^{-1}\sigma_l n_{time} + t_{pulse} \right\}, \quad \text{(VI.57)}$$

where t_{pulse} is the pulse duration, for SST-1M the pulse duration used is $t_{pulse} \simeq 50$ ns. The optimum parameters that reduce the event size while not removing too much of the tails of the event are found for $n_{space} = 3$ and $n_{time} = 4$.

An example of a reconstructed gamma-ray event is presented in fig. VI.12. The corresponding projected likelihood profile as function of each of the EAS parameters $\vec{\theta}$ is shown in fig. VI.13

Conclusion The log-likelihood defined in eq. (VI.43) allows to intertwine the time and space development of the EAS as modelled in eqs. (VI.31) and (VI.34). Thus the orientation angle of the image ψ is not only constrained by the spatial part but also by its time part. Additionally, the time and space reconstruction use the pulse template h(t) offering better

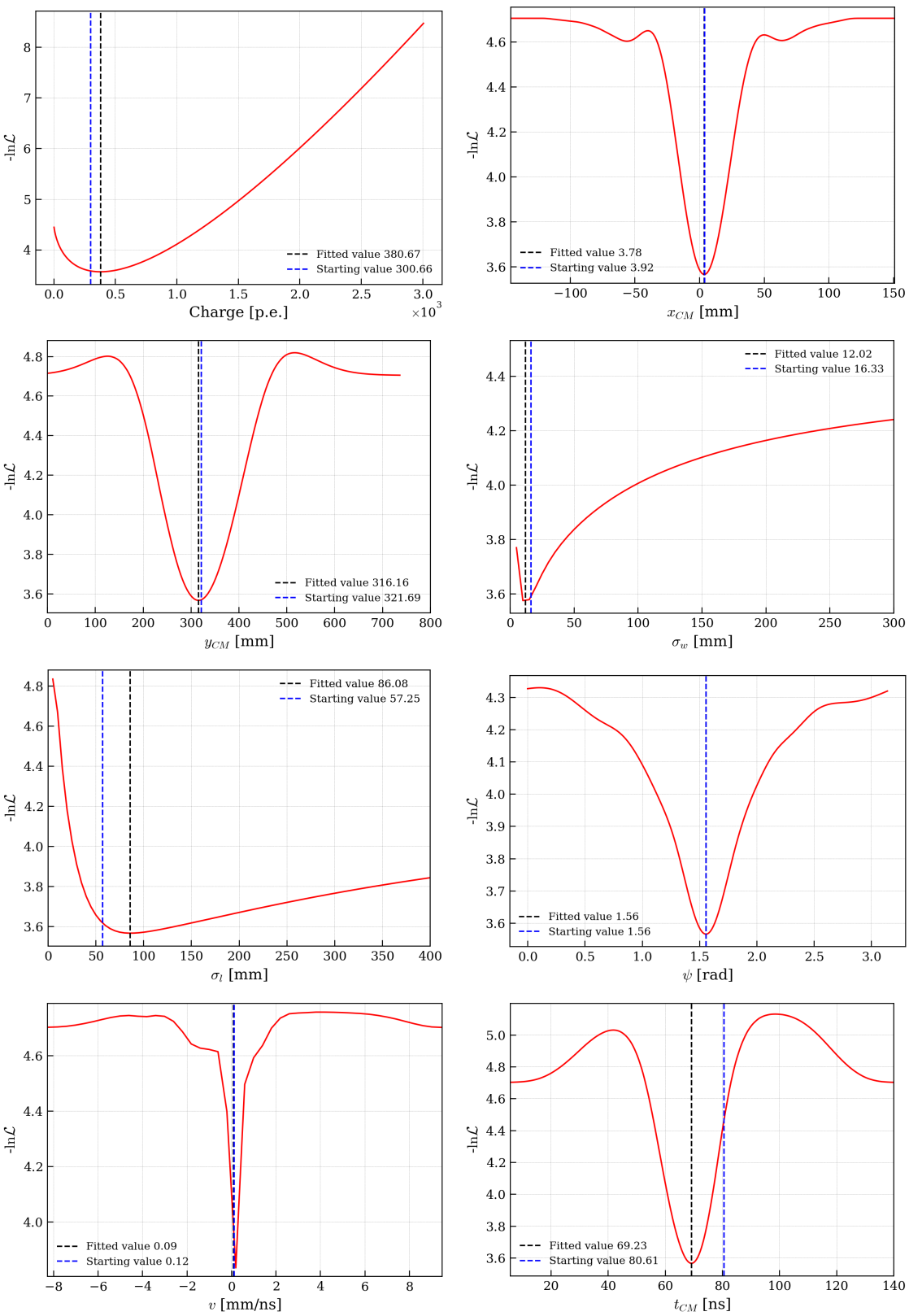

Figure VI.13. In red, negative log-likelihood profiles as function of the fit parameters $\vec{\theta}$. The negative log-likelihood is divided by the number of pixels and samples kept for the minimization. The initialization parameter are indicated with dashed-blue lines while the end parameters are indicated with dashed-black lines. The profiles correspond to the event shown in fig. VI.12.

resolution than using the procedures from section VI.2.1 and eq. (VI.13). Moreover, the log-likelihood $\ln \mathcal{L}$ includes pixel-wise fluctuations caused by the Poisson statistics or by the sensor response. In particular, the optical cross-talk μ_{XT} is statistically propagated through the reconstruction while the charge reconstruction from eq. (VI.13) only assumes average optical cross-talk. The resolution to single photo-electron is part of the likelihood via the parameter σ_s. The parameter σ_e takes into account the fluctuations of the waveform signal induced by electronic noise and NSB.[3] This parameter can be computed with interleaved images. These clocked-triggered images are acquired during gamma-ray observation and allow to retrieve snapshots of the night-sky. The parameter σ_e can be estimated from standard deviation of the images waveforms. Finally, the log-likelihood offers a way to self-clean the images as its maximization finds the optimal parameters $\vec{\theta}$ given the expected time-space parameterization and the observed waveforms knowing the calibration parameters $\vec{\theta}_c$.

The problems of the standard image parameterization, pointed out in the previous section, such as: the need to find an optimum integration window Δt of the waveforms maximizing signal-to-noise ratio; the necessity to clean the images based on two optimized thresholds; the fact that the timing parameters are dependent on the initially reconstructed direction of the image; the fact that the Poisson, NSB and sensor fluctuations are not taken into account by the standard image parameterization are all solved by maximizing the log-likelihood defined in eq. (VI.43).

VI.3 Reconstruction and identification of the primary particle

The processing of the raw data waveforms by maximizing the log-likelihood defined in eq. (VI.43) reduces directly the waveforms into image parameters. These image parameters are used to reconstruct the energy and direction of the primary particle initiating the EAS as well as the type of the particle. Here is presented the reconstruction of the properties of the primary particle for a single telescope. The analysis can be performed for an array of Cherenkov telescopes, which increases the precision of the end result. Specifically, the reconstruction of the incoming direction of the primary particle is much improved for stereoscopic reconstruction since the first interaction point in the atmosphere can be obtained from the crossings of the EAS images. In the case of a single telescope, the primary particle direction has to be inferred from a single image.

The properties of the primary particle are reconstructed using random forests regression and classification models. Other regression or classification model could be used but the fact that these are decision trees makes the model easily understandable. To be more precise, the importance of each of the image parameters can be obtained. This ensures that the models are properly interpreting the physical properties of the EAS event. The properties could also be inferred from semi-analytical formula but this approach has shown to have poorer performance than supervised training models [132]. Machine learning based reconstruction are currently investigated for IACTs [133, 134, 135].

The simulated triggered events, presented in section VI.1, are parameterized by maximizing the likelihood defined in section VI.2.2. The surviving probability of the events as

[3] These fluctuations are assumed to be normally distributed. While this is certainly a good model for the electronic noise, it is only a valid approximation of the NSB induced fluctuations at large NSB light levels.

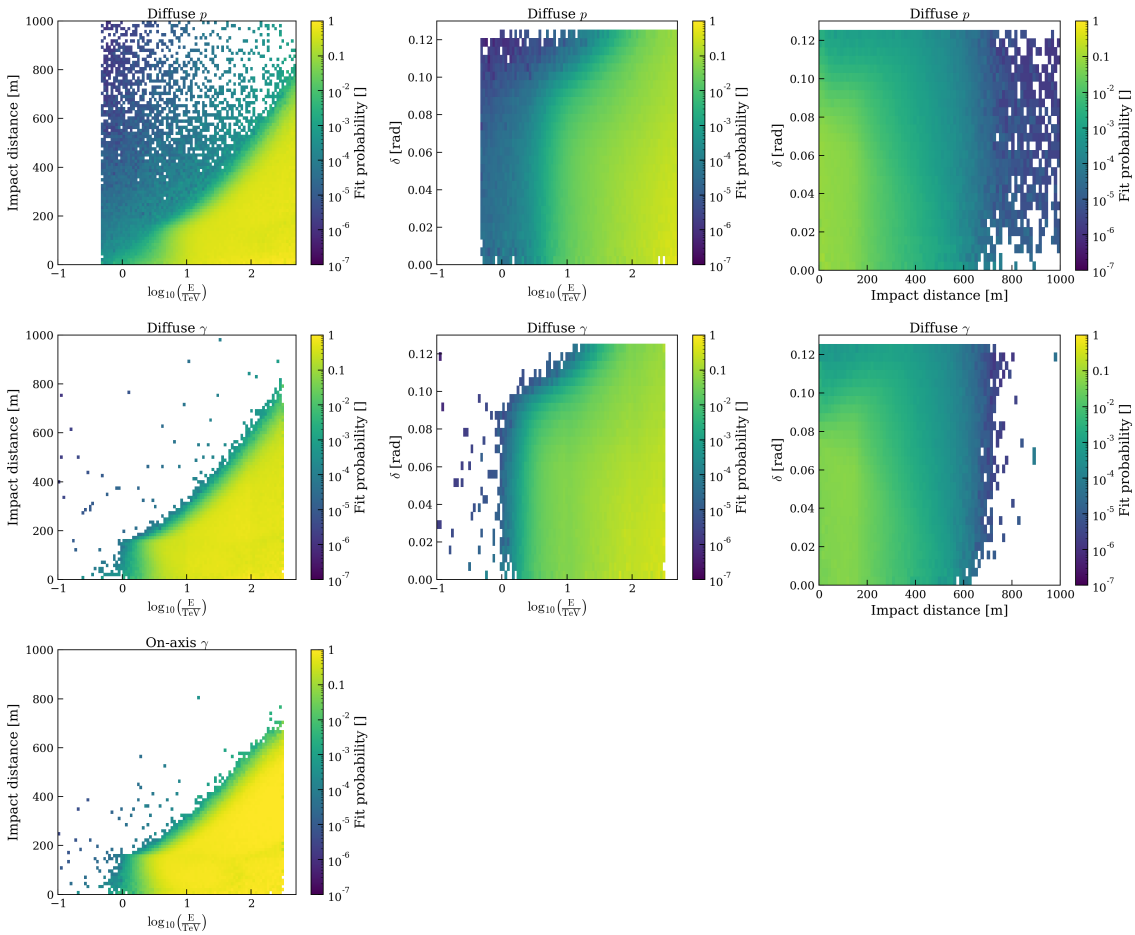

Figure VI.14. Probability of the events surviving the likelihood reconstruction defined in section VI.2.2 as function of the energy, the impact distance and the angular offset δ of the primary particle. Top: Diffuse protons. Middle: Diffuse gamma-rays. Bottom: On-axis gamma-rays.

function of the energy, impact distance and angular offset is shown in fig. VI.14. An event for which the minimum of the negative log-likelihood $-\ln \mathcal{L}$ is found is defined to have survived the reconstruction.

The random forests are trained on the Monte Carlo simulation data described in section VI.1 using the *scikit-learn* python library [136].

In section VI.3.1, the quality cuts applied to the data-set are presented. In section VI.3.2, the performance of the gamma versus hadron classification is presented. In section VI.3.3, the energy reconstruction random forest regressor is presented as well as its bias and resolution. Finally, in section VI.3.4, the performance of the direction reconstruction of the primary particle is shown.

VI.3.1 Data quality cuts

The trigger settings allow to select events which look like EAS images by selecting events that show an excess of clustered photo-electrons in time and space. Although this is efficient in reducing the number of triggered events induced by NSB fluctuations, it requires additional data selection criteria to keep the highest quality images. The quality

of the images can be assessed from the total number of photo-electrons contained in the image (the higher the better), from area of the reconstructed ellipse in comparison to the pixel area, from the ratio of the width to length of the reconstructed ellipse and from the containment of the ellipse within the camera frame.

First, if the brightness of the image is low in comparison to the background fluctuations it would lead into badly reconstructed parameters. Second, if the eccentricity of the reconstructed ellipse is to small it can be expected that the image is contained in a straight row of pixels therefore the width of the ellipse is poorly reconstructed (i.e. the width is comparable to the pixel radius). Third, if part of the Cherenkov signal is leaking out the camera frame the image parameters are not reliable. The quality cuts are defined as:

$$\mu \geq \mu_0; \tag{VI.58}$$

$$\frac{\sigma_w}{\sigma_l} = \sqrt{1-e^2} \geq e_0; \tag{VI.59}$$

$$c_0 \leq \mathtt{containment} \leq c_1, \tag{VI.60}$$

where μ is the reconstructed number of photo-electron in the image, e is the eccentricity of the reconstructed ellipse of width σ_w and length σ_l and the containment as defined as in eq. (VI.28).

The threshold values: μ_0, e_0, c_0 and c_1 are estimated from the distributions of the image quality parameters shown in fig. VI.15. The 2D correlation figures for the data quality parameters are found in figs. VI.16 to VI.18.

The cosmic-ray spectrum (and gamma-ray sources spectra) can be described by a power-law spectrum depending of the energy as $E^{-\gamma}$, $\gamma > 0$. Therefore the observed Cherenkov light emitted by the EASs should follow a power-law spectrum as well. As can be seen from fig. VI.15a, the total number of photo-electron follows a power law above ~ 100 p.e.. At this threshold the distribution reaches a maximum. A further descend of the distribution is expected below this maximum. Below ~ 60 p.e the slope changes. This is due to the NSB background fluctuations that artificially increases the total number of p.e. in the image. Thus this value is used as a quality cut. As the on-axis gamma-rays are always positioned between the center of the camera and its edge, the steepening of the slope of the size parameter distribution from 10^4 p.e. can be explained by the fact that these events are leaking out of the camera as can be seen from figs. VI.16 to VI.18.

The distribution of the width over length is shown in fig. VI.15b. As can be seen the protons have a larger width than the gamma-rays. This is understood by the fact that hadronic showers tend to create sub-showers which can be far from the main shower. The gamma-ray events (diffuse or on-axis) have the same distribution of eccentricity apart from an excess seen at about ~ 0.18 width over length for the on-axis gamma-rays.

In fig. VI.15c the distribution of the containment parameter is shown. The diffuse gamma-rays and protons show the same containment parameter distribution. As expected the diffuse particle are less contained than the on-axis gamma-rays. In figs. VI.16 to VI.18, the distribution of the containment parameter against the distance of the centroid of the ellipse to the camera center r_{CM} can be seen. From this figure, it can be seen that events which have a containment smaller than 0.5 are leaking out of the camera.

Based on the observations in figs. VI.15 to VI.18 the following quality cuts have been applied:

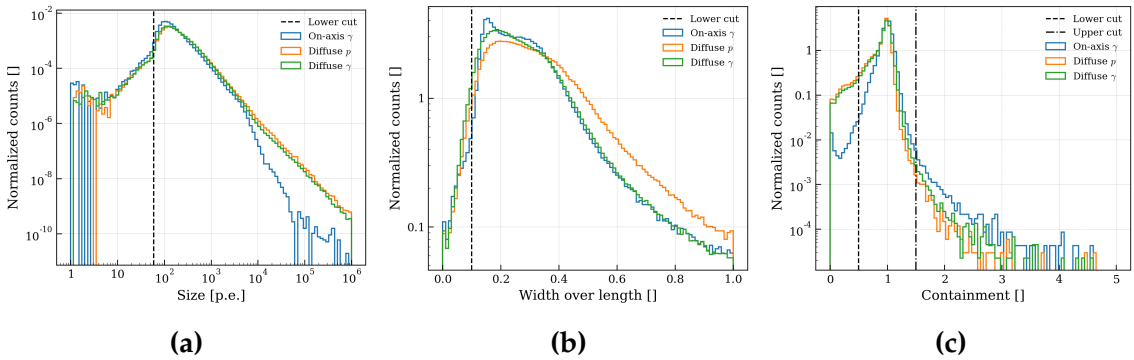

(a) **(b)** **(c)**

Figure VI.15. Image quality parameters distribution for on-axis gammas (blue), diffuse protons (orange) and diffuse gammas (green) obtained from the Monte Carlo simulation presented in section VI.1. From left to right are shown: the size parameter, the width over length ratio and the containment parameter. The distributions are shown before the quality cuts (all triggered events). The vertical lines indicate the quality cuts used.

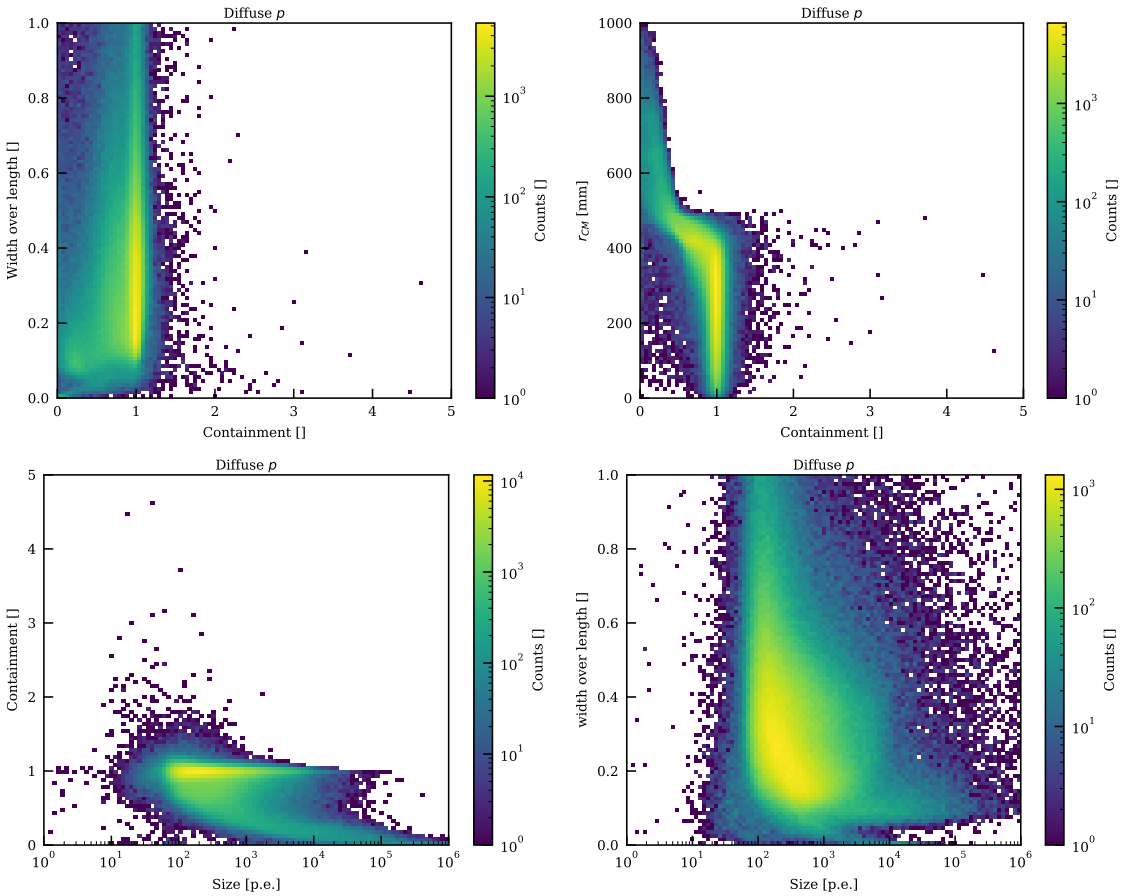

Figure VI.16. Two dimensional distribution of the quality cut parameters: width over length; containment; size as well as the distance of the ellipse centroid to the camera center for diffuse protons.

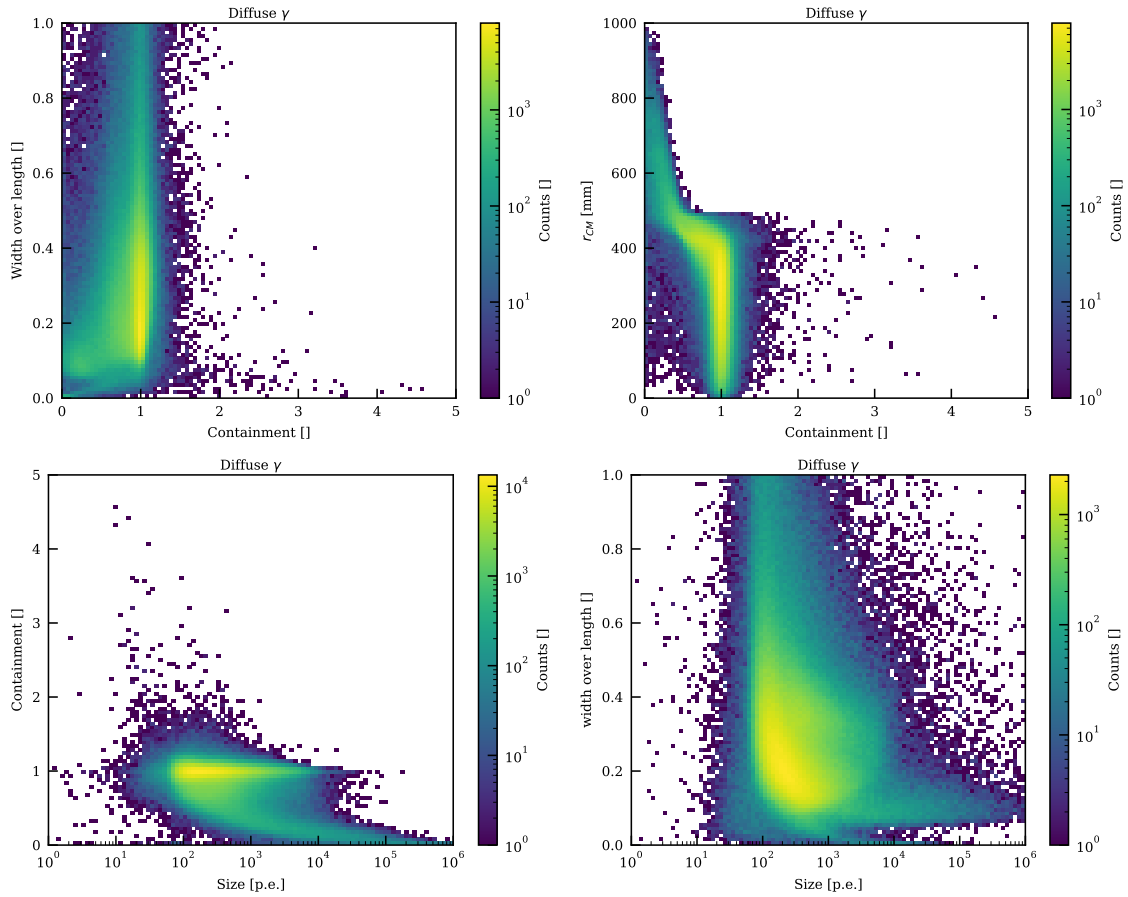

Figure VI.17. Two dimensional distribution of the quality cut parameters: width over length; containment; size as well as the distance of the ellipse centroid to the camera center for diffuse gamma-rays.

$$\begin{aligned} \mu_0 &= 60 \text{ p.e.}; \\ e_0 &= 0.1; \\ c_0 &= 0.5,\ c_1 = 1.5. \end{aligned} \tag{VI.61}$$

In fig. VI.19 the distribution of the simulated events after the quality cuts are shown. These distribution can be compared to the distribution of the trigger probability in fig. VI.2. It can be seen that the quality cuts discard events regardless of their energy, impact parameter nor angular offset. This can also be seen from figs. VI.20 and VI.21, where the effective areas and differential trigger rates as function of the energy after each steps are shown. The quality cuts are discarding events only based on their quality. Nonetheless, it can be noticed that a few events have been removed at the highest energies and small impact parameter. This can be understood by the fact that such event appear very large in comparison to the camera frame. Therefore they are removed by the containment quality cut.

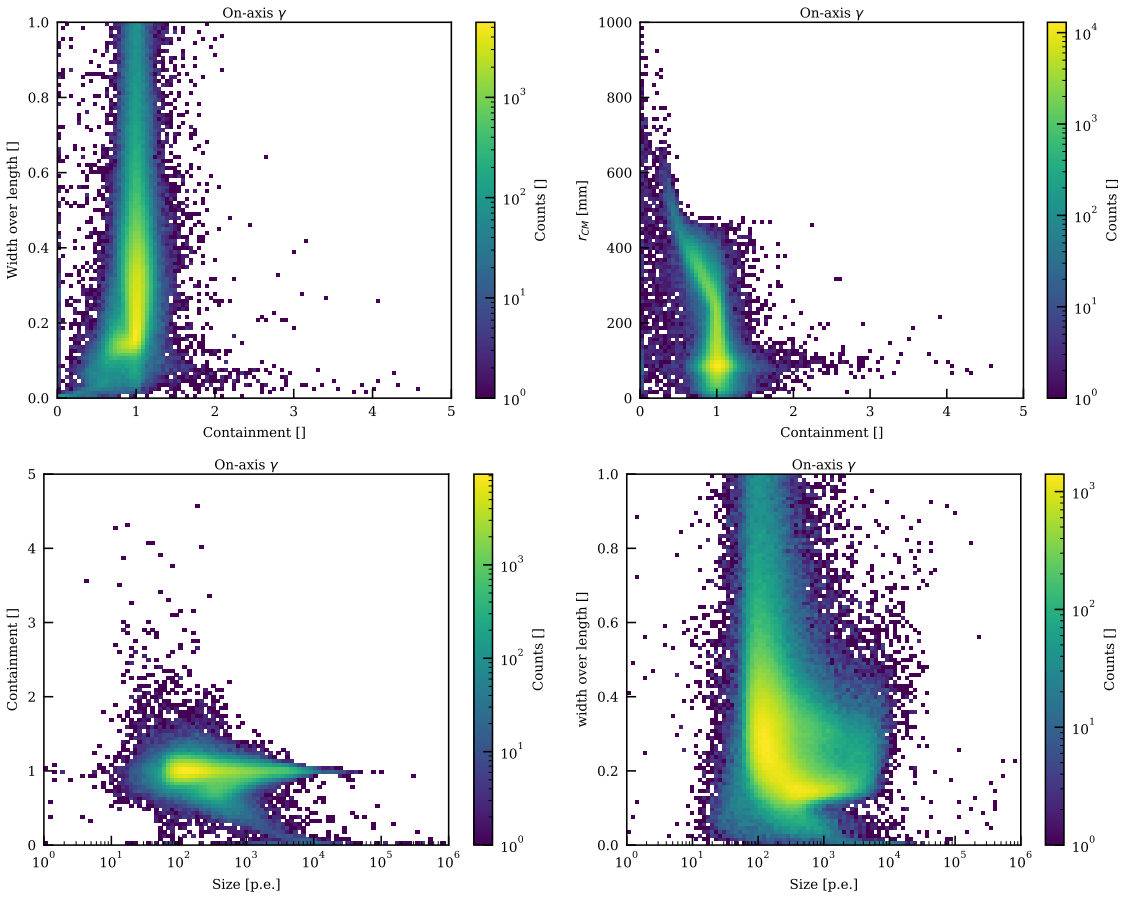

Figure VI.18. Two dimensional distribution of the quality cut parameters: width over length; containment; size as well as the distance of the ellipse centroid to the camera center for on-axis gamma-rays.

VI.3.2 Gamma-ray and hadron separation

As can be seen in fig. VI.21, even after the quality cuts, most of the events are protons. The sample is still dominated by diffuse protons. There is about 1.86×10^3 more proton background events than gamma-ray events. The distribution of the image parameters, after the quality cuts, for diffuse gamma-ray and diffuse protons is shown in fig. VI.22. One can see, that the parameters that differentiate the most gammas between protons are related to the shape of the image, i.e. width, length, area and width over length. It is also observed that the distributions of the diffuse particles (gammas and protons) is different that from on-axis gammas. The differences in ellipse centroid coordinates (x_{CM}, y_{CM}, ϕ and r_{CM}) between diffuse particles and on-axis gammas are understood by the fact that the source, for the first are located anywhere in the camera frame, and for the second at the center of the camera frame. The same reasoning applies to the α distribution, where α is computed as in eq. (VI.27) with $x_{source} = y_{source} = 0$ mm.

The gamma against hadron separation algorithm is applied to the sample (after the quality cuts) in order to maximize the signal over noise ratio. For this purpose a random forest classification is used. The training sample is composed of diffuse gammas and diffuse protons, although for real data the gammas are on-axis and not diffuse. Choosing, diffuse gammas allows to not bias the reconstruction based on the alignment of the shower

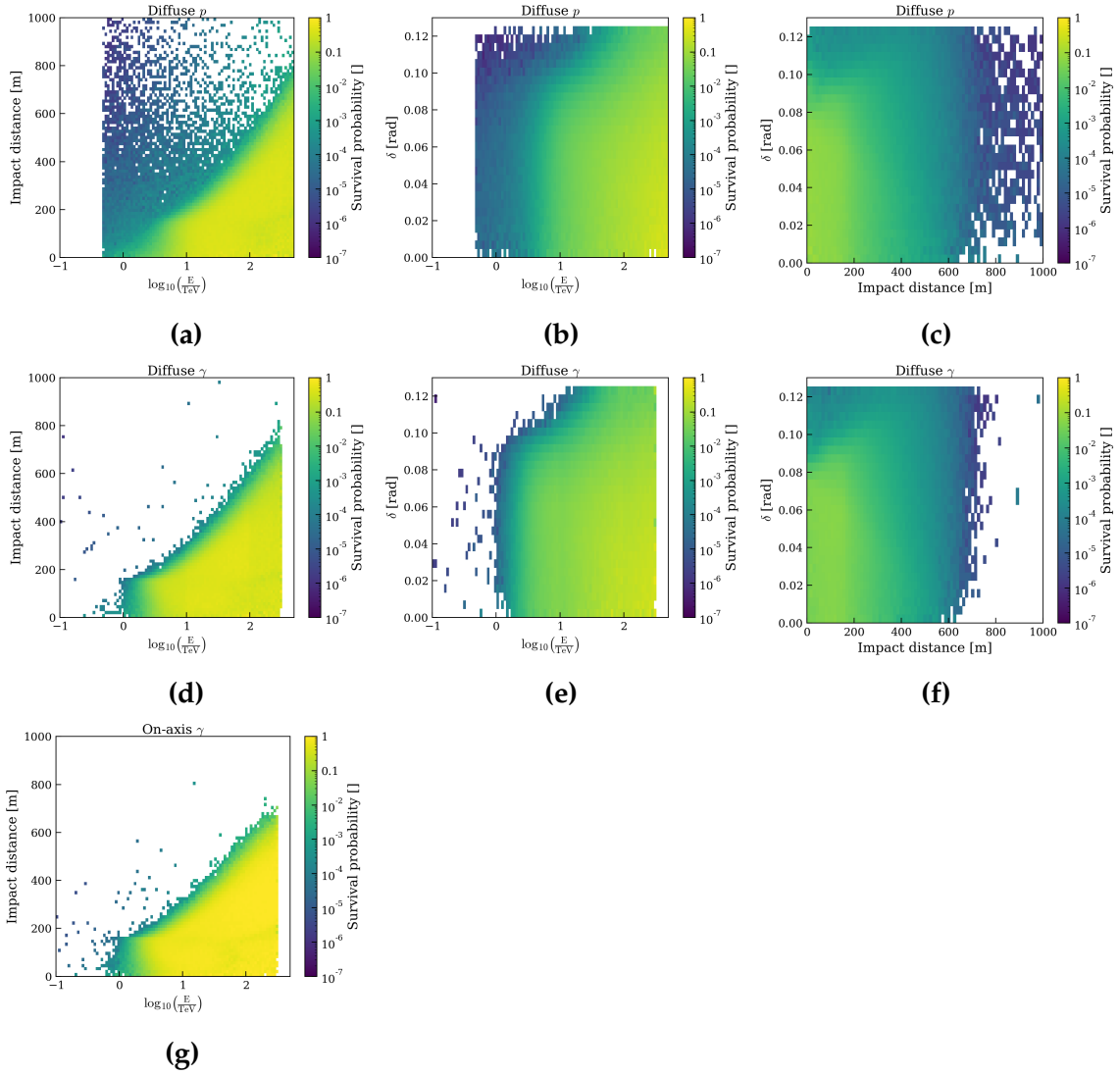

Figure VI.19. Probability of the events surviving the likelihood reconstruction defined in section VI.2.2 and the quality cuts defined in eq. (VI.61) as function of the energy, the impact distance and the angular offset δ of the primary particle. Top: Diffuse protons. Middle: Diffuse gamma-rays. Bottom: On-axis gamma-rays. For the initialization of the fit the standard reconstruction from section VI.2.1 is used with the cleaning parameters $T_{\mathrm{picture}} = T_{\mathrm{bound}} = 10$ p.e.

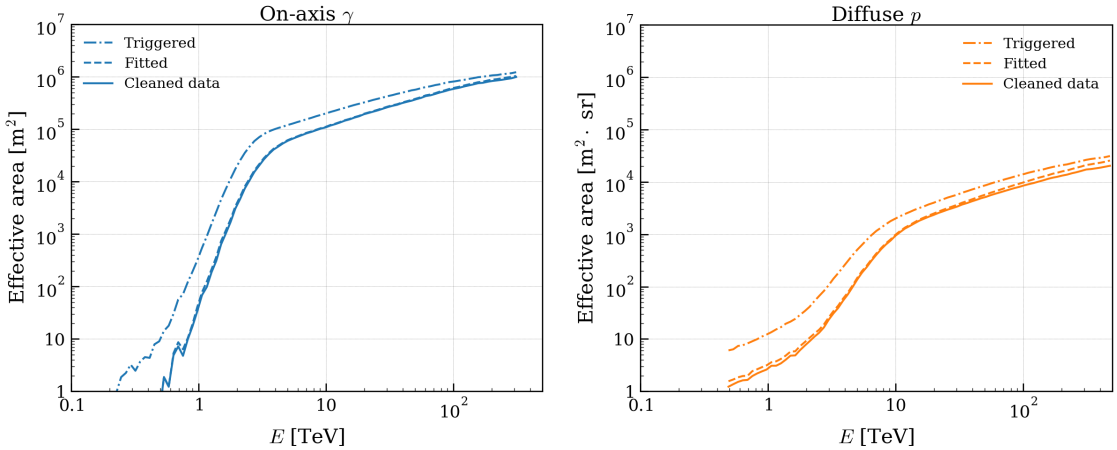

(a) **(b)**

Figure VI.20. Effective areas as function of energy for on-axis gamma-rays (left) and diffuse protons (right). The effective areas after each step of the reconstruction are shown: triggered events (dashed-dotted); are the parameterization (dashed); after the data quality cuts (solid). The effective areas are computed as explained in section VI.1.2

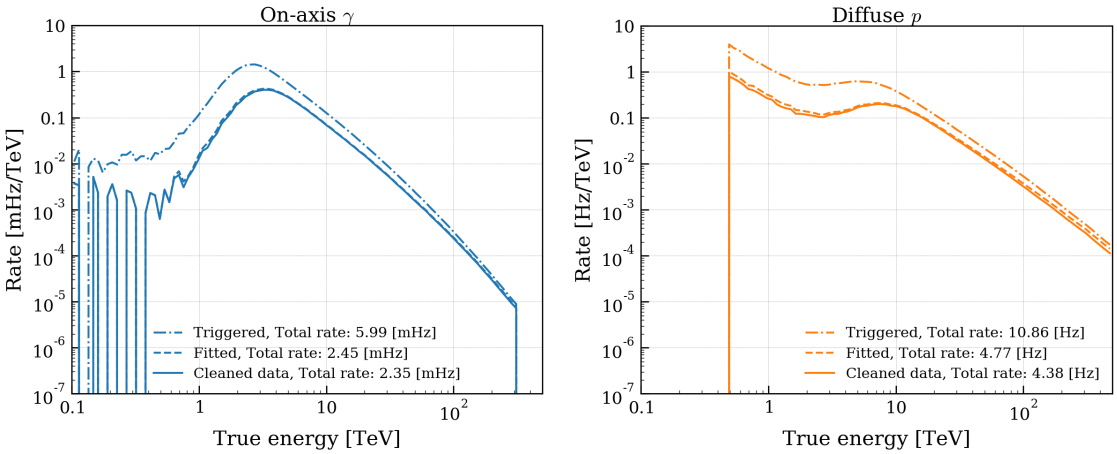

(a) **(b)**

Figure VI.21. Differential rates as function of energy for on-axis gamma-rays (left) and diffuse protons (right). The differential rates after each step of the reconstruction are shown: triggered events (dashed-dotted); are the parameterization (dashed); after the data quality cuts (solid). The differential rates are computed as explained in section VI.1.2

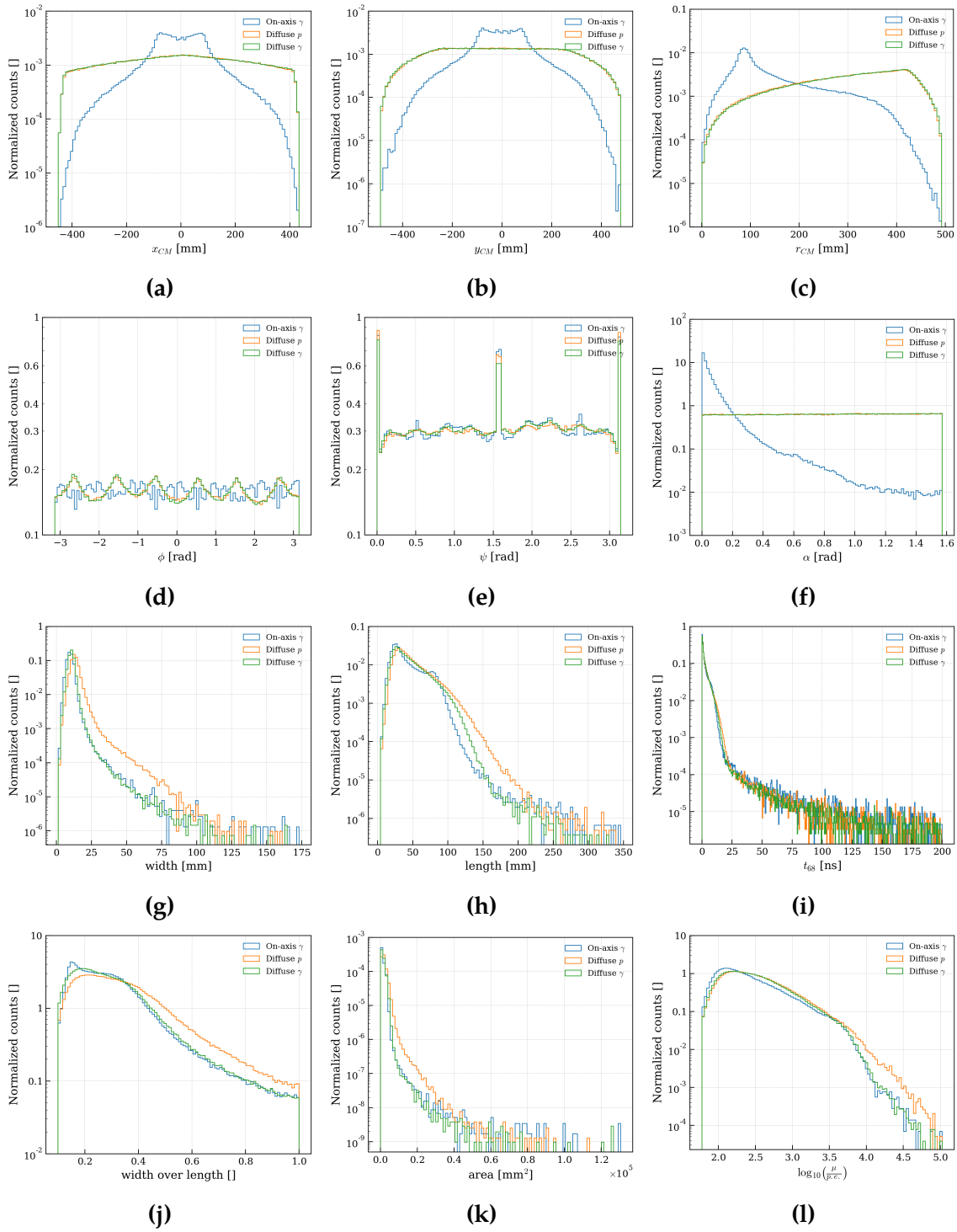

Figure VI.22. Image parameter distribution after the quality cuts for: on-axis gamma-rays (blue); diffuse protons (orange) and diffuse gamma-rays (green).

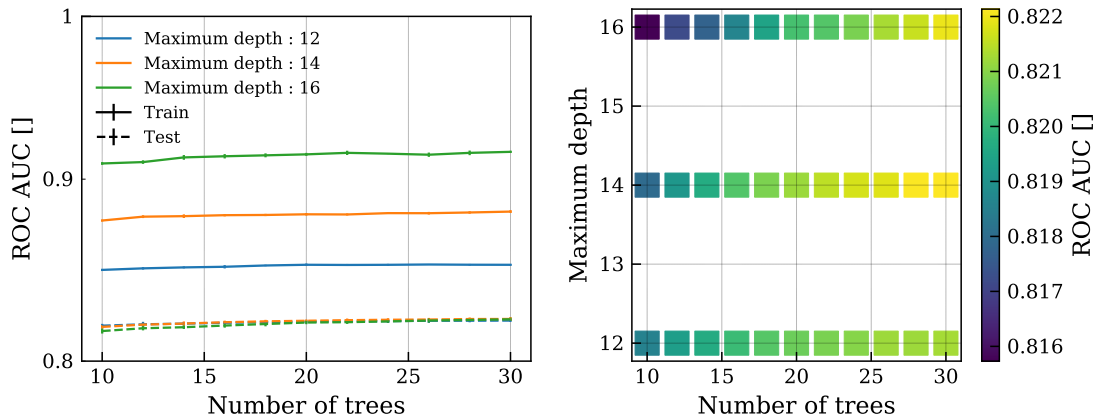

(a) **(b)**

Figure VI.23. Left: ROC AUC of the random forest gamma/hadron classifier as function of the number of trees and for different maximum depths of the trees. The dashed line represent the average ROC AUC on the k-fold testing data-sets while the solid lines represent the same score on the training data-sets. The error bars represent the variance of the k ROC AUC scores. Right: Average ROC AUC of the k-fold testing data-sets as function of random forest hyper-parameters: number of trees and maximum depth.

toward the center of the camera frame. Moreover, it allows to discriminate gammas against protons based on the shape of the image rather that its position. Additionally, some of the image parameters related to the ellipse position, used for the classification, are discarded. The parameters used are:

- the total number of photo-electron μ;
- the kurtosis;
- the skewness;
- the length σ_l;
- the width σ_w;
- the velocity v;
- the time duration t_{68};
- the density ρ;
- the longitudinal density ρ_l;
- the lateral density ρ_w;
- the area.

In order to prevent the random forest to over-fit training sample, a k-fold cross-validation is applied, with $k = 5$. The hyper-parameters of the random forest: the number of decision trees and maximum depth of the trees have been explored to find the best ROC (Receiver Operating Characteristic) AUC (Area Under Curve). The results are shown in fig. VI.23. The hyper-parameters maximizing the training scores are found for a random forest with 30 trees of maximum depth 14 nodes.

The ROC for this configuration is shown in fig. VI.24 together with the confusion matrices, considering a gammaness cut of 0.5.[4] The ROCs for the training and testing datasets are comparable which shows that the random forest is not over-trained. Moreover, the ROC AUCs, for both samples, are comparable and reach ~ 0.87. The gammaness distributions, as calculated by the random forest, are shown in fig. VI.25.

[4]Each event with a gammaness above 0.5 is considered as a gamma-ray while below it is considered as a proton/hadron.

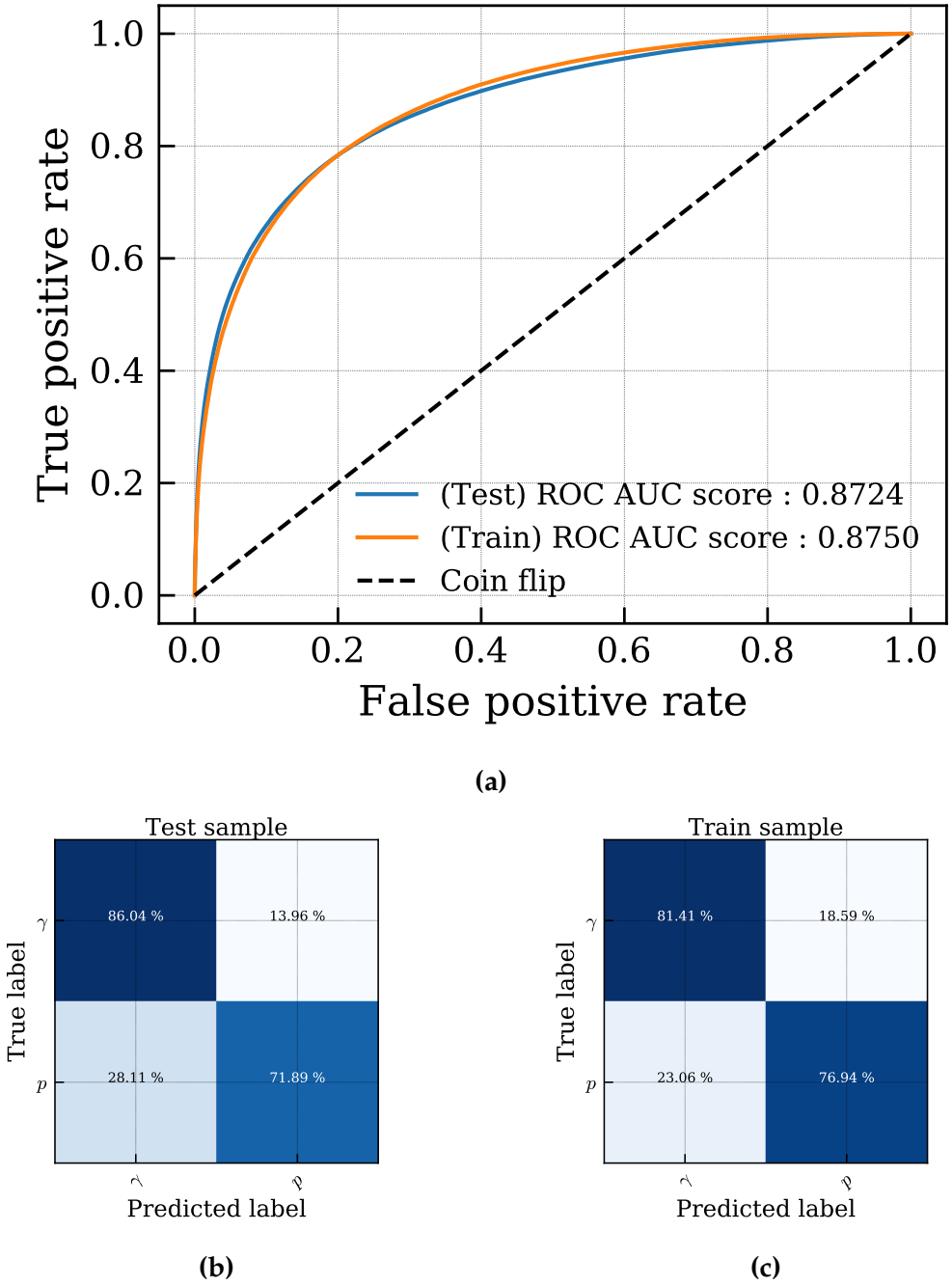

Figure VI.24. Top: ROC curve for the training and testing data-sets. Bottom: Confusion matrix for the test sample (left) and the train sample (right).

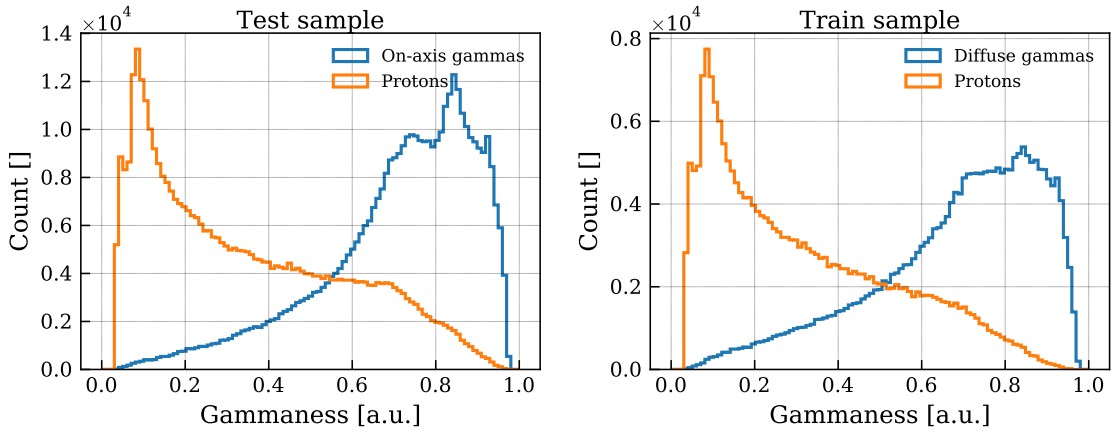

(a) **(b)**

Figure VI.25. Gammaness, as calculated by the random forest classifier, distributions for the testing (left) and training samples (right).

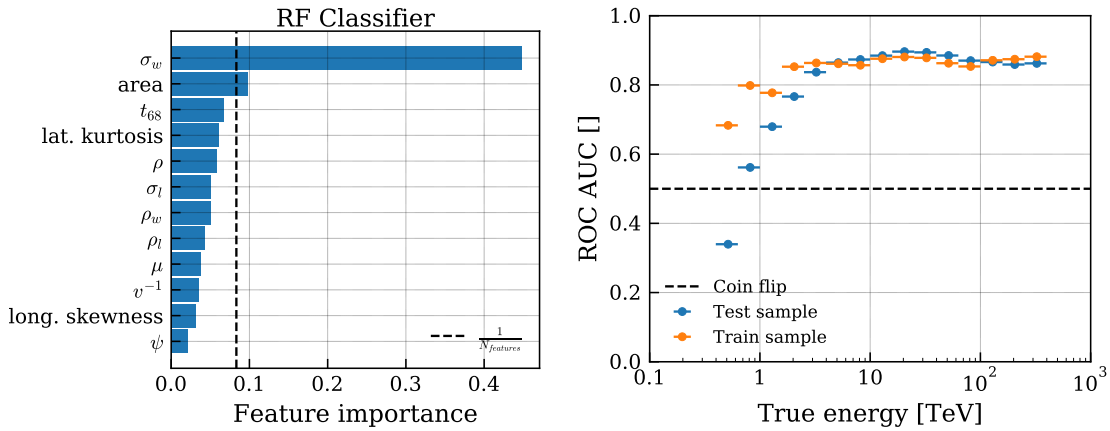

(a) **(b)**

Figure VI.26. Left: Feature importance of the random forest classifier. Right: ROC AUC in bins of energy for the training and testing data-sets.

This score is given for all of the primary particle energies. As shown in fig. VI.26, the ROC AUC in bins of energy is worse at the lowest energies, even passing below 0.5, and reaches a plateau of ROC AUC ~ 0.9 after ~ 2 TeV. Below 2 TeV, the large differences between the training and testing scores, and the fact that testing score drops below 0.5 for energies lower than 0.6 TeV can be understood by the poor statics at these energies. In fig. VI.26 is also shown the feature importance for the gamma/hadron separation. The width appears as the most important feature. This can be understood from the distribution of the width parameter in fig. VI.22. From this figure it can be noticed that the features related to the shape of the image are used and important to discriminate between the two classes. The orientation angle ψ of the images does not play an important role as it is the least contributing feature. Therefore, the model understood that the orientation of the image has no importance in the determination of the particle type.

VI.3.3 Energy reconstruction

To reconstruct the energy of the gamma-ray events, a random forest regression model is used. The length of first interaction of the gamma-ray depends on its energy, the centroid distance r_{CM} of on-axis gamma-ray is correlated to the primary energy. In order to avoid to bias the energy reconstruction, it is trained on diffuse gamma-rays but evaluated on on-axis gamma-rays. The training image parameters used are the same as the ones used for the gamma/hadron separation. A k-fold cross-validation, with $k = 5$, is also applied. The hyper-parameters of the regressor are optimized by maximizing the coefficient of determination R^2.[5]

The feature importance of the energy regressor is shown in fig. VI.27 (left) where it can be observed that the three most important features are the time of 68.2% containment t_{68}, the size parameter μ and the area of the ellipse. Obviously, the number of Cherenkov photons created by the EAS's charged particles is increasing with increased energy. Within the Cherenkov light pool the photon density is quite constant (for a given energy) but outside the density of photons decreases rapidly and therefore the detected number of photo-electrons is lower. This can be seen in fig. VI.5 (right). The size parameter gives a lower limit for the energy estimate. In fig. VI.5 (right), the events observed from the light pool correspond to the maximal intensity in each energy bin. The parameters t_{68} and the ellipse area allow the RF to interpret the impact parameter of the EAS (see fig. VI.5 left).

In fig. VI.27 (right) is shown the energy migration matrix. The resolution and bias of the energy reconstruction can be observed from fig. VI.28. On the right of this figure is shown the distribution of the relative energy difference as function of the simulated energy. On the left of this figure is shown the energy bias (median) and energy resolution (68.2% containment) in bins of simulated energy. The energy bias is above 0.25 for energies lower than 10 TeV and reaches down to 0 for energies between 10 TeV and 100 TeV. The bias then becomes negative (underestimation) for energies higher than 100 TeV down to about −0.1. The rather large biases below 10 TeV and above 100 TeV can be explained by the lack of statistics. The quality cuts remove a lot of the lowest energy events while the number of simulated events at the highest energy is low. The energy resolution reaches 0.4 above 10 TeV and goes down to 0.2 at about 300 TeV.

VI.3.4 Direction reconstruction

To reconstruct the point of origin in the sky of an EAS event a RF regression model is used. To reconstruct the source camera coordinates (x_{source}, y_{source}), the model has to learn that it is located on the major axis of the ellipse and at a certain distance of its center. In order to simplify, the reconstruction the RF is trained to reconstruct the displacement vector (DISP). The vector DISP, $\overrightarrow{DISP}$, is the vector between the camera coordinates of the source and the reconstructed centroid coordinates (x_{CM}, y_{CM}):

$$\overrightarrow{DISP} = (x_{source} - x_{CM}, y_{source} - y_{CM}). \tag{VI.62}$$

An illustration of the DISP vector is shown in fig. VI.4.

[5]The coefficient of determination is defined as $R^2 = 1 - \frac{SS_{res}}{SS_{tot}}$. Where SS_{res} is the sample squared sum of the differences between the sample values and the sample mean. SS_{tot} is the sample squared sum of the differences between the sample values and the predicted values. A perfect regression model has an R^2 of 1.

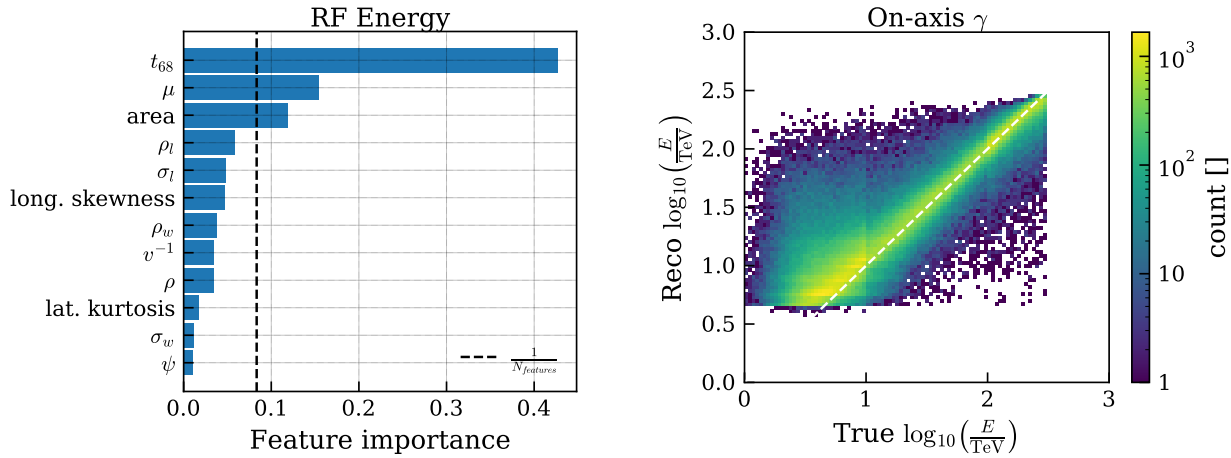

(a) **(b)**

Figure VI.27. Left: Feature importance of the random forest energy regression model. Right: Reconstructed energy versus simulated energy migration matrix. The dashed line indicates the ideal energy reconstructor.

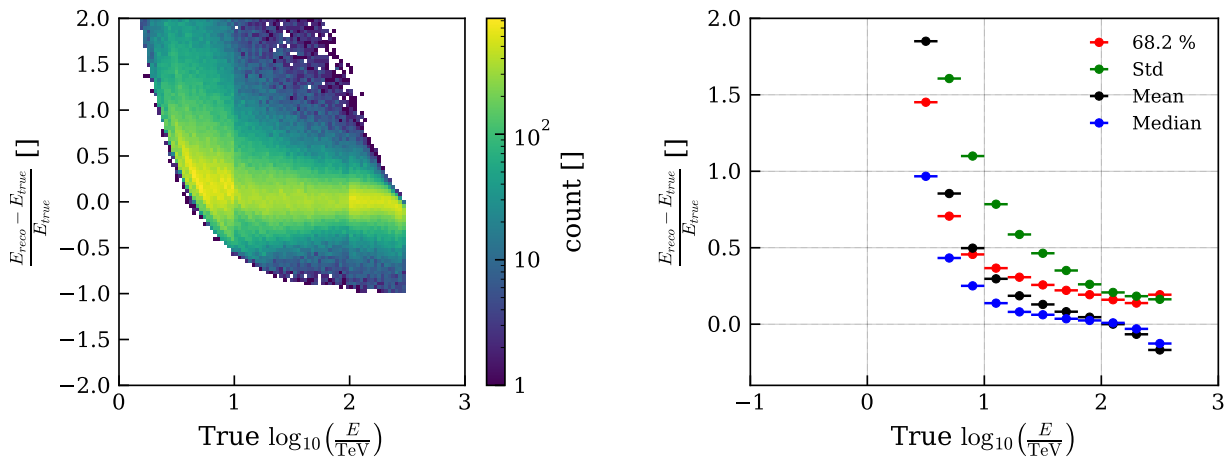

(a) **(b)**

Figure VI.28. Left: two-dimensional histogram of the relative energy resolution as function of the simulated energy. Right: Median (blue) mean (black), standard deviation (green) and 68.2% containment (red) of the relative energy resolution as function of the simulated energy.

This coordinate transformation, simplifies the training process since the RF does not need to know the position of the ellipse in the camera frame to reconstruct the source position. Additionally, if the RF would be trained on point gamma-rays, the source position to reconstruct would always be the same (i.e. $x_{source} = y_{source} = 0$). Therefore the regression model would learn to return the same value for all inputs and would not learn to reconstruct the source position.

The RF is trained on diffuse gamma-rays and tested on point gamma-rays. The model uses the same regression features as for the energy regressor. The model is trained using a k-fold ($k = 5$) cross-validation technique to search for the best combination of the RF hyper-parameters (number of trees and maximum depth of a tree) that maximize the coefficient of determination R^2. The result of this search are shown in fig. VI.29 (right). The best combination of hyper-parameters is used to evaluate the performances of the RF. The feature importance of the RF regressor are shown in fig. VI.29 (left).

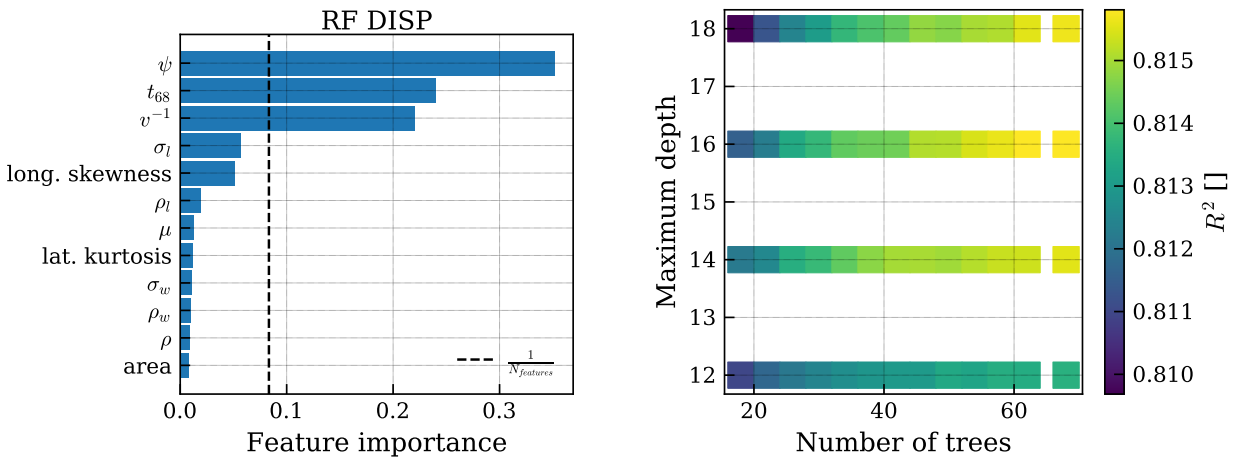

(a) **(b)**

Figure VI.29. Left: Feature importance of the random forest DISP regressor. Right: Average of the cross-validation ($k = 5$) test coefficient of determination R^2 for the DISP random forest regressor.

The most important feature is the orientation angle of the ellipse ψ since the source is supposed to be on the major axis of the ellipse. Then come parameters that measure the longitudinal displacement: t_{68} and v^{-1} which inform on the velocity at which the image moves; length σ_l and longitudinal skewness which measure the second and third order momenta of the ellipse in the longitudinal direction. The rest of the parameters do not play any significant role in the direction reconstruction.

The reconstructed source position of the test samples (diffuse protons and on-axis gammas) are shown in fig. VI.30. It can be seen that the reconstructed source position of diffuse protons is indeed diffuse. In fact the 68% containment radius R_{68} measures 4.2 deg which correspond to about half of the camera FoV. On the contrary, the angular resolution, defined as R_{68}, for the on-axis gamma-rays is about 0.67 deg.

The angular resolution mentioned correspond to the angular resolution for all triggered event. In fact, the resolution depends on the energy of the primary particle of the EAS. The angular resolutions as function of the simulated and reconstructed energies are shown in fig. VI.31.

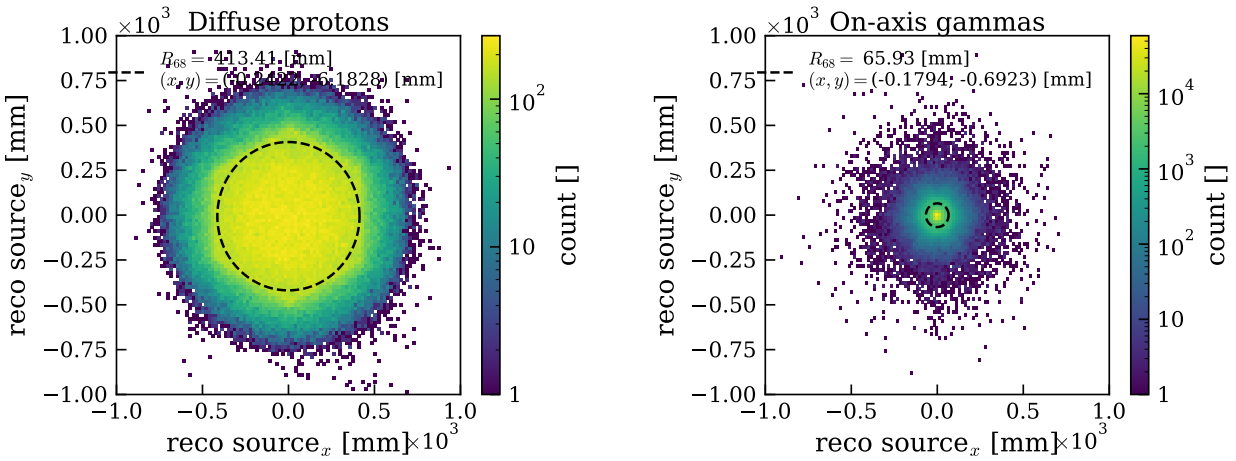

(a) **(b)**

Figure VI.30. Reconstructed source coordinates of the diffuse protons test sample (left) and point gamma-rays sample (right). The dashed circle, centered at the mean reconstructed position, indicates the 68% containment radius.

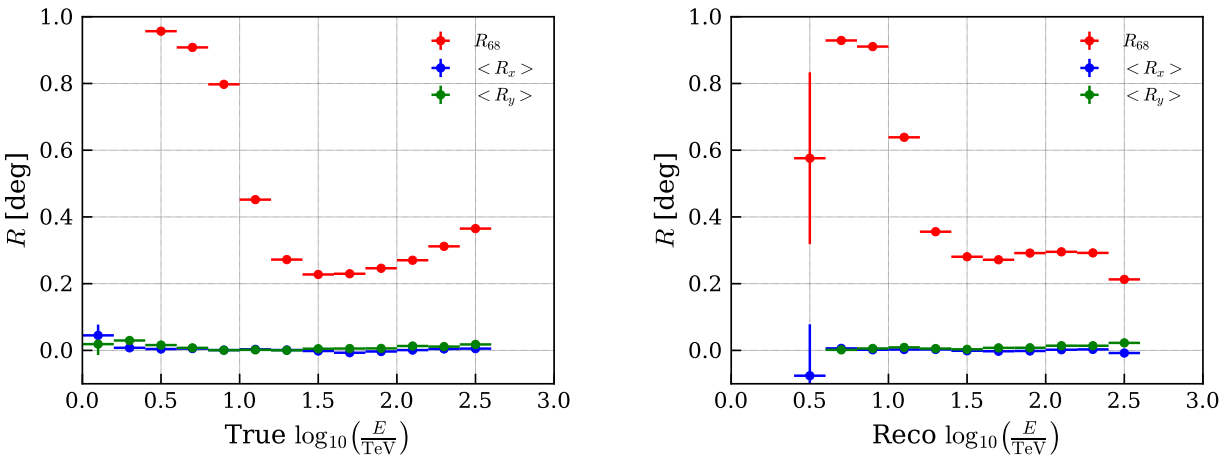

(a) **(b)**

Figure VI.31. Angular resolutions (red) and angular bias (blue and green) in bins of simulated energy (left) and reconstructed energy (right). The angular resolution is computed as the 68% containment radius R_{68}.

Additionally, to understand what improves the angular resolution, the distribution of the α parameter as function of width over length and t_{68} is shown in fig. VI.32. One can see that elongated ellipses (i.e. small width over length) have better angular resolution than "rounded" ellipses (i.e. width over length $\sim$ 1). Additionally, the longer the event lasts the better the angular resolution. For almost instantaneous events (i.e. $t_{68} \sim 0$ ns) there is no lever arm to constraint the ellipse direction based on the image velocity.

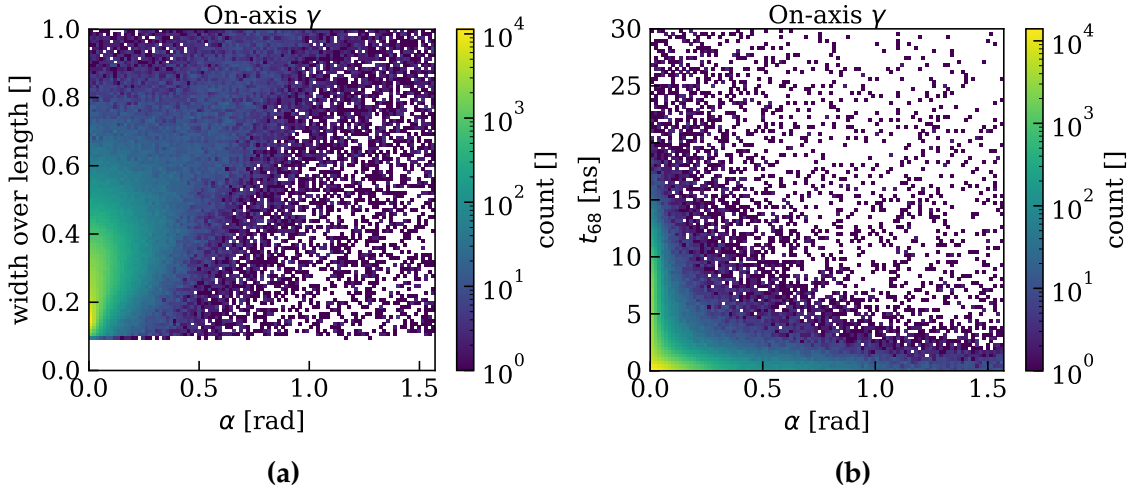

Figure VI.32. Off-axis angle α between the source position and orientation angle of the ellipse ψ for on-axis gamma-rays. The α parameter is shown as function of the width over length (left) and t_{68} (right) parameter. The sample is shown after the quality cuts defined in section VI.3.1.

VI.4 Sensitivity to the Crab energy spectrum

In section VI.2 reduction of the waveforms into image parameters is explained and in section VI.3 is explained how these image parameters can be used to infer the energy, gammaness and direction of a triggered EAS events. The performances in terms of gamma/hadron separation, angular and energy resolutions are given. However, these do not inform on the sensitivity of the reconstruction pipeline and the telescope to a given gamma-ray source.

VI.4.1 Final event selection

The sensitivity of the telescope is computed by looking at the significance of gamma-identified events excess for various bins of energy. Each on-axis gamma-ray and each diffuse proton of the test sample are reconstructed using the image parameterization described in section VI.2.2 while the energy, direction and gammaness are reconstructed using the trained RF models from section VI.3. The events are re-weighted such that the rates of each events correspond the to the proton spectrum (see eq. (I.6)) for the diffuse proton sample and to the Crab Nebula spectrum for on-axis gamma-rays (see eq. (I.40)). The weights are computed as explained in section VI.1.4.

To identify the gamma-like events two of the RFs output are used: the gammaness and the DISP. The first, as its name suggest informs on the likelihood of an event to be a gamma-ray event. While the second is used to define a circular region, of angular radius θ, around the expected source position (x_{source}, y_{source}).

VI.4.2 Differential flux sensitivity computation

The differential flux sensitivity F to a flux Φ is computed in bins of energy E_i. The energy bins E_i are logarithmically spaced and 5 energy bins are created per energy decade. The differential flux sensitivity is defined as:

$$F(E_i) = \frac{N_{on} - \alpha N_{off}}{N_{5\sigma}(N_{on}, N_{off}, \alpha)} \Phi(E_i) = \frac{N_\gamma}{N_{5\sigma}(N_{on}, N_{off}, \alpha)} \Phi(E_i) \tag{VI.63}$$

where $T_{on} = 50$ h is the observation time on the source, $T_{off} = 250$ h is observation period off the source, $\alpha = \frac{T_{on}}{T_{off}} = 0.2$ is the ratio between the observation times, N_{on} is the number of events on the source, N_{off} is the number of events off the source and where $N_{5\sigma}$ is number of excess (gamma-ray) required to reach a Li&Ma [137] significance $S_{Li\&Ma}$ of 5. The Li&Ma significance is defined as:

$$S_{Li\&Ma} = \sqrt{2\left(N_{on} \ln\left[\frac{1+\alpha}{\alpha}\left(\frac{N_{on}}{N_{on}+N_{off}}\right)\right] + N_{off} \ln\left[(1+\alpha)\left(\frac{N_{off}}{N_{on}+N_{off}}\right)\right]\right)}. \tag{VI.64}$$

Additionally, two conditions are required to compute the sensitivity:

- The number of excess gamma should be greater or equal to 10 in each energy bin: $N_\gamma = N_{on} - \alpha N_{off} \geq 10$.
- The excess should be above 5% of the background in each energy bin: $\frac{N_\gamma}{\alpha N_{off}} \geq 0.05$.

VI.4.3 Optimization of the differential flux sensitivity

Final selection cuts on the events are applied to reject background events. Events from which the gammaness is smaller than a threshold g_0 are rejected. As gamma-ray events should come from a point in the sky, events for which the reconstructed source position is at an angular distance θ bigger than a certain threshold θ_0 are also rejected. The two selection cuts, θ_0 and g_0, are chosen such that the differential flux sensitivity, defined in eq. (VI.63), is minimized. This minimization of the sensitivity is done independently for each bin of reconstructed E_i (obtained from the RF energy regressor). The corresponding scan of gameness and θ^2 cuts are shown in fig. VI.34.

The gammaness cuts g_0 and θ_0^2 cuts minimizing the differential flux sensitivity for each reconstructed energy bin are shown in fig. VI.33. The corresponding differential flux sensitivity is shown in fig. VI.35. As can be seen, even after 50 h of observation the SST-1M telescope is not able to detect the Crab with at 5σ confidence level. This can be explained by the high NSB simulated for the Krakow observational conditions (290 MHz NSB rate). The NSB fluctuations reduce the image quality and pushes the minimum trigger image to high values which in the end reduces the number of events at the lowest energies. For ideal observational conditions, a lower energy threshold is expected as well as better sensitivity below 30 TeV.

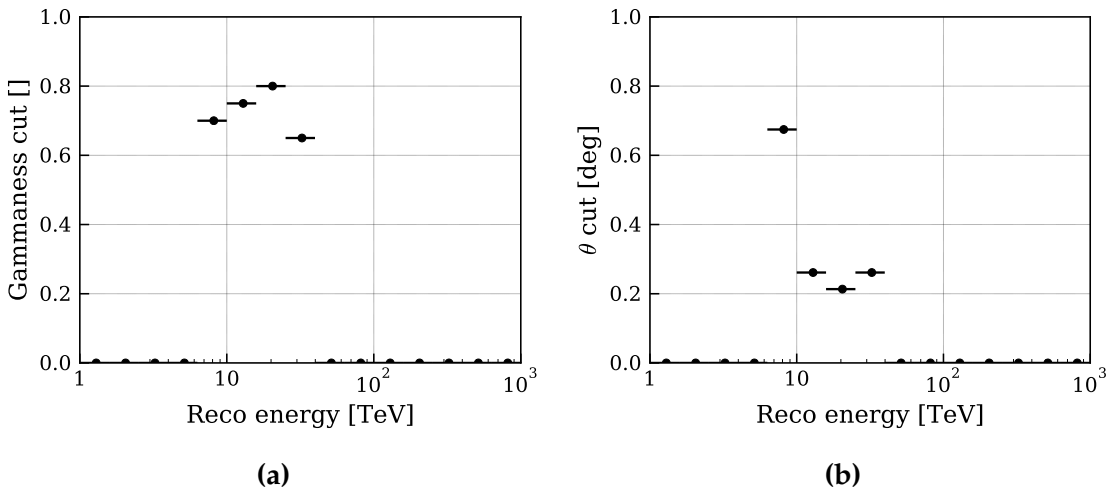

Figure VI.33. Gammaness (left) and θ^2 (right) cuts minimizing the differential flux sensitivity shown in fig. VI.35 for each bin of reconstructed energy.

VI.5 Event reconstruction of the CTA large-sized telescope

The sensitivity of the analysis for the SST-1M telescope was presented. However, it was shown that with the high NSB condition of the Kraków site it is difficult to detect the Crab Nebula at a significant level. To compare the likelihood-based method that has been applied to the SST-1M, the analysis has been carried to an other Cherenkov telescope: the CTA LST. Fortunately, the LST simulations have been widely used and the sensitivity for the standard analysis, as described in section VI.2.1, have been computed by member of the LST collaboration. In particular, the LST collaboration uses the *lstchain* [138] software for the reconstruction of the image parameters.

The LST Monte Carlo *prod3* was used. It corresponds to a simulation production of the CTA. These simulations are produced with the same simulation software as for the ones in section VI.1. However, the configuration is adapted for the LST telescope and uses the latest instrument description.

First, a brief explanation on how the method was adapted to the LST is given. Then, the sensitivities and performances are compared and discussed.

VI.5.1 Configuration

The likelihood defined in eq. (VI.43) requires to define the calibration parameters. In particular, the pulse template of the LST has been changed. In fig. VI.36 are shown the LST pulse templates $h(t)$ for the high and low gain channels. The gain selection is based on the pulse amplitude. The likelihood is calculated for the selected channel only.

The single photo-electron gain smearing was estimated at $\sigma_s = 0.57$ p.e. Then since the optical cross-talk is an effect present in SiPMs and not in PMTs (the photo-sensors used for the LST) the optical cross-talk was set to $\mu_{XT} = 0$.

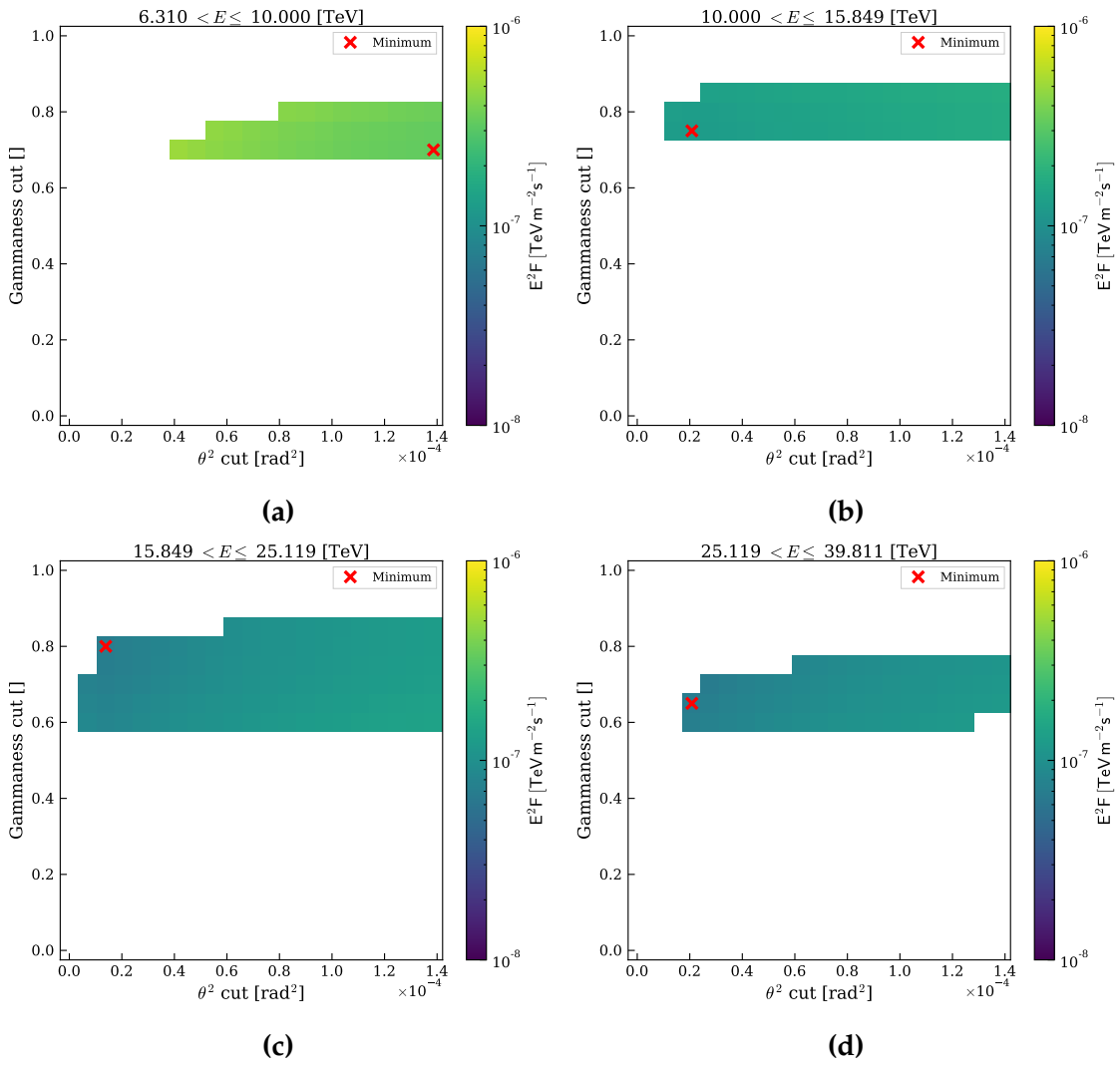

Figure VI.34. Differential flux sensitivity as a function of the cut in the angular distance θ^2 and the gammaness for different reconstructed energy bins. The bins in energy are increasing in reading order. The minimum differential sensitivity is indicated on each plot with a red cross corresponding to the optimal cuts shown in fig. VI.33.

VI.5.2 Performance comparison

The sensitivity is computed as described previously. In addition the diffuse electron background is added to calculation.

A fare comparison between the *lstchain* sensitivity and the one of this work is shown in fig. VI.37. The sensitivities with *lstchain* are computed with three waveform integration methods, namely: *GlobalPeak*, *LocalPeak*, *NeighborPeak*. The first integrates the waveforms within a time window that is identical for all pixels. The second integrates the waveforms within a time window that is unique for each pixel and centered at the maximum of the waveforms. The last, integrates the waveforms within a time window centered at the maximum of the averaged waveforms of neighboring pixels. The same quality cuts (size greater than 200 p.e. and leakage[6] smaller than 0.2) were used. Moreover, the same θ^2

[6]The leakage is defined as the fraction of cleaned pixels that fall on the last two pixel rows of the camera

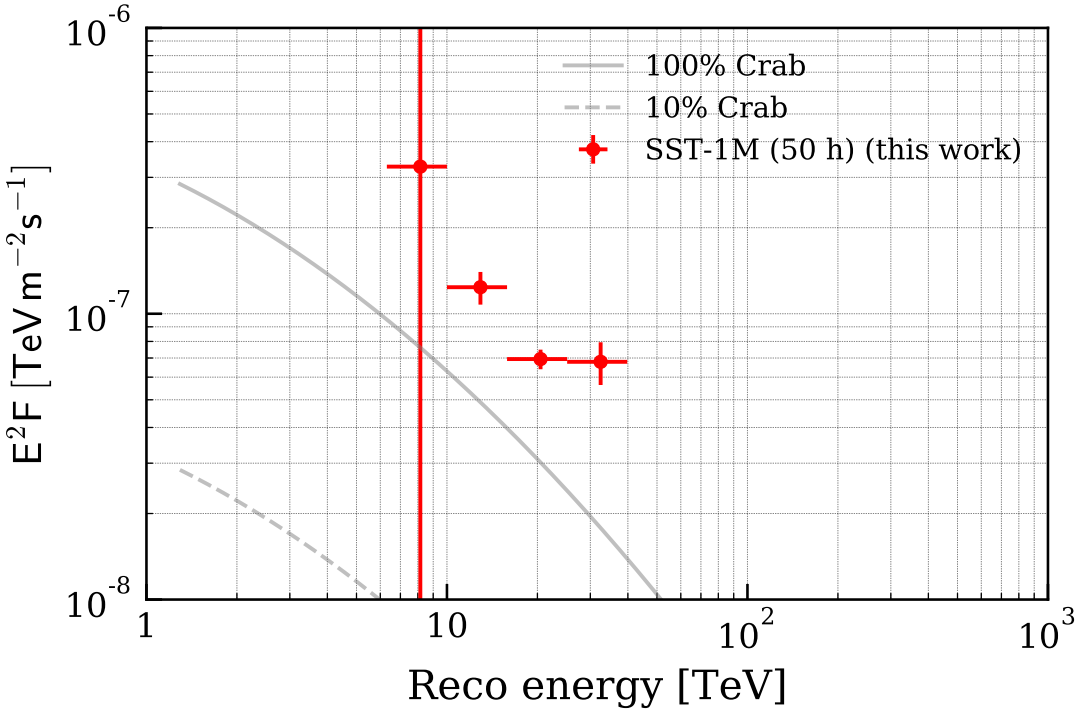

Figure VI.35. Differential flux sensitivity as a function of the reconstructed energy for the SST-1M telescope (red). The differential flux sensitivity is multiplied by E^2. An on-axis exposure of 50 h is assumed. The gray lines represent fractions of the Crab Nebula flux.

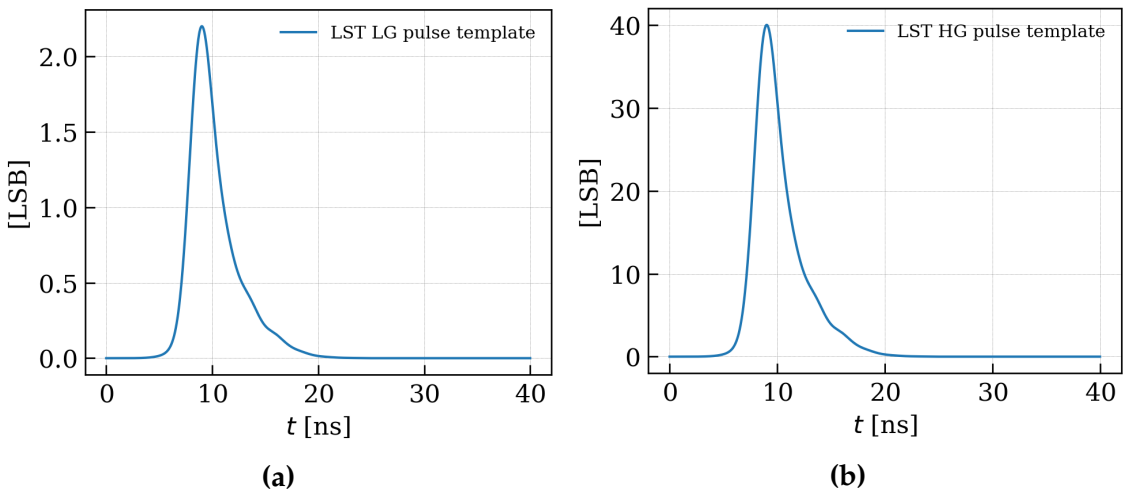

Figure VI.36. Pulse templates for the low (left) and high (right) gain channels of the LST *prod3* simulations. The amplitude is given in units of LSB for 1 p.e. which correspond to 2.2 LSB per p.e. for the low gain channel and 40 LSB per p.e. for the high gain channel. The two pulses are identical.

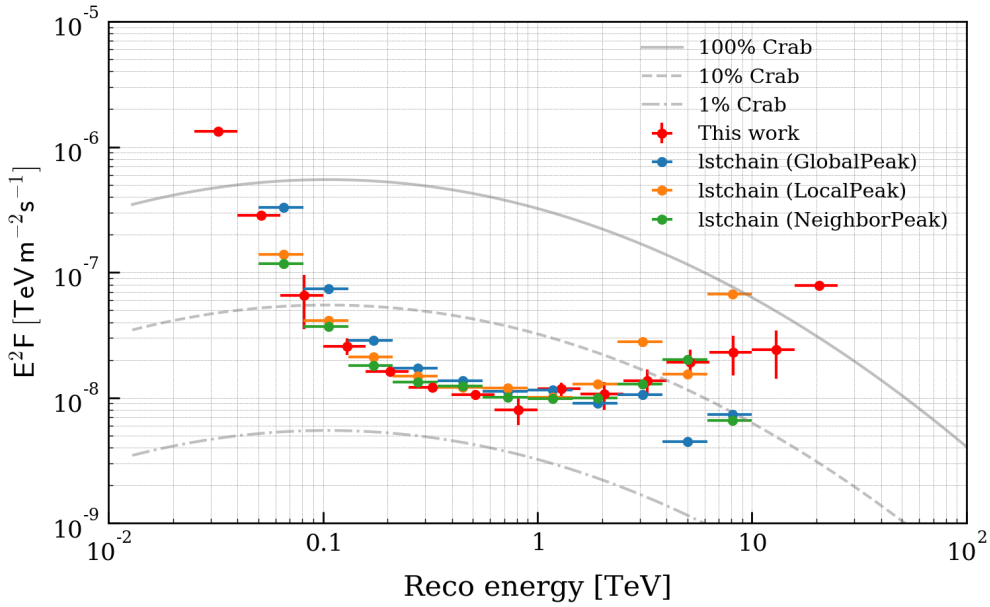

Figure VI.37. Comparison of the flux sensitivity obtained with the *lstchain* reconstruction software with three charge integration reconstruction (blue, orange and green). The flux sensitivity obtained with this work is shown in red and uses the same quality and final selection cuts.

cuts are used for all energy bins and an optimization of the gammaness cut is done for each energy bin individually. The "standard" analysis sensitivities and the "likelihood" analysis sensitivity are comparable. This work, however, extends the sensitivity to one energy bin in the low energy and to two energy bins at the highest gamma-ray energies. The improved sensitivity at low energy is particularly interesting for the LST since the sensitivity of the CTA at high energy will be covered by the MSTs.

The sensitivity was then computed by optimizing the θ^2 and gammaness cuts for the lowest flux sensitivity (as done in section VI.4.3). The obtained sensitivity and the corresponding final selection cuts are shown in fig. VI.38. The sensitivity is improved when compared to the "standard" analysis is all bins of energy. In particular, the improvement is significant above 0.1 TeV. The flux sensitivity almost reaches 1% of the Crab Nebula flux around 1 TeV.

The flux sensitivity for different quality cuts is shown in fig. VI.39. It reaches similar flux sensitivity compare to the MAGIC stereoscopic array. The figure shows also that an increase in the leakage cut improves the flux sensitivity at high-energy (above 1 TeV). The size cuts explored do not seem to significantly affect the flux sensitivity.

The features importance for energy and direction regression as well as for the classifier are shown in fig. VI.40.

The energy and angular resolution as well as the performance of the gamma/hadron classifier are shown in fig. VI.41.

field of view.

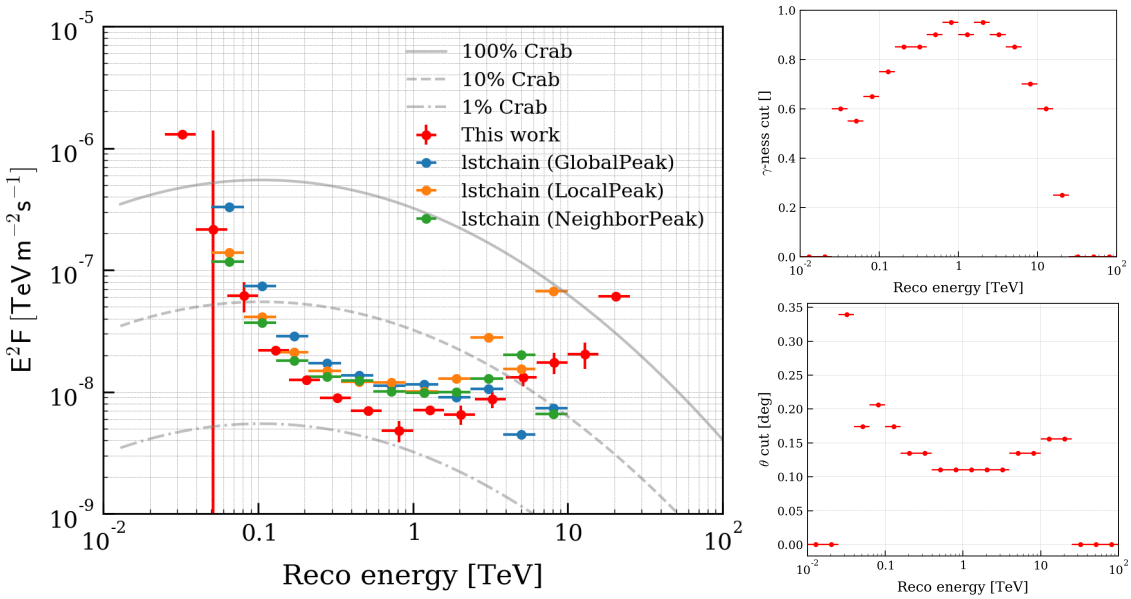

Figure VI.38. Left: Flux sensitivity as function of the reconstructed energy compared to the standard analysis (orange, blue, green). Right: Corresponding gamma-ness and θ cut as function of energy. The standard analysis uses a $\theta < 0.3°$ cut and an optimized cut of gamma-ness.

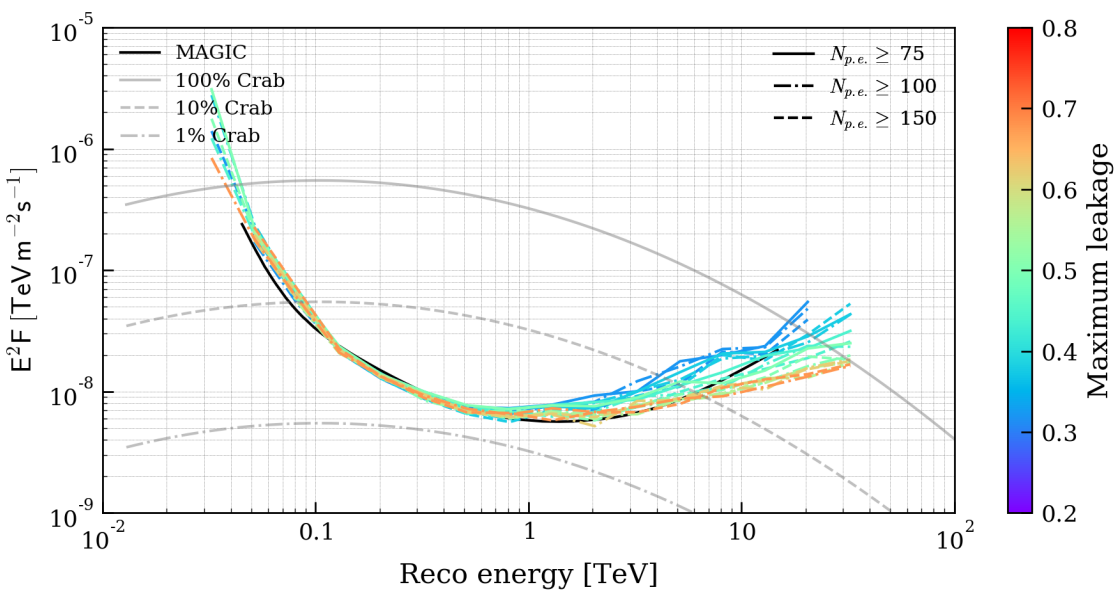

Figure VI.39. Flux sensitivity as function of the reconstructed energy compared to the MAGIC (stereo) sensitivity and for different quality cuts.

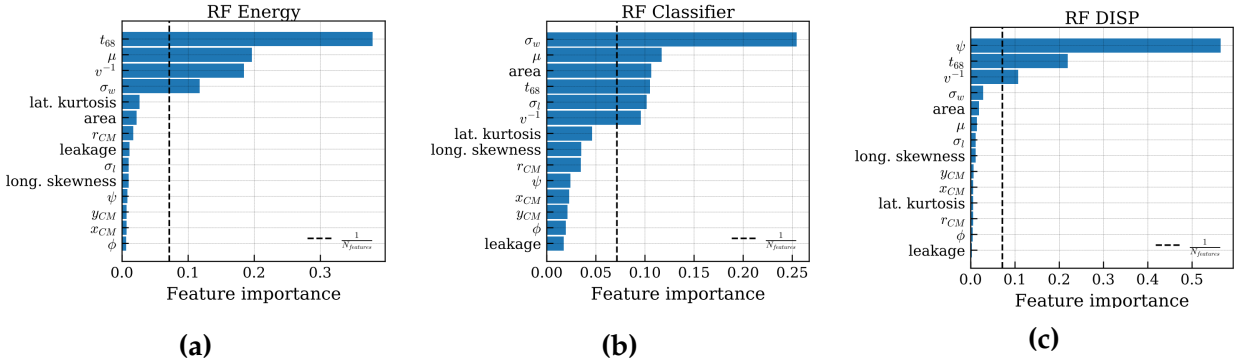

Figure VI.40. Feature importance for: energy regression (left), gamma/hadron separation (center) and direction reconstruction (right) of the LST random forests.

VI.6 Conclusion

A likelihood-based method for reconstructing the image parameters has been described. This likelihood results from the calibration of SiPM which is presented in chapter V. The likelihood combines the spatial and time part of the Cherenkov signal. This method has been applied to the SST-1M and LST Monte Carlo simulations.

In particular, when applied to the SST-1M it was shown that the sensitivity of the telescope is not sufficient to detect the Crab Nebula in 50 h of observations for the Kraków night-sky background conditions. However the analysis can be used for the next observational site of the SST-1M telescope in the hope to detect the Crab Nebula.

When compared to the LST standard reconstruction technique the method shows improvement in terms of sensitivity. To be more precise the sensitivity when optimizing the final selection cut reaches the one of the two MAGIC telescopes. Moreover the method is able to extend the sensitivity to low and high energies. In particular at high-energy the method is able to reconstruct leaking events at the edge of the camera and thus improves the sensitivity of the instrument. The improvement at low energy is supposedly attributed to "self-cleaning" feature of the method which is able to detect at lower signal over noise ratio.

Further improvement of the method could yield better sensitivity. For instance, the simplistic two-dimensional normal distribution could be replaced by a more realistic model taking into account the asymmetric longitudinal shower particle density profile. This would allow to measure the shower maximum and supposedly increase the energy resolution. Additionally, the time representation of the photon arrival time could be improved. The lateral time spread of the shower could also be taken into account. A better time representation of the event could improve again the sensitivity of the analysis. Reconstruction of muon events (used for calibration purposes, see section V.4), could also be performed with the method presented here. The spatial model would need to be adapted to a ring shape. For the time model, one can consider that muon signals are instantaneous as they have intrinsic time-spread of $\mathcal{O}(200\ \mathrm{ps})$) [139].

As an additional remark, the method takes into account the single pixel resolution via the use of the pixel likelihood. This in principle should enhance the sensitivity of the analysis for well characterized Cherenkov cameras. Thus the method performances should improve as the instrument is better characterized. In this work, the simulation considered that each pixel has similar charge resolution.

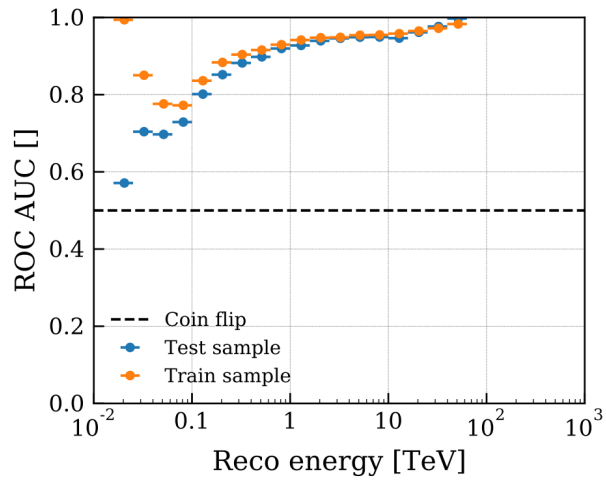

(a)

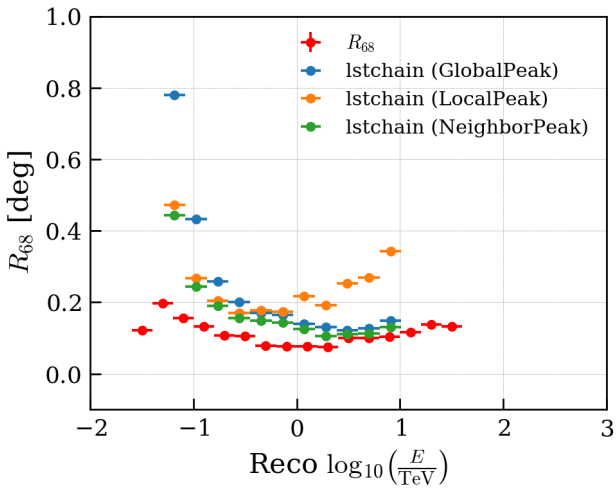

(b)

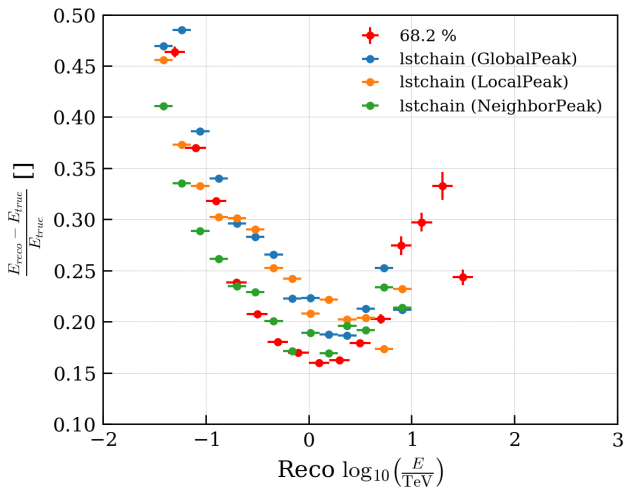

(c)

Figure VI.41. Top: ROC AUC as a function of the reconstruct red energy. Middle: Angular resolution as a function of the reconstructed energy. Bottom: Energy resolution as a function of the reconstructed energy.

Furthermore, the method could be more sensitive for high-resolution cameras where the EAS Cherenkov image is seen in great detailed. For instance, the LST camera foresees an upgrade with smaller ($\sim 0.05°$ pixel angular size) SiPM pixels and the SCT telescope has slightly bigger pixels ($\sim 0.07°$) but with wider field of view.

One disadvantage of this method is its computational time consumption. Nonetheless, several possible approximations of the likelihood function have been presented in order to reduce the computation time.

The method was applied to single telescope but could be adapted to stereo reconstruction. The log-likelihood would need to be summed over the telescopes. In this case, geometrical consideration on the orientation and position of the telescope with respect to the EAS would need to be implemented.

Finally, the results obtained here need to be confirmed by applying the presented analysis on telescope real data.

Chapter VII

Neutrino correlation analysis with ultra high-energy cosmic rays in the galactic magnetic field

As seen in section I.4.1 there is a connection between hadronic cosmic-rays and neutrinos. The hadronic interactions of cosmic-ray protons or nuclei produce charged pions which decay into neutrinos. In this context a correlation study between astrophysical neutrino directions and cosmic rays directions has been conducted.

However, as mentioned in section I.7, the angular resolution of cosmic-ray particle is limited as they undergo successive magnetic deflection along their voyage towards us. The deflection angle in the galactic magnetic field can be estimated with eq. (I.46). Moreover, the deflection angle is inversely proportional to the cosmic-ray energy E and proportional to the atomic number Z.

Following this, the correlation study has been limited to the highest energetic cosmic-rays in order to reduce the deflection scale. UHECRs from the Telescope Array (TA) [36] and the Pierre Auger Observatory (PAO) [34] respectively above 57 EeV and 52 EeV are used.

On the other side, the neutrinos being neutral particle are not deflected by magnetic fields. Thus they should point back to the sources of cosmic-rays. As already mentioned in section IV.1.5, the detection of astrophysical neutrinos on the ground is affected by a large atmospheric neutrino background. Based on this, the background has been reduced by selecting the best astrophysical neutrino candidates.

In section VII.1, the data sample used in this analysis is presented. In section VII.2, the analysis method is explained and its sensitivity is given. Finally, in section VII.3 the results of the correlation study are presented.

This work is the continuation of an analysis presented in [140] with updated statistics and refined galactic deflection models. The work has been presented in [141]. In addition, the sensitivity and upper limits of this analysis are given.

VII.1 Data sample

VII.1.1 Neutrino data sample

The neutrino sample comprises neutrino events from two neutrino detectors: IceCube [95] (see chapter IV) and ANTARES [142]. The samples from both telescopes are selected for their high signalness. In particular, high-energy events are less likely to come from atmospheric background.

The IceCube sample is composed of three sub-datasets:

- 7.5 years of Higher-Energy Starting Events (HESE) [143];
- 9 years of Extremely High-Energy event (EHE) alerts [144];
- 7 years of through-going muons from charged current interactions of ν_μ from the northern sky [145].

The HESE sample is composed of both cascade-like events and track-like events (see chapter IV for a definition of the event types). The cascade-like events have an angular resolution of about 15° (above 100 TeV) while the track-like events have an angular resolution of about 1°. The EHE event sample is composed of high-resolution ($\leq 1°$) track-like event in energies from 500 TeV to 10 PeV. The through-going muons sample is composed of tracks with energies beyond 200 TeV from the northern sky (reducing the atmospheric background).

Regarding the neutrino sample from ANTARES, it is selected from the 9 year point-source sample [146]. It comprises CC and NC interactions of all neutrino flavors. The angular resolution of this sample is estimated to be less than 0.5° at 10 TeV. Additionally, a selection on signalness greater than 40% is applied to this sample. This selection reduces the ANTARES sample to 3 track-like events.

The neutrino sample is then divided into two samples of track-like events and of cascade-like events. This is done in order to distinguish events with high angular resolution from low angular resolution. Additionally, cascade-like events suffer less from atmospheric background. In total, the neutrino sample is composed of 76 cascade-like events and 84 track-like events (see table VII.1). The likelihood sky-maps for both samples are shown in fig. VII.1. These maps are obtained from the stacking of single likelihood sky-maps. Each sky-map represents a neutrino event direction probability. The HESE sample provides likelihood maps which are computed for each event. However for the other samples only the angular uncertainty is given. In this case, the likelihood maps were generated from the angular uncertainty associated to the event using a gaussian point spread function. If the events angular uncertainty were undetermined, the sample median angular error was used as substitute.

VII.1.2 Ultra high-energy cosmic ray sample

From PAO $N_{PAO} = 324$ events with energies above 52 EeV and zenith angle below 80° are used. These events have an angular resolution less than 0.9°. The energy statistical uncertainty is less than 12% while the energy systematic uncertainty is estimated to be

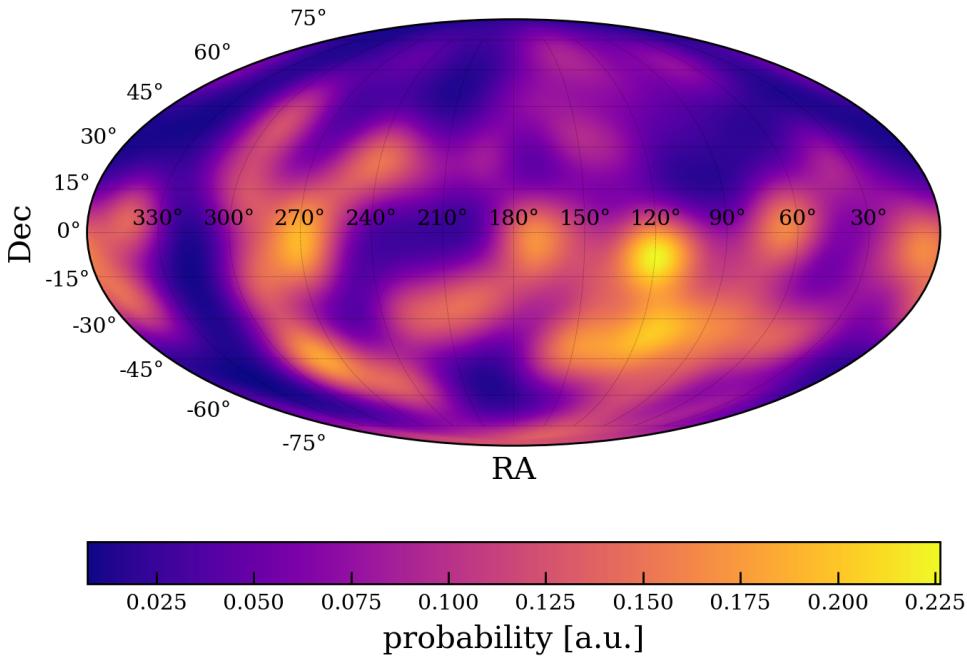

(a)

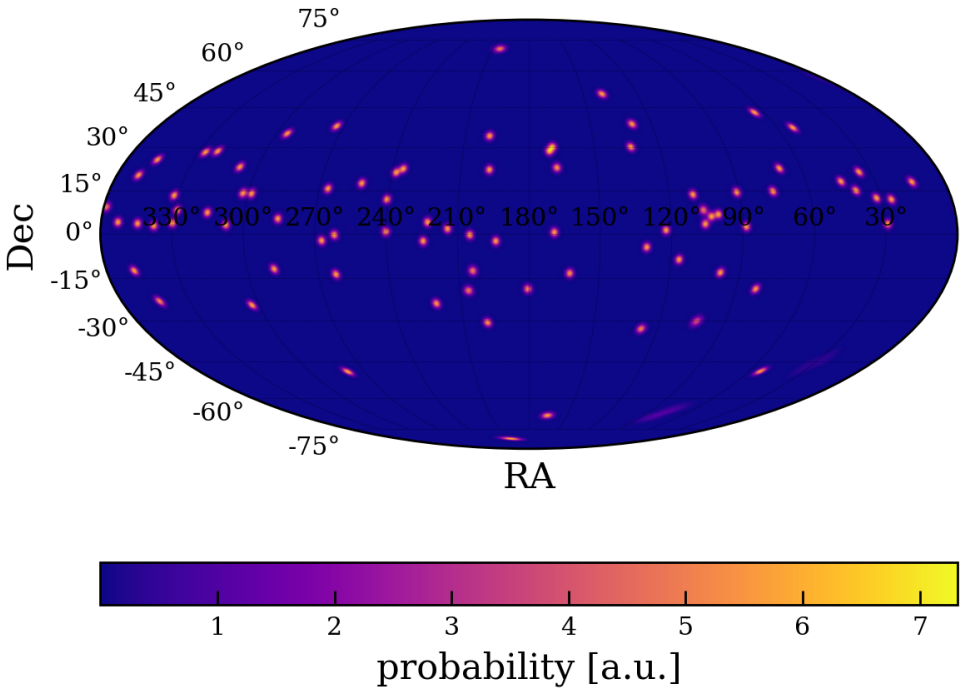

(b)

Figure VII.1. Likelihood sky-maps of the neutrino cascade-like (top) and track-like (bottom) event samples in equatorial coordinates.

Event type	Cascades	Tracks			
Sample name	HESE	ANTARES	HESE	EHE	Through-going muon
Number of events N_ν	76	3	26	20	35

Table VII.1. Summary of the neutrino cascade-like and track-like samples selected from IceCube and ANTARES.

14% [147, 148, 149]. These events have been recorded with the surface detector of the PAO from January 2004 up to April 2017.

From the TA, $N_{TA} = 143$ events with energy beyond 57 EeV and zenith angle below 55° have been selected. Regarding the energy resolution it is estimated to be 20% with a systematic uncertainty of 22%. TA estimates the angular resolution of these events to about 1.5° [150].

For both PAO and TA, the atomic number of each event is not provided. The atomic number measurement is only well constrained for EASs observed with fluorescence telescopes (where the shower maximum X_{max} can be measured). These telescopes collect the fluorescence light emitted by ultra-high energy EASs similarly as done by Cherenkov telescopes. The light yield of fluorescence light is much smaller than Cherenkov light (for the same EAS energy). However, its isotropic emission allows to detect showers at large distances. Thus, these telescope are well suited for very high-energy EASs. As for Cherenkov telescopes, they suffer from night-sky background and moon light and thus their duty cycle is limited. For these reasons, the majority of events from PAO and TA are obtained with the surface detector only. Thus the composition of UHECRs above $\mathcal{O}(100)$ EeV is poorly constrained due to the lack of statistics. Nonetheless, measurements of the UHECR composition by TA and PAO [151, 152] attribute a light mixture composition of proton and helium of the UHECRs between $\simeq 10$ EeV and $\simeq 100$ EeV.

The PAO and TA energy scale at the energies beyond $\mathcal{O}(\mathrm{EeV})$ do not match between the two experiments. In particular the energy spectra measured by both experiments are different [153]. To correct for that a scaling of both energy measured by each experiment is applied. Thus an increase of 14% to the PAO reconstructed energies and of -14% for the TA reconstructed energies are applied. These corrections are in accordance with the estimated systematic uncertainties. The UHECRs are shown in fig. VII.2 on the celestial sphere and the distribution in bins of energy is shown in fig. VII.3.

VII.2 Analysis method

In this analysis, the neutrino likelihood maps (see fig. VII.1) are considered as cosmic-ray sources maps. The analysis searches for the number of cosmic-ray events n_s that come from the neutrino sources. The parameter n_s is obtained by maximizing the log-likelihood:

$$\ln \mathcal{L}(n_s) = \sum_{i=1}^{N_{PAO}} \ln\left(\frac{n_s}{N_{CR}} S^i_{PAO} + \frac{N_{CR} - n_s}{N_{CR}} B^i_{PAO}\right) + \sum_{i=1}^{N_{TA}} \ln\left(\frac{n_s}{N_{CR}} S^i_{TA} + \frac{N_{CR} - n_s}{N_{CR}} B^i_{TA}\right), \quad \text{(VII.1)}$$

where $N_{CR} = N_{PAO} + N_{TA}$, S^i is the signal Probability Density Function (PDF) of the event i and B^i is the background PDF of the event i. The log-likelihood is separated in

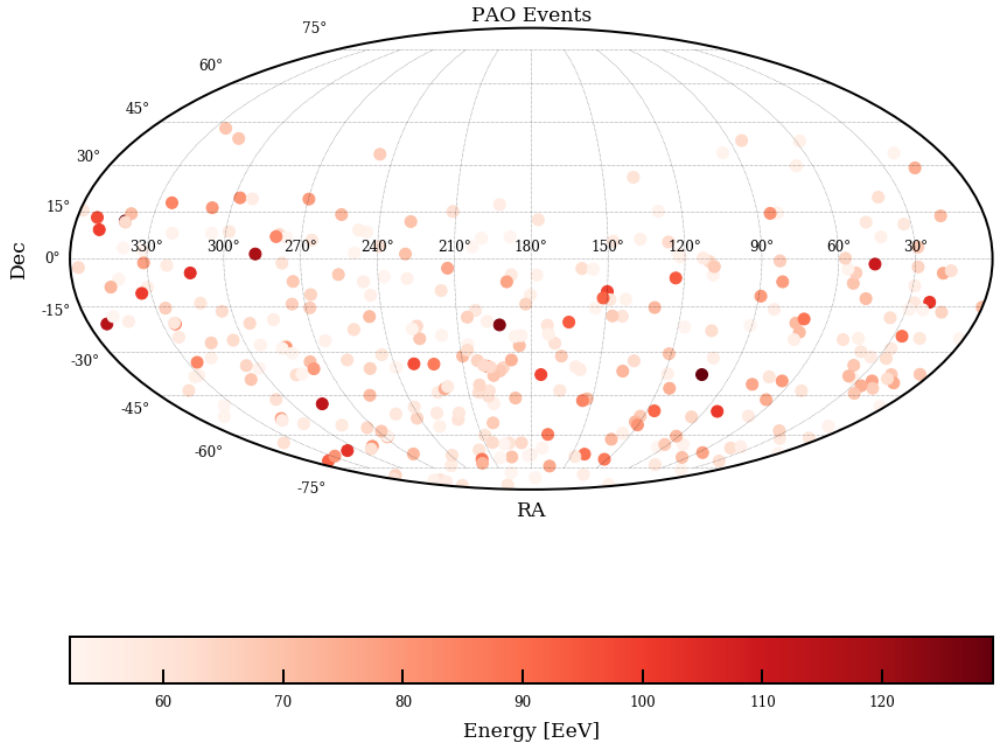

(a)

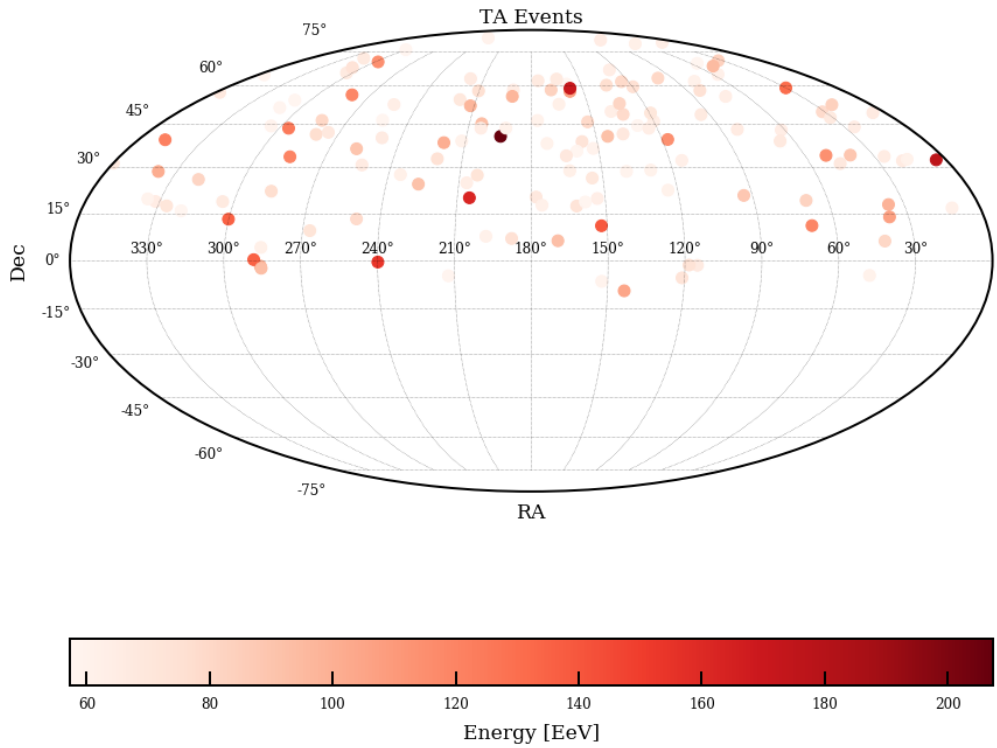

(b)

Figure VII.2. UHECRs events selected for this analysis. The figures show the UHECRs and their energy on the celestial sphere (in equatorial coordinates) from TA (top) and PAO (bottom).

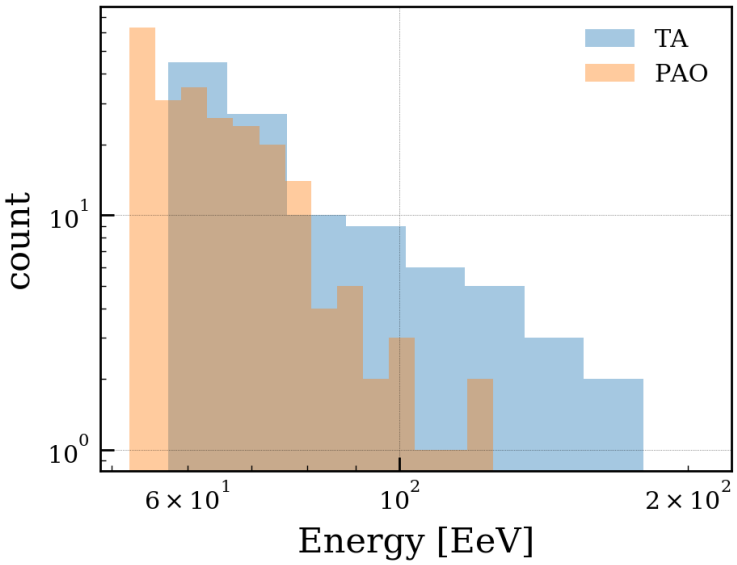

Figure VII.3. Number UHECRs in bins of energy from TA (blue) and PAO (orange).

two terms: one for each UHECR observatory. This is because the exposure and angular uncertainties of both observatories are different.

Additionally, one defines the null hypothesis H_0 as the background hypothesis where no UHECR event is correlated to the neutrino direction and the alternative hypothesis H_1 (signal hypothesis) is defined has when at least one UHECR event is correlated to the neutrino direction:

$$H_0 : n_s = 0, \tag{VII.2}$$

$$H_1 : n_s > 0. \tag{VII.3}$$

Background PDF The background PDF determines the probability of an event coming from background. For an isotropic background the background PDF is defined by the exposure of the instrument. For PAO and TA which use surface detectors (for this sample) the exposure is determined by geometrical consideration and only depend on the declination δ [154]. For a detector at latitude a_0 being efficient to detect particles with zenith angle less that θ_m, the exposure is given by:

$$\omega(\delta) \propto \cos a_0 \cos\delta \sin\alpha_m + \alpha_m \sin a_0 \sin\delta, \tag{VII.4}$$

where

$$\alpha_m = \begin{cases} 0 & \text{if } \xi > 1, \\ \pi & \text{if } \xi < -1, \\ \cos^{-1}\xi & \text{otherwise.} \end{cases}, \tag{VII.5}$$

and

$$\xi = \frac{\cos\theta_m - \sin a_0 \sin\delta}{\cos a_0 \cos\delta}. \tag{VII.6}$$

The exposure of TA and PAO as function of the declination δ are shown in fig. VII.4. The two experiments complement well each other allowing to reach a full-sky sensitivity.

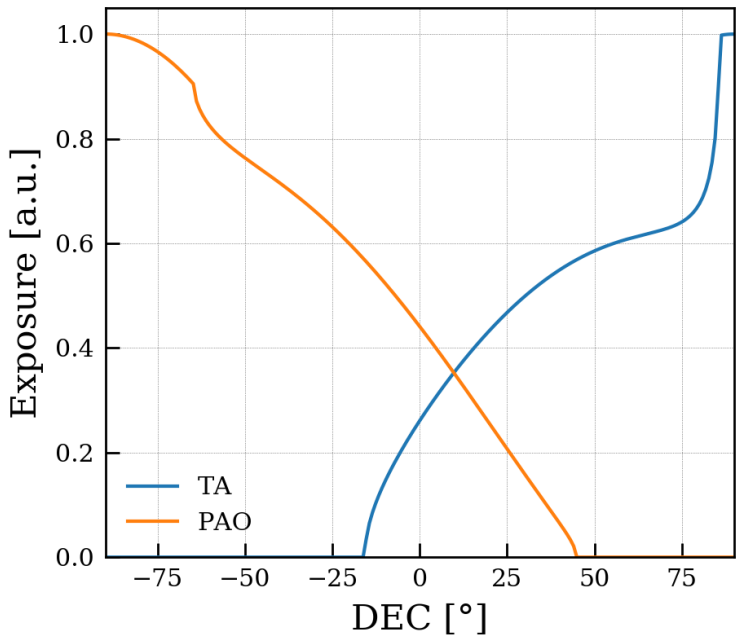

Figure VII.4. Relative exposure of the PAO (orange) and the TA (blue) as function of the declination.

Signal PDF The signal PDF S^i for the event i is determined by the stacked neutrino likelihood sky-maps (see fig. VII.1). In addition, the exposure ω of the UHECR observatory is also taken into account. The signal PDF is defined as:

$$S^i(\alpha_i,\ \delta_i,\ E_i) = \omega(\delta_i) \sum_{j=i}^{N_\nu} S_j(\alpha_i,\ \delta_i,\ \sigma_i(E_i)), \tag{VII.7}$$

where $S_j(\alpha_i,\ \delta_i, \sigma_i(E_i))$ is the likelihood of the event i to come from the neutrino event j, $\sigma_i(E_i)$ is the angular error of the cosmic-ray event i which depends on energy (see section VII.2.1), N_ν is the number of sources (i.e. the number of neutrino sky-maps), α_i and δ_i the right ascension and declination of the UHECR event i.

The angular uncertainty of the event i depends on the angular uncertainty of the experiment and the magnetic deflection θ_{RMS} (see eq. (I.46)). It is expressed as:

$$\sigma_i^2 = \sigma^2_{TA/PAO_i} + \theta^2_{RMS_i}. \tag{VII.8}$$

The likelihood maps $S_j(E_i)$ are obtained from the convolution of the neutrino likelihood maps with a two-dimensional normal distribution of angular width σ_i. Depending on the location of the neutrino event j (i.e. the source j) different magnetic deflection are used.

VII.2.1 Galactic magnetic deflection

In previous analysis, the magnetic deflection was considered as in eq. (I.46) and for three atomic numbers (Z =1, 2, 3) since the composition of UHECRs is not known. Here the deflection model is updated to consider the significant different deflection scale from galactic northern and southern hemispheres. As shown in fig. VII.5 for both galactic magnetic field models in [32, 33] the deflection scale for 100 EeV protons is different. In

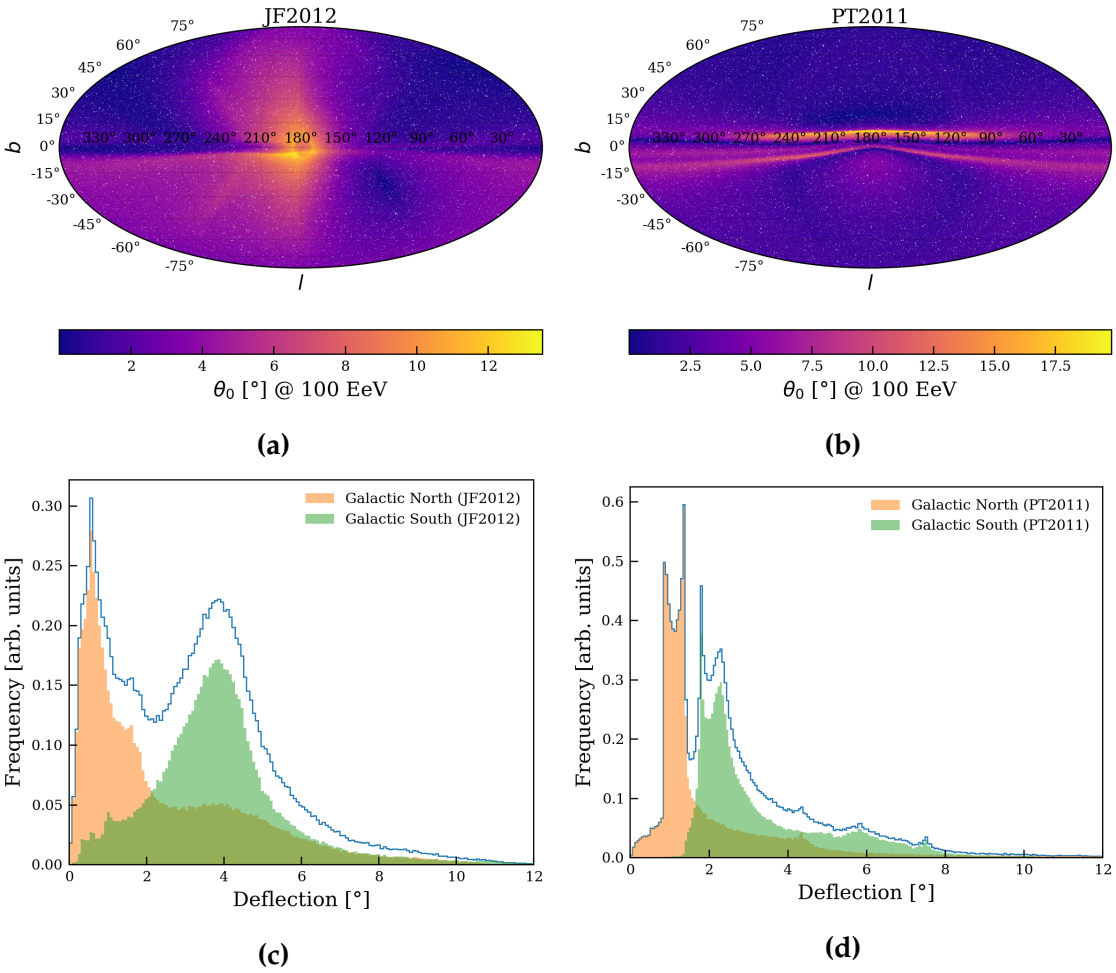

Figure VII.5. Galactic magnetic deflection scale for 100 EeV protons (Z = 1). The top figures show the deflection scale on the celestial sphere in galactic coordinates. The bottom figure shows the distribution of galactic magnetic deflections. For top and bottom, the figures show the model of [32] (left) and of [33] (right).

fact the median deflection scales for the galactic northern hemisphere are 2.4° and 2.3° respectively for the models in [32, 33]. For the galactic southern hemisphere the deflection scales are 3.9° and 3.4° respectively.

Averages deflection scales of the two galactic magnetic field models are considered. For the galactic northern and southern hemispheres this corresponds to 2.4° and 3.7°. In order to attribute a deflection which corresponds to the northern or southern galactic hemisphere the central coordinates of the neutrino are used.

VII.2.2 Sensitivity and discovery potential

Simulations of the UHECRs are performed to evaluate the significance of the results, the sensitivity and discovery potential of the analysis. To be more precise, the simulations generate n_s UHECRs coming from sources and $N_{CR} - n_s$ background event. This operation is repeated once sufficient statistic is reached.

For each simulated sample of N_{CR} UHECR the log-likelihood, defined in eq. (VII.1), is

Neutrino event type	Z	Sensitivity n_s	3σ discovery potential n_s
Cascades	1	56.6	113.9
	2	60.9	128.6
	3	64.2	135.1
Tracks	1	9.79	20.00
	2	9.82	20.76
	3	10.32	20.82

Table VII.2. Sensitivity and discovery potential of the correlation analysis of neutrino arrival directions and UHECRs arrival directions.

maximized and the corresponding $\hat{n}_s$ is obtained. In addition, one defines a test statistic (TS) as:

$$TS = -2\left(\ln \mathcal{L}(0) - \ln \mathcal{L}(\hat{n}_s)\right), \tag{VII.9}$$

with $\mathcal{L}(0)$ being the likelihood of the null-hypothesis H_0 (see eq. (VII.2)).

The $N_{CR} - n_s$ isotropic background events are generated according to the exposures of their respective experiment.

The n_s signal event energies are randomly chosen according to the energy spectra measured for each observatory. The position is attributed by the signal PDF which takes into account: detector exposure, galactic magnetic deflection and neutrino coordinates.

The number of background and signal events is randomly shared between events from PAO and TA according to the probability of belonging to each observatory. This probability is given by the fraction of events in each observatory (e.g. N_{PAO}/N_{CR} for PAO).

One defines, the sensitivity as the lowest simulated n_s for which 90% of its TS distribution is above the background ($n_s = 0$) TS distribution. While the 3σ discovery potential is defined as the lowest simulated n_s for which 50% of its TS distribution is 3σ above the background ($n_s = 0$) TS distribution.

The analysis was performed for three deflection scales corresponding to three atomic numbers Z =1, 2, 3. The sensitivities and 3σ discovery potentials for the track-like and cascade-like events are shown in table VII.2.

VII.3 Results

The results of this analysis are summarized in table VII.3. The most significant result is obtained for the cascade-like events with an atomic number $Z = 3$. This corresponds to a pre-trial p-value of 0.26 but when accounting the trial factor for having tested three different deflection scales the p-values increases to 0.78. Thus no significant correlation between the selected neutrino sample and the UHECRs from TA and PAO is observed.

In addition, the 90% confidence level (CL) upper limits for this analysis have been computed. The upper-limits are defined similarly as for the sensitivity. The are defined as the simulated n_s for which 90% of its TS distribution is above the TS observed from the

Neutrino event type	Z	p-value	TS	n_s	Upper limit n_s (90% CL)
Cascades	1	0.51 ± 0.01	2.61×10^{-6}	0.12	56.6
	2	0.38 ± 0.01	0.096	14.4	75.7
	3	0.26 ± 0.01	0.436	32.2	101.3
Tracks	1	1	0	0	9.79
	2	1	0	0	9.82
	3	1	0	0	10.32

Table VII.3. Results of the correlation analysis of neutrino arrival directions and UHECRs arrival directions.

data. In the case track-like events, where all TS obtained values are zero, the upper limits correspond to the sensitivity. The upper limits are show in table VII.3.

VII.4 Conclusion

A method for evaluating the significance of correlation between astrophysical neutrinos and UHECRs has been presented. The motivation behind this analysis arises from the hadronic processes in astrophysical accelerators. Such correlation might reveal source of neutrinos and UHECRs.

The dataset used from four different experiments have been introduced. The analysis, when compared to previous publications [140], has been updated to consider more realistically the galactic magnetic deflection. The performances in terms sensitivity and discovery potential of the analysis have been evaluated through Monte Carlo simulation of UHECRs.

The results from this analysis do not allow to conclude any significant correlation between UHECRs and neutrinos from IceCube and ANTARES. These results are compliant with the analysis presented in [141]. In particular, the third analysis in [141], which considers the UHECRs as sources rather than the neutrinos, obtains p-values all compatible with the background only hypothesis. Moreover, the first analysis presented in [141], which counts the neutrino-UHECR pairs for different angular scales, leads to similar conclusion.

The previous results obtained in [140] showed p-values for cascade-like events of the order of 10^{-4} when considering a magnetic deflection of 6° for 100 EeV helium. Thus the increased statistics in this work has revealed that the results presented in [140] might be attributed to statistical fluctuations.

Nonetheless the results of this analysis do not allow to conclude on the absence of correlation between the UHECRs and neutrinos. The galactic magnetic deflection and extra-galactic deflection are poorly known. Here the latest models of galactic magnetic field were applied. Additionally, the composition of UHECRs is not perfectly known and the atomic numbers used in this analysis might be too small. Besides, the UHECR horizon is limited by the GZK effect (see section I.7). This horizon is estimated between 10-100 Mpc depending on the UHECR composition. However the neutrinos might come from cosmological distances thus being not correlated to the UHECRs observed by TA and PAO. To conclude, the energy band of the UHECR considered in this analysis might be

to high for the ANTARES and IceCube neutrinos. The IceCube and ANTARES neutrinos might originate from hadronic interaction of lower energy cosmic-rays.

Conclusion

In this thesis, the fundamentals of cosmic-ray physics have been introduced. The composition and spectra of primary and secondary cosmic-rays have been shown. The cosmic-rays below the knee might originate from galactic accelerators, while the one above the ankle might primarily come from extra-galactic sources. The Fermi acceleration mechanism might explain the power-law spectral feature in particular for galactic sources such as SNRs. The hadronic and leptonic processes responsible for the production of neutrino and gamma-ray secondaries allow us to locate and characterize the cosmic-ray accelerators.

The detection principle of gamma-rays and high-energy neutrinos on the ground have been explained. The interaction of these messengers with air or ice produce charged secondaries that are detectable via the Cherenkov effect.

The current and future instruments of ground-based gamma-ray astronomy have been presented. In particular, the CTA and the SST-1M project have been detailed. The IceCube neutrino telescope has been also presented.

The calibration of the SST-1M camera has proven that its performance meets the requirement of the CTA. The method developed to calibrate the SiPMs was used to characterize the entire camera on a pixel-by-pixel basis. The photo-electron likelihood (and its method of maximization) used in the context of this work can be applied to other SiPM cameras. The parameter extracted allowed us to develop the Monte Carlo simulation models. Nonetheless, additional work is required for the flat-fielding of the camera. Especially, the on-site characterization with a flasher would be interesting to perform after appropriate calibration. Moreover, the inclusion of NSB fluctuations in the photo-electron likelihood might be useful to calibrate the camera on-site as done in the laboratory conditions.

Following the steps of the calibration results, the flux sensitivity of the SST-1M telescope has been obtained. The method used to reconstruct the Cherenkov images is based on likelihood maximization. Time and spatial constraints of the Cherenkov emission are used. In addition, the photo-sensor charge resolution is statistically propagated. The reconstruction method has been compared to standard techniques and promising results have been shown. In particular, with adequate final selection cuts, the sensitivity of the LST reaches the one of the MAGIC stereoscopic system. The full potential of the likelihood reconstruction method has not yet been exploited. Especially, the use of more realistic image models and time development models could improve the overall performance. Moreover, modification of the likelihood to account for stereoscopic reconstruction would be interesting. The geometrical constraints on the orientation of the array with respect to the EAS need to be found. To confirm the potential of this image reconstruction method, the processing of real telescope data would be interesting.

A correlation study between the UHERCs and the neutrinos based on a likelihood maximization has been conducted. Its application inspired the development of the likelihood based reconstruction for the SST-1M and LST telescopes. The correlation study is the follow-up of a previous 3σ excess correlation. The increased statistics and refined galactic magnetic deflection model have shown that this excess was a statistical fluctuation. The 90% confidence level upper limits on the number of correlated UHECRs have been established. The results are also confirmed by other similar analyses. Nonetheless, the results do not allow to draw any conclusion on the correlation between UHECRs and neutrinos. The horizon differences between neutrinos and UHECRs might lead to a small correlation fraction. In addition, the galactic and extra-galactic deflections might be underestimated. Additionally, the composition of UHECRs above the ankle is poorly known and the atomic number considered might be too small. Finally, the energy range of the neutrino used might be associated with lower energy cosmic-rays than UHECRs.

Bibliography

[1] B. Falkenburg and W. Rhode, From Ultra Rays to Astroparticles, A Historical Introduction to Astroparticle Physics. Springer, 2012.

[2] V. Hess, On the Observations of the Penetrating Radiation during Seven Balloon Flights, 1808.02927.

[3] W. Kolhörster, Messungen der durchdringenden Strahlungen bis in Höhen von 9300 m, Verh. Dtsch. Phys. Ges. **16** (03, 2020) 719–721.

[4] G. Bazilevskaya, M. Krainev, Y. Stozhkov, A. Svirzhevskaya and N. Svirzhevsky, Stratospheric measurements of cosmic rays in the 19th–22nd solar activity cycles, Advances in Space Research **14** (1994) 779 – 782.

[5] J. Clay, P. van Alphen and C. Hooft, Results of the Dutch Cosmic Ray Expedition 1933: II. The magnetic latitude effect of cosmic rays a magnetic longitude effect, Physica **1** (1934) 829 – 838.

[6] W. Baade and F. Zwicky, Cosmic Rays from Super-Novae, Proceedings of the National Academy of Sciences **20** (1934) 259–263, [https://www.pnas.org/content/20/5/259.full.pdf].

[7] I. S. Bowen, R. A. Millikan and H. V. Neher, New High-Altitude Study of Cosmic-Ray Bands and a New Determination of Their Total Energy Content, Phys. Rev. **44** (Aug, 1933) 246–252.

[8] C. D. Anderson, The Positive Electron, Phys. Rev. **43** (Mar, 1933) 491–494.

[9] S. H. Neddermeyer and C. D. Anderson, Note on the Nature of Cosmic-Ray Particles, Phys. Rev. **51** (May, 1937) 884–886.

[10] P. Carlson and A. A. Watson, Erich Regener and the maximum in ionisation of the atmosphere, 2014.

[11] Particle Data Group collaboration, P. Zyla et al., Review of Particle Physics, PTEP **2020** (2020) 083C01.

[12] C. Evoli, The Cosmic-Ray Energy Spectrum, Oct., 2018. 10.5281/zenodo.2360277.

[13] A. Pacini, Cosmic rays: Bringing messages from the sky to the Earth's surface, Revista Brasileira de Ensino de Física **39** (01, 2017) .

[14] K. Bernlöhr, A. Barnacka, Y. Becherini, O. Blanch Bigas, E. Carmona, P. Colin et al., Monte Carlo design studies for the Cherenkov Telescope Array, Astroparticle Physics **43** (Mar., 2013) 171–188, [1210.3503].

[15] "Radiology Café." https://www.radiologycafe.com.

[16] I. Collaboration, Evidence for High-Energy Extraterrestrial Neutrinos at the IceCube Detector, Science **342** (2013) , [https://science.sciencemag.org/content/342/6161/1242856.full.pdf].

[17] E. Fermi, On the Origin of the Cosmic Radiation, Physical Review **75** (Apr., 1949) 1169–1174.

[18] T. K. Gaisser, R. Engel and E. Resconi, Cosmic Rays and Particle Physics. Cambridge University Press, 2 ed., 2016, 10.1017/CBO9781139192194.

[19] Andrii Neronov, "High-Energy Astrophysics." April, 2015.

[20] M. Meyer, D. Horns and H. S. Zechlin, The Crab Nebula as a standard candle in very high-energy astrophysics, Astronomy and Astrophysics **523** (Nov., 2010) A2, [1008.4524].

[21] J. Aleksić, S. Ansoldi, L. Antonelli, P. Antoranz, A. Babic, P. Bangale et al., Measurement of the Crab Nebula spectrum over three decades in energy with the MAGIC telescopes, Journal of High Energy Astrophysics **5-6** (Mar, 2015) 30–38.

[22] D. Caprioli, Understanding hadronic gamma-ray emission from supernova remnants, JCAP **05** (2011) 026, [1103.2624].

[23] T. D. Matteo, A. King and N. J. Cornish, Black Hole Formation and Growth. Springer Berlin Heidelberg, 2019, 10.1007/978-3-662-59799-6.

[24] B. Sarkar, Active Galactic Nuclei (AGN) and Xray studies of Galaxy M51, Master's thesis, Tezpur University, 06, 2011.

[25] S. Kelner, F. A. Aharonian and V. Bugayov, Energy spectra of gamma-rays, electrons and neutrinos produced at proton-proton interactions in the very high energy regime, Phys. Rev. D **74** (2006) 034018, [astro-ph/0606058].

[26] C. Spiering, Towards high-energy neutrino astronomy, The European Physical Journal H **37** (July, 2012) 515–565.

[27] A. Cooray, Extragalactic Background Light: Measurements and Applications, 1602.03512.

[28] W. B. Atwood, A. A. Abdo, M. Ackermann, W. Althouse, B. Anderson, M. Axelsson et al., THE LARGE AREA TELESCOPE ON THE *FERMI GAMMA-RAY SPACE TELESCOPE MISSION*, The Astrophysical Journal **697** (may, 2009) 1071–1102.

[29] MAGIC collaboration, E. Aliu et al., Very-High-Energy Gamma Rays from a Distant Quasar: How Transparent Is the Universe?, Science **320** (2008) 1752, [0807.2822].

[30] H.E.S.S. collaboration, F. Aharonian et al., A low level of extragalactic background light as revealed by gamma-rays from blazars, Nature **440** (2006) 1018–1021, [astro-ph/0508073].

[31] P. Chen and K. D. Hoffman, Origin and evolution of cosmic accelerators - the unique discovery potential of an UHE neutrino telescope: Astronomy Decadal Survey (2010-2020) Science White Paper, 0902.3288.

[32] R. Jansson and G. R. Farrar, A New Model of the Galactic Magnetic Field, The Astrophysical Journal **757** (Aug, 2012) 14.

[33] M. S. Pshirkov, P. G. Tinyakov, P. P. Kronberg and K. J. Newton-McGee, Deriving global structure of the Galactic Magnetic Field from Faraday Rotation Measures of extragalactic sources, Astrophys. J. **738** (2011) 192, [1103.0814].

[34] The Pierre Auger Collaboration, The Pierre Auger Cosmic Ray Observatory, Nuclear Instruments and Methods in Physics Research Section A: Accelerators, Spectrometers, Detectors and Associated Equipment **798** (Oct, 2015) 172–213.

[35] A. Aab, P. Abreu, M. Aglietta, I. F. M. Albuquerque, I. Allekotte, A. Almela et al., An Indication of Anisotropy in Arrival Directions of Ultra-high-energy Cosmic Rays through Comparison to the Flux Pattern of Extragalactic Gamma-Ray Sources, The Astrophysical Journal **853** (feb, 2018) L29.

[36] H. Kawai, S. Yoshida, H. Yoshii, K. Tanaka, F. Cohen, M. Fukushima et al., Telescope Array Experiment, Nuclear Physics B - Proceedings Supplements **175-176** (2008) 221 – 226.

[37] Pierre Auger, Telescope Array collaboration, A. di Matteo et al., Full-sky searches for anisotropies in UHECR arrival directions with the Pierre Auger Observatory and the Telescope Array, PoS **ICRC2019** (2020) 439, [2001.01864].

[38] D. Heck, "CORSIKA – an Air Shower Simulation Program." https://www.ikp.kit.edu/corsika/ (accessed: 12.04.2020).

[39] "Nuclear Power." https://www.nuclear-power.net.

[40] M. de Naurois and D. Mazin, Ground-based detectors in very-high-energy gamma-ray astronomy, Comptes Rendus Physique **16** (2015) 610 – 627.

[41] A. De Angelis and M. Pimenta, Particle Detection. Springer International Publishing, Cham, 2018, 10.1007/978-3-319-78181-5_4.

[42] W. Heitler, The Quantum Theory of Radiation (third ed.). Oxford University Press, London, 1954.

[43] J. Holder, Atmospheric Cherenkov Gamma-ray Telescopes, 1510.05675.

[44] J. Matthews, A Heitler model of extensive air showers, Astroparticle Physics **22** (2005) 387 – 397.

[45] R. Ulrich, R. Engel and M. Unger, Hadronic multiparticle production at ultrahigh energies and extensive air showers, Phys. Rev. D **83** (03, 2011) .

[46] R. Springer, The High Altitude water Cherenkov (HAWC) Observatory, Nuclear and Particle Physics Proceedings **279-281** (2016) 87 – 94.

[47] T. C. Weekes, The Atmospheric Cherenkov Imaging Technique for Very High Energy Gamma-ray Astronomy, arXiv:astro-ph/0508253.

[48] A. Acharyya, I. Agudo, E. Angüner, R. Alfaro, J. Alfaro, C. Alispach et al., Monte Carlo studies for the optimisation of the Cherenkov Telescope Array layout, Astroparticle Physics **111** (2019) 35 – 53.

[49] "Air shower Cherenkov light simulations." https://www.mpi-hd.mpg.de/hfm/CosmicRay/ChLight/ChLat.html.

[50] A. M. Hillas, Cerenkov Light Images of EAS Produced by Primary Gamma Rays and by Nuclei, in 19th International Cosmic Ray Conference (ICRC19), vol. 3, p. 445, Aug., 1985.

[51] C. Benn and S. Ellison, Brightness of the night sky over La Palma, New Astronomy Reviews **42** (Nov, 1998) 503–507.

[52] "*SkyCalc - ESO Sky Model Calculator*." http://www.eso.org/observing/etc/doc/skycalc/helpskycalc.html.

[53] C. Alispach *et* al., SST-1M TDR and Annexed document repository, Oct, 2018.

[54] I. A. Samarai, C. Alispach, F. Cadoux, V. Coco, D. della Volpe, Y. Favre et al., Performance of a small size telescope (SST-1M) camera for gamma-ray astronomy with the Cherenkov Telescope Array, 2017.

[55] "H.E.S.S. High Energy Stereoscopic System." https://www.mpi-hd.mpg.de/hfm/HESS/.

[56] T. Weekes, H. Badran, S. Biller, I. Bond, S. Bradbury, J. Buckley et al., VERITAS: the Very Energetic Radiation Imaging Telescope Array System, Astroparticle Physics **17** (May, 2002) 221–243.

[57] S. Klepser, The magic telescopes - status and recent results, 2011.

[58] "VERITAS Very Energetic Radiation Imaging Telescope Array System." https://veritas.sao.arizona.edu/.

[59] "The MAGIC telescopes." https://magic.mpp.mpg.de/.

[60] B.S. Acharya *et* al., Introducing the CTA concept, Astroparticle Physics **43** (2013) 3 – 18.

[61] S. P. Wakely and D. Horan, TeVCat: An online catalog for Very High Energy Gamma-Ray Astronomy, International Cosmic Ray Conference **3** (2008) 1341–1344.

[62] P. A. Caraveo, The golden age of high-energy gamma-ray astronomy: the Cherenkov Telescope Array in the multimessenger era, La Rivista del Nuovo Cimento **43** (Apr., 2020) 281–318.

[63] S. Archambault *et al.*, Gamma-ray observations under bright moonlight with VERITAS, Astropart. Phys. **91** (2017) 34–43, [1703.01307].

[64] MAGIC collaboration, D. Guberman *et al.*, Using UV-pass filters for bright Moon observations with MAGIC, PoS **ICRC2015** (2016) 1237, [1509.02048].

[65] H. Anderhub *et al.*, Design and operation of FACT - the first G-APD Cherenkov telescope, JINST **8** (2013) P06008, [arXiv:1304.1710].

[66] S. Vercellone, The key science projects of the Cherenkov telescope array, AIP Conference Proceedings **1792** (2017) 030001.

[67] "CTA Performance." https://www.cta-observatory.org/science/cta-performance/.

[68] C. Adams, G. Ambrosi, M. Ambrosio, C. Aramo, W. Benbow, B. Bertucci et al., Prototype Schwarzschild-Couder Telescope for the Cherenkov Telescope Array: Commissioning Status of the Optical System, 1909.11403.

[69] G. Pühlhofer, C. Bauer, S. Bernhard, M. Capasso, S. Diebold, F. Eisenkolb et al., FlashCam: a fully-digital camera for the medium-sized telescopes of the Cherenkov Telescope Array, 2015.

[70] J.-F. Glicenstein, O. Abril, J.-A. Barrio, O. B. Bigas, J. Bolmont, F. Bouyjou et al., Nectarcam : a camera for the medium size telescopes of the cherenkov telescope array, 2015.

[71] G. Pareschi, The ASTRI SST-2M prototype and mini-array for the Cherenkov Telescope Array (CTA), in Ground-based and Airborne Telescopes VI (H. J. Hall, R. Gilmozzi and H. K. Marshall, eds.), vol. 9906, pp. 1992 – 2004, International Society for Optics and Photonics, SPIE, 2016. DOI.

[72] A. Dmytriiev, L. Dangeon, G. Fasola, H. Sol, A. Zech, J. Gironnet et al., Assessment of the GCT prototype's optical system implementation and other key performances for the Cherenkov Telescope Array, 1909.11450.

[73] A. M. Brown, A. Abchiche, D. Allan, J.-P. Amans, T. P. Armstrong, A. Balzer et al., The GCT camera for the Cherenkov Telescope Array, Ground-based and Airborne Telescopes VI (Jul, 2016) .

[74] The CTA Consortium, Science with the Cherenkov Telescope Array, .

[75] J. Aasi, B. P. Abbott, R. Abbott, T. Abbott, M. R. Abernathy, K. Ackley et al., Advanced LIGO, Classical and Quantum Gravity **32** (Mar, 2015) 074001.

[76] A. De Angelis, M. Roncadelli and O. Mansutti, Evidence for a new light spin-zero boson from cosmological gamma-ray propagation?, Phys. Rev. D **76** (2007) 121301, [0707.4312].

[77] M. Meyer, D. Montanino and J. Conrad, On detecting oscillations of gamma rays into axion-like particles in turbulent and coherent magnetic fields, JCAP **09** (2014) 003, [1406.5972].

[78] Wikipedia, "Photomultiplier tube — Wikipedia, The Free Encyclopedia." http://en.wikipedia.org/w/index.php?title=Photomultiplier%20tube&oldid=986730978, 2020.

[79] SensL, "Introduction to SiPM, Technical Note." https://www.sensl.com/downloads/ds/TN%20-%20Intro%20to%20SPM%20Tech.pdf, 2011.

[80] S. Vinogradov, Analytical models of probability distribution and excess noise factor of solid state photomultiplier signals with crosstalk, Nucl. Instrum. Meth. A **695** (2012) 247.

[81] K. Tayabaly, D. Spiga, R. Canestrari, G. Bonnoli, M. Lavagna and G. Pareschi, Roughness tolerances for Cherenkov telescope mirrors, in Optics for EUV, X-Ray, and Gamma-Ray Astronomy VII (S. L. O'Dell and G. Pareschi, eds.), vol. 9603, pp. 43 – 56, International Society for Optics and Photonics, SPIE, 2015. DOI.

[82] SST-1M sub-Consortium collaboration, J. A. Aguilar, A. Basili, V. Boccone, F. Cadoux, A. Christov, D. della Volpe, T. Montaruli, L. Płatos, M. Rameez, Design, optimization and characterization of the light concentrators of the single-mirror small size telescopes of the Cherenkov Telescope Array, Astropart. Phys. **60** (2015) 32–40, [1404.2734].

[83] M. Heller *et* al., The SST-1M project for the Cherenkov Telescope Array, PoS(ICRC2019)694 (2019) .

[84] M. Heller *et* al., An innovative silicon photomultiplier digitizing camera for gamma-ray astronomy, Eur. Phys. J. **C77** (2017) 47, [arXiv:1607.03412].

[85] C. Alispach, J. Borkowski, F. Cadoux, N. D. Angelis, D. D. Volpe, Y. Favre et al., Large scale characterization and calibration strategy of a SiPM-based camera for gamma-ray astronomy, Journal of Instrumentation **15** (nov, 2020) P11010–P11010, [2008.04716].

[86] FACT collaboration, M. L. Knoetig, *et* al., FACT - Long-term stability and observations during strong Moon light, in Proceedings, 33rd Int. Cosmic Ray Conference (ICRC2013): Rio de Janeiro, Brazil, July 2-9, 2013, p. 0695, 2013. 1307.6116.

[87] A. Nagai, C. Alispach, A. Barbano, C., V. Coco, D. della Volpe et al., Characterization of a large area silicon photomultiplier, Nuclear Instruments and Methods in Physics Research Section A: Accelerators, Spectrometers, Detectors and Associated Equipment **948** (2019) 162796.

[88] J. A. Aguilar *et* al., The front-end electronics and slow control of large area SiPM for the SST-1M camera developed for the CTA experiment, Nucl. Instrum. Meth. **A830** (2016) 219–232.

[89] E. Lyard and R. W. for the CTA Consortium, End-to-end data acquisition pipeline for the Cherenkov Telescope Array, 2017.

[90] "*protozfitsreader*." https://github.com/cta-sst-1m/protozfitsreader.

[91] Super-Kamiokande collaboration, A. Renshaw et al., First Indication of Terrestrial Matter Effects on Solar Neutrino Oscillation, Phys. Rev. Lett. **112** (2014) 091805, [1312.5176].

[92] K. Hirata et al., Observation in the Kamiokande-II Detector of the Neutrino Burst from Supernova SN 1987a, Phys. Rev. D **38** (1988) 448–458.

[93] L. Rädel, M. Erdmann and C. Wiebusch, Measurement of High-Energy Muon Neutrinos with the IceCube Neutrino Observatory, in PhD thesis, 2017.

[94] F. Halzen, Building a New Window on the Universe, 2018.

[95] M. Aartsen, M. Ackermann, J. Adams, J. Aguilar, M. Ahlers, M. Ahrens et al., The IceCube Neutrino Observatory: instrumentation and online systems, Journal of Instrumentation **12** (Mar, 2017) P03012–P03012.

[96] "IceCube South Pole Neutrino Observatory." https://icecube.wisc.edu/.

[97] M. Ahlers, K. Helbing and C. Pérez de los Heros, Probing particle physics with IceCube, The European Physical Journal C **78** (Nov, 2018) .

[98] IceCube Collaboration, Evidence for High-Energy Extraterrestrial Neutrinos at the IceCube Detector, Science **342** (Nov, 2013) 1242856–1242856.

[99] M. Aartsen, M. Ackermann, J. Adams, J. A. Aguilar, M. Ahlers, M. Ahrens et al., Multimessenger observations of a flaring blazar coincident with high-energy neutrino IceCube-170922A, Science **361** (2018) , [https://science.sciencemag.org/content/361/6398/eaat1378.full.pdf].

[100] M. Aartsen, M. Ackermann, J. Adams, J. Aguilar, M. Ahlers, M. Ahrens et al., Time-Integrated Neutrino Source Searches with 10 Years of IceCube Data, Physical Review Letters **124** (Feb, 2020) .

[101] The CTA consortium, Design concepts for the Cherenkov Telescope Array CTA: an advanced facility for ground-based high-energy gamma-ray astronomy, Experimental Astronomy **32** (Dec, 2011) 193–316.

[102] S. S. Zhang, B. Y. Bi, C. Wang, Z. Cao, L. Q. Yin, T. Montaruli et al., SiPM-Based Camera Design and Development for the Image Air Cherenkov Telescope of LHAASO, Springer Proc. Phys. **212** (2018) 17–21.

[103] N. Budnev, I. Astapov, P. Bezyazeekov, A. Borodin, M. Brückner, D. Chernykh et al., TAIGA—A hybrid array for high-energy gamma astronomy and cosmic-ray physics, Nuclear Instruments and Methods in Physics Research Section A: Accelerators, Spectrometers, Detectors and Associated Equipment **958** (2020) 162113.

[104] J. A. Aguilar *et* al., Front-end and slow control electronics for large area SiPMs used for the single mirror Small Size Telescope (SST-1M) of the Cherenkov Telescope Array (CTA), Proc.SPIE **9915** (2016) 9915 – 9915 – 8.

[105] A. Nagai, C. Alispach, D. della Volpe, M. Heller, T. Montaruli, S. Njoh et al., Studies of SiPM behaviour under continuous background light illumination, in prep. (2019) .

[106] Gianluca, Chiozzi and Birger, Gustafsson and Bogdan, Jeram and Mark, Plesko and Matej, Sekoranja and Gasper, Tkacik and K., Zagar, CORBA-based common software for the ALMA project, .

[107] "*digicampipe*." https://github.com/cta-sst-1m/digicampipe.

[108] K. Kosack *et* al., ctapipe: A Low-level Data Processing Framework for CTA, Proceedings of Science ICRC19 (2019) .

[109] J.A. Aguilar *et* al., DigiCam: fully digital compact camera for SST-1M telescope, in Society of Photo-Optical Inst. Eng. (SPIE) Conf. Series, vol. 9147, p. 5, aug, 2014. DOI.

[110] P. Rajda *et* al., DigiCam - Fully digital compact read-out and trigger electronics for the SST-1M telescope proposed for the cherenkov telescope array, PoS(ICRC2015)931 (2015) , [arXiv:1508.06082].

[111] N. De Angelis, Studies of readout electronics and optical elements for a gamma-ray telescope, Master's thesis, Université de Genève, 2019.

[112] CTA Consortium collaboration, S. Toscano et al., Using muon rings for the optical throughput calibration of the SST-1M prototype for the Cherenkov Telescope Array, PoS **ICRC2015** (2016) 735, [1509.00266].

[113] F. Goebel, K. Mase, R. Mirzoian, M. Teshima and M. Meyer, Absolute energy scale calibration of the MAGIC telescope using muon images, in Proceedings, 7th Workshop on Towards a Network of Atmospheric Cherenkov Detectors 2005: Palaiseau, France, April 27-29, 2005, pp. 199–203, 2005.

[114] H.E.S.S. collaboration, R. Chalme-Calvet, M. de Naurois and J. P. Tavernet, Muon efficiency of the H.E.S.S. telescope, in International Workshop on Atmospheric Monitoring for High-Energy Astroparticle Detectors (AtmoHEAD 2013) Gif-sur-Yvette, France, June 10-12, 2013, 2014. 1403.4550.

[115] VERITAS collaboration, D. Hanna, Calibration Techniques for VERITAS, 0709.4479.

[116] A. Biland et al., Calibration and performance of the photon sensor response of FACT – The First G-APD Cherenkov telescope, JINST **9** (2014) P10012, [1403.5747].

[117] M. Garczarczyk, S. Schlenstedt, L. Oakes, U. Schwanke and the MST Team, Status of the Medium-Sized Telescope for the Cherenkov Telescope Array, PoS(ICRC2015)959 (2015) , [arXiv:1509.01361].

[118] L. Nozka, H. Hiklova, P. Horvath, M. Hrabovsky, D. Mandat, M. Palatka et al., Monitoring of mirror degradation of fluorescence detectors at the Pierre Auger Observatory due to dust sedimentation, Journal of Instrumentation **13** (may, 2018) T05005–T05005.

[119] I. A. Samarai, C. Alispach, F. Cadoux, V. Coco, D. della Volpe, Y. Favre et al., Development of a strategy for calibrating the novel SiPM camera of the SST-1M telescope proposed for the Cherenkov Telescope Array, PoS(ICRC2017)800 (2017) , [arXiv:1709.03920].

[120] M. L. Knoetig, J. Hose and R. Mirzoyan, SiPM Avalanche Size and Crosstalk Measurements with Light Emission Microscopy, IEEE Transactions on Nuclear Science **61** (2014) 1488–1492.

[121] V. Chmill, E. Garutti, R. Klanner, M. Nitschke and J. Schwandt, On the characterisation of SiPMs from pulse-height spectra, Nucl. Instrum. Meth. **A854** (2017) 70–81, [1609.01181].

[122] K. Bernlöhr, sim_telarray Reference Manual, 2019.

[123] J. Juryšek *et* al., Monte Carlo study of single SST-1M prototype for Cherenkov Telescope Array, PoS(ICRC2019)708 (2019) , [arXiv:1907.08061].

[124] S. Le Bohec, B. Degrange, M. Punch, A. Barrau, R. Bazer-Bachi, H. Cabot et al., A new analysis method for very high definition Imaging Atmospheric Cherenkov Telescopes as applied to the CAT telescope, Nuclear Instruments and Methods in Physics Research Section A: Accelerators, Spectrometers, Detectors and Associated Equipment **416** (Nov, 1998) 425–437.

[125] R. Parsons and J. Hinton, A Monte Carlo template based analysis for air-Cherenkov arrays, Astroparticle Physics **56** (Apr, 2014) 26–34.

[126] J. Juryšek, The observations of gamma ray sources and calibration of the Cherenkov Telescope Array Observatory. PhD thesis, Charles University, 2020.

[127] K. Kosack, J. Watson, M. Nöthe, J. Jacquemier, A. Mitchell, D. Neise et al., cta-observatory/ctapipe: v0.9.1, Oct., 2020. 10.5281/zenodo.4084989.

[128] M. Heß, K. Bernlöhr, A. Daum, M. Hemberger, G. Hermann, W. Hofmann et al., The time structure of Cherenkov images generated by TeV γ-rays and by cosmic rays, Astroparticle Physics **11** (Jul, 1999) 363–377.

[129] E. Aliu, H. Anderhub, L. Antonelli, P. Antoranz, M. Backes, C. Baixeras et al., Improving the performance of the single-dish Cherenkov telescope MAGIC through the use of signal timing, Astroparticle Physics **30** (2009) 293 – 305.

[130] F. James and M. Winkler, MINUIT User's Guide, .

[131] iminuit team, "iminuit – a python interface to minuit." https://github.com/iminuit/iminuit.

[132] J. Albert, E. Aliu, H. Anderhub, P. Antoranz, A. Armada, M. Asensio et al., Implementation of the Random Forest method for the Imaging Atmospheric Cherenkov Telescope MAGIC, Nuclear Instruments and Methods in Physics Research Section A: Accelerators, Spectrometers, Detectors and Associated Equipment **588** (2008) 424 – 432.

[133] I. Shilon, M. Kraus, M. Büchele, K. Egberts, T. Fischer, T. Holch et al., Application of deep learning methods to analysis of imaging atmospheric Cherenkov telescopes data, Astroparticle Physics **105** (Feb, 2019) 44–53.

[134] R. D. Parsons and S. Ohm, Background rejection in atmospheric Cherenkov telescopes using recurrent convolutional neural networks, The European Physical Journal C **80** (May, 2020) .

[135] T. Vuillaume, M. Jacquemont, L. Antiga, A. Benoit, P. Lambert, G. Maurin et al., GammaLearn - first steps to apply Deep Learning to the Cherenkov Telescope Array data, in 23rd International Conference on Computing in High Energy and Nuclear Physics (CHEP 2018), (Sofia, Bulgaria), July, 2018.

[136] F. Pedregosa, G. Varoquaux, A. Gramfort, V. Michel, B. Thirion, O. Grisel et al., Scikit-learn: Machine Learning in Python, Journal of Machine Learning Research **12** (2011) 2825–2830.

[137] T. P. Li and Y. Q. Ma, Analysis methods for results in gamma-ray astronomy., Astrophysical Journal **272** (Sept., 1983) 317–324.

[138] "*lstchain*." https://github.com/cta-observatory/cta-lstchain.

[139] M. Gaug, S. Fegan, A. M. W. Mitchell, M. C. Maccarone, T. Mineo and A. Okumura, Using Muon Rings for the Calibration of the Cherenkov Telescope Array: A Systematic Review of the Method and Its Potential Accuracy, The Astrophysical Journal Supplement Series **243** (Jul, 2019) 11.

[140] The IceCube, Pierre Auger and Telescope Array collaborations, Search for correlations between the arrival directions of IceCube neutrino events and ultrahigh-energy cosmic rays detected by the Pierre Auger Observatory and the Telescope Array, Journal of Cosmology and Astroparticle Physics **2016** (jan, 2016) 037–037.

[141] IceCube, Pierre Auger, Telescope Array, ANTARES collaboration, A. Barbano, Search for correlations of high-energy neutrinos and ultra-high energy cosmic rays, PoS **ICRC2019** (2020) 842, [2001.09057].

[142] ANTARES collaboration, M. Ageron et al., ANTARES: the first undersea neutrino telescope, Nucl. Instrum. Meth. **A656** (2011) 11–38, [1104.1607].

[143] IceCube collaboration, R. Abbasi et al., The IceCube high-energy starting event sample: Description and flux characterization with 7.5 years of data, 2011.03545.

[144] IceCube collaboration, M. G. Aartsen et al., Differential limit on the extremely-high-energy cosmic neutrino flux in the presence of astrophysical background from nine years of IceCube data, Phys. Rev. **D98** (2018) 062003, [1807.01820].

[145] IceCube collaboration, C. Haack and C. Wiebusch, A measurement of the diffuse astrophysical muon neutrino flux using eight years of IceCube data., PoS **ICRC2017** (2018) 1005.

[146] ANTARES collaboration, A. Albert et al., First all-flavor neutrino pointlike source search with the ANTARES neutrino telescope, Phys. Rev. **D96** (2017) 082001, [1706.01857].

[147] C. Bonifazi and Pierre Auger Collaboration, The angular resolution of the Pierre Auger Observatory, Nuclear Physics B Proceedings Supplements **190** (May, 2009) 20–25, [0901.3138].

[148] Pierre Auger collaboration, P. Abreu et al., The Pierre Auger Observatory I: The Cosmic Ray Energy Spectrum and Related Measurements, in 32nd International Cosmic Ray Conference, Beijing 2011, 2011. 1107.4809.

[149] Pierre Auger collaboration, B. Dawson, The Energy Scale of the Pierre Auger Observatory, PoS **ICRC2019** (2019) 231.

[150] T. Abu-Zayyad, R. Aida, M. Allen, R. Anderson, R. Azuma, E. Barcikowski et al., The Cosmic-Ray Energy Spectrum Observed with the Surface Detector of the Telescope Array Experiment, Astrop. J. **768** (May, 2013) L1, [1205.5067].

[151] W. Hanlon, Telescope Array 10 Year Composition, PoS **ICRC2019** (2020) 280, [1908.01356].

[152] M. Plum, Measurements of the Mass Composition of UHECRs with the Pierre Auger Observatory, in Proceedings of 2016 International Conference on Ultra-High Energy Cosmic Rays (UHECR2016), 2016. https://journals.jps.jp/doi/pdf/10.7566/JPSCP.19.011011. DOI.

[153] AbuZayyad, Tareq, Deligny, Olivier, Ikeda, Daisuke, Ivanov, Dmitri, Lhenry-Yvon, Isabelle, Maris, Ioana et al., Auger-TA energy spectrum working group report, EPJ Web Conf. **210** (2019) 01002.

[154] P. Sommers, Cosmic ray anisotropy analysis with a full-sky observatory, Astropart. Phys. **14** (2001) 271–286, [astro-ph/0004016].